INSIGHTS ON ADSORPTIVE AND CATALYTIC WATER REMEDIATION USING METAL CHALCOGENIDES AND BISMUTH BASED NANOMATERIALS

Thesis submitted to the
University of Calicut in partial fulfilment of
the requirements for the award of the degree of

DOCTOR OF PHILOSOPHY IN PHYSICS

Under the Faculty of Science

SRAVANDAS P

DEPARTMENT OF PHYSICS

UNIVERSITY OF CALICUT

KERALA, INDIA-673635

AUGUST 2024

INSIGHTS ON ADSORPTIVE AND CATALYTIC WATER REMEDIATION USING METAL CHALCOGENIDES AND BISMUTH BASED NANOMATERIALS.

Ph.D. Thesis in Physics

Author:

SRAVANDAS P
Research Scholar
Laboratory for Mesoscopic Science and Devices
Department of Physics
University of Calicut
Calicut University P.O- 673635
Kerala, India
Email: sravandasp@uoc.ac.in

Under the guidance of

Dr. LIBU K. ALEXANDER
Associate Professor
Department of Physics
University of Calicut
Calicut University P.O- 673635
Kerala, India
Email: LKA@uoc.ac.in

UNIVERSITY OF CALICUT
DEPARTMENT OF PHYSICS

Dr. LIBU K. ALEXANDER   Room F12, Dept. of Physics
PhD (IIT Bombay), PDF (Paris, Canberra)   Calicut University PO, Kerala
Associate Professor   INDIA, 673635
Email: LKA@uoc.ac.in   Tel: +91- 9645611252

CERTIFICATE

Certified that the work presented in the thesis, entitled '**INSIGHTS ON ADSORPTIVE AND CATALYTIC WATER REMEDIATION USING METAL CHALCOGENIDES AND BISMUTH BASED NANOMATERIALS**' is based on the authentic record of research carried out by **Mr. SRAVANDAS P** under my guidance in the Department of Physics, University of Calicut, Calicut University P.O, Kerala-673635 and this work has not been included in any other thesis submitted previously for the award of any degree. Also certified that the corrections suggested by the adjudicators have been incorporated in the revised thesis.

Calicut University   Dr. Libu K. Alexander

10-01-2025

UNIVERSITY OF CALICUT
DEPARTMENT OF PHYSICS

Dr. LIBU K. ALEXANDER   Room F12, Dept. of Physics
PhD (IIT Bombay), PDF (Paris, Canberra)   Calicut University PO, Kerala
Associate Professor   INDIA, 673635
Email: LKA@uoc.ac.in   Tel: +91- 9645611252

CERTIFICATE

Certified that the work presented in the thesis, entitled '**INSIGHTS ON ADSORPTIVE AND CATALYTIC WATER REMEDIATION USING METAL CHALCOGENIDES AND BISMUTH BASED NANOMATERIALS**' is based on the authentic record of research carried out by **Mr. SRAVANDAS P** under my guidance in the Department of Physics, University of Calicut, Calicut University P.O, Kerala-673635 and this work has not been included in any other thesis submitted previously for the award of any degree.

Calicut University   Dr. Libu K. Alexander

06-08-2024

DECLARATION

I hereby declare that the work presented in the thesis entitled '**INSIGHTS ON ADSORPTIVE AND CATALYTIC WATER REMEDIATION USING METAL CHALCOGENIDES AND BISMUTH BASED NANOMATERIALS'** is based on the original work done by me under the guidance of Dr. Libu K. Alexander, Associate Professor, Department of Physics, University of Calicut, Calicut University (P.O), Kerala- 673635 and has not been included in any other thesis submitted previously for the award of any degree. The contents of the thesis are undergone plagiarism check using iThenticate software at C.H.M.K. Library, University of Calicut, and the similarity index found within the permissible limit. I also declare that the thesis is free from AI generated contents.

Calicut University   SRAVANDAS P

06-08-2024

Signature of the Guide

"There is a single light of science, and to brighten it anywhere is to brighten it everywhere."

- Isaac Asimov

ABSTRACT

Water pollution has recently garnered increased attention due to its severe negative impacts on life and the planet's ecosystem. Given the essential role of water in sustaining a healthy life, sourcing clean freshwater is one of the most pressing challenges facing modern society. The grave situation demands further advancements in sustainable water use practices and the developing of cost-effective wastewater treatment technologies.

This thesis focuses on the remediation of organic and inorganic pollutants in wastewater using nanomaterials as nano-adsorbents and nano-catalysts. The primary goal is to develop nanomaterials and demonstrate their effectiveness, at the laboratory level, in adsorption and catalytic processes for water remediation. It addresses four common but toxic industrial effluents—surfactants, phosphate ions, antibiotics, and industrial dyes—using adsorptive and catalytic strategies with metal chalcogenides and Bi-based nanomaterials.

We synthesized CuS nanostructures and demonstrated their effectiveness as adsorbents and catalysts for removing sodium dodecyl sulfate (SDS) from water. The efficient decomposition of SDS was achieved through adsorption and advanced oxidation processes driven by hemi-micelle enhanced adsorption and the synergistic action of H_2O_2. The fast catalytic decomposition of SDS resembles a Fenton-like process. This study is the first to report the use of metal chalcogenides for surfactant removal from water.

We developed a dual-functional MnS nanomaterial for the removal of phosphate ions and Congo Red dye. Synthesized via a hydrothermal route, the MnS nanomaterials exhibited a phosphate adsorption capacity of 160.73 mg P/g. Adsorption studies indicated a spontaneous, exothermic process with mechanisms involving electrostatic attraction, surface complexation, and ion exchange. MnS maintained selective phosphate adsorption despite competing ions and demonstrated high sonocatalytic efficiency by degrading Congo Red dye within 10 minutes. These findings highlight MnS as a promising non-lanthanum or zirconium material for phosphate removal from wastewater and a sonocatalyst for textile dye degradation.

We synthesized $BiOBr_{(1-x)}Cl_x$ nanoplates with varied Br:Cl ratios using a co-precipitation method, showing superior visible-light-driven photocatalytic activity

compared to BiOCl and BiOBr. Morphological, optical, and structural analyses revealed that halide alloying successfully tuned the optical bandgap in the samples from 3.39 eV to 2.75 eV, enhancing their light-harvesting capabilities. The $BiOBr_{0.25}Cl_{0.75}$ sample achieved 89% and 99% degradation efficiency for ciprofloxacin and tetracycline hydrochloride, respectively, within 20 minutes. The high performance is due to its large surface area, suitable morphology, band gap, and effective electron-hole separation in the solid solution. The material is recyclable, stable, and adaptable to aquatic environments, making it a promising eco-friendly photocatalyst for antibiotic pollution control.

We developed a heterojunction $BiVO_4$ structure by combining distinct crystal phases to overcome limitations in traditional $BiVO_4$ photocatalysts, such as poor charge transport and surface adsorption. A hydrothermal method was used to synthesize tetragonal, monoclinic, and monoclinic/tetragonal $BiVO_4$ phases. The photocatalytic activity, particularly for Rhodamine B degradation, was enhanced using ultrasonic sound waves. The study revealed that the crystalline phases significantly affect photo-sono-induced charges, providing deeper insight into the mechanisms behind improved sonophotocatalytic activity.

This study scientifically demonstrates, at the laboratory level, the effective removal of toxic contaminants found in industrial effluents using innovative adsorbents, photocatalysts, sonocatalysts, and sonophotocatalysis. These findings reveal the potential of these nanomaterials for scalable and energy-efficient water purification. An in-depth analysis of the mechanism and the kinetics and thermodynamics of the adsorption and catalytic processes is also reported. The research underscores the promise of metal chalcogenides and bismuth-based nanomaterials as innovative solutions for addressing water pollution challenges.

ഗവേഷണ സംഗ്രഹം

ഭൂമിയിലെ ആവാസവ്യവസ്ഥയെയും ജീവന്റെ നിലനില്പിനെയും ഗുരുതരമായി ബാധിച്ചുകൊണ്ടിരിക്കുന്ന ജല മലിനീകരണം എന്ന വിപത്ത് ഗവേഷണ മേഖലയിൽ ഉൾപ്പെടെ, വർദ്ധിച്ച ശ്രദ്ധ ആകർഷിച്ചിരിക്കുന്നു. ആരോഗ്യകരമായ ജീവിതം നിലനിർത്തുന്നതിൽ ശുദ്ധജലത്തിനുള്ള പങ്ക് ഒഴിച്ചുകൂടാനാവാത്തതാണ്. ആയതുകൊണ്ടുതന്നെ ശുദ്ധജലത്തിന്റെ അപര്യാപ്തത ആധുനിക സമൂഹം നേരിടുന്ന ഏറ്റവും പ്രധാനപ്പെട്ട വെല്ലുവിളികളിൽ ഒന്നാണ്. ലോകമെമ്പാടുമുള്ള ജലമലിനീകരണ സ്രോതസ്സുകളെ പരിഗണിക്കുമ്പോൾ, ജലമലിനീകരണത്തിന്റെ ഏറിയ പങ്കും വ്യവസായ ശാലകളിൽ നിന്നും പുറംതള്ളുന്ന വലിയ അളവിലുള്ള മലിന ജലത്തിൽനിന്നാണ്. ഇത്തരം വ്യാവസായിക മാലിന്യങ്ങളെ ജലസ്രോതസ്സുകളിലേക്ക് നിർബാധം ഒഴുക്കിവിടുകയാണ് സാധാരണയായി കാണാറുള്ളത്. അവയുണ്ടാക്കുന്ന ഗുരുതരമായ ആരോഗ്യപ്രശ്നങ്ങളും പാരിസ്ഥിതിക പ്രശ്നങ്ങളും എടുത്തുപറയേണ്ടുന്ന പ്രത്യാഘാതങ്ങൾ ആണ്. ഗുരുതരമായ ഈ സാഹചര്യം പരിഗണിക്കുമ്പോൾ, സുസ്ഥിരമായ ജല-വിനിയോഗ രീതികളിലും മാലിന്യജല ശുദ്ധീകരണ സാങ്കേതികവിദ്യകളുടെ ആവിർഭാവത്തിലും കൂടുതൽ മുന്നേറ്റം ആവശ്യമാണ് എന്ന തിരിച്ചറിവിലേക്ക് നാം ചെന്നെത്തുന്നു. ഇത്തരം ജലസംസ്കരണ യന്ത്രസംവിധാനങ്ങൾക്ക് (waste-water treatment plants) കാര്യക്ഷമമായി പ്രവർത്തിക്കുവാനുതകുന്ന പദാർത്ഥങ്ങൾ വികസിപ്പിച്ചെടുക്കുക, അവയെ പറ്റി സമഗ്രമായി പഠനം നടത്തുക, അത്തരം സങ്കേതങ്ങൾക്ക് ശാസ്ത്രീയമായ അടിത്തറ ഉണ്ടാക്കുക എന്നുള്ളതുമാണ് ഈ ഗവേഷണ പ്രബന്ധത്തിന്റെ പ്രധാന ലക്ഷ്യം.

അധിശോഷണം (adsorption), ഉൽപ്രേരണം (catalysis) എന്നീ പ്രക്രിയകൾ ഉപയോഗിച്ചുള്ള ജലശുദ്ധീകരണം ഗവേഷണ മേഖലകളിൽ ഏറെ ശ്രദ്ധയാകർഷിച്ചുകൊണ്ടിരിക്കുന്നതും മികവുറ്റതുമായ മാർഗ്ഗങ്ങളാണ്. ഈ മേഖലയിലുള്ള പുതിയ സാധ്യതകളെ മനസ്സിലാക്കുകയും അവയെ പരിപോഷിപ്പിച്ചുകൊണ്ടുള്ള നൂതനമാർഗ്ഗങ്ങൾ മാലിന്യജല ശുദ്ധീകരണ ശാസ്ത്ര-സാങ്കേതികവിദ്യകൾക്ക് സമഗ്ര സംഭാവനയായി നൽകിക്കൊണ്ട് മുന്നേറുക എന്നുള്ളതും ഞങ്ങളുടെ ഗവേഷണ ലക്ഷ്യത്തിൽ ഉൾപ്പെടുന്നു. അതിനായി അധിശോഷകങ്ങളായും (adsorbents) ഉൽപ്രേരകങ്ങളായും (catalysts) പ്രയോജനപ്പെടുത്താൻ കഴിയുന്ന നാനോപദാർത്ഥങ്ങൾ വികസിപ്പിച്ചെടുക്കുകയും അവ ഉപയോഗിച്ച് കൊണ്ട് മാലിന്യജലത്തിലെ കാർബണികവും അകാർബണികവുമായ മലിനീകാരികളെ പൂർണ്ണമായും നശിപ്പിക്കുകയും അവയുടെ ഫലപ്രാപ്തി പരീക്ഷണശാലാ തലത്തിൽ തെളിയിക്കുകയുമാണ് ഈ ഗവേഷണപഠനത്തിലൂടെ ഞങ്ങൾ പ്രധാനമായും ലക്ഷ്യമിടുന്നത്. വ്യവസായശാലകൾ പുറംതള്ളുന്നതും ഗുരുതര പാരിസ്ഥിതിക പ്രശ്നങ്ങൾ ഉണ്ടാക്കുന്നതുമായ നാല് മലിനീകാരികളെയാണ് (pollutants) ഈ പഠനത്തിൽ ഞങ്ങൾ ശ്രദ്ധകേന്ദ്രീകരിച്ചിരിക്കുന്നത്. സർഫക്റ്റാന്റുകൾ, ഫോസ്ഫേറ്റ് അയോണുകൾ, ആന്റിബയോട്ടിക്കുകൾ, വ്യാവസായിക ചായങ്ങൾ എന്നിവ അവയിൽ ഉൾപ്പെടുന്നു.

ഒന്നാമതായി , ഞങ്ങൾ CuS നാനോപദാർത്ഥങ്ങൾ വികസിപ്പിച്ചെടുക്കുകയും, അവയെ ഉപയോഗപ്പെടുത്തിക്കൊണ്ട് ജലത്തിൽ നിന്ന് സോഡിയം ഡോഡെകൈൽ സൾഫേറ്റ് (SDS) എന്ന മലിനീകാരിയെ അധിശോഷണപ്രക്രിയ വഴി ഫലപ്രദമായി നീക്കം ചെയ്യാൻ കഴിയുന്നു എന്നും കണ്ടെത്തി. വ്യാവസായിക അടിസ്ഥാനത്തിൽ ഉപയോഗിക്കുന്ന മറ്റു അധിശോഷകങ്ങളെ താരതമ്യം ചെയ്യുമ്പോൾ, CuS

നാനോപദാർത്ഥങ്ങൾക്ക് വളരെ ഉയർന്ന അധിശോഷണ വ്യാപ്തി (adsorption density) ഉള്ളതായി കണ്ടെത്തി. ഇതിനു പിന്നിലുള്ള ശാസ്ത്രീയ വശങ്ങളെ സമഗ്രമായി പഠിക്കുകയും അധിശോഷണക്രിയാവിധി (Mechanism of adsorption) നിർദ്ദേശിക്കുകയും ചെയ്തു. ഞങ്ങൾ വികസിപ്പിച്ചെടുത്ത CuS നാനോപദാർത്ഥങ്ങൾ കേവലം അധിശോഷകങ്ങൾ മാത്രമായല്ല പ്രവർത്തിക്കുന്നത്, അതിനെ കൂടാതെ അവയുടെ ഉൽപ്രേരക സ്വഭാവവും പ്രയോജനപ്പെടുത്തി, SDS തന്മാത്രകളെ (ഹൈഡ്രജൻ പെറോക്സൈഡ് തന്മാത്രകളുടെ സാന്നിധ്യത്തിൽ) പൂർണ്ണമായും വിഘടനം നടത്തുകയും ചെയ്യുന്നു എന്നും കണ്ടെത്തി. CuS നാനോപദാർത്ഥങ്ങൾ ഹൈഡ്രജൻ പെറോക്സൈഡ് തന്മാത്രകളുടെ സാന്നിധ്യത്തിൽ മാത്രം ആണ് ഇത്തരം ഉൽപ്രേരണം കാണിക്കുന്നത്. വളരെ വേഗത്തിൽ നടക്കുന്നതായി കണ്ടെത്തിയ SDS ന്റെ അപചയപ്രവർത്തനം 'ഫെന്റൺ രാസപ്രക്രിയയെ' അനുകരിക്കുന്നതായി ഞങ്ങൾ അനുമാനിക്കുന്നു. അധിശോഷണ പ്രവർത്തനങ്ങളുടെയും ഉൽപ്രേരകങ്ങളെ അടിസ്ഥാനമാക്കിയുള്ള SDS അപചയ പ്രവർത്തനത്തിന്റെയും താപഗതികം (thermodynamics) വിശദമായി പഠിക്കുകയും അവയുടെ താപഗതിക സാധ്യത മനസിലാക്കുകയും ചെയ്തു. എല്ലാ അധിശോഷകങ്ങൾക്കും ഇത്തരം ഉൽപ്രേരക സ്വഭാവം ഉണ്ടാകണം എന്നില്ല. ഈ രണ്ടു സ്വഭാവവും CuS നാനോപദാർത്ഥങ്ങളിൽ സമ്മിശ്രമായി സമ്മേളിക്കുന്നതിനാൽ ഞങ്ങൾ വികസിപ്പിച്ചെടുത്ത CuS നാനോപദാർത്ഥങ്ങളെ ഉൽപ്രേരക-അധിശോഷകങ്ങൾ (catalytic- adsorbents) എന്ന് വിശേഷിപ്പിക്കുന്നു. ജലത്തിൽ നിന്നും സർഫാക്റ്റന്റ് നീക്കം ചെയ്യുന്നതിന് ലോഹ ചാൽക്കോജനൈഡുകൾ ഉപയോഗിക്കുന്നത് റിപ്പോർട്ട് ചെയ്യുന്ന ആദ്യത്തെ പഠനമാണിത്.

രണ്ടാമതായി, ഫോസ്ഫേറ്റ് അയോണുകളും കോംഗോ റെഡ് (CR) ചായവും മലിനജലത്തിൽ നിന്ന് നീക്കം ചെയ്യുന്നതിന് ഒരു ദ്വൈത പ്രവർത്തന സ്വഭാവമുള്ള MnS

നാനോ പദാർത്ഥങ്ങൾ വികസിപ്പിച്ചെടുത്തു. ഹൈഡ്രോതെർമൽ മാർഗത്തിലൂടെ സംശ്ലേഷണം ചെയ്ത MnS നാനോപദാർത്ഥങ്ങൾക്ക് ഉയർന്ന ഫോസ്ഫേറ്റ് അധിശോഷണ വ്യാപ്തി (adsorption density) ഉണ്ടായിരുന്നു. വിവിധങ്ങളായ അധിശോഷണ സമതാപവക്രങ്ങൾ (adsorption isotherms) പ്രയോജനപ്പെടുത്തിക്കൊണ്ട് MnS നാനോപദാർത്ഥങ്ങളും ഫോസ്ഫേറ്റ് അയോണുകളും തമ്മിലുള്ള അധിശോഷണക്രിയാവിധി നിർദ്ദേശിക്കുകയും ചെയ്തു. അതുകൂടാതെ MnS നാനോപദാർത്ഥങ്ങൾ മറ്റൊരു സവിശേഷ പ്രവർത്തനവും കാണിക്കുന്നതതായി ഞങ്ങൾ കണ്ടെത്തി. ഉയന്ന ആവൃത്തിയിലുള്ള ശബ്ദതരംഗങ്ങളുടെ സാനിധ്യത്തിൽ MnS നാനോപദാർത്ഥങ്ങൾ ഉത്തേജിക്കപ്പെടുകയും, അവ വലിയ തന്മാത്രകളെ വിഘടിപ്പിക്കാൻ കഴിയുന്ന അഡ്വാൻസ്ഡ് ഓക്സീകരണ പ്രക്രിയക്ക് കാരണമാകുന്നു എന്നും പരീക്ഷണ-നിരീക്ഷണങ്ങളിലൂടെ മനസ്സിലാക്കുവാൻ കഴിഞ്ഞു. ഇത്തരത്തിൽ, കോംഗോ റെഡ് എന്ന വ്യാവസായിക ചായത്തെ 10 മിനുട്ടിനുള്ളിൽ പൂർണമായും നശിപ്പിക്കുകയും, CR തന്മാത്രകളെ വിഘടിപ്പിച് കാർബൺ ഡൈഓക്സൈഡ്, ജലതന്മാത്രകൾ എന്നിവയായി മാറ്റുകയും ചെയ്യുന്നു എന്നും മനസ്സിലാക്കി. ഇതിനുപിന്നിലുള്ള രാസപ്രവർത്തനങ്ങളും അവയെ ശബ്ദതരംഗങ്ങൾ എങ്ങനെ സ്വാധീനിക്കുന്നു എന്നും സമഗ്രമായി പഠിച്ചു. CR തന്മാത്രകളുടെ നശീകരണക്രിയാവിധി (degradation mechanism) എങ്ങനെ ആകാം എന്നും ഈ പഠനത്തിൽ ഞങ്ങൾ നിർദ്ദേശിക്കുന്നു. അൾട്രാസോണിക് ശബ്ദതരംഗങ്ങളുടെ സാനിധ്യത്തിൽ നടക്കുന്ന ഇത്തരം അഡ്വാൻസ്ഡ് ഓക്സീകരണ പ്രക്രിയക്ക് ശാസ്ത്രഭാഷയിൽ പറയുന്ന പേരാണ് 'ശബ്ദ-പ്രചോദന ഉൽപ്രേരണം' അഥവാ sonocatalysis. ജലശുദ്ധീകരണ മേഖലയിൽ ഏറെ പ്രയോജനപ്പെടുത്താവുന്ന നൂതനമായ മാർഗ്ഗം ആണിത്. ഇവിടെ ശ്രദ്ധിക്കേണ്ടതായ ഒരു പ്രധാന കാര്യം, MnS നാനോ പദാർത്ഥങ്ങൾ ഫോസ്ഫേറ്റ്

അധിശോഷകങ്ങളായി മാത്രം അല്ല പ്രവർത്തിക്കുന്നത്, മറിച്ച് ശബ്ദതരംഗങ്ങളുടെ സാനിധ്യത്തിൽ CR തന്മാത്രകളെ വിഘടിപ്പിക്കുവാൻ കഴിവുള്ള ഉൽപ്രേരകവുമാണ്. അതായത്, MnS നാനോ പദാർത്ഥങ്ങൾ ഒരു ദ്വൈത പ്രവർത്തന സ്വഭാവമുള്ള സവിശേഷത പ്രകടിപ്പിക്കുന്നു. ഈ പ്രവർത്തനങ്ങളുടെ എല്ലാം താപഗതികം, അപചയ പ്രവർത്തനഗതികം (decomposition reaction kinetics), വിഘടനപ്രവർത്തനത്തെ സ്വാധീനിക്കുന്ന ഘടകങ്ങൾ, പദാർത്ഥങ്ങളുടെ പുനരുപയോഗം (reusability) തുടങ്ങിയ ശാസ്ത്രീയ വശങ്ങൾ സമഗ്രമായി പഠിച്ചു. ഈ കണ്ടെത്തലുകൾ, MnS നാനോ പദാർത്ഥങ്ങളെ ജലത്തിൽ നിന്നും ഫോസ്ഫേറ്റ് അയോണുകൾ നീക്കം ചെയ്യുന്നതിനും ടെക്സ്റ്റൈൽ ചായം പൂർണ്ണമായും വിഘടിപ്പിക്കുന്നതിനും ഉള്ള ഒരു വാഗ്ദാനവസ്തുവായി പ്രയോജനപ്പെടുത്താവുന്നതുമാണ് എന്ന് സമർത്ഥിക്കുന്നു.

മൂന്നാമതായി, ഞങ്ങൾ ശ്രദ്ധകേന്ദ്രീകരിച്ചത് ആധുനിക ഔഷധനിർമ്മാണശാലകളിൽനിന്നും പുറന്തള്ളപ്പെടുന്ന മലിനീകാരികളെ പറ്റിയായിരുന്നു. പാരിസ്ഥിതികമായി ഏറെ പ്രയാസം വരുത്തുന്നതും, മരുന്നുകളോട് ഉയർന്ന പ്രതിരോധശേഷിയുള്ള രോഗാണുക്കളെ (drug-resistant bacteria) വളർത്തികൊണ്ടുവരുവാൻ പര്യാപ്തവുമായ ആന്റിബയോട്ടിക്കുകളുടെ സാനിധ്യം പല ജലാശയങ്ങളിലും ഇതിനോടകം കണ്ടെത്തിയിട്ടുണ്ട്. രോഗശമനത്തിനായി നമ്മൾ ആന്റിബയോട്ടിക് മരുന്നുകൾ കഴിക്കുമ്പോൾ അവ ഫലപ്രാപ്തി നേടിത്തരാത്തതിന്റ കാരണം ഇത്തരം മരുന്നുകളെ അതിജീവിക്കുവാൻ കഴിയുന്ന രീതിയിൽ വളർന്നു വന്ന രോഗാണുവിന്റെ ശേഷിയാണ്. ആയതിനാൽ ജലത്തിലുള്ള ഇത്തരം ആന്റിബയോട്ടിക്കുകളെ പൂർണമായും നിർമാർജ്ജനം ചെയ്യുന്നതിനായി ഫലപ്രദമായ ഒരു ജലശുദ്ധീകരണമാർഗ്ഗം ഞങ്ങൾ അവലംബിച്ചു. ദൃശ്യപ്രകാശത്തെ പ്രയോജനപ്പെടുത്തിക്കൊണ്ട് വലിയ തന്മാത്രകളെ വിഘടിപ്പിക്കുവാൻ കഴിയുന്ന

അഡ്വാൻസ്ഡ് ഓക്സീകരണ പ്രക്രിയക്ക് 'പ്രകാശ-പ്രചോദന ഉൽപ്രേരണം' അഥവാ photocatalysis എന്നാണ് പറയുന്നത്. ഇതിനായി പ്രകാശ-പ്രചോദന ഉൽപ്രേരകങ്ങളെ (photocatalysts) വികസിപ്പിച്ചെടുക്കേണ്ടതുണ്ട്. ഒരു സഹ-അവക്ഷിപ്ത രൂപീകരണ (co-precipitation) രീതി ഉപയോഗിച്ച് BiOCl, BiOBr എന്നീ നാനോപ്ലേറ്റുകൾ സംശ്ലേഷണം ചെയ്തു. കൂടാതെ ഇതേ രീതി അവലംബിച്ച് വ്യത്യസ്ത Br:Cl മോളാർ അനുപാതങ്ങളുള്ള നാനോപ്ലേറ്റുകൾ വികസിപ്പിച്ചെടുക്കുകയും ചെയ്തു. വ്യത്യസ്ത Br:Cl മോളാർ അനുപാതങ്ങളുള്ള നാനോപ്ലേറ്റുകളെ BiOCl, BiOBr എന്നീ നാനോപ്ലേറ്റുകളുടെ ഉൽപ്രേരണപ്രവർത്തനങ്ങളുമായി താരതമ്യം ചെയ്യുമ്പോൾ, അവയെല്ലാം മികച്ച ആന്റിബയോട്ടിക് വിഘടനാപ്രവർത്തനം നടത്തുന്നതായി കണ്ടെത്തി. ഇപ്രകാരം വികസിപ്പിച്ചെടുത്ത ഉൽപ്രേരകങ്ങളുടെ ഓപ്റ്റിക്കൽ ബാൻഡ് ഗ്യാപ്പ് 3.39 eV മുതൽ 2.75 eV വരെ വിജയകരമായി ചിട്ടപ്പെടുത്തി എടുക്കുവാൻ സാധിച്ചു, അവയുടെ പ്രകാശം-ശേഖരിക്കാനുള്ള കഴിവുകൾ വർദ്ധിപ്പിച്ചു. ഇത്തരം പദാർത്ഥങ്ങൾ ഉപയോഗിച്ച് 20 മിനുട്ടിനുള്ളിൽ തന്നെ സിപ്രോഫ്ലോക്സാസിൻ (CIP), ടെട്രാസൈക്ലിൻ ഹൈഡ്രോക്ലോറൈഡ് (TCH) എന്നീ ആന്റിബയോട്ടിക്കുകളെ യഥാക്രമം 89%, 99% വിഘടനം നടത്തി അപചയന ഫലപ്രാപ്തി കൈവരിച്ചു. ഇത്തരം വിഘടന പ്രവർത്തനങ്ങളുടെ രസഗതികം (chemical kinetics), വിഘടനത്തിന്റെ നിരക്ക്, വിഘടനത്തെ സ്വാധീനിക്കുന്ന ഘടകങ്ങൾ, വിഘടനപ്രവർത്തനത്തിന്റെ താപഗതികം, ഉൽപ്രേരകങ്ങളുടെ പുനരുപയോഗ സാദ്ധ്യതകൾ എന്നിവയെല്ലാം സമഗ്രമായി പഠിച്ചു. ഈ പദാർത്ഥങ്ങൾ ചുരുങ്ങിയത് 5 തവണ പുനരുപയോഗിക്കാവുന്നതാണ്, സ്ഥിരതയുള്ളതാണ്, ജലീയ പരിസ്ഥിതികൾക്ക് അനുയോജ്യമാണ്, ഇത് ആന്റിബയോട്ടിക് മലിനീകരണം നിയന്ത്രിക്കുന്നതിനുള്ള ഒരു വാഗ്ദാന-പരിസ്ഥിതി സൗഹൃദ പ്രകാശ-പ്രചോദന ഉൽപ്രേരകമായി കണക്കാക്കാവുന്നതാണ്.

നാലാമതായി , പരമ്പരാഗത പ്രകാശ-പ്രചോദന ഉൽപ്രേരകങ്ങളിൽ സാധാരണയായി കാണാറുള്ള, ദുർബലമായ ചാർജ് ട്രാൻസ്പോർട്ടും ഉപരിതല അധിശോഷണ പരിമിതികളും മറികടക്കുന്നതിനുമായി ഞങ്ങൾ ഒരു പദാർത്ഥത്തിന്റെ തന്നെ വ്യത്യസ്ത ക്രിസ്റ്റൽ അവസ്ഥകൾ സംയോജിപ്പിച്ച് ഒരു ഭിന്നാത്മക സന്ധി (heterojunction) ഘടന വികസിപ്പിച്ചു. അതിനായി ബിസ്മത് വനഡേറ്റ് എന്ന നാനോപദാർത്ഥത്തെയാണ് പ്രയോജനപ്പെടുത്തിയത്. ഇവയുടെ ടെട്രഗോണൽ, മോണോക്ലിനിക്, മോണോക്ലിനിക്/ടെട്രഗോണൽ ക്രിസ്റ്റൽ അവസ്ഥകളിൽ ഉള്ള ബിസ്മത് വനഡേറ്റ് നാനോപദാർത്ഥങ്ങൾ സംശ്ലേഷണം ചെയ്യാൻ ഒരു ഹൈഡ്രോതെർമൽ രീതി ഉപയോഗിച്ചു. ഈ പദാർത്ഥങ്ങളുടെ പ്രകാശ-പ്രചോദന ഉൽപ്രേരണത്തെ അടിസ്ഥാനപ്പെടുത്തിയുള്ള വിഘടന സ്വഭാവം പഠിക്കുന്നതിനായി റോഡാമൈൻ ബി (RhB) എന്ന വ്യാവസായിക ചായത്തെയാണ് ഉപയോഗിച്ചത്. ദൃശ്യപ്രകാശത്തിന്റെയും ബിസ്മത് വനഡേറ്റ് നാനോപദാർത്ഥത്തിന്റെയും സാന്നിധ്യത്തിൽ RhB അപചയനത്തിന് വിധേയമാകുകയും, 90 മിനിറ്റുകൾ കൊണ്ട് ഏകദേശം 90% നശിക്കപ്പെടുകയും ചെയ്തതായി കണ്ടെത്തി. എന്നാൽ ഈ പ്രവർത്തനങ്ങളുടെ കാര്യക്ഷമത വർദ്ധിപ്പിക്കുന്നതിനായി അൾട്രാസോണിക് ശബ്ദ തരംഗങ്ങളെയും മലിനജലത്തിലേക്ക് കടത്തിവിട്ടു. ശബ്ദത്തിന്റെയും പ്രകാശത്തിന്റെയും സംയോജിതമായ പ്രവർത്തനം കാരണം RhB തന്മാത്രകളുടെ അപചയപ്രവർത്തനം കാര്യക്ഷമമായി ത്വരിതപ്പെടുകയും ചെയ്തതായി കണ്ടെത്തി. ശബ്ദതരംഗങ്ങളുടെ സാന്നിധ്യത്തിലും, പ്രകാശത്തിന്റെ സാന്നിധ്യത്തിലും, ശബ്ദത്തിന്റെയും പ്രകാശത്തിന്റെയും ഒരുമിച്ചുള്ള സാന്നിധ്യത്തിലും RhB വിഘടനം എങ്ങനെ സാധ്യമാകുന്നു എന്നുള്ളത് സമഗ്രമായി താരതമ്യം ചെയ്തു പഠിച്ചു. ഇവിടെയും RhB വിഘടന പ്രവർത്തനങ്ങളുടെ രസഗതികം, വിഘടനപ്രവർത്തനത്തിന്റെ നിരക്ക്,

വിഘടനപ്രവർത്തനത്തെ സ്വാധീനിക്കുന്ന ഘടകങ്ങൾ, വിഘടനപ്രവർത്തനത്തിന്റെ താപഗതികം, ഉൽപ്രേരകങ്ങളുടെ പുനരുപയോഗ സാദ്ധ്യതകൾ എന്നിവയെല്ലാം വിശദമായി പഠിച്ചു. ഇത്തരത്തിലുള്ള ഭിന്നാത്മക സന്ധി ഘടനകങ്ങൾ പ്രകാശ-ശബ്ദ-പ്രേരിത ചാർജുകളെ (photo-sono-induced charges) ഗണ്യമായി ബാധിക്കുന്നുവെന്നും അവയെക്കുറിച്ചുള്ള ഈ പഠനം മെച്ചപ്പെട്ട ശബ്ദ-പ്രകാശ-പ്രചോദിത-ഉൽപ്രേരണങ്ങൾക്ക് (Sonophotocatalysis) പിന്നിലെ ക്രിയാവിധി കൂടുതൽ ആഴത്തിലുള്ള ധാരണ നൽകുന്നുവെന്നും ഉറപ്പുനൽകുന്നു.

ചുരുക്കത്തിൽ, ഈ ഗവേഷണ പഠനം വ്യാവസായശാലകൾ പുറത്തു തള്ളുന്ന മലിനജലത്തിൽ അടങ്ങിയിരിക്കുന്ന വിഷ മാലിന്യങ്ങളെ ഫലപ്രദമായി നീക്കം ചെയ്യുന്നതിന് ലോഹ ചാൽക്കോജനൈഡുകളും ബിസ്മത്ത് അടിസ്ഥാനമാക്കിയുള്ള അധിശോഷകങ്ങളും ഉൽപ്രേരകങ്ങളും ഉപയോഗിച്ച് നൂതന ശാസ്ത്രീയ മാർഗങ്ങൾ നിർദ്ദേശിക്കുന്നു. ഈ കണ്ടെത്തലുകൾ ജല ശുദ്ധീകരണത്തിനായി നാനോപദാർത്ഥങ്ങളുടെ സാധ്യതകൾ വ്യക്തമാക്കുന്നു. അധിശോഷണ പ്രക്രിയകൾ, വിവിധ ഉൽപ്രേരണ പ്രക്രിയകളുടെ പ്രവർത്തനരീതികൾ, ഗതികശാസ്ത്രവും താപഗതിശാസ്ത്രവും ഉൾപ്പെടെയുള്ള ആഴത്തിലുള്ള വിശകലനങ്ങൾ ഈ പഠനത്തിന്റെ ഭാഗമായി അവതരിപ്പിച്ചിരിക്കുന്നു. തീർച്ചയായും ഈ ഗവേഷണപ്രബന്ധം പരിസ്ഥിതിസൗഹൃദമായ വ്യവസായവളർച്ചക്ക് ആവശ്യമായ ശാസ്ത്രസാങ്കേതികമുന്നേറ്റത്തിനും ഒരു മുതൽക്കൂട്ടായി വർത്തിക്കും എന്ന് പ്രതീക്ഷിക്കുന്നു.

സൂചകപദങ്ങൾ : ജലശുദ്ധീകരണം, അധിശോഷണം, ശബ്ദ-പ്രചോദിത ഉൽപ്രേരണം, പ്രകാശ-പ്രചോദിത-ഉൽപ്രേരണം, ശബ്ദ-പ്രകാശ-പ്രചോദിത-ഉൽപ്രേരണം, സർഫക്റ്റാന്റുകൾ, ഫോസ്ഫേറ്റ് അയോണുകൾ, ആന്റിബയോട്ടിക്കുകൾ, വ്യാവസായിക ചായങ്ങൾ.

ACKNOWLEDGEMENT

Expressing the depth of my gratitude, affection, and admiration for the incredible individuals who have played a crucial role in bringing my Ph.D. thesis to life is a challenging endeavour. I have been incredibly fortunate to receive the generous cooperation and splendid support of family members, friends, lab mates, well-wishers, and various institutions throughout my research journey. Their contributions have been invaluable, and my heart swells with gratitude as I acknowledge their unwavering assistance and encouragement. Each one of them has left an indelible mark on this work, making it a true collective achievement.

I would like to express my deepest gratitude to my research supervisor, Dr. Libu K. Alexander, for his unwavering support, guidance, and encouragement throughout the course of my research. His invaluable insights, expertise, and dedication have been instrumental in shaping this work. I am profoundly grateful for the freedom he provided, allowing me to explore and develop my ideas, as well as for his steadfast support during challenging times. His patience, support, insight, and inspiration have been truly remarkable, reflecting his complete dedication to excellence. Dr. Libu K. Alexander also deserves special thanks for creating a research environment that fosters independent thought and creativity. I am indebted to him for his invaluable suggestions, advice, and support throughout my Ph.D. work, which have significantly improved my skills and ability to think creatively. Each meeting with him added crucial aspects to the implementation of my research and broadened my perspective. His guidance and encouragement have greatly enriched my academic life. From him, I have learned to think critically, select problems, solve them, and present their solutions. He has provided the best training for developing writing and presentation skills, exceeding all my expectations for my research journey. It has been a great pleasure and privilege to work with him. He was the best choice I could have made for an advisor.

I am deeply grateful to Dr. Mohammed Shahin Thayyil, Head of the Department, Department of Physics, University of Calicut, for his support in the successful submission of this thesis. I also wish to acknowledge all the former HoDs, faculty members, non-teaching staff, and office staff of the department of physics for their invaluable contributions and assistance throughout my research journey. I wish to express my sincere gratitude to the Heads of the Chemistry Department and the Nanoscience and Technology Department for their help and support.

can express. Every moment spent with them is a treasure, and these beautiful memories will forever remain vivid in my heart.

I am profoundly grateful to my parents, Mohandas P and Bhamini K B, for their pure love, care, prayers, and unbroken support in both my academic and personal life. My father, who was the first to teach me to observe nature and the world around us, instilled in me a curiosity that inspired my journey as a science aspirant and researcher. He taught me how to focus on my goals and overcome challenges with constant faith and strong determination. My mother, with her incredible positivity, has been a beacon of hope through every challenge and failure I've faced. Her constant support has helped me overcome every difficulty in my life and research. I dedicate this thesis to them with all my heart.

With profound gratitude, I thank my siblings, Saidas P and Sariga P, for their unrelenting support in my research life and the completion of my thesis. I am especially indebted to my sister, Sariga P, who has spent the last six years caring for my daughter. The selfless dedication and safe, loving environment she created for my daughter have allowed me to focus on my research with peace of mind, assured that my child is in the most caring and capable hands.

Words cannot fully capture the depth of my love and gratitude for my truly exceptional soulmate, friend, and life partner, Mrs. Anukrishna A K. She has devoted herself entirely to supporting me through the journey of completing this research, showing remarkable patience and understanding. Her faithful support and boundless love, without ever imposing pressure, have been crucial in balancing her roles as a partner and parent. Her steadfast belief in me, combined with her endless patience, care, and support, has played an integral role in the successful completion of this thesis.

I am deeply grateful to my daughter, Ima Sravan, for her remarkable cooperation and understanding throughout this demanding period. Despite my frequent absences due to the rigorous demands of research, she has always been cheerful and eager to spend time with me. Her patience and love, without a single complaint, have been a source of immense comfort and strength during this journey.

I dedicate this work to all those who have guided and supported me, drawing strength from the belief that their encouragement and inspiration have made this achievement possible.

With a heart full of humility and reverence, I surrender everything to the Almighty, seeking His divine guidance and grace. I place all my hopes, struggles, and achievements in His hands, trusting in His boundless wisdom and love.

SRAVANADS P

PUBLICATIONS

1. Sravandas P., & Alexander, L. K. (2025). Dual-functional MnS nanomaterials: Efficient adsorbent for phosphate removal and sonocatalyst for textile dye degradation. *Journal of Physics and Chemistry of Solids (2025), 196, 112409.*

2. Sravandas P., & Alexander, L. K. (2024). 3D-Micro-Flower like $BiOBr_{1-x}Cl_x$ Nanoplate Solid Solution: A facile and rapid room-temperature synthesis with excellent photocatalytic decomposition of antibiotics in water. *Colloids and Surfaces A: Physicochemical and Engineering Aspects, 135748.*

3. Sravandas P., & Alexander, L. K. (2024). Isotype $BiVO_4$ Heterostructure and the Effect of Photo-Sono Induced Electron-Hole Pair. *Journal of Environmental Chemical Engineering*, 12(5), 113240.

4. Sravandas P., & Alexander, L. K. (2024). Fast catalytic degradation of an industrial surfactant driven by Hemi-micellization on facile synthesized CuS nanoflower. *Emergent Materials*, *7*(1), 209-220.

5. Sravandas P., & Alexander, L. K. (2021). Facile hydrothermal synthesis and Sonophotocatalytic performance of novel Bi_2WO_6 structure on the degradation of Rhodamine B. *Materials Today: Proceedings*, *46*, 2925-2929.

6. Sravandas P and L. K. Alexander (2022), Ultrasonic Sound-Visible light-driven catalytic performance of Facile Synthesized Bismuth Vanadate Nanorods, Proceedings book: ISBN 978-81-950313-5-1 (AMALIT-2022).

7. Sravandas P and L. K. Alexander, Removal of Detergent contents from water using CuS (2020), Proceedings book: ISBN NO: 978-81-942768-0-7 (2020, KSCSTE).

PAPERS PRESENTED IN INTERNATIONAL/NATIONAL CONFERENCES

1. *'Removal of Detergent contents from water using CuS'*, Sravandas P and L. K. Alexander, in the **32nd Kerala Science Congress** organized by KSCSTE, Government of Kerala held at Yuvakshetra Institute of Management Studies, Mundur, Palakkad, Kerala, India on 25-27 January 2020.

2. *'Facile Hydrothermal Synthesis and Sonophotocatalytic Performance of novel Bi_2WO_6 Structure on the Degradation of Rhodamine B.'*, Sravandas P and L. K. Alexander, in the **International Conference** on Advances in Material Science and Chemistry (ICAMSC-2020), organized by Department of Chemistry, Amrita Vishwa Vidyapeetham, Amritapuri Campus, Kerala on 10-12 August 2020.

3. *'Ultrasonic Sound-Visible light-driven catalytic performance of Facile Synthesized Bismuth Vanadate Nanorods.'*, Sravandas P and L. K. Alexander, in the **international conference** on The New Normal: Crisis Resilience and Re-Invention (AMALIT 2022) organized by Amal college of advanced studies, Nilambur on 15-17 February 2022.

4. *'Optical Tunability of Lead-free Halide Perovskite by Halide Alloying'*, Sravandas P and L. K. Alexander, in the **13th National Workshop** on Fluorescence and Raman Spectroscopy, Organized by Fluorescence Society, IISER Thiruvanathapuram, Kerala, India on January 06-11, 2023

5. *'Piezoelectric-Induced Internal Electric Field in Bismuth Vanadate Nanorods for Boosting the Photocatalytic Degradation of Organic Pollutants'*, Sravandas P and L. K. Alexander, in the 7th **International Conference** on Nanoscience and Nanotechnology (ICONN-2023), organized by SRM Institute of Science and Technology, Kattankulathur - 603 203, Tamil Nadu, India on March 27 - 29, 2023.

6. *'Harmonizing Adsorption and Ultrasound-aided Catalysis for the Removal of Congo Red from Aqueous Solution Using CuS Nanoflakes'*, Sravandas P and L. K. Alexander, in the **International Conference** on Advanced Materials for Sustainability ICAMS 2023, Organized by School of Physical Science, University of Calicut during 21-23 December 2023.

AWARDS

1. ***Best poster presentation award*** for the paper *'Removal of Detergent contents from water using CuS'*, Sravandas P and L. K. Alexander, in the **32nd Kerala Science Congress** organized by KSCSTE, *Government of Kerala* held at Yuvakshetra Institute of Management Studies, Mundur, Palakkad, Kerala, India on 25-27 January 2020.

2. ***Best paper presentation award*** for the paper '*Facile Hydrothermal Synthesis and Sonophotocatalytic Performance of novel Bi_2WO_6 Structure on the Degradation of Rhodamine B.'*, Sravandas P and L. K. Alexander, in the **International Conference** on **Advances in Material Science and Chemistry (ICAMSC-2020),** organized by Department of Chemistry, Amrita Vishwa Vidyapeetham, Amritapuri Campus, Kerala on 10-12 August 2020.

3. ***Best paper presentation award*** for the paper *'Harmonizing Adsorption and Ultrasound-aided Catalysis for the Removal of Congo Red from Aqueous Solution Using CuS Nanoflakes',* Sravandas P and L. K. Alexander, in the **International Conference on Advanced Materials for Sustainability ICAMS 2023,** Organized by School of Physical Science, University of Calicut during 21-23 December 2023.

CONTENTS

PREFACE

Escalation in pollution degrades water quality and diminishes its natural regenerative capacity, leading to a growing scarcity of clean water. Major capital cities, such as New Delhi in India, struggle to meet the water demands of their inhabitants. With the ever-increasing global population and rising water needs for food production and irrigation, water reuse is essential to address these challenges and support economic growth. Additionally, water regulations for effluent discharge are becoming more stringent to protect the water quality of natural reservoirs. There is an urgent need to implement wastewater reuse programmes across all industrial sectors. However, improvements are still necessary to achieve sustainable water utilisation practices and to develop cost-effective wastewater treatment technologies.

Water contaminants are generally classified into inorganic toxic elements, organic chemicals, and microorganisms. Inorganic toxic elements include various metallic elements such as mercury, cadmium, lead, chromium, and copper, as well as anionic pollutants like nitrate, phosphate, sulfate, and chloride, which can significantly impact water quality and ecosystem health. Typical organic contaminants in water include pharmaceuticals, personal care products, endocrine disruptors, pesticides, organic dyes, detergents, and common industrial organic wastes like phenolics, halogens, and aromatics.

Several technologies are used for water treatment, each with advantages and drawbacks. Adsorption has emerged as the most effective method to remove pollutants from water without secondary potential pollution - at an acceptable cost. Adsorption involves a fluid (water) and a solid phase (the adsorbent). The dissolved contaminants (adsorbates) are transferred from the liquid phase to the adsorbent surface, thus purifying the water. Adsorption is favoured for water treatment due to its low cost, high efficiency, ease of operation, and the ability to use various solid materials as adsorbents.

Advanced Oxidation Processes (AOPs) are also highly effective for treating contaminated water. They generate powerful oxidising agents, primarily hydroxyl radicals (•OH), to degrade a wide range of organic pollutants. AOPs involve chemical, photochemical, sonochemical, or electrochemical methods to produce these radicals. Recent advancements in AOPs focus on enhancing catalyst efficiency, stability, and reusability and developing hybrid systems that combine different AOPs for improved

performance. The development of novel catalysts, such as doped metal oxides, chalcogenides, nanocomposites, heterojunctions, and supported catalysts, aims to increase the generation of hydroxyl radicals and extend the applicability of AOPs under various environmental conditions.

Nanomaterials have garnered significant interest worldwide for their potential in water treatment. Compared to conventional technologies like activated carbon, nanomaterials provide better and more efficient remediation for water pollutants due to their high surface area and reactivity. Advanced developments in nano absorbents and nano-catalysts reduce the concentrations of toxic compounds in water and enhance water quality for health.

Considering all the factors mentioned, we have decided to scientifically demonstrate, at the laboratory level, the effective removal of toxic contaminants found in industrial effluents using innovative adsorbents, photocatalysts, sonocatalysts, or sonophotocatalysis.

This thesis focuses on the remediation of organic and inorganic pollutants in wastewater using nanomaterials as nano adsorbents and nano-catalysts. Specifically, it addresses four common, but toxic industrial effluents: surfactants, phosphate ions, antibiotics, and industrial dyes, which severely impact ecosystems and water reservoirs. We employ adsorptive and catalytic strategies using metal chalcogenides and Bi-based nanomaterials - prioritising versatility, cost-effectiveness, and efficiency. This thesis provides an account of nanomaterial synthesis, a comprehensive analysis of pollutant removal, and explores the science and thermodynamics behind the remediation processes. Our research aims to advance wastewater treatment technologies, improve catalyst performance, and contribute to a cleaner, healthier environment.

Based on the aforementioned motivation, this thesis is organised into five interconnected objectives. The primary goal is to develop nanomaterials and demonstrate, at the laboratory level, their effectiveness in adsorption and catalytic processes for water remediation. The specific objectives include:

1. Synthesise and characterise a novel material tailored for the efficient removal and degradation of sodium dodecyl sulfate (SDS), a prevalent anionic surfactant in agrochemical, pharmaceutical, oil, paper, mining, and textile wastewater, and elucidate the associated removal mechanisms.

2. Design and develop a naturally abundant material for the selective removal of phosphate ions from wastewater, focusing on understanding the fundamental mechanisms driving the adsorption and ion exchange processes.

3. Investigate the synergistic effects of ultrasonic waves and visible light in the degradation of abundant pollutants, including antibiotics and industrial dyes, to optimise catalytic processes for the treatment of industrial effluents.

4. Explore the potential of oxyhalide solid solutions in the photodegradation of antibiotics in aqueous environments, aiming to understand the material's photocatalytic behaviour and efficiency.

5. Synthesise and evaluate an isotype heterojunction photocatalytic material for its efficacy in water remediation, with a focus on unravelling the material's photocatalytic mechanisms and applicability in environmental cleanup.

In order to accomplish objective 1, we synthesised CuS nanostructures. In the thesis, we demonstrated that the CuS nanoflowers are highly effective as adsorbents and catalysts for removing and decomposing sodium dodecyl sulfate (SDS) in water. The efficient decomposition of surfactants from effluents can be achieved through adsorption and advanced oxidation processes. The 100% catalytic decomposition of SDS was achieved within 11 minutes, with activity approximated to a Fenton-like process. The fast catalytic decomposition of SDS into CO_2 and water is driven by hemi-micelle enhanced adsorption and the synergistic action of H_2O_2. The mechanism of surfactant adsorption on CuS nanoflowers was understood through various adsorption isotherm models. The kinetics of adsorption were also thoroughly examined. The adsorption thermodynamics were studied and observed to be endothermic and enthalpy-driven. In summary, we combined the adsorption and Fenton-like catalytic activity of CuS to completely remove SDS from water. Our work is the first report of metal chalcogenides being used to remove surfactants.

To meet the goal of objective 2, we introduced a dual-functional MnS nanomaterial for removing phosphate ions and Congo Red textile dye. MnS nanomaterials were synthesised via a hydrothermal route. Batch adsorption experiments revealed a phosphate adsorption capacity of 160.73 mg P/g, which is commendable for an adsorbent in its bare form. The adsorption isotherm and kinetic studies were conducted to gain a detailed

understanding of the adsorption process. The thermodynamics of the process were studied thoroughly, indicating a spontaneous, exothermic process, confirming favourable adsorption. FTIR analysis confirmed the adsorption mechanism, which includes electrostatic attraction, surface complexation, and ion exchange. MnS maintained its adsorption capacity despite competing ions, demonstrating a selective affinity for phosphate ions. MnS also showed high sonocatalytic efficiency, degrading Congo Red dye within 10 minutes of ultrasonic irradiation. The degradation mechanism of Congo Red dye in the sonocatalytic process was proposed. This novel metal chalcogenide material exhibits exceptional affinity for phosphate ions and Congo Red dye molecules, surpassing La-based adsorbents in efficacy. These findings underscore MnS as a promising alternative to lanthanum or zirconium-based materials for the removal of phosphate and textile dyes from wastewater. The results suggest that MnS nanomaterials are promising for practical applications in phosphate removal and textile dye degradation from wastewater.

To explore objectives 3 and 4, we synthesised a series of $BiOBr_{(1-x)}Cl_x$ nanoplates solid solutions with varied Br:Cl molar ratios through a simple co-precipitation method. These solid solutions exhibited superior visible-light-driven photocatalytic activity compared to pristine BiOCl and BiOBr. Successful tuning of the optical bandgap from 3.39 eV to 2.75 eV in the samples has been achieved through halide alloying. Notably, the $BiOBr_{0.25}Cl_{0.75}$ sample demonstrated exceptional performance, achieving 89% and 99% degradation efficiency for ciprofloxacin (CIP) and tetracycline hydrochloride (TCH), respectively, within 20 minutes under optimum conditions. The outstanding performance is attributed to factors such as a large specific surface area, suitable morphology and band gap, effective separation of photo-generated electron-hole pairs, and the presence of meso-size pores in the structure. Thermodynamic studies confirmed the exothermic and spontaneous nature of the photocatalytic reactions. The proposed degradation pathways of CIP and TCH and the photocatalytic mechanisms were elucidated. The $BiOBr_{(1-x)}Cl_x$ solid solution exhibits facile recyclability, robust stability, and adaptability to aquatic environments, establishing its potential as a promising eco-friendly photocatalyst for antibiotic pollution control.

Owing to its suitable energy band and strong catalytic capacity, $BiVO_4$ has received extensive attention in photocatalysis. To address objective 5, we propose a straightforward approach to address the challenges of insufficient compatibility, poor charge transport characteristics, and limited surface adsorption properties commonly found in traditional

BiVO$_4$ photocatalysts. A heterojunction BiVO$_4$ structure was developed by incorporating two distinct crystal phases within a single semiconducting material. A facile hydrothermal procedure was used to synthesise distinct crystalline phases of BiVO$_4$ photocatalysts, viz., tetragonal, monoclinic, and monoclinic/tetragonal heterophase. The physicochemical characteristics of the pristine and isotype BiVO$_4$ heterojunctions were characterised using various techniques. The photocatalytic activity of BiVO$_4$ samples was examined by monitoring the degradation of Rhodamine B (RhB). Ultrasonic sound waves were employed within the reaction medium to boost the degradation reaction. The study examined the photocatalytic, sonocatalytic, and sonophotocatalytic activity of BiVO$_4$ microcrystals concerning the degradation of RhB dye. The results showed that the crystalline phases of BiVO$_4$ samples significantly influence the behaviour of photo-sono-induced charges. This would provide greater insight into the intrinsic reasons for the enhancement in sonophotocatalytic activity.

In conclusion, this thesis highlights significant progress in water remediation using metal chalcogenides and Bi-based nanomaterials. Through systematic research, we developed four nanomaterials—CuS nanoflowers, MnS nanomaterials, BiOBr$_{(1-x)}$Cl$_x$ solid solutions, and heterojunction BiVO$_4$ structures—each demonstrating exceptional performance in removing various industrial pollutants, such as sodium dodecyl sulfate, phosphate ions, antibiotics, Congo red dye, and Rhodamine B dye. These findings reveal the potential of these nanomaterials for scalable and energy-efficient water purification and offer valuable insights into the mechanisms of adsorption and catalytic processes. The research underscores the promise of metal chalcogenides and bismuth-based nanomaterials as innovative solutions for addressing water pollution challenges.

LIST OF FIGURES

LIST OF TABLES

ABBREVIATIONS USED IN THE THESIS

AOP	**:**	Advanced Oxidation Process
RO	:	Reverse Osmosis
WAO	:	Wet Air Oxidation
MOF	:	Metal Organic Framework
PFO	:	Pseudo First Order
PSO	:	Pseudo Second Order
IPD	:	Intra Particle Diffusion
VB	:	Valance Band
CB	:	Conduction Band
US	:	Ultra Sound
SL	:	Sono Luminescence
VLD	:	Visible Light Driven
L-H	:	Langmuir-Hinshelwood
TST	:	Transition State Theory
XRD	:	X-ray Diffraction
FE-SEM	:	Field Emission Scanning Electron Microscopy
UV-Vis	:	Ultraviolet Visible
Vis	:	Visible
DRS	:	Diffuse Reflectance Spectroscopy
BET	:	Brunauer–Emmett–Teller
BJH	:	Barrett–Joyner–Halenda
TPD	:	Temperature Programmed Desorption
FTIR	:	Fourier Transform Infrared Spectroscopy

HPLC	: High-Performance Liquid Chromatography
TOC	: Total Organic Carbon
JCPDS	: Joint Committee on Powder Diffraction Standards
CCD	: Charge Coupled Device
SERS	: Surface-Enhanced Raman Spectroscopy
RRE	: Resonance Raman Effect
SEM	: Scanning Electron Microscopy
MBAS	: Methylene Blue Active Substances
CR	: Congo Red
SDS	: Sodium Dodecyl Sulfate
RhB	: Rhodamine B
PL	: Photoluminescence
HMC	: Hemi-Micelle Concentration
TSA	: Two-Step Adsorption
AC	: Activated Carbon
CIP	: Ciprofloxacin
TCH	: Tetracycline Chloride
CuS	: Copper Sulfide
MnS	: Manganese Sulfide
BiOBr	: Bismuth oxybromide
BiOCl	: Bismuth oxychloride
$BiOBr_{(1-x)}Cl_x$	: Bismuth oxybromide-chloride solid solutions
$BiVO_4$	: Bismuth Vanadate

CHAPTER 1

Introduction

To start with….

BENGALURU WATER CRISIS: AS SHORTAGE DEEPENS, TECHIES 'MOVE AWAY' FROM INDIA'S SILICON VALLEY
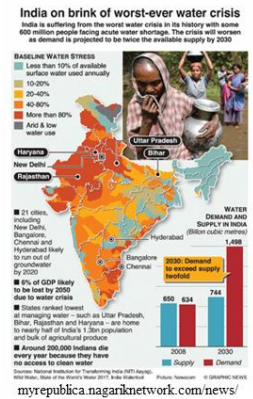
Missions box Press release 24/03/2024

India on brink of worst-ever water crisis

myrepublica.nagariknetwork.com/news/

India's water crisis

600 million Indians face high to extreme stress over water

IAS express 20/11/2022

"Water and air, the two essential fluids on which all life depends, have become global garbage cans."

-Jacques-Yves Cousteau

This introduction chapter highlights the urgent need for wastewater remediation in the current context. This chapter discusses the necessity of advanced wastewater treatment systems and explores potential improvements through emerging technologies, such as adsorption and advanced oxidation process-based catalysis. It also outlines the motivation for this research and the specific objectives aimed at enhancing the effectiveness of current wastewater treatment methodologies.

The thesis, entitled ***'Insights on Adsorptive and Catalytic Water Remediation Using Metal Chalcogenides and Bismuth Based Nanomaterials',*** addresses the critical global challenge of water pollution, which has recently garnered increased attention due to its severe negative impacts on life and the planet's ecosystem. Given the essential role of water in sustaining a healthy life, sourcing clean freshwater is one of the most pressing challenges facing modern society.

The thesis focuses on the remediation of organic and inorganic pollutants in wastewater using nanomaterials. It systematically summarises the various types of pollutants and the different classes of nanomaterials used for water remedial applications. Water contaminants are generally classified into inorganic toxic elements, organic chemicals, and microorganisms. Inorganic toxic elements encompass a variety of metallic elements such as mercury, cadmium, lead, chromium, and copper. Additionally, anionic pollutants like nitrate, phosphate, sulfate, and chloride fall under this category. These substances can significantly degrade water quality and pose serious risks to ecosystem health. Organic contaminants in water typically include pharmaceuticals, personal care products, endocrine disruptors, pesticides, organic dyes, detergents, and common industrial organic wastes like phenolics, halogens, and aromatics. These organic pollutants can disrupt biological processes and accumulate in the environment, leading to long-term ecological and human health issues. In this thesis, we are focused on four classes of pollutants commonly found in industrial effluents:

- ❖ Surfactants - a significant components of cleaning products like detergents and personal care products.
- ❖ Phosphate ions, particularly from food, textile, cosmetics, rubber, and drug effluents.
- ❖ Antibiotics are a significant pharmaceutical industry pollutant.
- ❖ Industrial dyes.

These four classes of pollutants can have severe impacts on ecosystems and water reservoirs. We have chosen adsorptive and catalytic water remediation strategies for successful removal and degradation. These methods are versatile, cost-effective, capable of removing various pollutants or pollutant mixtures and producing high-quality treated effluent [1]. We have selected metal chalcogenides and Bi-based nanomaterials for this process because these materials are emerging as effective solutions for water remediation applications.

This study comprehensively analyses each problem and thoroughly addresses the remedial solutions for practical industrial applications. The research focuses on the scientific aspects of the water remediation process, exploring the underlying science and mechanisms behind all processes. This provides insights into adsorptive and catalytic water remediation using metal chalcogenides and Bi-based nanomaterials.

1.1. WATER REMEDIATION

The growing population, industrial expansion, and insufficient rainfall have led to a global water scarcity crisis. Numerous methods and solutions have been implemented to restore water resources [2]. However, restoration solutions such as rainwater harvesting only offer partial relief. Approximately 4 billion people worldwide have access to unsafe water, leading to a significant rise in acute waterborne illnesses. This issue is expected to worsen due to the massive discharge of pollutants and micropollutants from industrial and agricultural activities into natural water sources. Therefore, restoration in terms of purity is also a significant part of the solution [3].

A substantial number of toxic pollutants enter groundwater and freshwater bodies due to modern human activities, including industrial operations, municipal and domestic household activities, and agricultural processes [4]. Even small amounts of toxic materials, such as heavy metals, organic dyes, pharmaceuticals, pesticides, and polycyclic aromatic hydrocarbons, can pose significant health risks. These elements are known to cause genetic mutations, cancer, neurological damage, teratogenic effects, and severe harm to various organs, including the reproductive, respiratory, and gastrointestinal systems, as well as the liver. Therefore, the direct or indirect contamination of freshwater reservoirs by toxic elements significantly reduces water quality and contributes to water scarcity [5].

Chlorination is widely used for disinfection in municipal treatment plants but is limited to removing microorganisms. These methods are insufficient for completely degrading pollutants, and removing inorganic heavy metal ions remains challenging. Additionally, it is essential to remove harmful substances from industrial wastewater [6]. Adsorption and coagulation, common water purification methods, merely transfer pollutants from one phase to another without destroying or eliminating them [7]. Other conventional water treatment techniques, such as membrane filtration, sedimentation, precipitation, ion exchange, solvent extraction, reverse osmosis, distillation, and

chemical treatments, are costly and often generate secondary pollutants [8]. These limitations have spurred rapid research and development in Advanced Oxidation Processes (AOP) as innovative water treatment methods. Moreover, developing a cost-effective treatment that can convert pollutants into less harmful forms is highly relevant [9].

This thesis explores the roles of adsorption and catalysis in water remediation, focusing on advanced methods to remove and degrade pollutants. Developing and optimising these techniques can create more effective and sustainable solutions to address the global water crisis and improve water quality for all.

1.2. THE IMPORTANCE OF WASTEWATER TREATMENT

Wastewater pollution poses a significant threat to ecosystems and human health, with 42% of household wastewater globally not being appropriately treated, according to UN Water reports [10]. This inadequate treatment degrades freshwater sources, which is crucial for maintaining biodiversity and ensuring safe drinking water. Currently, only 11% of domestic and industrial wastewater is being reused, despite an untapped potential for wastewater reuse estimated at 320 billion cubic meters per year [11,12]. This volume could surpass the capacity of global desalination efforts by more than tenfold, presenting a substantial opportunity to alleviate water scarcity.

Despite these potentials, water quality monitoring is insufficient in many regions. 60 % of assessed water bodies in 89 countries have good ambient water quality, yet routine water quality data collection is lacking in most countries [13]. This gap leaves over 3 billion people at risk, as the health of their freshwater ecosystems remains uncertain. Groundwater, which often constitutes the largest share of freshwater resources in many countries, is particularly under-monitored [14]. Of the 89 countries with water quality data, only 52 have information about groundwater conditions, posing a critical challenge for comprehensive water resource management [15].

Furthermore, wastewater contributes to global greenhouse gas emissions, accounting for about 1.57% of the total, comparable to the climate impact of the worldwide aviation industry. This underscores the urgent need for improved wastewater management practices to protect water quality and public health and mitigate climate change impacts. Advancing technologies and strategies for wastewater treatment and

reuse can play a pivotal role in addressing these interconnected challenges, making it an essential focus for sustainable water management [16].

A significant part of the solution is reducing pollution and enhancing wastewater management. Effective pollution control measures are essential to prevent contaminants from entering water sources, while advanced wastewater treatment technologies can recycle and purify used water, making it suitable for various applications. These strategies protect public health by providing clean drinking water and contribute to the sustainability of water resources, which is crucial in the face of climate change and increasing water scarcity [17].

Despite the growing need, wastewater management is often neglected. Untreated wastewater from industries is a major issue, where a large proportion of wastewater is discharged untreated into the nearest water body. This practice exposes water bodies to industrial effluents, cloth dyes, toxic chemicals, and pharmaceutical wastes. Implementing comprehensive water management practices can help mitigate the impact of human activities on natural water systems and ensure that future generations have access to this vital resource [18].

1.3. METHODS FOR REMOVING POLLUTANTS FROM WASTEWATER

Several techniques have been employed to enhance water management and wastewater treatment, including:

- **Reverse Osmosis (RO):** Reverse osmosis (RO) is an effective water remediation technology that utilises a semi-permeable membrane to remove ions, molecules, and larger particles from water. By applying high pressure, RO forces water through the membrane, allowing only smaller water molecules to pass while rejecting contaminants such as salts, organic compounds, and microorganisms. The technology is crucial for desalinating seawater and brackish water, especially in arid regions, due to the membrane's pore size of 0.1 to 1 nm. However, RO systems are energy-intensive and prone to membrane fouling by organic and inorganic matter, which can reduce efficiency. Ongoing advancements aim to improve membrane materials and fouling mitigation, enhancing RO's sustainability and cost-effectiveness [19].

- **Membrane Separation:** Membrane separation is a highly effective technology for water remediation, utilising semi-permeable membranes to filter contaminants from water selectively. Various processes—microfiltration, ultrafiltration, nanofiltration, and reverse osmosis—differ by pore size and operational pressure, enabling the removal of particles, microorganisms, and dissolved substances. Microfiltration and ultrafiltration handle larger particles and suspended solids, while nanofiltration and reverse osmosis target smaller molecules and ions. Advantages include low energy consumption and modular scalability. However, challenges such as membrane fouling, high operational costs, and maintenance needs persist, necessitating ongoing advancements in membrane materials and methods. Despite these issues, membrane separation is a promising solution for high-quality water treatment, addressing complex contaminants and regulatory requirements [20].

- **Flocculation and Coagulation:** Flocculation and coagulation are crucial for removing suspended particles and contaminants in water treatment. Coagulation adds coagulants like aluminium sulfate or ferric chloride to neutralise particle charges, causing aggregation into larger clusters. Flocculation then gently mixes these clusters into larger, settleable masses, enhancing sedimentation and filtration efficiency. Despite their benefits, these processes generate sludge that requires disposal and can leave chemical residuals in treated water, posing environmental and health risks. Chemical costs and careful dosing are also critical, and these methods may not remove all contaminants, necessitating additional treatments [21].

- **Electrocoagulation:** Flocculation and coagulation are crucial for removing suspended particles and contaminants in water treatment. Coagulation adds coagulants like aluminium sulfate or ferric chloride to neutralise particle charges, causing aggregation into larger clusters. Flocculation then gently mixes these clusters into larger, settleable masses, enhancing sedimentation and filtration efficiency. Despite their benefits, these processes generate sludge that requires disposal

and can leave chemical residuals in treated water, posing environmental and health risks. Chemical costs and careful dosing are also critical, and these methods may not remove all contaminants, necessitating additional treatments [22].

- **Biological Treatment:** Biological treatment for water remediation uses microorganisms—bacteria, fungi, and algae—to degrade organic contaminants through bioremediation. Methods such as activated sludge, biofilters, and bioreactors efficiently remove organic pollutants and nutrients in ambient conditions with lower energy requirements than physical and chemical methods. However, these processes are sensitive to environmental conditions, can be slow, require careful monitoring, and may produce secondary waste needing further treatment. Additionally, they may not effectively address all pollutants, such as heavy metals and non-biodegradable substances, often necessitating supplementary water treatments [23].

- **Ion Exchange:** Ion exchange removes ionic contaminants from water using resins with charged functional groups that swap ions with those in the solution. It effectively targets heavy metals, nitrates, and specific ions with high selectivity. However, it can be costly due to resin expenses and frequent regeneration involving potentially harmful chemicals. It also doesn't address non-ionic contaminants and may require pre-treatment to adjust pH and ionic strength. Disposal of spent regenerants and exhausted resins poses environmental challenges, necessitating sustainable waste management [24].

- **Desalination:** Desalination is vital for addressing freshwater scarcity, using methods like reverse osmosis (RO) and thermal distillation to remove salts and impurities from seawater or brackish water. RO forces water through a semi-permeable membrane, while thermal distillation heats water to produce steam, leaving salts behind. Despite its effectiveness, desalination is energy-intensive and costly, with high carbon emissions and environmental concerns related to brine disposal. Additionally, infrastructure and maintenance costs are significant, particularly for developing regions. Advancements are needed to

improve energy efficiency, reduce environmental impact, and lower costs [25].

- **Ozonation:** Ozonation is an advanced oxidation process for water remediation that uses ozone (O_3) to degrade organic pollutants, disinfect pathogens, and remove odours and tastes. Ozone is generated from oxygen via electric discharge or ultraviolet radiation and introduced into the water, oxidising contaminants into less harmful substances. It effectively treats a range of pollutants, including pesticides and pharmaceuticals. However, ozonation has high energy and operational costs, requires on-site ozone production, and can produce harmful by-products like bromate. Additional treatment may also be needed to mineralise persistent organic pollutants fully [26].

- **Fenton's Process:** The Fenton process is an advanced oxidation method for degrading organic pollutants in water, utilising hydroxyl radicals generated from hydrogen peroxide (H_2O_2) and ferrous iron (Fe^{2+}). It operates effectively at room temperature and atmospheric pressure and is relatively low-cost. However, it requires acidic conditions (optimal pH around 3), generating ferric hydroxide sludge that complicates waste management. The process can also be hindered by scavengers that react with hydroxyl radicals, and the need for continuous addition of hydrogen peroxide and iron salts impacts sustainability and resource efficiency [27].

- **Wet Air Oxidation:** Wet Air Oxidation (WAO) is a process that removes organic contaminants from wastewater by oxidising them with air or oxygen at temperatures between 150°C and 320°C and pressures of 5 to 20 MPa. It generates hydroxyl radicals and other oxidative species to break down complex organic molecules into less harmful compounds. WAO is effective for high-strength industrial wastewater and refractory substances but requires costly, specialised equipment and is energy-intensive. It can also produce secondary pollutants and may not be suitable for wastewater with low contaminant concentrations or high inorganic salt content [28].

AOPs are gaining popularity due to their ability to rapidly and non-selectively degrade contaminants through complete mineralisation or transformation into less toxic compounds. These processes are highly effective in treating wastewater and producing potable water, offering significant degradation rates and broad applicability advantages. An overview of the different technologies used for wastewater treatment in the industrial effluents is shown in Fig.1.1.
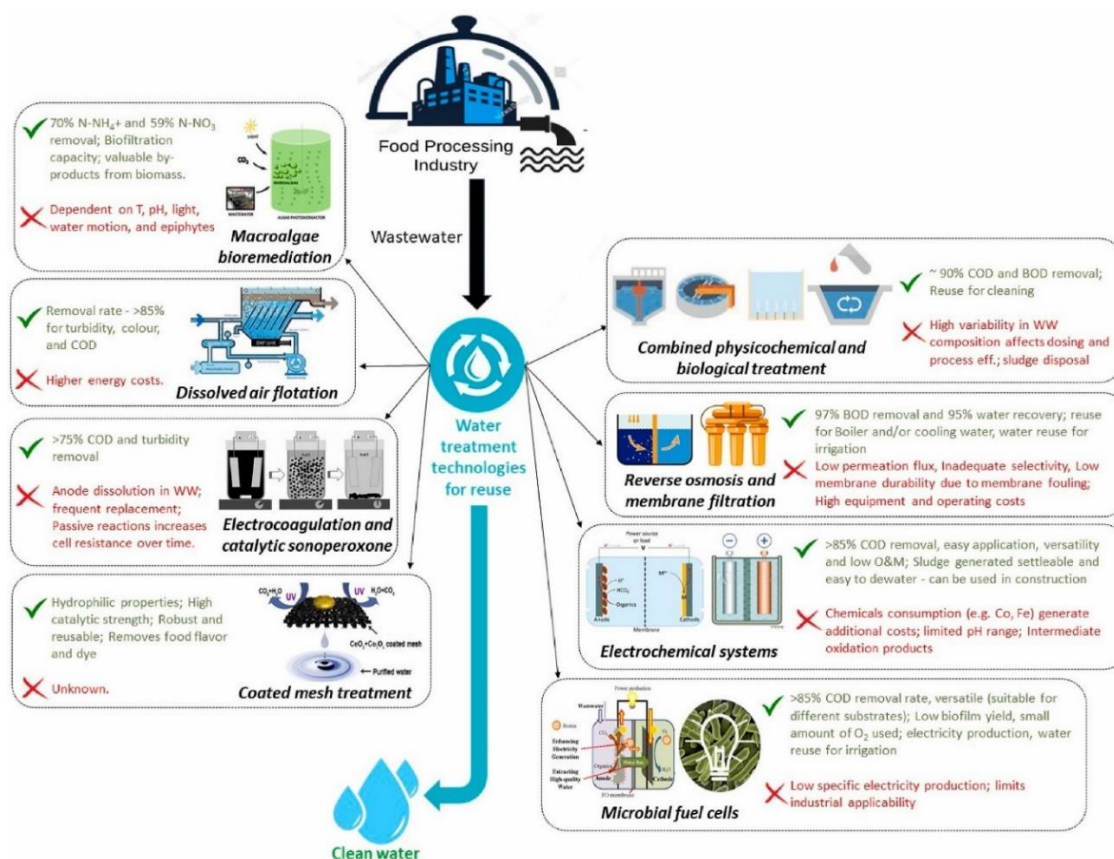
Fig.1.1. *An overview of the different technologies used for wastewater treatment in the industrial effluents. The figure is adapted from [29].*

1.4. ADSORPTIVE WATER REMEDIATION

The adsorption process is an efficient and adaptable physical method for treating wastewater. It is a surface phenomenon characterised by an increase in the concentration of a specific component at the interface between two phases, applicable at both laboratory and industrial scales. Adsorption is a versatile and cost-effective method for removing various pollutants, eliminating any pollutants or pollutant mixture and producing high-quality treated effluent. Additionally, the process is reversible, as adsorbents can be regenerated using appropriate desorption procedures. The type of adsorbent used significantly impacts the economic sustainability and effectiveness of the adsorption process [30].

Considering the literature, the critical aspects of applying adsorption for water treatment include selecting, developing, and characterising adsorbent materials, optimising adsorption processes, mathematical modeling, developing regeneration procedures, and applying them to actual samples. Cost evaluation is also essential, as it involves all these aspects and must be assessed on a case-by-case basis.

1.4.1. Adsorbents for Water Remedial Applications

Adsorbents play a crucial role in adsorptive water remediation because they effectively remove contaminants through selective binding and retention on their surfaces. Their high efficiency is attributed to their large surface area and specific affinity for pollutants, enabling the removal of contaminants even at low concentrations. Adsorbents offer versatility, as different materials can be tailored to target particular pollutants, providing customised solutions for various water contamination issues. They are also cost-effective, with many options for regeneration and reuse, making them practical for large-scale applications. The rapid response of adsorption processes allows for quick water treatment, which is advantageous in emergencies. Additionally, adsorbents typically produce minimal secondary pollution compared to some chemical treatments, contributing to a cleaner and more sustainable water remediation approach. Their scalability, from laboratory to industrial use, further underscores their importance in improving water quality and environmental protection [31].

The selection, development, and characterisation of adsorbent materials are crucial for designing an effective adsorption process for water treatment. An ideal adsorbent should possess the following attributes [32]:

- Low cost and availability
- Chemical stability
- Mechanical stability
- Desirable textural and physicochemical properties
- High adsorption capacity
- High efficiency
- Shows fast kinetics
- Regeneration and reuse potential

Developing an adsorbent that meets all these criteria is challenging. However, extensive research has led to the development of various adsorbent materials for water treatment.

These include carbon-based materials such as chars, biochar, activated carbons, coals, and nanomaterials; chitin and chitosan derivatives; biosorbents and agro-industrial wastes; inorganic materials like zeolites, layered double hydroxides, and geopolymers; metal-organic frameworks (MOFs); and silica-based materials [33]. The literature provides extensive information on these materials' preparation methods and advanced characterisation techniques [33]. Despite the availability of well-developed and characterised adsorbents, ongoing research is essential to create new materials that fulfil all the desired characteristics, leading to more efficient adsorption processes for water treatment.

1.5. CATALYTIC WATER REMEDIATION

Conventional water treatment technologies often fall short of fully mineralising refractory water contaminants, which are pollutants resistant to degradation. This inefficiency highlights the need for more effective alternatives, such as catalytic processes. Catalytic processes offer significant advantages, including faster reaction rates (kinetics), higher selectivity for target contaminants, and reduced energy consumption. Despite these benefits, implementing these processes on an industrial scale has been challenging [34].

Advanced Oxidation Processes (AOPs) lead these technologies by utilising highly reactive species for efficient pollutant breakdown. Incorporating sonocatalysis, photocatalysis, and sonophotocatalysis into AOPs marks significant progress in this field. Visible light-driven catalytic technologies harness solar energy to activate catalysts, offering a sustainable and cost-effective water treatment solution; this process is called photocatalysis. Ultrasound-assisted catalysis employs ultrasound radiation to enhance catalytic reactions, resulting in faster and more efficient pollutant degradation, known as sonocatalysis. Ultrasound and visible light irradiation are highly effective chemical-free methods for degrading various wastewater pollutants [35].

Although photocatalysis has been commonly used for water treatment, its long reaction times and diminished effectiveness due to water pollutants limit its practical application. Ultrasound irradiation can enhance photocatalytic efficiency through simultaneous irradiation. Despite their limitations, combining visible light irradiation and ultrasound shows promise for degrading organic pollutants in wastewater. Studies

indicate that this combined approach, termed sonophotocatalysis, is more efficient than either method alone [36].

Recent research on sonocatalysts and sonophotocatalysts for pollutant degradation is emerging, supported by numerous review articles highlighting the high potential of photocatalysis, sonocatalysis, and sonophotocatalysis for organic pollutant degradation [37]. This thesis focuses on water remediation through these catalytic processes. It elaborates on degradation mechanisms, the impact of various operating parameters on process performance, and the synergistic effects of sonophotocatalysis. The evaluations compare individual processes, identify degradation pathways, and highlight research gaps.

1.5.1. Catalysts for Water Remedial Applications

Catalysts are highly relevant in water remedial applications because they significantly enhance the degradation and removal of a wide range of contaminants. Their primary function is to accelerate chemical reactions without being consumed in the process, making them efficient and cost-effective for repeated use. An ideal catalyst for water remedial applications should possess the following attributes [38]:

- High Activity
- Selectivity
- Stability and Durability
- Non-toxicity
- Renderability
- Efficient Light Utilisation
- Ease of Separation
- Cost-effectiveness
- Environmental Compatibility

Developing a catalyst that meets all desired attributes for water remedial applications is complex. However, significant research efforts have resulted in various catalytic materials for water treatment. These include metal oxides such as TiO_2, ZnO, CuO, and SnO_2; metal sulfides like MoS_2, ZnS, CdS, and SnS_2; advanced composites including graphene-based composites and heterostructured materials; carbon-based catalysts; and novel materials like metal-organic frameworks (MOFs) and graphitic carbon nitride (g-C_3N_4) [39,40,41]. The literature offers extensive information on these catalysts' synthesis

methods and advanced characterisation techniques. Despite the progress in developing well-characterised and efficient catalysts, ongoing research is crucial to design new materials that meet all the desired properties, ultimately enhancing the effectiveness and sustainability of catalytic water treatment processes.

1.6. METAL CHALCOGENIDES

As told at the beginning of this chapter, the thesis work attempts to unravel the applicability of a few metal chalcogenides for water remediation purposes. Group 16 of the periodic table, known as the chalcogens, includes oxygen, sulfur, selenium, tellurium, and polonium. Oxygen and sulfur are non-metals, selenium and tellurium are metalloid semiconductors, and polonium is a metal. Transition metal chalcogenides, which include tellurides, sulfides, and selenides (denoted as M-tellurides, M-sulfides, and M-selenides, where M represents a transition metal), have long intrigued researchers. Chalcogenides are ideal for visible-light harvesting and related applications due to their lower band gaps than most oxides [42]. Within this group, metal sulfides have attracted the most research attention because of their low band gap energy, superior light-harvesting capabilities, and diverse applications. Chalcogenides can be categorised into three distinct groups based on their composition: those containing alkali or alkaline-earth metals, transition metals, or elements from the main group. Some distinctive characteristics of metal chalcogenides are highlighted below [42]:

- Less dense chalcogens, essential to life, are non-toxic.
- Heavier chalcogens, such as tellurium, selenium, and polonium, are toxic and potentially hazardous.
- Chalcogens show significant variation in atomic sizes, but they all have six valence electrons.
- An increase in atomic weight leads to higher density, melting, and boiling points and a larger nuclear radius.
- Non-metals like oxygen, sulfur, and selenium, as well as semimetals such as tellurium and polonium, can conduct electricity.

Transition metal chalcogenides have recently garnered significant research interest due to their versatile elemental composition, tunable bandgaps, earth abundance, excellent optoelectrical properties, visible light activity, and catalytic stability. These

materials and their composites can be broadly classified into binary (e.g., CuS, ZnTe, CdS, ZnSe), ternary (e.g., Cu_2WS_4, $CuFeS_2$), quaternary (e.g., Cu_2FeSnS_4), and heterostructure (e.g., $AgInS_2/SnIn_4$, $Cu_2ZnSnSe_4$) categories. Each category can be doped with conductors to enhance their applications [43].

Metal chalcogenides are employed in diverse applications such as solar cells, optoelectronic sensors, fluorescent labelling for particle detection and tracking, and cancer diagnosis. These nanostructures are also used in superconductors, fuel cells, photovoltaics, photocatalysts, and energy storage devices. Notably, NiS, a sulphide-based chalcogenide, has attracted significant interest due to its abundant phases and potential in rechargeable lithium batteries [44]. These materials have gained popularity as components in solar absorber devices, benefiting from the quantum size effect and higher specific surface areas than their bulk counterparts. Chalcogenide-based materials and other nanomaterials are utilised to remove environmental pollutants, including dyes, chlorinated organic compounds, organophosphorus chemicals, volatile organic compounds, and halogenated herbicides [44]. A brief description of various applications of transition metal chalcogenides and oxides is shown in the following diagram Fig.1.2.
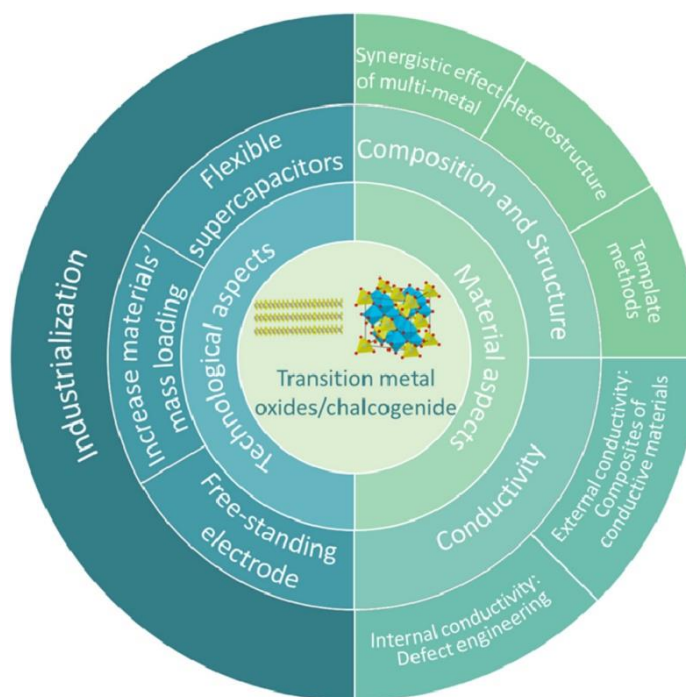
Fig.1.2. The summary of various applications of transition metal-chalcogenides. The figure is adapted from [45].

Due to their unique architecture and dimensions, nanomaterials exhibit distinctive properties ideal for advanced water treatment strategies. Addressing environmental

pollution and energy constraints necessitates the development of novel nanocomposites. Transition metal chalcogenide catalysts are studied for their stability, optoelectronic behaviour, and ability to absorb visible light, making them suitable for wastewater treatment applications. Extensive research has explored their use in water purification through adsorption, photocatalysis, antimicrobial disinfection, persulfate/peroxy monosulfate activation, and Fenton-like processes [45].

Furthermore, their versatile composition allows for easy doping with various elements, enabling fine-tuning for specific contaminants. Their flexibility in morphology provides for the synthesis of materials with optimal surface properties and reactivity. Metal chalcogenides also demonstrate good chemical stability in aqueous environments, making them suitable for long-term water treatment applications. Certain metal chalcogenides are less toxic and more environmentally friendly than metal oxides, reducing potential environmental impact. These attributes make metal chalcogenides a promising class of materials for efficient and sustainable water remediation [46].

This thesis has focused on specific metal chalcogenides that exhibit exceptional affinity towards certain pollutants commonly found in wastewater. The pollutants chosen in this study include sodium dodecyl sulfate and phosphate ions, which are major components of many industrial effluents. Researchers are actively seeking materials with high affinity for these contaminants to enhance the treatment of industrial effluents. We have evaluated various metal chalcogenides for their affinity towards these pollutants and identified copper sulfide (CuS) and manganese sulfide (MnS) as promising candidates for the aforementioned process. A detailed description of the remediation process using these materials is provided in Chapters 4 and 5. This research contributes to developing more efficient and sustainable materials for wastewater treatment, addressing critical environmental and industrial needs.

1.7. BISMUTH BASED NANOMATERIALS

Bi-based nanomaterials are another class of nanocomposites explored in this thesis for water remediation. They have diverse and impactful applications across various fields. In environmental remediation, they are used for photocatalysis to degrade organic pollutants and adsorption to capture heavy metals. In electronics and optoelectronics, bismuth-based nanomaterials, such as bismuth telluride and bismuth antimony, play critical roles in thermoelectric devices and optoelectronic components due to their unique electrical properties. They are also utilised as catalysts in chemical reactions, offering

high activity and selectivity for processes such as oxidation and reduction. Bi-based nanomaterials are employed in medicine for imaging, drug delivery, and targeted cancer therapy. They are also used in sensitive sensors for detecting gases and biological molecules and in energy storage and conversion devices like batteries and supercapacitors, where they enhance electrochemical performance. Overall, Bi-based nanomaterials are integral to environmental, electronic, catalytic, medical, and energy advancements [47]. A brief description of various applications of Bi-based nanomaterials is shown in the following diagram Fig.1.3.
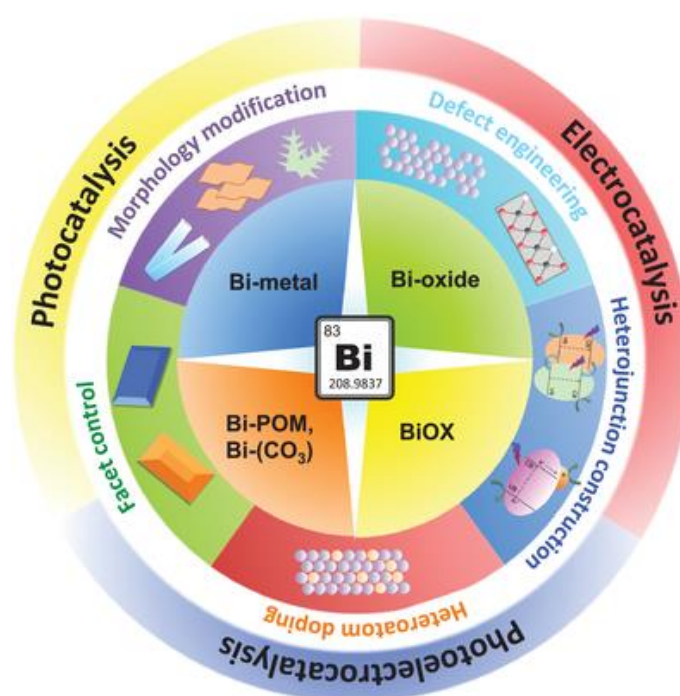
Fig.1.3. *The summary of various applications of Bi-based nanomaterials. The figure is adapted from [48].*

Bi-based nanomaterials are increasingly replacing traditional bulk materials and semiconductor-based catalysts in advanced technologies due to their unique properties, including large specific surface areas, diverse sizes, and morphologies, which enhance their functionality and sustainability. For instance, the tetragonal matlockite structure of BiOCl, which forms compact sheets, significantly increases its surface area and catalytic efficiency for pollution reduction. This has led to a growing focus on understanding the relationship between the physical-chemical characteristics, resulting morphology, and synthesis methods of these materials. Moreover, the cost-effectiveness and eco-friendliness of Bi-based nanomaterials make them valuable for applications in

photocatalysis and heavy metal detection. Bi-based catalysts can be synthesised through simple, energy-efficient, cost-effective methods, such as rapid wet chemical processes. Additionally, the conduction band (CB) and valence band (VB) positions of Bi-based photocatalysts can be finely tuned for various photo-redox reactions [49].

Researchers have explored a wide range of photocatalytic applications, from wastewater treatment to dye-sensitised solar cells, hydrogen evolution, CO_2 reduction, and NO oxidation. TiO_2 is a popular photocatalyst due to its excellent performance, low cost, and non-toxicity. However, TiO_2 has a wide band gap (3.2 eV) and is only effective under ultraviolet light, limiting its utility under sunlight. Therefore, developing photocatalysts responsive to visible light is essential. Bi-based compounds offer a promising alternative with their ability to act as visible-light photocatalysts. Bi-based compounds are highly effective as visible-light-activated photocatalysts due to their semi-metallic nature, allowing them to function directly as semiconductor photocatalysts or serve as co-catalysts to enhance the photocatalytic performance of target materials. Common Bi-based photocatalysts, including sulfides (Bi_2S_3), multiple oxides (Bi_2WO_6, $BiVO_4$, $BiPO_4$), halogen oxides (BiOCl, BiOBr, BiOI), and Bi-rich compounds, often feature a characteristic layered structure and exhibit favourable optical properties [50].

To enhance the photocatalytic activity of Bi-based catalysts, researchers employ various strategies. This study focuses on special modification techniques for Bi-based materials used in selected catalytic applications, addressing gaps in the literature that often emphasise preparation methods and morphology. We have adopted two strategies to enhance photocatalytic efficiency: developing solid solutions and isotype heterojunctions of Bi-based nanomaterials.

The formation of solid solutions significantly enhances catalytic efficiency by creating a homogeneous mixture of different elements at the atomic level. This process tunes electronic and structural properties, optimising active sites, enhancing charge transfer, and increasing catalyst stability [51]. These modifications improve performance in various catalytic processes, such as increased reaction rates, higher selectivity, and more excellent resistance to deactivation.

Isotype heterojunctions enhance photocatalytic efficiency by combining two crystal structures with different electronic properties within the material. This junction facilitates efficient charge separation and transfer by creating a built-in electric field at

the interface, reducing the recombination of photo-generated electron-hole pairs. Consequently, more charge carriers are available for catalytic reactions, improving overall activity. Isotype heterojunctions can also optimise light absorption across a broader spectrum, enhancing solar energy utilisation and boosting performance in applications like pollutant degradation, hydrogen production, and CO_2 reduction [52].

In this research, we developed BiOBr-Cl solid solutions using an in-situ co-precipitation approach, investigating the impact of different Br to Cl molar ratios and assessing their photocatalytic activity in degrading Ciprofloxacin and Tetracycline hydrochloride antibiotics. We also synthesised and thoroughly characterised various crystalline phases of $BiVO_4$, including the isotype heterostructure of tetragonal-monoclinic $BiVO_4$, and studied its sonophotocatalytic activity towards the degradation of rhodamine B dye. To our knowledge, there is no prior report on using hierarchical $BiVO_4$ structures as a sonophotocatalyst for degrading organic pollutants under visible light. This study provides experimental evidence and insights into the significance of solid solutions and isotype heterojunctions in various catalytic water remedial applications. Furthermore, we investigated the synergistic effects of the photocatalytic and sonocatalytic processes on dye degradation and presented a comprehensive evaluation by comparing the outcomes with those of individual processes. A detailed description of the remediation process using these materials is provided in Chapters 6 and 7

1.8. MOTIVATION OF THE WORK

The escalating challenges associated with water pollution and the limitations of conventional treatment methods drive the motivation for this research. The objective is to explore and optimise novel approaches for water remediation that combine adsorption and advanced catalytic processes. This research aims to enhance the efficiency and scope of pollutant removal.

This section outlines the rationale behind the study and the specific goals it seeks to achieve - including the development of high-performance adsorbents and catalysts and the evaluation of their effectiveness in various remediation scenarios. The motivation for this thesis-related research work can be listed as follows:

<u>Motivation statement</u>: To scientifically demonstrate, at a laboratory level, the efficient removal of toxic contaminants prevalent in industrial effluents using innovative adsorbents, photocatalysts, sonocatalysts or sonophotocatalysts.

❖ The surfactants present in industrial effluents pose a significant environmental challenge. Our primary motivation was to explore efficient methods for decomposing these surfactants through adsorption and advanced oxidation processes, thereby mitigating their environmental impact.

❖ Removing phosphate ions, antibiotics, and textile dyes from wastewater is a critical challenge in industrial treatment systems. By introducing novel materials with specific affinities for these pollutants, we were motivated to enhance the efficiency of wastewater treatment processes significantly.

❖ Incorporating ultrasonic sound waves into catalytic reactions offers a promising approach to enhance the efficiency of photocatalytic environmental remediation applications. We were motivated to combine this innovative approach to boost the effectiveness of existing treatment methods.

❖ Researchers are actively seeking new materials to replace TiO_2-based photocatalysts. We were motivated to develop materials that can match or surpass TiO_2 in photocatalytic performance.

❖ We were motivated to build a theoretical backbone for our experimental findings related to adsorption and catalysis processes.

❖ We were motivated to study the thermodynamic properties of adsorption and catalytic processes. It is essential to ensure the scientific feasibility and efficiency of these methods.

In conclusion, our research is driven by the critical need to address environmental challenges associated with industrial effluents. By focusing on the efficient decomposition of surfactants, the removal of persistent pollutants, and the development of innovative catalytic processes, we aim to advance wastewater treatment technologies significantly. Ultimately, we are committed to pioneering advanced strategies that improve catalyst performance and contribute to a cleaner, healthier environment.

1.9. OBJECTIVES OF THE WORK

The primary objective of this thesis is to develop nanomaterials and scientifically demonstrate, at a lab level, the adsorption and catalytic processes for water remediation. Specific objectives include:

1. Develop a suitable material for removing and degrading sodium dodecyl sulfate, an anionic surfactant commonly found in industrial agrochemical, pharmaceutical, oil, paper, mining, and textile wastewater, and explore the underlying mechanisms.

2. Develop a naturally abundant material designed for removing phosphate ions from wastewater and investigate the underlying mechanisms of the removal process.

3. Advance the applicability of ultrasonic sound waves and visible light to degrade prevalent pollutants, such as antibiotics and industrial dyes, to treat industrial effluents. And utilise the combined effect of ultrasonic sound and visible light to improve catalytic degradation processes.

4. Explore the utility of oxyhalide solid solutions for degrading antibiotics or dyes in aqueous medium.

5. Develop and investigate the relevance of an isotype heterojunction photocatalytic material for water remediation activity.

1.10. OVERVIEW OF THE THESIS

Chapter 2 offers a detailed overview of adsorption and catalysis techniques for water remediation, focusing on theoretical aspects and various catalytic processes like sonocatalysis, photocatalysis, and sonophotocatalysis. It emphasises the role of adsorption in removing water contaminants and explains how adsorbents interact with pollutants. The chapter aims to build a foundational understanding of these processes and their importance in mitigating water pollutants, providing insights into advanced treatment methods for environmental remediation.

Chapter 3 details the experimental techniques employed for synthesising, characterising, and applying metal chalcogenides and Bi-based nanomaterials in water remediation. The synthesis methods include solid-state reactions, hydrothermal

processes, and co-precipitation techniques. Additionally, the experimental techniques and the characterisation methods used in this study are thoroughly discussed.

Chapter 4 discusses our attempt to adsorb and catalytically degrade sodium dodecyl sulfate (SDS) in water using a metal chalcogenide, copper sulfide (CuS). This pioneering method combines CuS's adsorption capacity with Fenton-like catalytic activity to completely remove SDS, marking a novel approach in metal chalcogenide-based surfactant removal. Our detailed kinetic, thermodynamic, and catalytic studies provide crucial insights into the mechanisms of SDS removal by CuS, with potential applications in water purification.

In Chapter 5, we report our investigation on employing another metal chalcogenide, manganese sulfide (MnS), to remove phosphate ions and congo red dye from water simultaneously. We achieved efficient pollutant degradation by integrating MnS's adsorption properties with its sonocatalytic capabilities under ultrasound, contributing significantly to metal chalcogenide-based phosphate ion removal strategies.

Chapter 6 reports our exploration of synthesising and utilising 3D mesoporous flower-like $BiOBr_{(1-x)}Cl_x$ solid solutions as heterogeneous photocatalysts for antibiotic degradation. Our study examined the impact of varying Br/Cl content on photocatalytic performance, unveiling intricate mechanisms responsible for the exceptional efficiency of these solid solution nanoplates in antibiotic degradation.

Chapter 7 discusses our work on developing isotype $BiVO_4$ heterojunctions for enhanced sonophotocatalytic degradation of Rhodamine B (RhB). We observed the first instance of RhB sonophotocatalysis in this unique monoclinic/tetragonal heterojunction system by varying surfactant dosage. The chapter advances our understanding of the factors influencing sonophotocatalytic efficiency in isotype $BiVO_4$

Chapter 8 cover provides a summary and conclusions of the thesis. Chapter 9 lists our recommendations for future exploration of the present study.

Overall, this thesis underscores the versatility and effectiveness of metal chalcogenides and Bi-based nanomaterials in addressing diverse water pollution challenges. The findings in the thesis attempt to provide valuable insights and methodologies for sustainable water treatment, paving the way for scalable technologies to combat water pollution and ensure clean water access on a global scale.

1.11. REFERENCES

[1]   Yadav, K. K., Cabral-Pinto, M. M., Gacem, A., Fallatah, A. M., Ravindran, B., Rezania, S., ... & Homod, R. Z. (2024). Recent advances in the application of nanoparticle-based strategies for water remediation as a novel clean technology–A comprehensive review. *Materials Today Chemistry*, *40*, 102226.

[2]   Gude, V. G. (2017). Desalination and water reuse to address global water scarcity. *Reviews in Environmental Science and Bio/Technology*, *16*(4), 591-609.

[3]   Pal, M., Ayele, Y., Hadush, M., Panigrahi, S., & Jadhav, V. J. (2018). Public health hazards due to unsafe drinking water. *Air Water Borne Dis*, *7*(1000138), 2.

[4]   Zahoor, I., & Mushtaq, A. (2023). Water pollution from agricultural activities: A critical global review. *Int. J. Chem. Biochem. Sci*, *23*(1), 164-176.

[5]   Priyadarshanee, M., Mahto, U., & Das, S. (2022). Mechanism of toxicity and adverse health effects of environmental pollutants. In *Microbial biodegradation and bioremediation* (pp. 33-53). Elsevier.

[6]   Collivignarelli, M. C., Abbà, A., Benigna, I., Sorlini, S., & Torretta, V. (2017). Overview of the main disinfection processes for wastewater and drinking water treatment plants. *Sustainability*, *10*(1), 86.

[7]   Saravanan, A., Kumar, P. S., Jeevanantham, S., Karishma, S., Tajsabreen, B., Yaashikaa, P. R., & Reshma, B. (2021). Effective water/wastewater treatment methodologies for toxic pollutants removal: Processes and applications towards sustainable development. *Chemosphere*, *280*, 130595.

[8]   Alzahrani, S., & Mohammad, A. W. (2014). Challenges and trends in membrane technology implementation for produced water treatment: A review. *Journal of Water Process Engineering*, *4*, 107-133.

[9]   Tijani, J. O., Fatoba, O. O., Madzivire, G., & Petrik, L. F. (2014). A review of combined advanced oxidation technologies for the removal of organic pollutants from water. *Water, Air, & Soil Pollution*, *225*, 1-30.

[10]   Karri, R. R., Ravindran, G., & Dehghani, M. H. (2021). Wastewater—sources, toxicity, and their consequences to human health. In *Soft computing techniques in solid waste and wastewater management* (pp. 3-33). Elsevier.

[11]   Fito, J., & Van Hulle, S. W. (2021). Wastewater reclamation and reuse potentials in agriculture: towards environmental sustainability. *Environment, Development and Sustainability*, *23*(3), 2949-2972.

[12]   Dawoud, M. A. (2017, March). The role of treated wastewater reuse in water sustainability in GCC countries. In *WSTA 12th Gulf Water Conference 28-30 March, 2017 Kingdom of Bahrain Water in the GCC... Towards Integrated Strategies* (p. 504).

[13]   World Health Organization. (2016). Protecting surface water for health: Identifying, assessing and managing drinking-water quality risks in surface-water catchments.

[14]   Bae, J. (2021). *Clean Water for All: Examining Safe Drinking Water Act Violations of Water Systems and Community Characteristics* (Doctoral dissertation, University of South Florida).

[15] Lall, U., Josset, L., & Russo, T. (2020). A snapshot of the world's groundwater challenges. *Annual Review of Environment and Resources*, *45*(1), 171-194.

[16] Samberger, C. (2022). The role of water circularity in the food-water-energy nexus and climate change mitigation. *Energy Nexus*, *6*, 100061.

[17] Manikandan, S., Subbaiya, R., Saravanan, M., Ponraj, M., Selvam, M., & Pugazhendhi, A. (2022). A critical review of advanced nanotechnology and hybrid membrane based water recycling, reuse, and wastewater treatment processes. *Chemosphere*, *289*, 132867.

[18] Khan, W. U., Ahmed, S., Dhoble, Y., & Madhav, S. (2023). A critical review of hazardous waste generation from textile industries and associated ecological impacts. *Journal of the Indian Chemical Society*, *100*(1), 100829.

[19] Ahuchaogu, A. A., Chukwu, O. J., Obike, A. I., Igara, C. E., Nnorom, I. C., & Echeme, J. B. O. (2018). Reverse osmosis technology, its applications and nano-enabled membrane. *International Journal of Advanced Research in Chemical Science*, *5*(2), 20-26.

[20] Adam, M. R., Othman, M. H. D., Kurniawan, T. A., Puteh, M. H., Ismail, A. F., Khongnakorn, W., ... & Jaafar, J. (2022). Advances in adsorptive membrane technology for water treatment and resource recovery applications: A critical review. *Journal of Environmental Chemical Engineering*, *10*(3), 107633.

[21] Prakash, N. B., Sockan, V., & Jayakaran, P. (2014). Waste water treatment by coagulation and flocculation. *International Journal of Engineering Science and Innovative Technology*, *3*(2), 479-484.

[22] Islam, S. D. U. (2019). Electrocoagulation (EC) technology for wastewater treatment and pollutants removal. *Sustainable Water Resources Management*, *5*(1), 359-380.

[23] El-Sheekh, M. M., & Mahmoud, Y. A. (2017). Technological approach of bioremediation using microbial tools: bacteria, fungi, and algae. In *Handbook of research on inventive bioremediation techniques* (pp. 134-154). IGI Global.

[24] Arden, T. V. (2012). *Water purification by ion exchange*. Springer Science & Business Media.

[25] Aende, A., Gardy, J., & Hassanpour, A. (2020). Seawater desalination: A review of forward osmosis technique, its challenges, and future prospects. *Processes*, *8*(8), 901.

[26] Tripathi, S., & Hussain, T. (2022). Water and wastewater treatment through ozone-based technologies. In *Development in wastewater treatment research and processes* (pp. 139-172). Elsevier.

[27] Matavos-Aramyan, S., & Moussavi, M. (2017). Advances in Fenton and Fenton based oxidation processes for industrial effluent contaminants control-a review. *Int. J. Environ. Sci. Nat. Resour*, *2*(4), 1-18.

[28] Luan, M., Jing, G., Piao, Y., Liu, D., & Jin, L. (2017). Treatment of refractory organic pollutants in industrial wastewater by wet air oxidation. *Arabian Journal of Chemistry*, *10*, S769-S776.

[29] Shrivastava, V., Ali, I., Marjub, M. M., Rene, E. R., & Soto, A. M. F. (2022). Wastewater in the food industry: Treatment technologies and reuse potential. *Chemosphere*, *293*, 133553.

[30]   Shahmirzadi, M. A. A., Hosseini, S. S., Luo, J., & Ortiz, I. (2018). Significance, evolution and recent advances in adsorption technology, materials and processes for desalination, water softening and salt removal. *Journal of environmental management*, *215*, 324-344.

[31]   Peralta, M. E., Ocampo, S., Funes, I. G., Onaga Medina, F., Parolo, M. E., & Carlos, L. (2020). Nanomaterials with tailored magnetic properties as adsorbents of organic pollutants from wastewaters. *Inorganics*, *8*(4), 24.

[32]   De Gisi, S., Lofrano, G., Grassi, M., & Notarnicola, M. (2016). Characteristics and adsorption capacities of low-cost sorbents for wastewater treatment: A review. *Sustainable Materials and Technologies*, *9*, 10-40.

[33]   Dehghani, M. H., Karri, R. R., & Tyagi, I. (Eds.). (2023). *Sustainable Remediation Technologies for Emerging Pollutants in Aqueous Environment*. Elsevier.

[34]   Parvulescu, V. I., Epron, F., Garcia, H., & Granger, P. (2021). Recent progress and prospects in catalytic water treatment. *Chemical Reviews*, *122*(3), 2981-3121.

[35]   Kathuria, T., Mehta, A., Sharma, S., & Kumar, S. (2024). Review on ultrasound-enhanced activation of persulfate/peroxymonosulfate in hybrid advanced oxidation technologies. *Chemical Engineering Communications*, 1-25.

[36]   Mapukata, S., Ntsendwana, B., Mokhena, T., & Sikhwivhilu, L. (2023). Advances on sonophotocatalysis as a water and wastewater treatment technique: Efficiency, challenges and process optimisation. *Frontiers in Chemistry*, *11*, 1252191.

[37]   Theerthagiri, J., Lee, S. J., Karuppasamy, K., Arulmani, S., Veeralakshmi, S., Ashokkumar, M., & Choi, M. Y. (2021). Application of advanced materials in sonophotocatalytic processes for the remediation of environmental pollutants. *Journal of Hazardous Materials*, *412*, 125245.

[38]   Taghipour, S., Hosseini, S. M., & Ataie-Ashtiani, B. (2019). Engineering nanomaterials for water and wastewater treatment: review of classifications, properties and applications. *New Journal of Chemistry*, *43*(21), 7902-7927.

[39]   Venkateshaiah, A., Černík, M., & Padil, V. V. (2022). Metal oxide nanoparticles for environmental remediation. *Nanotechnology for Environmental Remediation*, 183-213.

[40]   Ali, S., Rehman, Z., Munir, A., Ullah, H., Butler, I. S., & Ahmad, S. B. (2024). Selected photoactive metal sulfides for environmental cleansing. *Inorganic Chemistry Communications*, 112568.

[41]   Nour AbouSeada, Maryam G. Elmahgary, Sameh O. Abdellatif, Khaled Kirah (2024), Synergistic integration of zirconium-based metal-organic frameworks and graphitic carbon nitride for sustainable energy solutions: A comprehensive review, *Journal of Alloys and Compounds,*1002, 175325.

[42]   Yadav, S., Yashas, S. R., & Shivaraju, H. P. (2021). Transitional metal chalcogenide nanostructures for remediation and energy: a review. *Environmental Chemistry Letters*, *19*(5), 3683-3700.

[43]   Okpara, E. C., Olatunde, O. C., Wojuola, O. B., & Onwudiwe, D. C. (2023). Applications of transition metal oxides and chalcogenides and their composites in water treatment: a review. Environ Adv 11: 100341.

[44]   Khan, M. S., Shariq, M., Bouzgarrou, S. M., Azooz, R. E., kashif Ali, S., Ghaly, W. A., & Hassan, K. F. (2024). Recent advancements in supercapacitors and their charge storage mechanism and progress in transition metal sulfide-based electrodes. *Physica Scripta*, *99*(6), 062001.

[45]   Zhu, X. (2022). Recent advances of transition metal oxides and chalcogenides in pseudo-capacitors and hybrid capacitors: A review of structures, synthetic strategies, and mechanism studies. *Journal of Energy Storage*, *49*, 104148.

[46]   Li, Y., Dong, H., Li, L., Tang, L., Tian, R., Li, R., ... & Zeng, G. (2021). Recent advances in waste water treatment through transition metal sulfides-based advanced oxidation processes. *Water Research*, *192*, 116850.

[47]   Batool, M., Nazar, M. F., Awan, A., Tahir, M. B., Rahdar, A., Shalan, A. E., ... & Zafar, M. N. (2021). Bismuth-based heterojunction nanocomposites for photocatalysis and heavy metal detection applications. *Nano-Structures & Nano-Objects*, *27*, 100762.

[48]   Utomo, W. P., Leung, M. K., Yin, Z., Wu, H., & Ng, Y. H. (2022). Advancement of bismuth-based materials for electrocatalytic and photo (electro) catalytic ammonia synthesis. *Advanced Functional Materials*, *32*(4), 2106713.

[49]   Han, Q. (2021). Advances in preparation methods of bismuth-based photocatalysts. *Chemical Engineering Journal*, *414*, 127877.

[50]   Zhang, L., Li, Y., Li, Q., Fan, J., Carabineiro, S. A., & Lv, K. (2021). Recent advances on Bismuth-based Photocatalysts: Strategies and mechanisms. *Chemical Engineering Journal*, *419*, 129484.

[51]   Ajiboye, T. O., Oyewo, O. A., & Onwudiwe, D. C. (2021). The performance of bismuth-based compounds in photocatalytic applications. *Surfaces and Interfaces*, *23*, 100927.

[51]   Kobayashi, H., Kusada, K., & Kitagawa, H. (2015). Creation of novel solid-solution alloy nanoparticles on the basis of density-of-states engineering by interelement fusion. *Accounts of chemical research*, *48*(6), 1551-1559.

[53]   Usai, S., Obregón, S., Becerro, A. I., & Colón, G. (2013). Monoclinic–tetragonal heterostructured BiVO4 by yttrium doping with improved photocatalytic activity. *The Journal of Physical Chemistry C*, *117*(46), 24479-24484.

CHAPTER 2

Overview of Adsorption and Catalysis
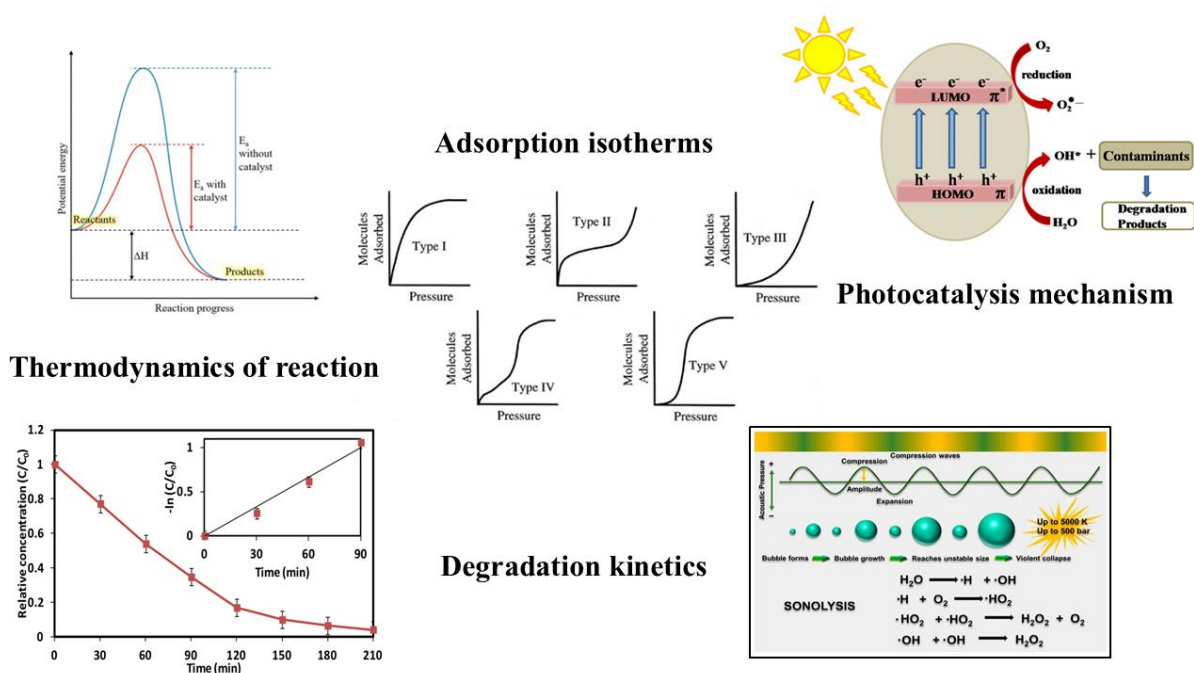
This chapter offers a comprehensive examination of adsorption and catalysis techniques for water remediation, emphasizing the theoretical fundamentals of adsorption and catalytic processes such as sonocatalysis, photocatalysis, and sonophotocatalysis.

2.1. INTRODUCTION

This chapter provides a comprehensive overview of adsorption and catalysis techniques for water remediation. The chapter delves into the fundamental theoretical aspects of adsorption and various catalytic processes, including sonocatalysis, photocatalysis, and sonophotocatalysis. It explores the importance of adsorption in removing contaminants from water and highlights the mechanisms through which adsorbents interact with pollutants. The chapter aims to establish a foundational understanding of these processes, highlighting their significance in mitigating water contaminants and pollutants. This overview gives readers insights into the mechanisms governing these advanced treatment methods, laying the groundwork for their application in environmental remediation efforts.

2.2. ADSORPTION

Adsorption is a surface phenomenon where molecules or ions from a liquid or gas adhere to the surface of a solid material. This process is driven by various interactions, including van der Waals forces, electrostatic attractions, and chemical bonding [1]. Adsorption can be categorised as chemisorption or physisorption based on the strength of the interaction between the adsorbate and the substrate. Physisorption occurs due to weak electrostatic interactions, such as London forces, dipole-dipole forces, and Van der Waals interactions, which can be easily broken. In contrast, chemisorption involves the formation of covalent bonds through sharing or transferring electrons, resulting in much stronger interactions [2]. Physisorption typically leads to multilayer formation on the adsorbent, while chemisorption forms a monolayer [3].

Adsorption plays a crucial role in water remediation because it effectively removes a wide range of contaminants, including heavy metals, organic pollutants, and inorganic ions [4]. The high surface area and porosity of adsorbents like activated carbon, metal oxides, and functionalised nanomaterials enhance their capacity to trap and immobilise pollutants from wastewater [5]. This method is advantageous for its simplicity, cost-effectiveness, and ability to achieve high removal efficiencies, making it a vital technique in the treatment and purification of water for safe environmental discharge and human consumption [6].

Choosing the proper adsorbent is crucial for developing an effective adsorption system. An ideal adsorbent should be low-cost, readily available, efficient, and have a high surface area and pore volume [7]. It should also exhibit mechanical, chemical, and

thermal stability, ease of desorption and reuse, fast kinetics, and high adsorption capacity [8].

2.2.1. Adsorption equilibrium

Adsorption equilibrium is achieved when the rate of molecules adsorbing onto a solid surface equals the desorption rate back into the fluid phase, resulting in a constant amount of adsorbate on the adsorbent over time. This equilibrium is typically described by adsorption isotherms, which are mathematical models that relate the amount of adsorbate on the adsorbent to its concentration in the fluid phase at a constant temperature. On a homogeneous surface, physical adsorption should follow a linear form at lower concentrations because there are no variations in the molecular state of the adsorption [9]. Henry's adsorption isotherm model is suitable for describing adsorbate adsorption at low concentrations, where all adsorbate molecules are isolated from their nearest neighbours [10]. The following linear expression describes the equilibrium concentrations of the adsorbate in the liquid and adsorbed phases:

$$q_e = KC_e \dots\dots (2.1)$$

where q_e is the adsorption density at equilibrium (mg adsorbate/g adsorbent), C_e is the equilibrium concentration (mg/L), and K is the adsorption equilibrium constant (L/mg) mentioned as Henry's law constant.

The adsorption capacity at equilibrium, q_e (mg/g), can be calculated by the following equation:

$$q_e = \frac{(C_0 - C_e) \times V}{m} \dots\dots (2.2)$$

where C_0 is the initial concentration of the adsorbate and C_e is the equilibrium concentration in mg/L, V is the volume of solution in L, and m is the mass of the adsorbent in g.

In addition, the quantity of adsorption at a time t, q_t (mg/g) can be calculated by equation (2.3)

$$q_t = \frac{(C_0 - C_t) \times V}{m} \dots\dots (2.3)$$

where C_t is the concentration of the adsorbate at a time t.

Understanding adsorption equilibrium is crucial for designing and optimising adsorption systems in various applications, such as water purification, gas separation, and catalysis. It provides insights into the capacity and efficiency of adsorbents, helping to predict their performance under different conditions [11].

2.2.2. Adsorption isotherms

Adsorption equilibrium relationships, or adsorption isotherms, describe how pollutants interact with adsorbent materials. This is vital for optimising adsorption mechanisms, expressing the surface properties and capacities of adsorbents, and designing effective adsorption systems. The shape of the adsorption isotherm provides quantitative information about the adsorption process and the extent of surface coverage by the adsorbate [12].
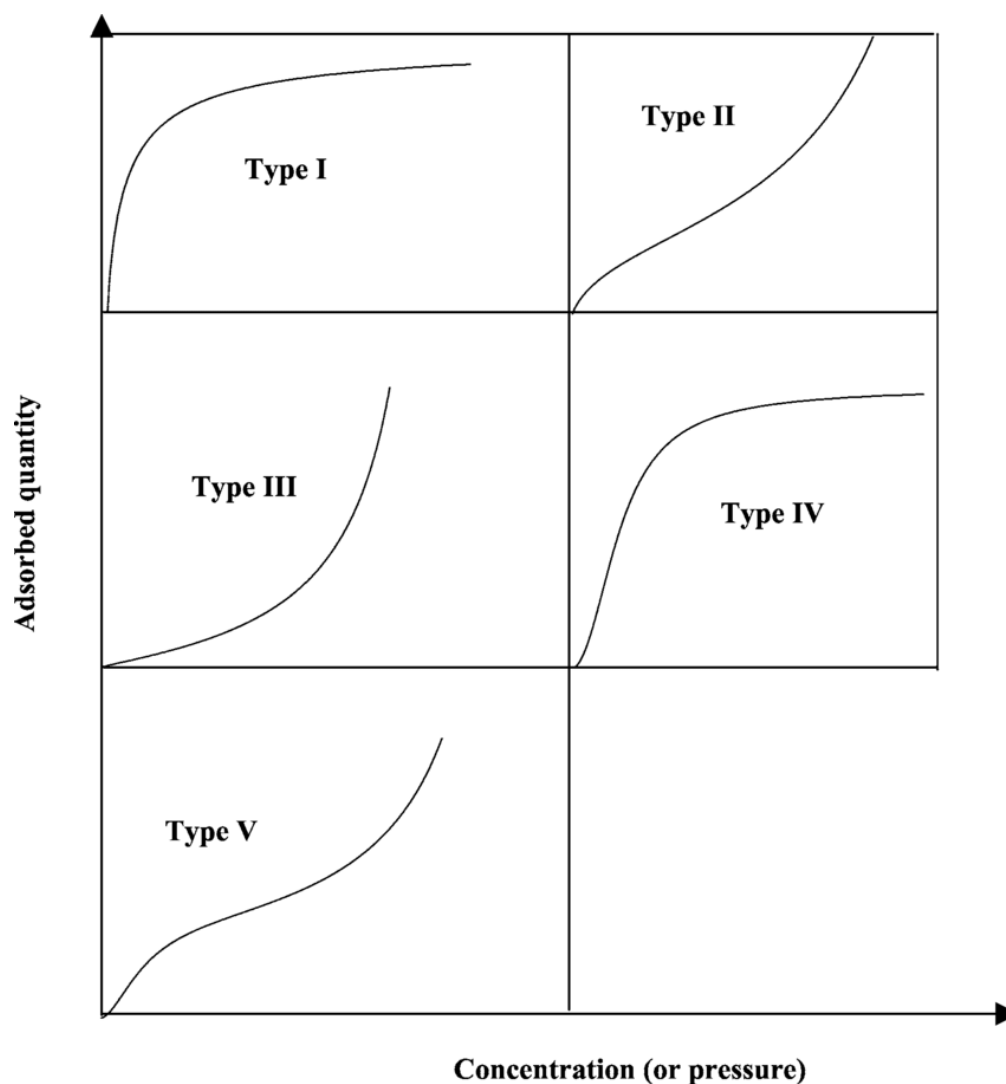
Fig.2.1. *The five types of adsorption isotherm, I to V, in the classification of Brunauer, Emett, and Teller. The figure is adapted from [13].*

The five isotherm shapes depicted in Fig. 2.1 each reflects unique conditions. These isotherms and the conditions leading to their occurrence are discussed below:

- Type I Isotherms: These occur when adsorption is limited to only a few molecular layers, typical of chemisorption, where all surface sites are occupied. In physical adsorption, Type I isotherms occur with microporous powders with pore sizes only a few molecular diameters wide. The molecules in such small pores encounter overlapping potentials from the pore walls, enhancing gas adsorption at low concentrations. The pores are filled at higher concentrations, leading to a plateau, indicating no further adsorption once the micropores are filled [14].

- Type II Isotherms: Commonly encountered on nonporous powders or powders with larger pore diameters. The knee of the isotherm usually occurs near the completion of the first adsorbed monolayer, with additional layers forming at higher pressures until saturation, where the number of adsorbed layers becomes infinite [15].

- Type III Isotherms: Characterised by heats of adsorption lower than the adsorbate heat of liquefaction. As adsorption proceeds, additional adsorption is facilitated because the adsorbate interaction with an adsorbed layer is more robust than with the adsorbent surface [16].

- Type IV Isotherms: Occur on porous adsorbents with pore radii ranging from approximately 15 to 1000 angstroms. The slope increase at higher pressures indicates increased adsorbate uptake as the pores fill. Similar to Type II isotherms, the knee of the Type IV isotherm generally occurs near the completion of the first monolayer [17].

- Type V Isotherms: Result from small adsorbate-adsorbent interaction potentials, similar to Type III isotherms, but are also associated with pores in the same range as those of Type IV isotherms [18].

2.2.3. Adsorption isotherm models

The mathematical correlation plays a crucial role in the modelling, operational design, and practical application of adsorption systems. It is typically depicted by graphically expressing the solid-phase concentration (adsorption density) against its residual concentration (equilibrium concentration). The physicochemical parameters and

underlying thermodynamic assumptions offer insights into the adsorption mechanism, surface properties, and the degree of affinity of the adsorbents.

Over the last decade, three fundamental approaches have shaped the development of various isotherm models. The first approach is based on kinetic considerations, defining adsorption equilibrium as a state of dynamic equilibrium where adsorption and desorption rates are equal [19]. The second approach focuses on thermodynamics, providing a framework for deriving different forms of adsorption isotherm models. The third approach emphasises the generation of characteristic curves, a potential theory. A notable trend in isotherm modelling is the use of multiple approaches, which leads to differences in the physical interpretation of model parameters [20].

There are two classes of isotherm models: monolayer and multilayer isotherms. A brief description of some isotherm models used for this study is described below.

2.2.3.1. Langmuir isotherm model

The Langmuir adsorption isotherm, initially developed to describe gas-solid phase adsorption onto activated carbon, has traditionally been used to quantify and compare the performance of various bio-sorbents [22]. This empirical model assumes monolayer adsorption, meaning the adsorbed layer is only one molecule thick. Adsorption can only occur at a finite number of definite localised sites that are identical and equivalent, with no lateral interactions or steric hindrance between the adsorbed molecules, even on adjacent sites [22]. The Langmuir isotherm describes homogeneous adsorption, where each molecule has constant enthalpies and sorption activation energy (indicating that all sites have equal affinity for the adsorbate), and there is no migration of the adsorbate across the surface [23].

The Langmuir equation for the adsorption of molecules on the homogeneous surface can be written as [24]:

$$q_e = \frac{q_{max} K_L C_e}{1 + K_L C_e} \dots\dots (2.4)$$

where q_e (mg/g) and C_e (mg/L) are the amount of adsorbate adsorbed per unit mass of adsorbent at equilibrium and adsorbate concentration at equilibrium, respectively. q_{max} (mg/g) is the maximum adsorption capacity, and K_L is the Langmuir adsorption equilibrium constant (L /mg) and is related to the free energy of adsorption.

The essential characteristics of the Langmuir isotherm can be expressed by a dimensionless constant called the separation factor R_L ,and it is given by

$$R_L = \frac{1}{1 + K_L C_0} \dots \dots (2.5)$$

Where C_0 (mg/L) is the initial concentration of the adsorbate solution and K_L is the Langmuir adsorption equilibrium constant (L /mg). A variation of the suitable area and the adsorbent's porosity can be correlated with K_L constant, implying that higher adsorption capacity can result from a large surface area and pore volume. The value of R_L indicates the adsorption process is to be favourable ($R_L < 1$), unfavourable ($R_L > 1$), linear ($R_L = 1$) or irreversible ($R_L = 0$) [24].

2.2.3.2. Freundlich isotherm model

The Freundlich adsorption isotherm model describes a reversible and non-ideal adsorption process. Unlike the Langmuir model, the Freundlich model is not limited to monolayer adsorption and can be applied to multilayer adsorption. In this model, the adsorption heat and affinities do not need to be uniformly distributed across the heterogeneous surface. The Freundlich isotherm model accounts for surface heterogeneity and the exponential distribution of active sites and their energies. The empirical formula for the Freundlich adsorption model is given by [25]:

$$q_e = K_F C_e^{\frac{1}{n_F}} \dots \dots (2.6)$$

Where K_F (L/mg) is the Freundlich adsorption isotherm constant related to the sorption capacity of the adsorbent and $\frac{1}{n_F}$ is adsorption intensity; it also indicates the relative distribution of the energy and the heterogeneity of the adsorbate sites. If the value of $\frac{1}{n_F}$ lies between 0 and 1 designates favourable adsorption isotherm. If it is greater than 1, it represents an unfavorable adsorption isotherm. When this value gets closer to zero, the adsorption isotherm becomes non-linear, indicating the irreversible isotherm [25].

2.2.3.3. Temkin isotherm model

The Temkin empirical isotherm model was initially used to describe hydrogen adsorption on platinum electrodes in an acidic solution, a chemisorption system. This model accounts for the interaction between the adsorbent and adsorbate, ignoring extremely high and low concentration values [26]. It assumes that the adsorption heat

(ΔH_{ads}) of all molecules in the layer decreases linearly with temperature rather than logarithmically as surface coverage increases. This adsorption isotherm model is only valid for an intermediate concentration range. The empirical formula of the isotherm model is [26]:

$$q_e = \frac{RT}{b_T} \ln(K_T C_e) \dots \dots (2.7)$$

Where b_T and K_T are Temkin isotherm constants, T is the absolute temperature, and R is the universal gas constant ($8.314 \, JK^{-1} mol^{-1}$). The constant b_T is related to adsorbate-adsorbent interactions.

2.2.3.4. Dubinin-Radushkevich isotherm model

The Dubinin-Radushkevich adsorption isotherm model is typically used to describe the adsorption mechanism involving Gaussian energy distribution on heterogeneous surfaces. Unlike the Langmuir and Freundlich models, the Dubinin-Radushkevich model is a semi-empirical equation that follows a pore-filling mechanism. This model assumes a multilayer adsorption process involving Van der Waals forces, making it applicable to physical adsorption processes [27]. The distinguishable feature of D-R and Temkin models with respect to other models is that they are temperature dependent, hence when the adsorption data at different temperatures are plotted as a function of the logarithm of the amount adsorbed versus the square of potential energy. It is usually applied to distinguish the physical or chemical adsorption of adsorbate molecules on the adsorbent. D-R model presumes a pore-filling mechanism for the adsorption process. The semi-empirical expression for this model is [27]:

$$q_e = q_{max} exp(-\beta \varepsilon^2) \dots \dots (2.8)$$

where β is the Dubinin-Radushkevich constant, R is the gas constant ($8.314 \, JK^{-1} mol^{-1}$), T is absolute temperature, and ε is Polanyi potential and is defined as

$$\varepsilon = RT \ln\left(1 + \frac{1}{C_e}\right) \dots \dots (2.9)$$

The constant, β is associated with the mean free energy of adsorption per mole of the adsorbate as it is transferred to the surface of the solid from an infinite distance in the solution, and this energy can be calculated using the equation [27]:

$$E = \frac{1}{\sqrt{2\beta}} \quad \text{... ...} \quad (2.10)$$

The value of E is used to predict whether the adsorption is physisorption or chemisorption. If the value of $E < 8 \; KJmol^{-1}$ the adsorption process is physisorption [27].

The linearised form of the D-R equation is

$$\ln q_e = \ln q_{max} - \beta\varepsilon^2 \quad \text{... ...} \quad (2.11)$$

From the slope and intercept of $\ln q_e$ versus ε^2 graph, we can calculate q_{max} and β.

2.2.3.4. Fowler-Guggenheim isotherm model

The Fowler-Guggenheim isotherm model considers the lateral interaction of the adsorbent molecules. The F-G model isotherm equation can be written as [28]:

$$C_e = \frac{\theta}{K_{FG}(1 - \theta)} exp\left(\frac{2\theta\omega}{RT}\right) \quad \text{... ...} \quad (2.12)$$

where K_{FG} is Fowler-Guggenheim equilibrium constant (L/mg), θ is fractional coverage, R is the universal gas constant ($8.314 \; JK^{-1}mol^{-1}$), T is absolute temperature, and w is interaction energy between adsorbed molecules $kJ^{-1}mol^{-1}$.

If the interaction between adsorbed molecules is attractive, then the heat of adsorption will increase with loading because of increased interaction between adsorbed molecules as loading increases (i.e., w = positive). However, if the interaction among adsorbed molecules is repulsive, then the heat of adsorption decreases with loading (i.e., w = negative). But when w = 0, then there is no interaction between adsorbed molecules, and the Fowler-Guggenheim isotherm reduces to the Langmuir equation [28].

The linearised form of F-G equation can be written as

$$\ln\left[\frac{C_e(1 - \theta)}{\theta}\right] = -\ln K_{FG} + \frac{2\theta\omega}{RT} \quad \text{... ...} \quad (2.13)$$

A plot of $\ln[Ce(1 - \theta)/\theta]$ versus θ is used to obtain the values for K_{FG} and w. It is important to note that this model only applies when surface coverage is less than 0.6 (θ < 0.6).

2.2.3.5. Sips isotherm model

Sips propose an isotherm model that combines the Langmuir and Freundlich models. The model describes the localised adsorption of the molecules without the adsorbate-adsorbate interactions. Sips isotherm model is given by the equation [29]:

$$q_e = \frac{A_S B_S C_e^{n_S}}{1 + B_S C_e^{n_S}} \dots \dots (2.14)$$

Where A_S and B_S are Sips isotherm constants, n_S is Sips exponent factor. The constant n_S is often regarded as the heterogeneity factor. The n_S parameter is usually greater than unity; therefore, the larger this parameter is, the more heterogeneous the system if its values close to (or exactly) 1 indicate a solid with relatively homogeneous binding sites. If n_S is unity, the equation reduces to Langmuir isotherm. At low adsorbate concentrations or $n_S \approx 0$ the Sips isotherm model effectively reduces to the Freundlich isotherm. Therefore, it does not follow Henry's law [29].

2.2.3.6. Hill isotherm model

This model assumes that adsorption is a cooperative phenomenon, with the ligand binding ability at one site on the macromolecule, which may influence different binding sites on the same macromolecule. The Hill equation was postulated to describe the binding of different species onto homogeneous substrates. The Hill isotherm model is represented by the equation [30]:

$$q_e = \frac{A_H C_e^H}{B_H + C_e^{n_H}} \dots \dots (2.15)$$

Where A_H and B_H are Hill isotherm constants, n_H is Hill exponent factor. In this model, three possibilities can occur $n_H > 1$, positive cooperativity in binding, $n_H = 1$, non-cooperative or hyperbolic binding, $n_H < 1$, negative cooperativity in binding [30].

2.2.4. Adsorption kinetics

The kinetic behaviour of adsorbates on adsorbents has been studied by examining the effect of time on sorption. Designing an effective and sustainable adsorption system requires a deeper understanding of the reaction dynamics, particularly the rate constants [31]. Adsorption kinetics determine the rate at which adsorption occurs and are influenced by factors such as the surface complexity of the adsorbent, solute concentration, temperature, and pH of the solution [31].

Adsorption kinetic models are classified into two groups: adsorption reaction models and adsorption diffusion models. Adsorption reaction models reveal the rate of adsorbate uptake by adsorbents but do not explain the underlying cause of adsorption [32]. In contrast, adsorption diffusion models account for external diffusion, internal (pore) diffusion, and the effect of mass action (i.e., adsorption/desorption between adsorbates and active sites of adsorbents). Therefore, adsorption reaction models should align with the proposed mechanisms defined by fitting adsorption diffusion models [32].

2.2.4.1. Pseudo-First-order (PFO) kinetic model

This is also known as the Lagergren model. The pseudo-first-order model is mainly used to analyse adsorption data obtained from the adsorption of adsorbates from aqueous solutions [33]. It describes the rate of adsorption, which is proportional to the number of unoccupied binding sites on adsorbents. This kinetic model is usually represented in the following equation [33]:

$$\frac{dq_t}{dt} = k_1(q_e - q_t) \dots \dots (2.16)$$

where q_t is adsorbate adsorbed onto adsorbent at time t (mg/g), q_e is equilibrium adsorption capacity (mg/g), and k_1 is rate constant per min. Integrating the above equation with initial condition $t = 0, q_t = 0$ we get the Non-linear form of the PFO equation:

$$q_t = q_e(1 - e^{-k_1 t}) \dots \dots (2.17)$$

2.2.4.2. Pseudo-Second-order (PSO) kinetic model

The pseudo-second-order kinetic model explains how adsorbates bind to adsorbents, where the interaction between adsorbates and functional groups on the adsorbent surface determines the adsorption capacity [34]. This model relies on equilibrium adsorption, which is influenced by both the initial adsorbate amount on the adsorbent surface and the equilibrium adsorbate amount. It is employed to determine the sorption process order and enables the assessment of sorption capacity. This model assumes that the rate of adsorption of the solute is proportional to the available sites on the adsorbent. The reaction rate is dependent on the amount of solute on the surface of the adsorbent. The model can be represented as [34]:

$$\frac{dq_t}{dt} = k_2(q_e - q_t)^2 \dots (2.18)$$

k_2 (g.min^{-1} mg^{-1}) is Pseudo Second Order rate constant. Applying the integral limits for t (0, t) and q_t(0, q_t), we get,

$$q_t = \frac{k_2 q_e^2 t}{1 + k_2 q_e t} \dots (2.19)$$

2.2.4.3.Intra-particle diffusion (IPD) model

The intra-particle diffusion model is used to identify the mechanism involved during the adsorption process, described by external mass transfer and intra-particle diffusion [35]. The solute adsorption in a solution involves mass transfer of adsorbate (film diffusion), surface diffusion, and pore diffusion. Film diffusion is independent, whereas surface and pore diffusion may occur simultaneously. This model can be represented by Weber and Morris equation [35]:

$$q_t = k_{id}\sqrt{t} + C \dots\dots (2.20)$$

Where k_{id} (mg g^{-1} min$^{1/2}$) is the rate constant of intra-particle diffusion and C is proportional to the boundary layer thickness. If the regression of q_t versus $t^{1/2}$ gives a straight line, then intra-particle diffusion is involved in the adsorption process, and if this line passes through the origin, then intra-particle diffusion is the sole rate-limiting step. In the case of multiple linear regions, the plot indicates the influence of external mass transfer on controlling the adsorption rate in single and binary systems. A significant value for *C* indicates the role of film diffusion [35].

2.2.4.4. Liquid film diffusion model

The Liquid Film Diffusion model is used to describe the kinetics of the adsorption process, mainly focusing on the initial stages, where the rate-limiting step is the diffusion of adsorbate molecules through the liquid film surrounding the adsorbent particles [36]. The model is helpful in understanding how quickly an adsorbate can transfer from the bulk solution to the surface of the adsorbent. The governing equation of the Liquid Film Diffusion model is [36]:

$$\ln(1 - F) = -k_{fd}t \dots\dots (2.21)$$

where: Fis the fraction of adsorbate adsorbed at time t, defined as $F = \frac{q_t}{q_e}$, q_t is the amount of adsorbate adsorbed at time *t* and q_e is the amount of adsorbate adsorbed at equilibrium. $k_{fd}$is the rate constant of liquid film diffusion (s^{-1})

The relation between $\ln(1-F)$ versus t suggests a linear relationship, where k_{fd} can be obtained from the slope of the resulting straight line. This model is beneficial in the initial stages of adsorption, where film diffusion is the dominant mechanism controlling the adsorption rate. The Liquid Film Diffusion model in various contexts makes them valuable resources for understanding the theory and practice of adsorption kinetics [36].

2.2.5. Thermodynamics of adsorption

Thermodynamic parameters of adsorption processes are readily evaluated because temperature influences adsorption. Assessing the thermodynamics of adsorption experiments is necessary to determine the spontaneity and feasibility of these processes. Consequently, experimental data from adsorption procedures are used to calculate thermodynamic parameters such as Gibbs free energy change (ΔG), enthalpy change (ΔH), entropy change (ΔS), and isoteric heat of adsorption (ΔH$_x$). The various thermodynamic parameters of the adsorption process can be determined using the variation of solute distribution coefficient (K_d) between the solid and liquid phases at different temperatures. The equilibrium solute distribution co-efficient of the process is defined as [37]:

$$K_d = \frac{q_e}{C_e} \dots\dots (2.22)$$

Where q_e and C_e are the adsorption density and concentration of adsorbate solution at adsorption equilibrium. The Gibb's free energy change in an adsorption process is usually related to the equilibrium constant by the Gibbs fundamental equation:

$$\Delta G^0 = -RT \ln(1000 \times K_d) \dots\dots (2.23)$$

where R is the universal gas constant (8.314 J mol−1 K−1), and T is the absolute temperature of the system (K), and the factor 1000 is multiplied by K_d to make it dimensionless K_d must be dimensionless. Since the adsorption was conducted using aqueous solutions with very low concentrations of the target compounds, the dimensionality of the K_d (L g $^{-1}$) can be easily converted into dimensionless values by multiplying the distribution coefficient by 1000 (as 1 L = 1000 g, and the solution density is 1 g mL^{-1}). The Gibb's free energy change of the reaction can also be written as [38]:

$$\Delta G = \Delta H - T\Delta S \dots (2.24)$$

Comparing the above two equations, we get,

$$-RT \ln(1000 \times K_d) = \Delta H - T\Delta S \dots\dots (2.25)$$

$$\ln(1000 \times K_d) = -\frac{\Delta H}{RT} + \frac{\Delta S}{R} \dots\dots (2.26)$$

This is called Van't Hoff's equation. Furthermore, the system's ΔH and ΔS values were determined from the slope and intercept of Van't Hoff plot $\ln(1000 \times K_d)$ versus 1/T), respectively. The calculation of ΔG resulted in negative values in all cases, indicating spontaneous adsorption. The spontaneity (increase in the negativity of ΔG values) was increased with the more favourable adsorption temperature.

The physical significance of each thermodynamic parameter in the adsorption process is briefly described below:

- **Gibbs Free Energy Change (ΔG):** Gibbs free energy change assesses the spontaneity and feasibility of adsorption processes. A negative ΔG value indicates a spontaneous process, while a positive ΔG value signifies a non-spontaneous process. The free energy change in adsorption is typically related to the equilibrium constant through the Gibbs fundamental equation [39].

- **Enthalpy Change (ΔH):** Enthalpy change (ΔH) represents the energy supplied as heat at constant pressure when the system does no extra work. In adsorption studies, the enthalpy change provides insights into the nature and mechanism of adsorption processes. A negative ΔH value implies an exothermic adsorption process, while a positive ΔH value indicates an endothermic process [40].

- **Entropy Change (ΔS):** Entropy change during adsorption can be determined from the Van't Hoff equation. A positive ΔS value indicates the affinity of the adsorbent towards the adsorbate, suggesting increased randomness at the solid/liquid interface with some structural changes in the adsorbent and adsorbate [41].

2.3. PHOTOCATALYSIS

Photocatalysis is a process where light activates a substance, known as a photocatalyst, which then alters the rate of a chemical reaction without undergoing any chemical change itself [42]. Unlike conventional thermal catalysts, which are activated by heat, photocatalysts are activated by photons of appropriate energy. The IUPAC says photocatalysis is "a catalytic reaction involving light absorption by the substrate." This

process involves activating semiconductor materials by specific wavelengths of light [43].

Photocatalysis is widely used to eliminate various pollutants, including alkanes, alkenes, phenols, aromatics, and pesticides, leading to the complete mineralisation of organic compounds. Although several photocatalysts, such as CdS, Fe_2O_3, ZnO, WO_3, and ZnS, have been studied, TiO_2 P25 has shown the best results [44].

This versatile process has diverse applications, including water and air purification, odour control, bacterial inactivation, hydrogen production through water splitting, and cancer cell treatment [45]. In wastewater treatment, photocatalysis offers distinct advantages by effectively destroying organic hazardous compounds that are challenging for conventional purification techniques. As an advanced oxidation process (AOP), photocatalysis uses UV or visible light to generate reactive oxygen species, such as hydroxyl radicals ($\cdot$OH) and superoxide radicals ($O_2\cdot^-$), from molecules like O_3, H_2O_2, and UV light [46]. These species facilitate the complete mineralisation of organic pollutants, degradation of by-products, and disinfection of waterborne pathogens.

Photocatalysis relies on photo-induced charge separation on the catalyst surface, where light activation enhances chemical reaction rates. Semiconductor-based photocatalysts are favoured for water purification due to their light absorption capabilities, efficient charge transport properties, prolonged excited-state lifetimes, and suitable electronic band structures. Photocatalysts with narrower bandgaps are especially effective in utilising visible light, constituting a significant portion of solar energy, making visible light-active photocatalysis a crucial technology for sustainable environmental applications [47].

2.3.1. Basic mechanism of Photocatalysis

The photocatalytic process begins when a semiconductor catalyst is illuminated with light energy exceeding its band gap. Electrons in the valence band (VB) are excited, moving to the conduction band (CB) and leaving behind holes (h^+). If these photogenerated electron-hole pairs recombine, energy is released, reducing the semiconductor's quantum efficiency in converting light into energy. When recombination minimises, electrons and holes migrate to the material's surface, initiating secondary reactions with adsorbed substances. Electrons can react with electron acceptors like O_2, producing superoxide radical anions ($O_2^{\cdot-}$), while holes can oxidise pollutants or H_2O to

generate hydroxyl radicals (·OH). These radicals are potent oxidising agents that efficiently mineralise organic compounds into water and carbon dioxide under prolonged exposure to high-energy UV light. Oxygen reduction is slower than pollutant oxidation in the photocatalytic degradation of pollutants, necessitating synchronised processes to prevent electron accumulation in the conduction band and enhance electron-hole recombination [48]. The schematic representation of degradation of pollutants using photocatalysis is shown in Fig.2.2.

$$Semiconductor + hv \rightarrow e_{CB}^- + h_{VB}^+$$

$$e_{CB}^- + h_{VB}^+ \rightarrow energy$$

$$e_{CB}^- + O_2 \rightarrow O_2^{-\cdot}$$

$$h_{VB}^+ + H_2O \rightarrow H^+ + OH\cdot$$

$$O_2^{-\cdot} + pollutant \rightarrow H_2O + CO_2$$

$$OH\cdot + pollutant \rightarrow H_2O + CO_2$$
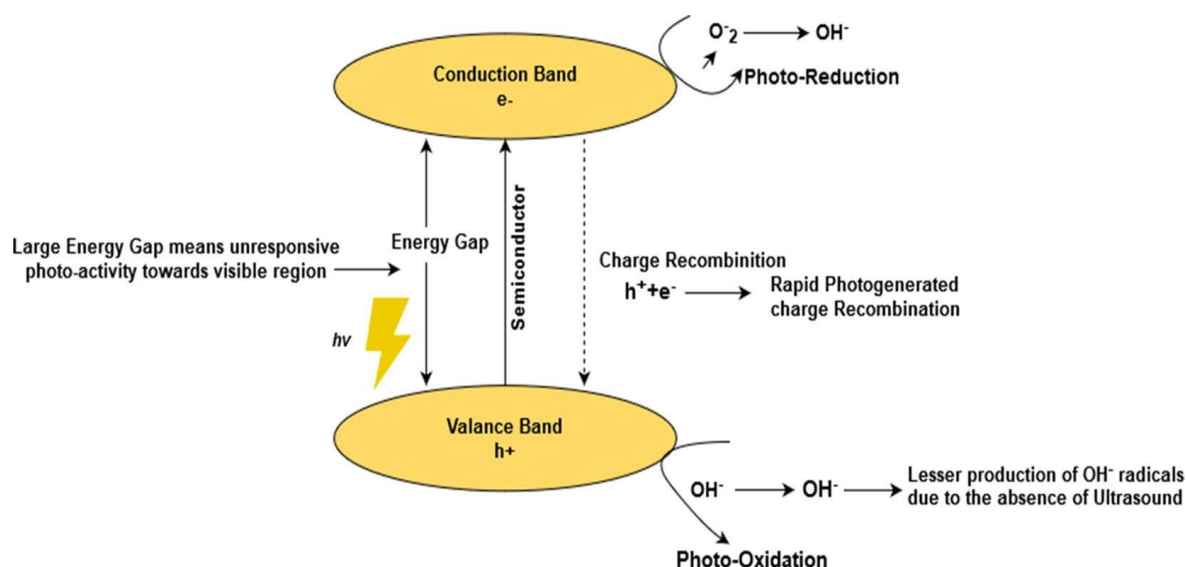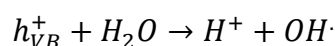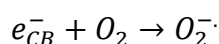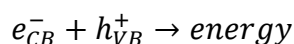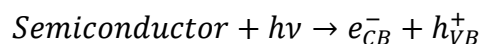
Fig.2.2. The schematic representation of photocatalytic degradation of pollutants. The figure is adapted from [49].

2.4. SONOCATALYSIS

Sonocatalysis is an advanced oxidation process (AOP) that combines a semiconductor catalyst with ultrasound (US) irradiation. The advantages of high-power ultrasonic irradiation include operational simplicity, safety, cleanliness, high penetrability in water, high degradation efficiency, and an environmentally friendly nature [50]. Ultrasonic sound waves in water, a process known as sonolysis, can degrade

a variety of recalcitrant organic compounds in wastewater. Sonolysis generates oxidising agents, such as hydroxyl radicals ($^{\bullet}OH$), through acoustic cavitation, which involves the nucleation, growth, and violent collapse of the microbubbles, creating local hot spots with extremely high temperatures and pressures [51]. These conditions lead to the dissociation of water molecules and the direct pyrolysis of volatile compounds. However, sonolysis alone is time-consuming, energy-intensive, and often insufficient for the complete degradation of azo dyes, limiting its practical application for wastewater treatment [52]. The schematic representation of the propagation of ultrasound in water and the formation of cavitation bubbles are shown in Fig.2.3.
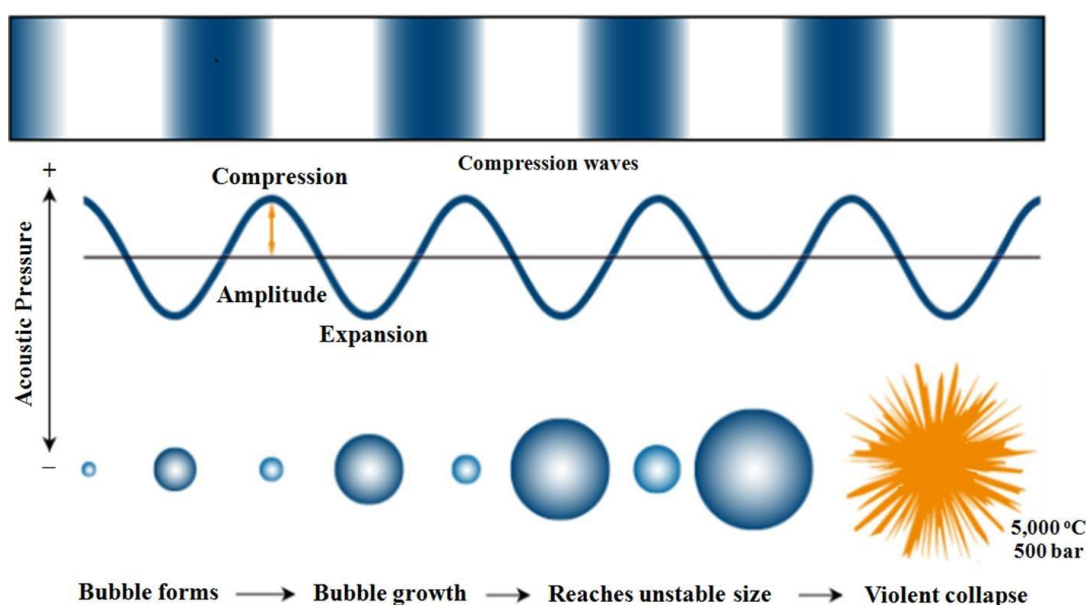
Fig.2.3. *The schematic representation of the propagation of ultrasound in water and the formation of cavitation bubbles. The figure is adapted from [49].*

These limitations can be addressed using an efficient heterogeneous catalyst during the sonolytic process. Unlike homogeneous nucleation in the bulk solution, solid particles provide favourable sites for cavity bubble nucleation at the solid surface or phase boundary. This significantly improves dye degradation rates compared to sonolysis alone [53]. Additionally, the light emitted during sonoluminescence (SL) from ultrasonic cavitation can excite electrons in the catalyst from the valence band (VB) to the conduction band (CB), producing electron-hole pairs. This photocatalytic mechanism further enhances dye degradation. The high temperatures at local hot spots also stimulate thermal excitation in the semiconductor, generating additional electron-hole pairs capable of dye degradation [54].

Sonocatalysis benefits from increased mass transfer and catalyst surface area, improving reaction rates and efficiency [55]. Furthermore, the process operates under mild conditions, typically at ambient temperature and pressure, reducing energy consumption compared to thermal methods. Ultrasound also prevents catalyst deactivation by continuously cleaning the catalyst surface, maintaining its activity over extended periods. This versatile technique is applicable to various water pollutants and can be combined with other treatment methods to enhance overall remediation efficiency [55].

2.4.1. Basic mechanism of Sonocatalysis

Sonolytic degradation of organic pollutants involves pyrolysis and free radical attack, with the violent collapse of cavitation bubbles generating short-lived hydroxyl radicals that oxidatively degrade organic compounds. However, achieving a rapid degradation rate with ultrasound alone demands significant energy, with over 50% lost to thermal dissipation, limiting the process's efficiency. Recent advancements have focused on sonocatalysis, which uses catalytically induced ultrasound irradiation to address these limitations. The catalyst provides additional active sites for cavitation, enhancing the production of reactive radicals. These radicals typically recombine to form H_2O, $HO•_2$, H_2O_2, and O_2^- [56].

$$H_2O +))) \rightarrow •OH + H•$$

$$•OH + H• \rightarrow H_2O_2$$

$$H• + O_2 \rightarrow HO•_2$$

$$2 •OH \rightarrow H_2O_2 + O_2$$

$$H_2O + •OH \rightarrow H_2O_2 + H•$$
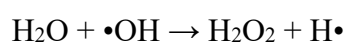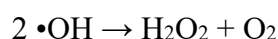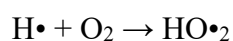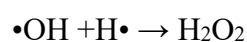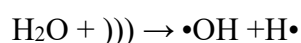
The presence of semiconductor particles promotes the preferential formation of nuclei at solid surfaces or phase boundaries, enhancing the creation of cavitation bubbles and free radicals like hydroxyl radicals ($•OH$). Heterogeneous nucleation occurs on surfaces and is more effective than homogeneous nucleation within the bulk solution due to lower thermodynamic barriers. This phenomenon, often seen on hydrophobic surfaces, is illustrated by the relationship between the maximum energy barriers of heterogeneous and homogeneous nucleation processes for cavitation bubble formation [49].

$$\Delta G_{het} = \frac{16\pi\sigma^3}{3P^2} f(\theta) = \Delta G_{hom} f(\theta) \dots\dots (2.27)$$

Here, ΔG_{het} is the maximum energy barrier for heterogeneous. ΔG_{hom} is the maximum energy barrier for homogeneous, π is mathematical constant (3.145), σ is the surface tension of water (J m^{-2}), θ is the contact angle between liquid and solid, and P is the sum of the partial pressure of the entrapped gas.

Furthermore, the bubble nucleation rate at solid surfaces is influenced by sonication parameters and the physicochemical properties of the solid particles. Sonication parameters include ultrasonic power, frequency, surface energy changes, aqueous temperature, and type of absorbed gas. The solid particles' properties, such as roughness, particle size, pore size, and wettability, also significantly determine the nucleation rate [49]. The functions of cavitation bubbles in sonolytic and sonocatalytic processes include heterogeneous nucleation, sonoluminescence, and thermal catalytic mechanisms are illustrated in Fig.2.4.
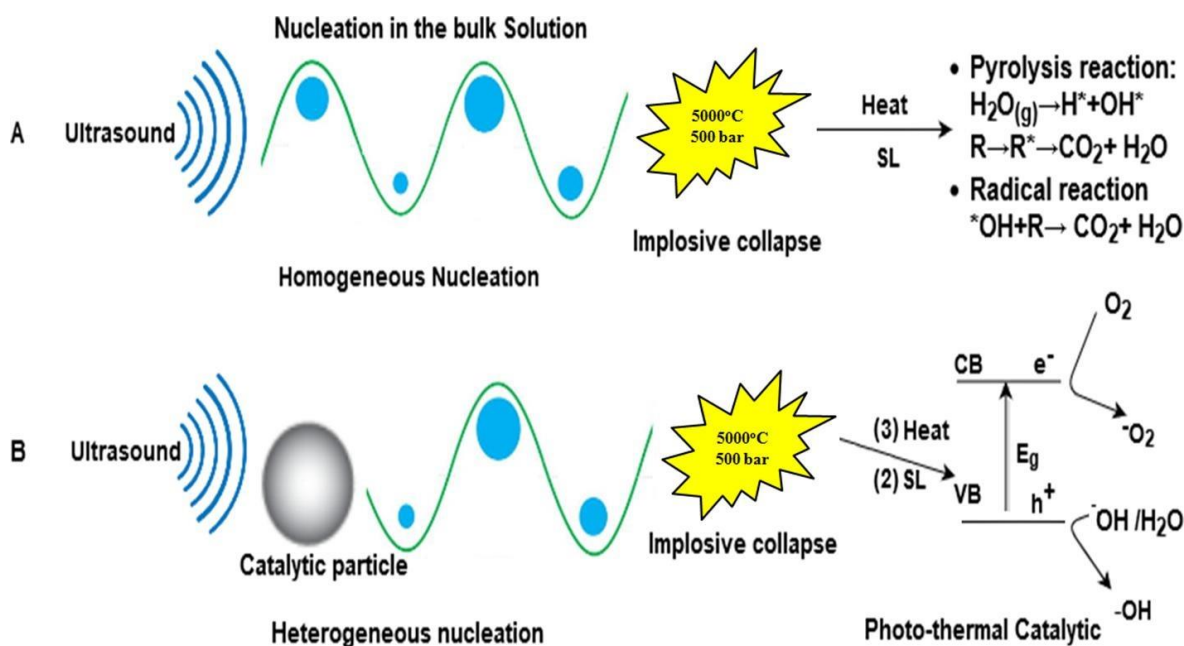
Fig.2.4. *The functions of cavitation bubbles in sonolytic and sonocatalytic processes include heterogeneous nucleation, sonoluminescence, and thermal catalytic mechanisms. The figure is adapted from [49].*

Sonoluminescence (SL) occurs when the collapse of a cavitation bubble emits light across a wide wavelength range (200–700 nm) with high intensity. When introducing a semiconductor catalyst during the ultrasonic process, the SL light energy, if higher than the semiconductor's band gap, can excite electrons from the valence band (VB) to the conduction band (CB), creating electron-hole pairs. These pairs react with oxidants to form reactive radicals, similar to the photocatalytic mechanism [56].

The hot spot theory suggests that the local high temperatures generated during cavitation can induce thermal excitation in the semiconductor, contributing to electron-hole pair production. This is due to the availability of highly oxidative holes generated by the thermal excitation of the semiconductor [56].

2.5. SONOPHOTOCATALYSIS

Photocatalytic degradation of organic compounds occurs via hydroxyl radicals generated on the photocatalyst during photolysis reactions. Combining photocatalytic and ultrasonic irradiation (sonophotocatalysis) accelerates the degradation rate of organic pollutants by increasing the generation of reactive radicals. The presence of a heterogeneous catalyst enhances the formation of cavitation bubbles by providing additional nuclei, which in turn boosts the pyrolysis of H_2O molecules and the formation of •OH radicals. This indicates a similarity between the mechanisms of the process and those of photocatalysis. These observations suggest that ultrasonic irradiation with a semiconductor catalyst may be preferred to enhance •OH formation. The synergistic effect between sonolysis and photocatalysis is mainly responsible for the reaction mechanism in the sonophotocatalytic degradation of organic pollutants. The combined ultrasound and photocatalytic process, or sonophotocatalysis, offers several advantages [49].

- In the liquid phase, sonolytic cleavage of water enhances the production of oxidising species.
- Ultrasonic irradiation induces de-aggregation, increasing the mass transfer of the organic pollutant to the catalyst surface.
- Acoustic cavitation prevents the aggregation of catalyst particles in aqueous solutions, thereby increasing the active surface area.
- Ultrasonic waves continuously clean the catalyst's surface, preventing the buildup of pollutants and their degradation intermediates.

2.5.1. Basic mechanism of Sonophotocatalysis

The sonophotocatalytic processes typically operate based on the hot-spot theory, sonoluminescence phenomenon, and visible light-driven (VLD) photocatalysis. By combining visible light and ultrasonic waves, the degradation of pollutants occurs through the following sequence of events [57]:

- **Nucleation:** The catalyst plays a role in the nucleation process by offering specific sites on its surface or at the boundaries between the liquid and solid phases. This facilitates the initiation of bubble formation, as well as their subsequent growth and eventual collapse, contributing to the overall bubble dynamics in the cavitation process.

- **Sonoluminescence (SL):** The phenomenon of sonoluminescence, which involves the sudden collapse of bubbles, can generate bursts of light within the wavelength range of 200-700 nm. Consequently, this stimulation affects the catalysts simultaneously, generating electron-hole pairs during a photocatalytic process.

- **Heat:** The high local temperature caused by the cavitation phenomenon can induce the decomposition of water molecules and the production of hydrogen (H) and hydroxyl (OH) radicals. Additionally, it can thermally excite electrons from the valence band (VB) to the conduction band (CB) of the semiconductor catalyst during a thermocatalytic process.

- **Photocatalysis:** The VLD-induced electron-hole separation and transport of photogenerated charge carriers on the surface of the catalyst leads to the formation of active species radicals and initiates the degradation of RhB.

- **Adsorption:** The catalyst's high surface area enhances the adsorption of dye molecules on its surface.

In accordance with the explained mechanism, the pollutant molecules are eliminated from the solution by binding to the catalyst's surface and undergo degradation due to the action of the free radicals produced through water pyrolysis and photo-thermal catalysis pathways [57]. The proposed mechanism of sonophotocatalytic degradation of pollutants from water is shown in Fig.2.5.
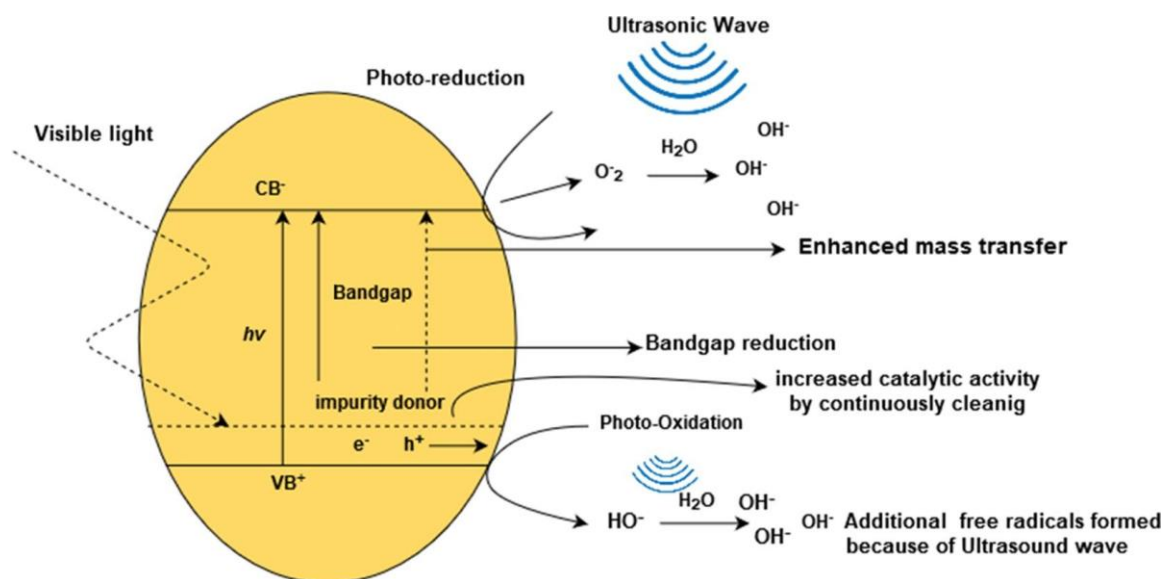
Fig.2.5. *Proposed mechanism for the sonophotocatalytic degradation process. The figure is adapted from [49].*

2.5.2. Evaluation of the synergistic effect during sonophotocatalytic process

Evaluating the synergistic enhancement in pollutant removal during a sonophotocatalysis based process is important to compare the effect of the hybrid process with individual processes (ultrasonic irradiation and photocatalysis). A quantitative way to estimate the synergistic effect during SPC process was done by calculating the synergy index. It is defined as [49]:

$$Synergy\ index = \frac{(k_{ap})_{SPC}}{(k_{ap})_{PC} + (k_{ap})_{SC}} \dots\dots (2.28)$$

Where $(k_{ap})_{SC}$, $(k_{ap})_{PC}$ and $(k_{ap})_{SPC}$ are the rate constants of the reaction for sonocatalysis, photocatalysis and sonophotocatalysis, respectively. A synergistic effect can be observed if the synergy index value was larger than 1.0.

2.6. KINETIC MODEL OF CATALYSIS

The Langmuir-Hinshelwood (L-H) mechanism is employed to characterise heterogeneous catalytic reactions through the following four steps [58]:

1. Adsorption of molecules onto the catalytic surface.

2. Dissociation of the adsorbed molecules.

3. Reaction of the dissociated molecules to form products.

4. Desorption of the products.

This model has been utilised to describe the heterogeneous catalytic degradation of organic wastewater. In step 1, the adsorption and desorption rates are represented by equations (2.29) and (2.30), respectively.

$$R_a = k_a(1 - \theta)C \dots \dots (2.29)$$

$$R_d = k_d\theta \dots \dots (2.30)$$

where k_a and k_d are adsorption and desorption rate constant, θ is a fraction of the coverage site, and C is a concentration of pollutant in a medium.

At equilibrium, $R_a = R_d$, which results

$$k_a(1 - \theta)C = k_d\theta \dots \dots (2.31)$$

$$\theta = \frac{KC}{1 + KC} \dots \dots (2.32)$$

Where $K = \frac{k_a}{k_d}$ is the adsorption equilibrium constant.

It is noted that organic molecules/ pollutant is adsorbed before catalytic degradation. Therefore, the degradation rate is proportional to θ. Then,

$$R_{deg} = k_{deg}\theta = \frac{k_{deg}KC}{1 + KC} \dots \dots (2.33)$$

Where k_{deg} is the rate of degradation (degradation constant).

According to the rate law of chemical reaction, the rate of degradation is also expressed as follows:

$$R_{deg} = -\frac{dC(t)}{dt} \dots \dots (2.34)$$

$$-\frac{dC(t)}{dt} = \frac{k_{deg}KC}{1 + KC} \dots \dots (2.35)$$

In a highly diluted dye solution, the term of KC becomes less than 1, $KC \text{ "}1 \Rightarrow 1 + KC \approx 1$. Then, under these circumstances:

$$-\frac{dC(t)}{dt} = kKC(t) \Rightarrow -\frac{dC(t)}{dt} = k_{app}C(t) \dots \dots (2.36)$$

Considering $k_{app} \approx k_{deg}K$ as the apparent rate constant of the reaction, the above equation represents the pseudo-first-order reaction kinetics as :

$$C(t) = C_0 e^{-k_{app}t} \ldots \ldots (2.37)$$

Thus, the apparent rate constant of the reaction k_{app} can be obtained by estimating the slope of the linear fit of $\ln\left(\frac{C_0}{C(t)}\right)$ versus time (t) [58].

2.6.1. Effect of various factors on catalytic degradation kinetics

- **Catalyst Dosage:** The amount of catalyst used significantly impacts pollutant removal efficiency. Khataee *et al*. observed that the degradation of moxifloxacin in water improves with an increase in catalyst dosage up to an optimal point, after which the efficiency declines. The improvement in degradation is due to the increased surface area, more active sites, and better light and sound absorption by the catalysts. These factors enhance the generation of oxidative radicals and the adsorption of pollutants on the nanocomposite surface, thereby increasing the pollutant removal rate [59].

- **Solution pH:** The pH of the solution is crucial in determining the rate and extent of antibiotic degradation. The initial pH affects the interface potential, surface charge, aggregation, and the status of the adsorbent surface [60].

- **Initial Pollutant Concentration:** The initial concentration of pollutants is a key parameter influencing degradation efficiency. This dependency can be understood in two ways: first, a linear relationship where the degradation rate either increases or decreases with pollutant concentration; second, a non-linear relationship where an optimal concentration results in a high degradation rate, but further increases in concentration lead to a gradual decline in the degradation rate [61].

- **Catalytic Particle Size:** Smaller photocatalyst particles are more favourable for catalytic degradation due to increased active sites. Xu et al. reported that the degradation rate of methylene blue in an aqueous solution follows the PFO model, with the modified rate constant k_{app} being a function of particle size (d_p), expressed as [62]:

$$k_{app} = -0.064 \ln d_p + 0.260 \ldots \ldots (2.38)$$

- **Dissolved Oxygen:** Dissolved oxygen can adsorb onto the photocatalyst surface, trapping electrons and preventing the recombination of hole-electron pairs, thus enhancing the catalytic degradation rate. The noncompetitive adsorption between dissolved oxygen and organic compounds has also been confirmed in the literature [58].

- **Temperature Effect:** Reaction temperature generally has a slight impact on catalysis. As temperature increases, the adsorption capacity of photocatalysts improves, leading to a higher degradation rate of organic compounds. The relationship between the degradation rate constant and temperature follows the Arrhenius equation. However, higher temperatures also enhance the recombination of hole-electron pairs, so the optimal temperature for catalytic degradation needs to be determined experimentally [58].

2.7. THERMODYNAMICS OF CATALYSIS

The transition state theory (TST) developed by Henry Eyring was used to analyse the thermodynamics of the catalytic degradation. According to the TST, the pre-equilibrium rate of the reaction $A + B \leftrightarrow AB^* \rightarrow P$ can be characterised as follows [57]:

$$r = \frac{k_B T}{h} K [A][B] \dots\dots (2.39)$$

where r refers to the rate of reaction, k_B, h, and K are, respectively, the constants of Boltzmann ($1.38 \times 10^{-23} J/K$), Planck ($6.62 \times 10^{-34} Js$) and reaction equilibrium. The rate constant of the reaction

$$k = \frac{k_B T}{h} K \dots\dots (2.40)$$

The thermodynamics relationship between the equilibrium constant and Gibbs energy of activation (ΔG) is as follows:

$$\Delta G = -RT \ln K \quad or \quad K = exp\left(-\frac{\Delta G}{RT}\right) \dots\dots (2.41)$$

Then, the rate constant becomes

$$k = \frac{k_B T}{h} K \quad \Rightarrow \quad k = \frac{k_B T}{h} exp\left(-\frac{\Delta G}{RT}\right) \dots\dots (2.42)$$

Furthermore,

$$\Delta G = \Delta H - T\Delta S \ldots\ldots (2.43)$$

where ΔH and ΔS are the enthalpy and entropy change of the reaction, respectively.

$$k = \frac{k_B T}{h} exp\left(-\frac{\Delta H - T\Delta S}{RT}\right) = \frac{k_B T}{h} exp\left(-\frac{\Delta H}{RT}\right) exp\left(\frac{\Delta S}{R}\right) \ldots\ldots (2.44)$$

This equation is called the *Eyring equation,* and its logarithmic form can be written as:

$$\ln\left(\frac{k}{T}\right) = -\frac{\Delta H}{R}\left(\frac{1}{T}\right) + \frac{\Delta S}{R} + \ln\left(\frac{k_B}{h}\right) \ldots\ldots (2.45)$$

By considering rate constant $k = k_{app}$ Eq. can be rewritten as follows:

$$\ln\left(\frac{k_{app}}{T}\right) = -\frac{\Delta H}{R}\left(\frac{1}{T}\right) + \frac{\Delta S}{R} + \ln\left(\frac{k_B}{h}\right) \ldots\ldots (2.46)$$

The values of ΔH and ΔS for the catalytic degradation can be calculated from the slope and intercept of the $\ln\left(\frac{k_{app}}{T}\right) - \frac{1}{T}$ plot.

- **Gibbs Free Energy Change (ΔG):** Gibbs free energy change evaluates the spontaneity and feasibility of catalytic reaction. A negative ΔG indicates a spontaneous process, while a positive ΔG signifies a non-spontaneous process.

- **Enthalpy Change (ΔH):** Enthalpy change represents the energy supplied as heat at constant pressure when the system does no extra work. In catalytic studies, ΔH provides insights into the nature and mechanism of catalysis. A negative ΔH indicates an exothermic process, while a positive ΔH suggests an endothermic process.

- **Entropy Change (ΔS):** The entropy change in catalysis reflects the disorder and randomness in the system. A positive ΔS indicates increased disorder and a less ordered transition state. At the same time, a negative ΔS suggests decreased disorder and a more ordered transition state, potentially implying less favourable reaction conditions.

2.7.1. Activation energy of catalysis

The Arrhenius equation was employed to calculate the activation energy of the reaction (E_a) and the frequency factor (A) [63]:

$$k_{app}(T) = A exp\left(-\frac{E_a}{RT}\right) \ldots \ldots (2.47)$$

where R and T are the universal gas constant ($8.314 \, J \, K^{-1} mol^{-1}$) and absolute temperature (K), respectively. The linear form of the Arrhenius equation is given by

$$\ln k_{app} = -\frac{E_a}{R}\left(\frac{1}{T}\right) + \ln A \ldots \ldots (2.48)$$

The slope of the $\ln k_{app} - \frac{1}{T}$ plot provided E_a.

Activation energy is the minimum energy required for reactants to undergo a chemical reaction. It represents the energy barrier that must be overcome for the reactants to be transformed into products. The activation energy is usually expressed in kilojoules per mole (kJ/mol).

The pre-exponential factor, also known as the frequency factor or Arrhenius constant, represents the frequency of collisions and the probability that collisions are favourably oriented for a reaction to occur. It encompasses aspects such as the number of collisions per unit of time and the fraction of collisions with the correct orientation for the reaction.

The pre-exponential factor has the same units as the rate constant k_{app}, which depends on the order of the reaction. For a first-order reaction, k_{app} has units of s^{-1}; for a second-order reaction, it has units of L/mol·s, and so on.

2.8. CONCLUSION

In conclusion, the chapter on *'Overview of Adsorption and Catalysis'* has thoroughly explored the theoretical foundations of adsorption and catalysis. Detailed explanations of adsorption and catalysis mechanisms have been provided, along with an in-depth discussion of the various theories and models that underpin these phenomena. This chapter has elucidated how these theoretical frameworks substantiate the experimental results obtained in this study by examining classical and contemporary models. The comprehensive analysis of adsorption isotherms, kinetic models, and catalytic mechanisms offers a solid theoretical base that supports the interpretation of the experimental data. This foundational knowledge is critical for understanding the complex interactions at play and for guiding future research in the field.

REFERENCES

[1]   Bruch, L. W., Cole, M. W., & Zaremba, E. (2007). *Physical adsorption: forces and phenomena*. Courier Dover Publications.

[2]   Guttmann, R., Hoja, J., Lechner, C., Maurer, R. J., & Sax, A. F. (2019). Adhesion, forces and the stability of interfaces. *Beilstein Journal of Organic Chemistry*, *15*(1), 106-129.

[3]   Scheufele, F. B., Módenes, A. N., Borba, C. E., Ribeiro, C., Espinoza-Quiñones, F. R., Bergamasco, R., & Pereira, N. C. (2016). Monolayer–multilayer adsorption phenomenological model: Kinetics, equilibrium and thermodynamics. *Chemical Engineering Journal*, *284*, 1328-1341.

[4]   Ambaye, T. G., Vaccari, M., van Hullebusch, E. D., Amrane, A., & Rtimi, S. J. I. J. O. E. S. (2021). Mechanisms and adsorption capacities of biochar for the removal of organic and inorganic pollutants from industrial wastewater. *International Journal of Environmental Science and Technology*, *18*(10), 3273-3294.

[5]   Siddeeg, S. M., Tahoon, M. A., Alsaiari, N. S., Shabbir, M., & Rebah, F. B. (2021). Application of functionalised nanomaterials as effective adsorbents for the removal of heavy metals from wastewater: a review. *Current Analytical Chemistry*, *17*(1), 4-22.

[6]   Aziz, K. H. H., Mustafa, F. S., Omer, K. M., Hama, S., Hamarawf, R. F., & Rahman, K. O. (2023). Heavy metal pollution in the aquatic environment: efficient and low-cost removal approaches to eliminate their toxicity: a review. *RSC advances*, *13*(26), 17595-17610.

[7]   De Gisi, S., Lofrano, G., Grassi, M., & Notarnicola, M. (2016). Characteristics and adsorption capacities of low-cost sorbents for wastewater treatment: A review. *Sustainable Materials and Technologies*, *9*, 10-40.

[8]   Gkika, D. A., Mitropoulos, A. C., & Kyzas, G. Z. (2022). Why reuse spent adsorbents? The latest challenges and limitations. *Science of the Total Environment*, *822*, 153612.

[9]   Dąbrowski, A. (2001). Adsorption—from theory to practice. *Advances in colloid and interface science*, *93*(1-3), 135-224.

[10] Madani, S. H., Sedghi, S., Biggs, M. J., & Pendleton, P. (2015). Analysis of adsorbate–adsorbate and adsorbate–adsorbent interactions to decode isosteric heats of gas adsorption. *ChemPhysChem*, *16*(18), 3797-3805.

[11] Wang, L., Shi, C., Pan, L., Zhang, X., & Zou, J. J. (2020). Rational design, synthesis, adsorption principles and applications of metal oxide adsorbents: a review. *Nanoscale*, *12*(8), 4790-4815.

[12]   Sing, K. S. (1998). Adsorption methods for the characterisation of porous materials. *Advances in colloid and interface science*, *76*, 3-11.

[13]   Khalfaoui, M., Knani, S., Hachicha, M. A., & Lamine, A. B. (2003). New theoretical expressions for the five adsorption type isotherms classified by BET based on statistical physics treatment. *Journal of colloid and interface science*, *263*(2), 350-356.

[14]   Sotomayor, F. J., Cychosz, K. A., & Thommes, M. (2018). Characterisation of micro/mesoporous materials by physisorption: concepts and case studies. *Acc. Mater. Surf. Res*, *3*(2), 34-50.

[15]   Gawande, S. M., Belwalkar, N. S., & Mane, A. A. (2017). Adsorption and its isotherm–theory. *International Journal of Engineering Research*, *6*(6), 312-316.

[16]   Donohue, M. D., & Aranovich, G. L. (1998). Classification of Gibbs adsorption isotherms. *Advances in colloid and interface science*, *76*, 137-152.

[17]   Lowell, S., Shields, J. E., Thomas, M. A., Thommes, M., Lowell, S., Shields, J. E., ... & Thommes, M. (2004). Adsorption isotherms. *Characterisation of porous solids and powders: surface area, pore size and density*, 11-14.

[18]   Buttersack, C. (2019). Modelling of type IV and V sigmoidal adsorption isotherms. *Physical Chemistry Chemical Physics*, *21*(10), 5614-5626.

[19]   Ruthven, D. M. (2006). Fundamentals of adsorption equilibrium and kinetics in microporous solids. In *Adsorption and Diffusion* (pp. 1-43). Berlin, Heidelberg: Springer Berlin Heidelberg.

[20]   Foo, K. Y., & Hameed, B. H. (2010). Insights into the modelling of adsorption isotherm systems. *Chemical engineering journal*, *156*(1), 2-10.

[21]   Ruthiraan, M., Abdullah, E. C., Mubarak, N. M., & Nizamuddin, S. (2018). Adsorptive removal of methylene blue using magnetic biochar derived from agricultural waste biomass: equilibrium, isotherm, kinetic study. *International Journal of Nanoscience*, *17*(05), 1850002.

[22]   Saadi, R., Saadi, Z., Fazaeli, R., & Fard, N. E. (2015). Monolayer and multilayer adsorption isotherm models for sorption from aqueous media. *Korean Journal of Chemical Engineering*, *32*, 787-799.

[23]   Saleh, T. A. (2022). Kinetic models and thermodynamics of adsorption processes: Classification. In *Interface science and technology* (Vol. 34, pp. 65-97). Elsevier.

[24]   Latour, R. A. (2015). The Langmuir isotherm: a commonly applied but misleading approach for the analysis of protein adsorption behavior. *Journal of biomedical materials research part A*, *103*(3), 949-958.

[25]   Said, K. A. M., Ismail, N. Z., Jama'in, R. L., Alipah, N. A. M., Sutan, N. M., Gadung, G. G., ... & Zauzi, N. S. A. (2018). Application of Freundlich and Temkin isotherm to study the removal of Pb (II) via adsorption on activated carbon equipped polysulfone membrane. *Int. J. Eng. Technol*, *7*(3.18), 91-93.

[26]   Chen, X., Hossain, M. F., Duan, C., Lu, J., Tsang, Y. F., Islam, M. S., & Zhou, Y. (2022). Isotherm models for adsorption of heavy metals from water-a review. *Chemosphere*, *307*, 135545.

[27]   Rudzinski, W., & Plazinski, W. (2007). Theoretical description of the kinetics of solute adsorption at heterogeneous solid/solution interfaces: On the possibility of distinguishing between the diffusional and the surface reaction kinetics models. *Applied surface science*, *253*(13), 5827-5840.

[28]   Jiang, Y., Chowdhury, S., & Balasubramanian, R. (2017). Nitrogen-doped graphene hydrogels as potential adsorbents and photocatalysts for environmental remediation. *Chemical Engineering Journal*, *327*, 751-763.

[29]   Saadi, R., Saadi, Z., Fazaeli, R., & Fard, N. E. (2015). Monolayer and multilayer adsorption isotherm models for sorption from aqueous media. *Korean Journal of Chemical Engineering*, *32*, 787-799.

[30]   Rangabhashiyam, S., Anu, N., Nandagopal, M. G., & Selvaraju, N. (2014). Relevance of isotherm models in biosorption of pollutants by agricultural byproducts. *Journal of Environmental Chemical Engineering*, *2*(1), 398-414.

[31]   Tan, K. L., & Hameed, B. H. (2017). Insight into the adsorption kinetics models for the removal of contaminants from aqueous solutions. *Journal of the Taiwan Institute of Chemical Engineers*, *74*, 25-48.

[32]   Qiu, H., Lv, L., Pan, B. C., Zhang, Q. J., Zhang, W. M., & Zhang, Q. X. (2009). Critical review in adsorption kinetic models. *Journal of Zhejiang University-Science A*, *10*(5), 716-724.

[33]   Lin, J., & Wang, L. (2009). Comparison between linear and non-linear forms of pseudo-first-order and pseudo-second-order adsorption kinetic models for the removal of methylene blue by activated carbon. *Frontiers of Environmental Science & Engineering in China*, *3*, 320-324.

[34] Ben-Ali, S., Jaouali, I., Souissi-Najar, S., & Ouederni, A. (2017). Characterisation and adsorption capacity of raw pomegranate peel biosorbent for copper removal. *Journal of cleaner production*, *142*, 3809-3821.

[35] Wu, J., Wang, T., Shi, N., & Pan, W. P. (2022). Insight into mass transfer mechanism and equilibrium modelling of heavy metals adsorption on hierarchically porous biochar. *Separation and Purification Technology*, *287*, 120558.

[36] Wang, Y., Wang, C., Huang, X., Zhang, Q., Wang, T., & Guo, X. (2023). Guideline for modelling solid-liquid adsorption: kinetics, isotherm, fixed bed, and thermodynamics. *Chemosphere*, 140736.

[37] Tran, H. N., You, S. J., & Chao, H. P. (2016). Thermodynamic parameters of cadmium adsorption onto orange peel calculated from various methods: A comparison study. *Journal of Environmental Chemical Engineering*, *4*(3), 2671-2682.

[38] Alnajrani, M. N., & Alsager, O. A. (2020). Removal of antibiotics from water by polymer of intrinsic microporosity: Isotherms, kinetics, thermodynamics, and adsorption mechanism. *Scientific reports*, *10*(1), 794.

[39] Ebelegi, A. N., Ayawei, N., & Wankasi, D. (2020). Interpretation of adsorption thermodynamics and kinetics. *Open Journal of Physical Chemistry*, *10*(3), 166-182.

[40] Sahmoune, M. N. (2018). Thermodynamic properties of heavy metals ions adsorption by green adsorbents. *Green Adsorbents for Pollutant Removal: Fundamentals and Design*, 193-213, 2018, Volume 18, ISBN: 978-3-319-92110-5

[41] Montoya, T., Coral, D., Franco, C. A., Nassar, N. N., & Cortés, F. B. (2014). A novel solid–liquid equilibrium model for describing the adsorption of associating asphaltene molecules onto solid surfaces based on the "chemical theory". *Energy & Fuels*, *28*(8), 4963-4975.

[42] Khan, M. M. (2023). Fundamentals and principles of photocatalysis. *Theoretical Concepts of Photocatalysis; Elsevier: Amsterdam, The Netherlands*, 15-32.

[43] Muñoz-Batista, M. J., & Luque, R. (2021). Heterogeneous, photocatalysis. *ChemEngineering*, 5(2), 26.

[44] Elmougi, M. M. E. (2020). *Using Photocatalysis Process for The Removal of Natural Organic Matter for Potable Water Purification* (Doctoral dissertation, Mansoura University). DOI:10.13140/RG.2.2.15622.50249

[45]   Truong, P. L., Kidanemariam, A., & Park, J. (2021). A critical innovation of photocatalytic degradation for toxic chemicals and pathogens in air. *Journal of Industrial and Engineering Chemistry*, *100*, 19-39.

[46]   Krystynik, P. (2021). Advanced oxidation processes (aops)—utilisation of hydroxyl radical and singlet oxygen. *Reactive Oxygen Species*.

[47]   Yang, H., Yang, B., Chen, W., & Yang, J. (2022). Preparation and photocatalytic activities of TiO2-based composite catalysts. *Catalysts*, *12*(10), 1263.

[48]   Yang, H., Yang, B., Chen, W., & Yang, J. (2022). Preparation and photocatalytic activities of TiO2-based composite catalysts. *Catalysts*, *12*(10), 1263.

[49]   Mandade, P. (2021). Introduction, basic principles, mechanism, and challenges of photocatalysis. In *Handbook of nanomaterials for wastewater treatment* (pp.137-154). Elsevier.

[50]   Abdurahman, M. H., Abdullah, A. Z., & Shoparwe, N. F. (2021). A comprehensive review on sonocatalytic, photocatalytic, and sonophotocatalytic processes for the degradation of antibiotics in water: Synergistic mechanism and degradation pathway. *Chemical Engineering Journal*, *413*, 127412.

[51]   Santhosh, M. V., Geethu, R., & Devaky, K. S. (2021). A novel, facile, and efficient two-step hydrothermal route for WS2 nanosheets and its optimistic exposure as competent industrial-level sonocatalyst. *Journal of Materials Science: Materials in Electronics*, *32*(7), 9357-9367.

[52]   Pang, Y. L., Abdullah, A. Z., & Bhatia, S. (2011). Review on sonochemical methods in the presence of catalysts and chemical additives for treatment of organic pollutants in wastewater. *Desalination*, *277*(1-3), 1-14.

[53]   Quddus, F., Shah, A., Iftikhar, F. J., Shah, N. S., & Haleem, A. (2023). Environmentally benign nanoparticles for the photocatalytic degradation of pharmaceutical drugs. *Catalysts*, *13*(3), 511.

[54]   Aquilano, D., Costa, E., Genovese, A., Massaro, F. R., & Rubbo, M. (2003). Heterogeneous nucleation and growth of crystalline micro-bubbles around gas cavities formed in solution. *Progress in crystal growth and characterisation of materials*, *46*(1-2), 59-84.

[55]   Ahmed, M. A., & Mohamed, A. A. (2023). Advances in ultrasound-assisted synthesis of photocatalysts and sonophotocatalytic processes: A review. *Iscience,*25, 108583

[56]   Theerthagiri, J., Lee, S. J., Karuppasamy, K., Arulmani, S., Veeralakshmi, S., Ashokkumar, M., & Choi, M. Y. (2021). Application of advanced materials in sonophotocatalytic processes for the remediation of environmental pollutants. *Journal of Hazardous Materials*, *412*, 125245.

[57]   Mehrizad, A., Behnajady, M. A., Gharbani, P., & Sabbagh, S. (2019). Sonocatalytic degradation of Acid Red 1 by sonochemically synthesised zinc sulfide-titanium dioxide nanotubes: Optimisation, kinetics and thermodynamics studies. *Journal of cleaner production*, *215*, 1341-1350.

[58]   Tran, H. D., Nguyen, D. Q., Do, P. T., & Tran, U. N. (2023). Kinetics of photocatalytic degradation of organic compounds: a mini-review and new approach. *RSC advances*, *13*(25), 16915-16925.

[59]   Khataee, A., Rad, T. S., Nikzat, S., Hassani, A., Aslan, M. H., Kobya, M., & Demirbaş, E. (2019). Fabrication of NiFe layered double hydroxide/reduced graphene oxide (NiFe-LDH/rGO) nanocomposite with enhanced sonophotocatalytic activity for the degradation of moxifloxacin. *Chemical Engineering Journal*, *375*, 122102.

[60]   Badawy, A. M. E., Luxton, T. P., Silva, R. G., Scheckel, K. G., Suidan, M. T., & Tolaymat, T. M. (2010). Impact of environmental conditions (pH, ionic strength, and electrolyte type) on the surface charge and aggregation of silver nanoparticles suspensions. *Environmental science & technology*, *44*(4), 1260-1266.

[61]   Ahmed, S., Rasul, M. G., Brown, R., & Hashib, M. A. (2011). Influence of parameters on the heterogeneous photocatalytic degradation of pesticides and phenolic contaminants in wastewater: a short review. *Journal of environmental management*, *92*(3), 311-330.

[62]   Xu, N., Shi, Z., Fan, Y., Dong, J., Shi, J., & Hu, M. Z. C. (1999). Effects of particle size of TiO2 on photocatalytic degradation of methylene blue in aqueous suspensions. *Industrial & Engineering Chemistry Research*, *38*(2), 373-379.

[63]   Braun, R. L., & Burnham, A. K. (1987). Analysis of chemical reaction kinetics using a distribution of activation energies and simpler models. *Energy & Fuels*, *1*(2), 153-161.

CHAPTER 3

Experimental Techniques
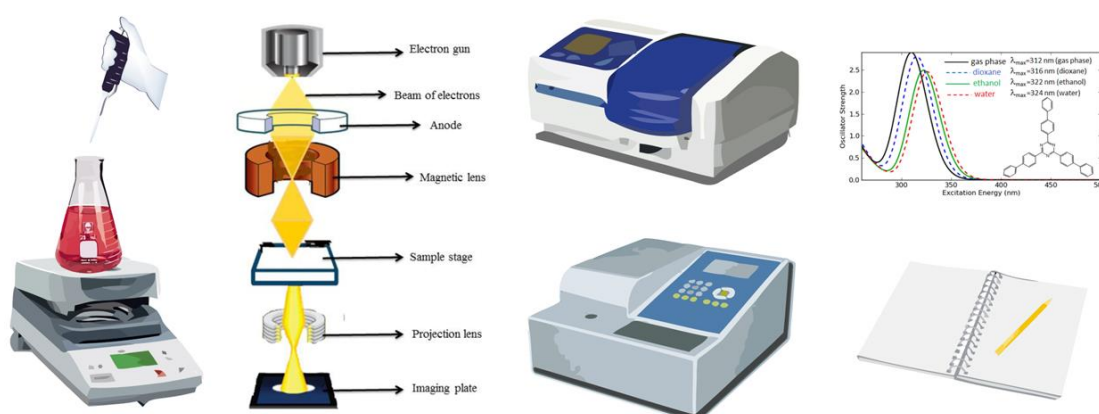
This chapter concentrates on the experimental methodologies employed for the synthesis, characterization, and evaluation of the water remediation potential of the synthesized nanomaterials.

3.1. INTRODUCTION

This chapter focuses on the experimental techniques used for the synthesis, characterisation, and investigation of the water remediation capability of the synthesised nanomaterials.

The synthesis methods discussed include solid-state reaction, hydrothermal, and co-precipitation techniques. Various aspects of these experimental techniques and the characterisation methods employed in this work are detailed. Structural characterisation was conducted using X-ray diffraction (XRD) and Raman analysis. The morphology, structure, and size were examined with Field Emission Scanning Electron Microscopy (FE-SEM). Ultraviolet-visible diffuse reflectance spectroscopy (UV-Vis DRS) and photoluminescence (PL) spectroscopy were utilised for optical and photocatalytic studies. Surface area and porosity were analysed using the Brunauer–Emmett–Teller (BET) and Barrett–Joyner–Halenda (BJH) techniques. Temperature-programmed desorption of NH_3 (NH_3-TPD) was carried out to estimate the adsorbent's active sites. The functional group and vibrational mode analyses were performed using Fourier Transform Infrared Spectroscopy (FTIR). Intermediates from various degradation processes were identified using High-Performance Liquid Chromatography (HPLC). The total organic carbon content was measured with a TOC analyser.

3.2. Methods for the synthesis of nanomaterials

The synthesis of nanomaterials involves various techniques designed to produce materials with specific properties tailored for environmental applications. The following methods are employed to synthesise metal chalcogenides and Bi-based nanomaterials, characterised by their unique structures and properties, making them effective for adsorption and catalytic processes in water treatment.

3.2.1. Solid state reaction

Solid-state synthesis is a widely adopted method for preparing nanomaterials, involving the direct reaction of solid reactants to yield the desired product. This process comprises several essential steps: mixing precursors, grinding, and high-temperature heating.

The initial materials, typically powders, are chosen based on their reactivity and suitability for forming the intended product. Common precursors include metal oxides, carbonates, and sulfides. The solid reactants are thoroughly mixed to ensure a

homogeneous distribution of components, often achieved through grinding with a mortar and pestle or mechanical ball milling. This grinding process increases the surface area of the reactants, enhancing their reactivity [1].

Solid-state reactions frequently involve diffusion mechanisms, where atoms or ions traverse the crystal lattice of the solid reactants, forming new bonds and creating the product. These reactions can be diffusion-controlled, with the reaction rate determined by the rate at which reactants diffuse through the solid matrix [2].

Upon completion of the reaction, the product is cooled to room temperature. The cooling rate can significantly influence the final properties of the nanomaterial. Additional treatments, such as washing, drying, or annealing, may be conducted to purify and enhance the properties of the synthesised nanomaterial.

Solid-state reactions are employed to synthesise various nanomaterials, including metal oxides, chalcogenides, and composites. Due to their unique physical and chemical properties, these nanomaterials are used in various applications such as catalysis, energy storage, sensors, and water treatment [3]. Nanomaterials synthesised through solid-state reactions often exhibit high stability, reactivity, and capacity for adsorbing or degrading contaminants in water remediation.

By optimising the conditions of the solid-state reaction, such as temperature, time, and precursor ratios, researchers can tailor the properties of the nanomaterials to meet specific application requirements. As a demonstrative example, a schematic representation of solid-state synthesis of $BiFeO_3$ nanoparticles is shown in Fig.3.1.
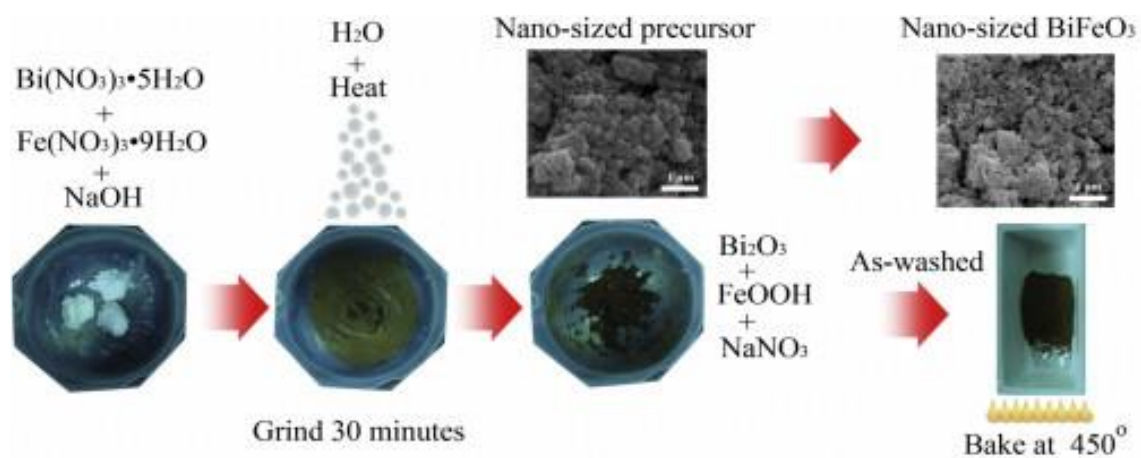
Fig.3.1. *The schematic representation of BiFeO₃ nanoparticles synthesised by solid state reaction [4].*

In this research, CuS nanoflowers were synthesised using a straightforward solid-state reaction method employing copper (II) chloride and thiourea as Cu and S sources precursors. We synthesised three different morphologies of CuS by varying the grinding time. The detailed procedure for the synthesis process can be found in Section 4.2.2 of Chapter 4.

3.2.2. Hydrothermal synthesis

Hydrothermal synthesis is an advanced technique to produce nanomaterials under controlled temperature and pressure conditions in an aqueous environment. The process begins with preparing aqueous solutions containing dissolved metal salts or other precursors, such as metal chlorides or nitrates. These solutions may include complexing agents to regulate reaction kinetics and influence product morphology. These prepared solutions are then introduced into a sealed vessel known as an autoclave, which is specifically designed to withstand the high temperatures and pressures required for hydrothermal reactions. Typically, the autoclave is heated to temperatures ranging from 100°C to 300°C, depending on the desired product, with the internal pressure elevated above atmospheric levels to maintain the aqueous phase and prevent boiling [5].

In this controlled environment, hydrolysis and nucleation of dissolved metal ions result in the formation of nanocrystals or crystalline phases. Factors such as reaction time, temperature, pressure, pH, and reactant concentration influence nanoparticle growth and crystallisation. Gradual cooling of the autoclave to room temperature prevents abrupt phase changes, promoting well-defined crystalline structures.

Post-reaction, nanoparticles are washed with distilled water or solvents to eliminate residual reactants and byproducts, a critical step for enhancing their purity, stability, and functionality. The purified nanoparticles are then dried under ambient conditions or gentle heating, yielding a dry powder suitable for characterisation and application.

Hydrothermal synthesis is widely used in producing nanomaterials for various applications, including catalysis, sensors, biomedical devices, and environmental remediation. Its ability to tailor nanomaterial properties at the atomic scale makes it a powerful tool for advancing materials science and technology. A Schematic diagram for the hydrothermal synthesis of o/h-WO$_3$ is shown in Fig.3.2.
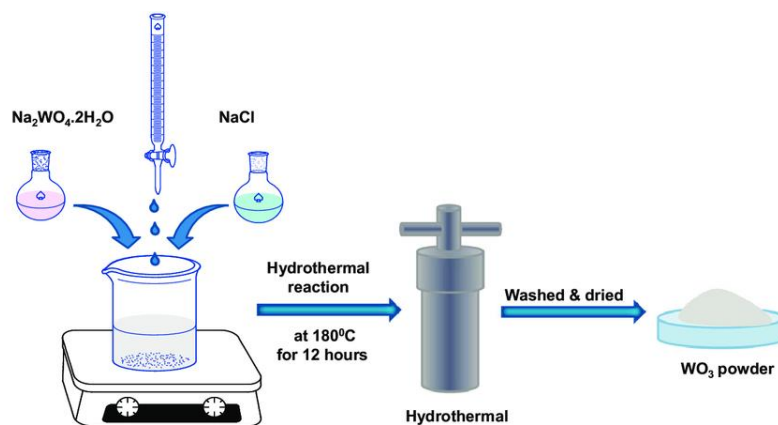
Fig.3.2. *Schematic diagram for the hydrothermal synthesis of o/h-WO₃ [6].*

In this study, MnS and bismuth vanadate nanomaterials were synthesised using a simple hydrothermal method. We obtained two distinct crystal phases of MnS by varying the reaction time and temperature. The morphology and crystallinity of bismuth vanadate could be changed by introducing a surfactant in the reaction medium. Moreover, we successfully synthesised an isotype heterojunction of $BiVO_4$ nanomaterials in this process. The detailed procedures for the synthesis processes are included in Chapters 5 and 7, respectively, for the synthesis of MnS and $BiVO_4$.

3.2.3. Co-precipitation method

The co-precipitation method is a versatile technique extensively used for synthesising nanomaterials with precise control over their composition, morphology, and structure. Initially, aqueous solutions containing soluble salts of desired metal ions, such as chlorides, nitrates, sulfates, or acetates, are prepared as precursors. These solutions are carefully mixed under controlled conditions, often at room temperature or slightly elevated temperatures, to ensure uniform distribution of metal ions throughout the solution. An appropriate precipitating agent is added dropwise or continuously to the mixed precursor solution under constant stirring or agitation. This precipitation process is driven by the reduction in the solubility of the metal hydroxides or carbonates as the pH of the solution increases [7].

After complete precipitation, the resulting nanoparticle suspension is separated from the solution using centrifugation or filtration. The collected nanoparticles undergo multiple washes with distilled water or a suitable solvent to eliminate residual salts and byproducts, ensuring the purity of the final product. Subsequently, the washed nanoparticles are dried under vacuum or at moderate temperatures to remove solvent and attain a dry powder form. Annealing, a heat treatment conducted at elevated temperatures

(typically between 200°C to 800°C), may also be applied to enhance crystallinity, phase purity, and overall structural stability of the nanoparticles.

The co-precipitation method is widely utilised for synthesising various nanomaterials, including metal oxides, hydroxides, carbonates, and sulfides. These materials are employed in diverse fields such as catalysis, biomedical sciences, environmental remediation, and energy storage, benefiting from their tailored chemical compositions and structural [8]. A Schematic representation of the synthesis of Fe_3O_4 nanoparticles using the co-precipitation method is shown in Fig.3.3.
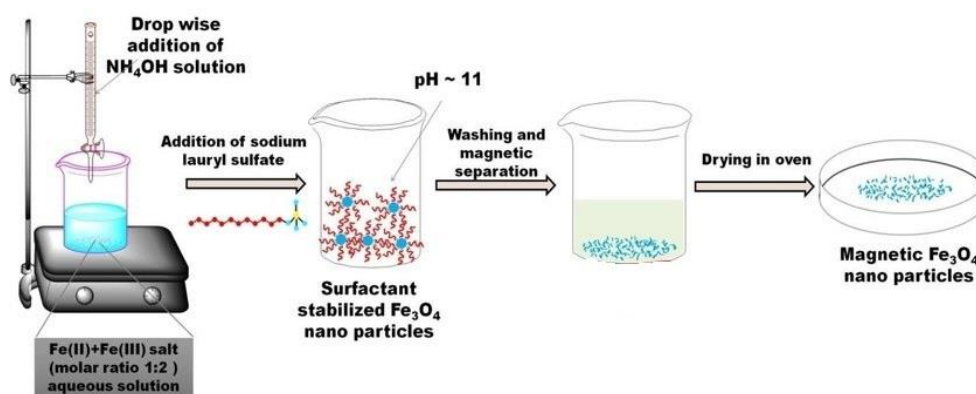
Fig.3.3. *Schematic representation of synthesis of Fe₃O₄ nanoparticles using co-precipitation method [9].*

In this research, bismuth oxyhalide solid solutions are synthesised using the co-precipitation method. Bismuth (III) nitrate and potassium halide salts serve as the precursors for bismuth and halides. The detailed synthesis method can be found in Section 6.2.2 of Chapter 6.

3.3. STRUCTURAL CHARACTERISATIONS

The structural characterisation of synthesised samples involved X-ray diffraction (XRD) and Raman spectroscopy. XRD confirmed the nanomaterials' formation and crystalline phases, providing lattice parameters and crystallinity information crucial for correlating structure with adsorptive and catalytic properties. Raman spectroscopy complemented XRD by offering insights into bonding environments and structural distortions, aiding in understanding the relationship between structure and catalytic activity.

3.3.1. X-Ray Diffraction analysis

X-ray diffraction (XRD) is a versatile, non-destructive technique that provides comprehensive information about the crystallographic structure of natural and

synthesised materials. It is a fundamental tool to determine the structural phase and degree of crystallinity in single crystals, bulk solids, and thin films. The principle of XRD is based on the diffraction of X-rays. When a material is irradiated with X-ray photons, its interaction with bound electrons results in coherent scattering, detected by electromagnetic photon detectors. If scattering centres are at non-random distances (integral multiples of the X-ray wavelength), the scattered waves interfere constructively, producing high-intensity diffracted waves. Analysing these diffraction patterns allows researchers to determine the sample's structure. The basic formulation for determining crystal structure, Bragg's law, was established in 1913 [10].

$$2d_{hkl} \sin \theta = n\lambda$$

Here, $n = 1,2,3..$, represents the order of diffraction, λ is the wavelength of the X-rays used, d_{hkl} is the distance between the lattice planes, and θ is the angle at which the diffraction peak is observed. A pictorial representation of the diffraction phenomenon is shown in Fig. 3.4.
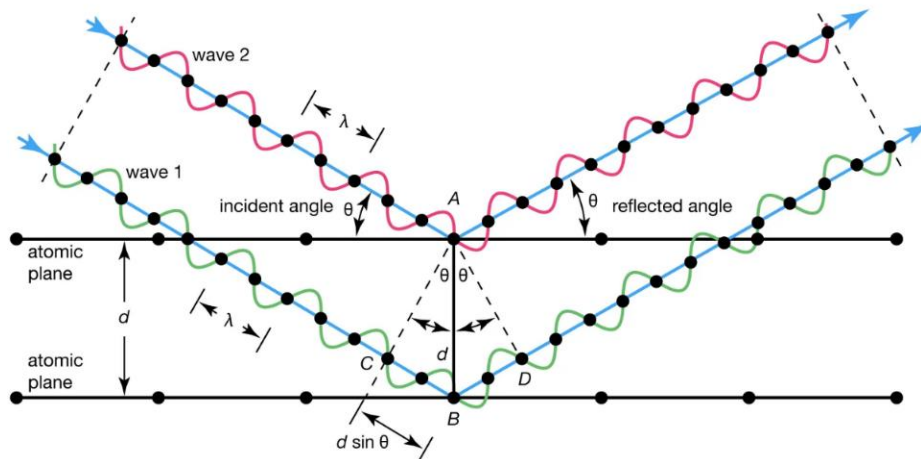
Fig.3.4. *The schematic representation of diffraction of X-rays from lattice planes. This figure is adapted from [11].*

Different scanning modes can be employed on the sample to determine various structural parameters, such as the 'θ-2θ' scan. In this technique, the angle between the sample and the X-ray plane is incrementally varied up to 'θ' while simultaneously moving the detector to '2θ'. This scan mode allows for assessing the phase purity, crystal structure, and symmetry type of the sample. X-rays used in diffraction are generated by bombarding a pure anode of a specific metal with high-energy electrons within a vacuum tube. For

instance, copper (Cu) X-ray tubes emit radiation with a wavelength of approximately 1.54 Å [12].

During the experiment, X-rays pass through two divergent slits: one between the X-ray source and the specimen and another between the specimen and the detector. These slits reduce background noise and collimate the radiation. The detector records the number of X-rays scattered by the sample, and the resulting data is plotted as a diffraction pattern showing X-ray counts versus the 2θ angle. The schematic diagram of the X-ray diffractometer is shown in Fig.3.5.
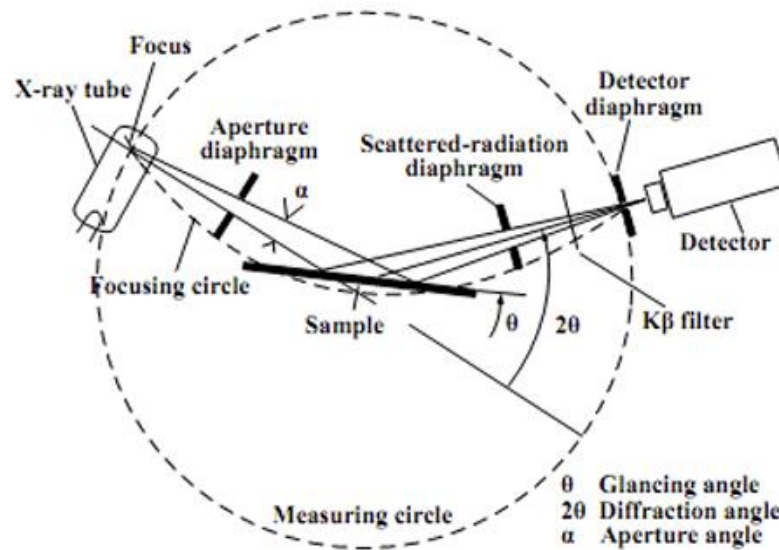
Fig.3.5. *Schematic representation of X-ray Diffractometer. This figure is adapted from [13].*

To analyse the crystal structure, diffraction peaks are converted into d-spacing values and compared with standard databases like the JCPDS (Joint Committee on Powder Diffraction Standards). This indexing helps identify the phases present. Additionally, the crystallite size can be determined using the Scherrer formula, as described in equation [14]:

$$D = \frac{K\lambda}{\beta \cos \theta}$$

where D is the crystallite size, K is the dimensionless shape factor (here taken to be 0.94), λ is the wavelength of the X-ray used, and β is the full width at half maximum corresponding to Bragg's angle θ. The micro-strain in the crystal lattice can be estimated using the equation:

$$\varepsilon = \frac{\beta}{4\tan\theta}$$

ε is the micro-strain, and β is the full width at half maximum corresponding to Bragg's angle θ.

XRD analysis was conducted on all the synthesised samples to assess their crystallinity and purity. The respective working chapters provide the detailed XRD analysis results for each synthesised sample.

Fig.3.6. *The image of X-ray diffractometer X'pert³ Powder Multi-Purpose X-ray Diffractometer used in the study - CSIF, University of Calicut.*

Specifications of the instrument used for the characterisation:

- Model   : **Rigaku Miniflex 600 diffractometer**,

   Department of Physics, University of Calicut

   X'pert³ Powder. It is a Floor Standing Multi-

Purpose

   X-ray Diffractometer, CSIF, University of Calicut.

- Source   : Cu K$_\alpha$ radiation, λ=1.5404 Å

3.3.2. Raman analysis

Raman spectroscopy is based on the Raman Effect, a scattering technique where the frequency of scattered radiation differs from the incident monochromatic radiation. This effect results from the inelastic scattering of incident photons interacting with vibrating molecules, providing insights into molecular vibrations. It serves as a versatile

tool for both qualitative and quantitative analysis of samples. Qualitative analysis involves determining the frequency of scattered radiation, while quantitative analysis relies on the intensity of these scattered photons [15]. The schematic representation of the formation of Raman scattered photons is shown in Fig.3.7.

In Raman spectroscopy, a sample is irradiated with a laser beam of monochromatic light, interacting with sample molecules to produce scattered light at frequencies different from the incident light. Raman spectra arise due to inelastic collisions between sample molecules and incident photons. Most scattered radiation maintains the incident frequency, known as Rayleigh scattering, with a small portion exhibiting Raman scattering at different frequencies. If the incident frequency exceeds the scattered energy, Stokes shifts occur in the spectrum, whereas anti-Stokes shifts occur when the incident frequency is lower [15].
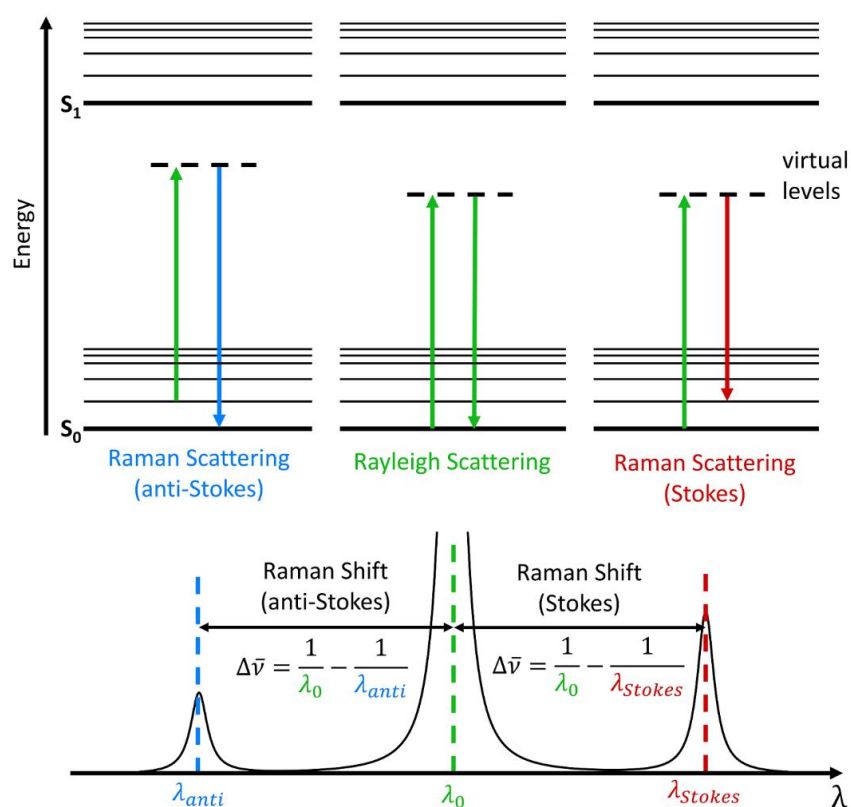
Fig.3.7. *Jablonski Diagram showing the origin of Rayleigh, Stokes and Anti-Stokes Raman Scatter. This figure is adapted from [16].*

The variation in molecular polarizability during molecular vibrations is essential for obtaining a Raman spectrum, displayed as intensity versus wavelength shift. The number of peaks in the spectrum corresponds to Raman-active modes, which are determined by the space group symmetry of crystalline solids and the point group symmetry of

molecules, making it a unique fingerprint of the material. Raman spectroscopy provides information on interatomic and molecular bond strengths, mechanical strain in solids, and the degree of crystallinity [15].

Instruments used for Raman spectroscopy include spectrophotometers equipped with filters and devices like tunable filters and CCD detectors to enhance data quality and acquisition speed. Advanced techniques such as Surface-Enhanced Raman Spectroscopy (SERS) and Resonance Raman Effect (RRE) enhance weak Raman signals. Micro-Raman spectrometers offer the advantage of analysing microscopic samples while minimising laser-induced sample damage through reduced spot sizes. It becomes a micro-Raman spectrometer when coupled with a microscope, enabling detailed analysis of small-scale samples [17]. The schematic diagram of parts of the Raman spectrometer with a microscope is shown in Fig.3.8.
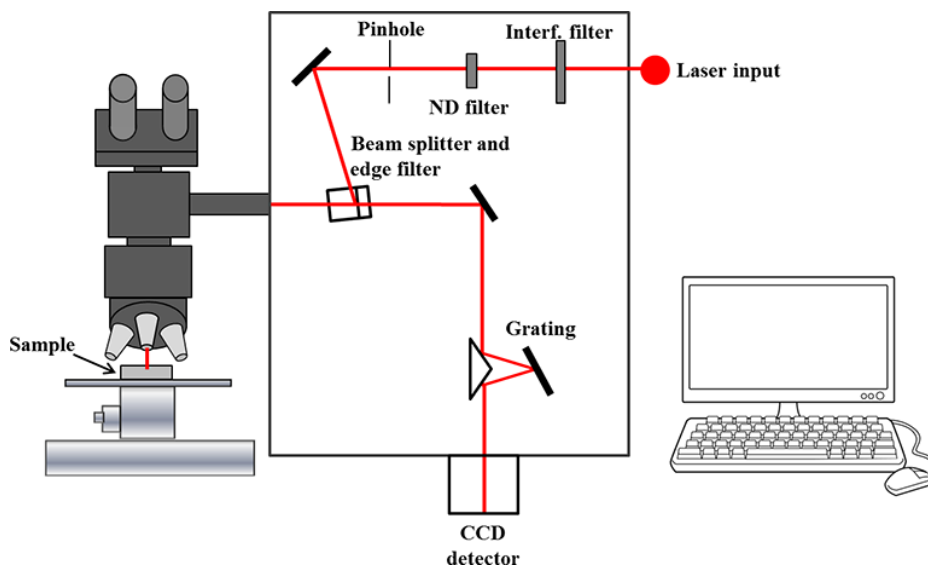
Fig.3.8. *Schematic diagram of parts of a Raman spectrometer with a microscope. The figure is adapted from [18].*

Raman analysis was conducted on all the synthesised samples to assess their purity and crystal structure. The respective working chapters provide the detailed Raman analysis results for each synthesised sample.

Fig.3.9. *The image of Micro-Raman Spectrometer-Department of Physics,*
University of Calicut.

Specifications of the instrument used for the characterisation:

- Model **: Jasco NRS 4100** (Micro Raman with 532 nm green laser)

  Department of Physics, University of Calicut.

- Laser : 532 nm, 20 mW

- Grating : 1800,1200 gr/mm

- Resolution : ± 0.2 cm^{-1}

- Detector : Air-cooled Peltier CCD detector (Max. -60°C), 1650 x 200 pixel, 16 μm x 16 μm, Visible to NIR.

3.4. GAS SORPTION AND POROSIMETRY CHARACTERISATIONS

Gas sorption and porosimetry characterisations are crucial for evaluating the surface area, porosity, and adsorption properties of materials, impacting their performance in catalysis, materials science, environmental science, and pharmaceuticals. The Brunauer-Emmett-Teller (BET) method determines specific surface area by nitrogen gas adsorption, measuring gas adsorption at various pressures and applying the BET equation. Chemisorption characterises catalysts by measuring gas adsorption through chemical interactions, providing insights into active sites, metal dispersion, and adsorbate-surface interaction strength. These techniques are essential for understanding and optimising material properties and catalytic processes.

3.4.1. The Brunauer-Emmett-Teller (BET) analysis

Surface area properties are particularly relevant to environmental applications of these materials; therefore, accurate surface area measurement is crucial for material characterisation. The Brunauer-Emmett-Teller (BET) surface adsorption technique is the most commonly used method for determining the surface area of nanosubstances. BET adsorption assumes that the material has a homogeneous surface and that adsorption occurs uniformly across the entire surface. Each adsorption site is either vacant or occupied by a single adsorbate molecule. The overall adsorption process can be expressed as a fractional coverage of the surface, with molecular interactions considered to be limited [19].

The energy required for adsorption on the surface layer is equivalent to the heat of adsorption. In contrast, the energy needed for each subsequent layer is equal to the heat of liquefaction, treating each layer as a condensed liquid. These kinetic processes are assumed to be uniform throughout the material. When saturation pressure (P_0) is reached, the number of adsorbed layers is sufficient for the material to be fully covered by condensed liquid-phase adsorbent. Based on these assumptions, the kinetic rates of adsorption and desorption can be determined from the surface coverage fraction, and the adsorption for each layer can be modelled using the Arrhenius equation [20].

To examine the reliability of the BET equation using experimental data, the equation is used in the following form:

$$\frac{P}{V(P_0 - P)} = \frac{1}{V_m\,C} + \frac{C-1}{V_m\,C}\left(\frac{P}{P_0}\right)$$

In the BET equation, V is the volume of gas adsorbed, $\left(\frac{P}{P_0}\right)$ is the relative pressure, V_m is the volume of the adsorbate as a monolayer, and C is the BET constant. The BET plot, which graphs $\frac{P}{V(P_0-P)}$ against $\left(\frac{P}{P_0}\right)$, should yield a straight line. The intercept and slope of this plot represent $\frac{1}{V_m\,C}$ and $\frac{C-1}{V_m\,C}$ respectively. Using those values, the constants V_m and C of the BET equation can be calculated.

The specific surface area (surface area per unit mass) can be calculated by the equation

$$S_A = \frac{V_m\,N A_{cs}}{M}$$

where N is the Avogadro's number (6.023×10^{23}), M is the molecular weight of adsorbate, A_{cs} is the adsorbate cross-sectional area ($16.2 Å^2$ for nitrogen)

The BJH (Barrett, Joyner, and Halenda) method is used to determine pore size distributions from experimental isotherms using the Kelvin model of pore filling. The total pore volume is calculated from the amount of vapour adsorbed at a relative pressure close to unity, assuming the pores are filled with liquid adsorbate. The equation for this calculation is given as follows [22]:

$$V_{liq} = \frac{P_a V_{ads} V_m}{RT}$$

where V_{ads} is the volume of gas adsorbed, V_{liq} is the volume of liquid N_2 in pores, V_m is the molar volume of liquid adsorbate ($N_2 = 34.7$ cm^3/mol), P_a is the ambient pressure, and T is the ambient temperature.

The average pore size can be assessed from the value of pore volume by assuming that the pores having cylindrical geometry and the average pore radius (r_p) can be articulated as

$$r_p = 2\frac{V_{liq}}{S}$$

BET analysis requires a pure, clean, and dry sample placed in a sample tube and degassed. This is achieved by connecting the tube to a vacuum pump and heating it for at least one hour to remove water vapour before analysis. During the nitrogen adsorption experiment, the samples are immersed in a liquid nitrogen bath, which helps achieve rapid kinetic equilibrium due to the cold temperature. The instrument introduces known amounts of high-purity nitrogen gas into the tube while recording the pressure (P/P_0). This data plots the BET equation and calculates the relevant surface area parameters [20].

The BET analysis determines the specific surface area, monolayer volume, and mean pore diameter of the adsorbents and catalysts synthesised in this research. Chapters 4, 5, 6, and 7 present the estimated values and isotherms for the concerned material.
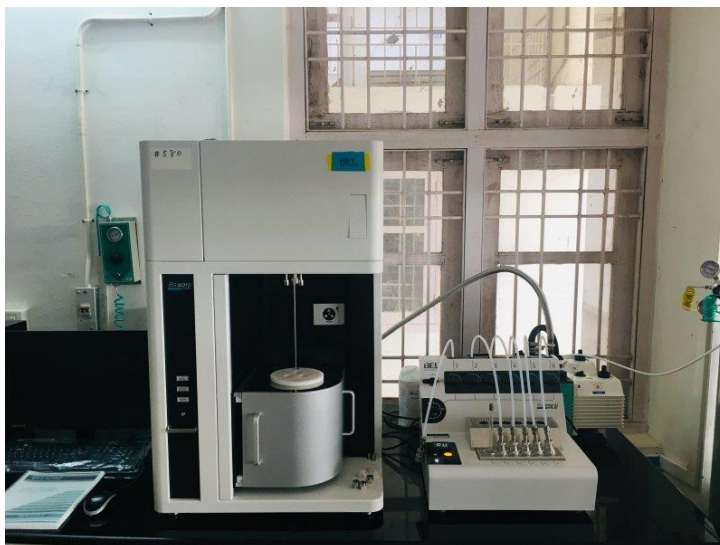
Fig.3.10. *The image of Brunnauer-Emmett-Teller (BET) analyser-BELSORP-max -CSIF, University of Calicut.*

Specifications of the instrument used for the characterisation:

- Model   : **BELSORP-max**

  CSIF, University of Calicut

- Measurement method : Volumetric gas adsorption method + AFSM TM,

  Standard mode ($P/P_0 = 10^{-8}$ to 0.997)

- Specific surface area   : 0.01 m^2 g^{-1} or more (N_2 / 77K)

- Analysis program   : BELMaster TM, Specific surface area by BET method,

  Meso-Pore analysis by BJH method.

3.4.2. Chemisorption analysis

Chemisorption analysis is crucial for quantifying acid or basic sites on catalyst surfaces by measuring gas interactions, thereby optimising catalyst performance in diverse applications such as chemical synthesis and environmental remediation. In metal-supported catalysts, factors such as metal dispersion rate, metal surface area, and metal particle size significantly influence both the cost and performance of the catalyst. Similarly, for solid acid catalysts, the number and strength of acid sites dictate their catalytic performance. Since catalytic reactions occur on the catalyst surface, the specific surface area plays a vital role in evaluating catalytic efficiency [22].

Temperature Programmed Desorption (TPD) using ammonia gas is a robust technique for estimating acid sites on catalyst surfaces. During TPD analysis, the catalyst is exposed to ammonia gas at low temperatures, where it adsorbs into acidic sites. The

catalyst is heated gradually while a carrier gas (typically helium or nitrogen) flows through the system. As the temperature rises, ammonia molecules desorb from the catalyst surface. The desorbed ammonia is detected using sensitive equipment like a thermal conductivity detector or mass spectrometer, generating a TPD profile that records the amount of ammonia desorbed at each temperature step [23].

The TPD profile reveals desorption temperature peaks corresponding to different acidic sites on the catalyst surface; stronger acid sites desorb ammonia at higher temperatures, whereas weaker sites desorb at lower temperatures. Each peak in the TPD profile represents a specific type of acidic site, and the area under each peak indicates the concentration or strength of the corresponding acid sites. Comparing TPD profiles between different catalysts or under varying reaction conditions allows researchers to study changes in acidity, providing valuable insights for catalyst design and optimisation in industrial and research settings [23]. TPD analysis using NH_3 was conducted to estimate the acid sites on MnS nanostructures in this research. Detailed characterisation analysis is described in Chapter 5.

Fig.3.11*. The image of Temperature Programmed Desorption (TPD) measurement system - BELCAT-M – CSIF, University of Calicut.*

Specifications of the instrument used for the characterisation:

- Model   **: BELCAT-M.**

    CSIF, University of Calicut

- Measurement principle   : Dynamic flow method.

- Detector   :Thermal Conductivity Detector

    (W-Re filament).

3.5. MORPHOLOGICAL CHARACTERISATION

Morphological characterisation is crucial in adsorption and catalysis as it provides detailed insights into the physical structure and surface properties of materials, which directly influence their performance and efficiency. This research examined the surface features and morphology of synthesised adsorbents and catalysts using scanning electron microscopy (SEM). The basic principles behind SEM are described below:

3.5.1. Scanning Electron Microscopy

In Scanning Electron Microscopy (SEM), a high-resolution surface image of a sample is produced through the interaction between a high-energy electron beam and the sample material. This interaction generates secondary electrons, backscattered electrons, X-rays, and auger electrons. The ejected electrons can be detected, and the corresponding signal provides information about the sample under study. These signals reveal details about the texture, chemical composition, and orientation of materials in the specimen. Data collected from a specific region of the sample surface forms a 2-D image. SEM can produce pictures of areas ranging from approximately 1 cm to 5 microns in width. Secondary electrons, which have low energy, provide topographical information and the shape of the sample, while backscattered electrons, which have high energy, convey compositional details. The yield of backscattered electrons depends on the atomic number of the constituent atoms, with heavier atoms appearing brighter in the images. Samples for SEM must be conductive; a carbon tape can be applied to the sample, and a very thin layer of gold or palladium can be coated over the sample to make it conductive [24].

Instrumentation in SEM is crucial for accurate imaging and analysis of samples. The electron gun is the source of the electron beam, which is usually generated using tungsten or lanthanum hexaborides. A tungsten tip is exposed to a high potential to produce a monochromatic beam of electrons. The condenser lens system, consisting of a

pair of lenses, plays a vital role in regulating the electron beam's energy. These lenses, in combination with the condenser and objective apertures, help to remove high-angle electrons, ensuring a focused and coherent beam.
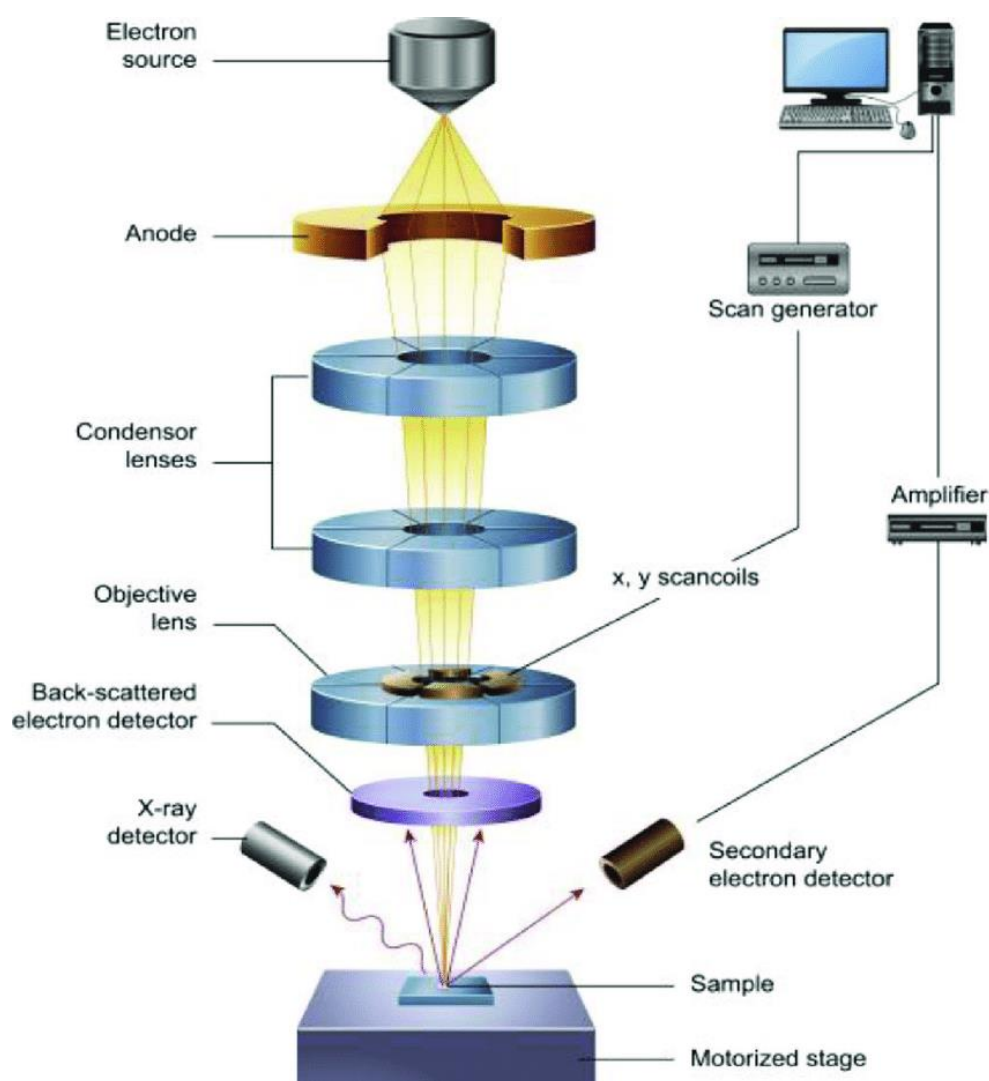
Fig.3.12. *The schematic representation of SEM. This figure is adapted from [25].*

Scanning coils are essential for directing this electron beam across the surface of the sample in a controlled manner. The objective lens then precisely focuses the beam onto the specific region of the sample that is being examined. The interaction between the electron beam and the sample generates various signals, such as secondary electrons and backscattered electrons, which are detected and analysed to form a detailed image on the screen. This process allows for the examination of the sample's surface texture, chemical composition, and material orientation with high resolution. The schematic representation of the SEM is shown in the Fig.3.12. [26].

In this research, all synthesised samples were characterised using Field Emission Scanning Electron Microscopy (FESEM) analysis to obtain high-resolution images of their surface morphology and structural details. The comprehensive analysis of each synthesised sample is thoroughly discussed in the corresponding working chapters 4, 5, 6, and 7.

Fig. 3.13. *The image of Field Emission-Scanning Electron Microscope-ZEISS GeminiSEM 300- CSIF, University of Calicut.*

Specifications of the instrument used for the characterisation:

- Model : **ZEISS GeminiSEM 300**
  CSIF, University of Calicut
- Acceleration Voltage : 0.02 - 30 kV
- Probe Current : 3 pA - 20 nA (100 nA configuration also available)
- Magnification : 12 – 2,000,000
- Electron Emitter : Thermal field emission type, stability better than 0.2 %/h
- Detectors available in basic configuration: In lens Secondary Electron detector. Everhart Thornley Secondary Electron detector.

3.6. OPTICAL CHARACTERISATIONS

The optical characterisation is essential for understanding the properties and performance of catalysts in photocatalytic and sonophotocatalytic applications. UV-Visible (UV-Vis) absorption spectroscopy and Diffuse Reflectance Spectroscopy (DRS) are primary techniques used to gain insights into the electronic structure, light absorption capabilities, and band gap energies of catalysts. These methods help identify the optimal light absorption range and the energy required for photocatalytic reactions and are crucial for enhancing catalytic activity in sonophotocatalysis.

3.6.1. UV-Visible spectroscopy.

UV-visible spectroscopy examines the interaction between ultraviolet and visible light with molecules, providing both qualitative and quantitative analysis of samples. This technique relies on the principle that an unknown substance absorbs light at specific wavelengths. When a sample is exposed to UV-visible light, some light is absorbed while the rest is transmitted. This transmitted light is then detected and recorded as a function of wavelength, producing the sample's UV-Vis spectrum. Each substance has a unique absorption pattern, creating a specific relationship between it and its UV-vis spectrum. The concentration of the sample is directly proportional to its absorbance, which can be determined using a calibration curve obtained from the UV-Vis spectrophotometer. This instrument measures the light intensity before and after it passes through a sample solution in a cuvette [27]. The Beer-Lambert law explains the relationship between concentration and absorbance, stating that absorbance (*A*) is proportional to the product of the concentration (*c*) of the solution and the path length (*l*). This law is beneficial for explaining the absorption behaviour of solutions with relatively low concentrations. The Beer-Lambert law can be expressed as [28]:

$$A = \ln\left(\frac{I}{I_0}\right) = \varepsilon c l$$

where I_0 is the initial intensity of light, I is the intensity of light after passing through the sample, and ε is the molar absorption coefficient.

The UV-visible spectrophotometer comprises several vital components that work together to measure the absorbance of a sample accurately. The primary parts include the light source, sample holder, diffraction grating, and detector. The light source provides a stable radiant energy output over the desired wavelength range. Tungsten filament and deuterium arc lamps are commonly used, though LEDs and xenon arc lamps are now

also utilised for visible light wavelengths. The sample holder is a transparent container that securely holds the sample during measurement. The diffraction grating, a crucial component, functions within the monochromator to split the incoming light into two beams using a half-mirrored device. One beam passes through the cuvette containing the sample, while the other passes through an identical cuvette holding the reference solution. Quartz cuvettes, transparent to UV radiation, are typically used for this purpose. Finally, the detector measures the transmitted light's intensity from the cuvette and displays the results on an LCD screen, providing the absorbance values needed for analysis [30]. The schematic representation of UV-Visible spectrometer is shown in Fig.3.14.
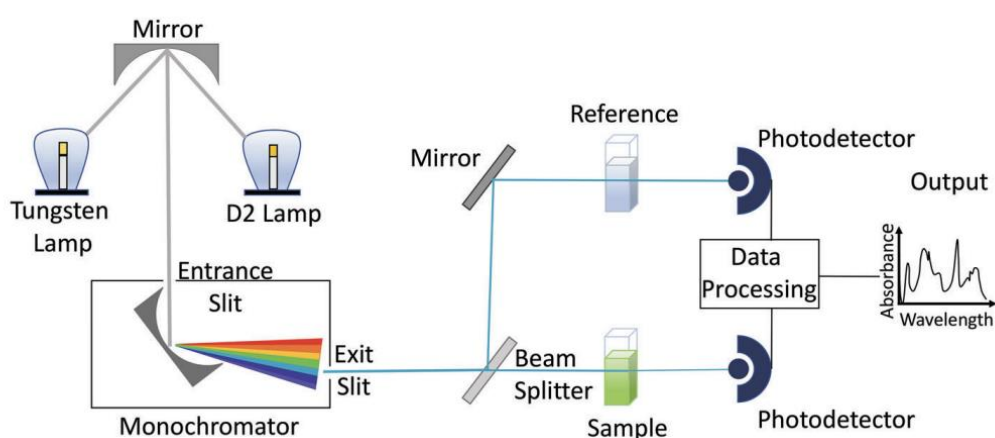
Fig.3.14. *The schematic representation of UV-visible spectrometer. This figure is adapted from [29].*

UV-visible spectroscopic analysis is essential for this research. All targeted pollutants in this study are identified and quantitatively analysed using UV-visible spectroscopy. The contaminants include sodium dodecyl sulfate, phosphate ions, Congo Red dye, Ciprofloxacin (an antibiotic), Tetracycline hydrochloride (an antibiotic), and Rhodamine B dye. All dyes and antibiotics are identified and quantified using UV-visible spectroscopy. Each molecule has characteristic peaks within the 200 nm to 900 nm range.

Since the concentration of a dye solution is proportional to its absorbance, we can plot the absorbance values against known dye concentrations to generate a calibration curve. If the Beer-Lambert law is followed, this calibration curve should be a straight line, indicating a direct proportionality between absorbance and dye concentration. To determine the dye concentration in an unknown sample, compare its absorbance to the calibration curve. The UV-visible spectrum of Rhodamine B and its calibration curve is shown in the Fig.3.15. and Fig.3.16.
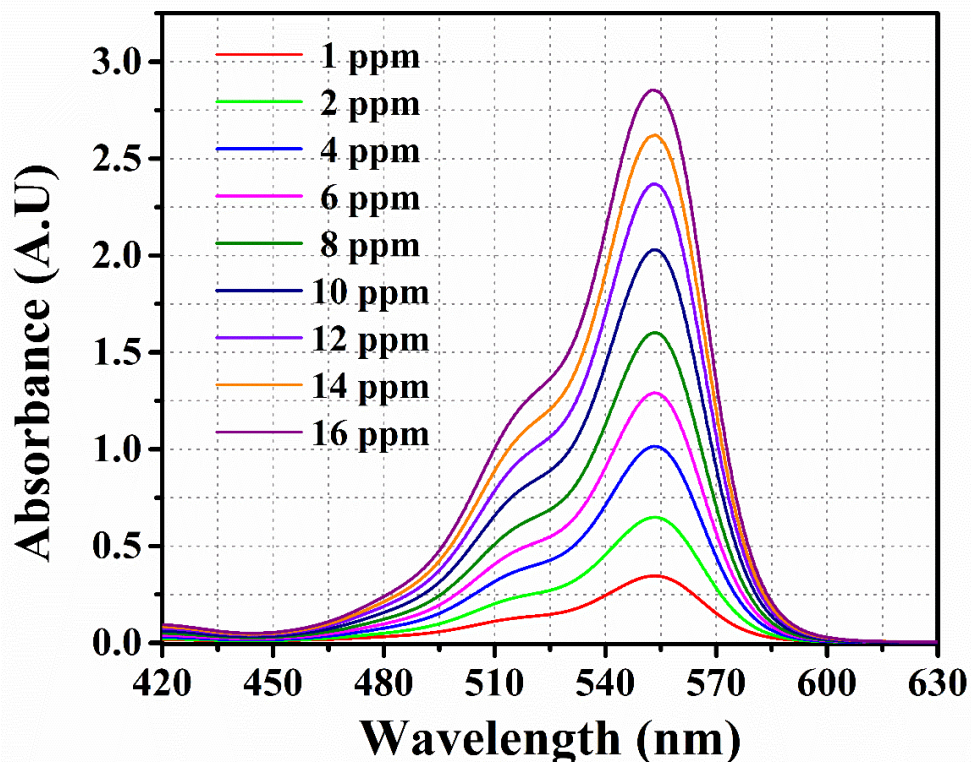
Fig.3.15. *UV-visible absorption spectrum of Rhodamine B. Its absorption peak is near 552 nm.*
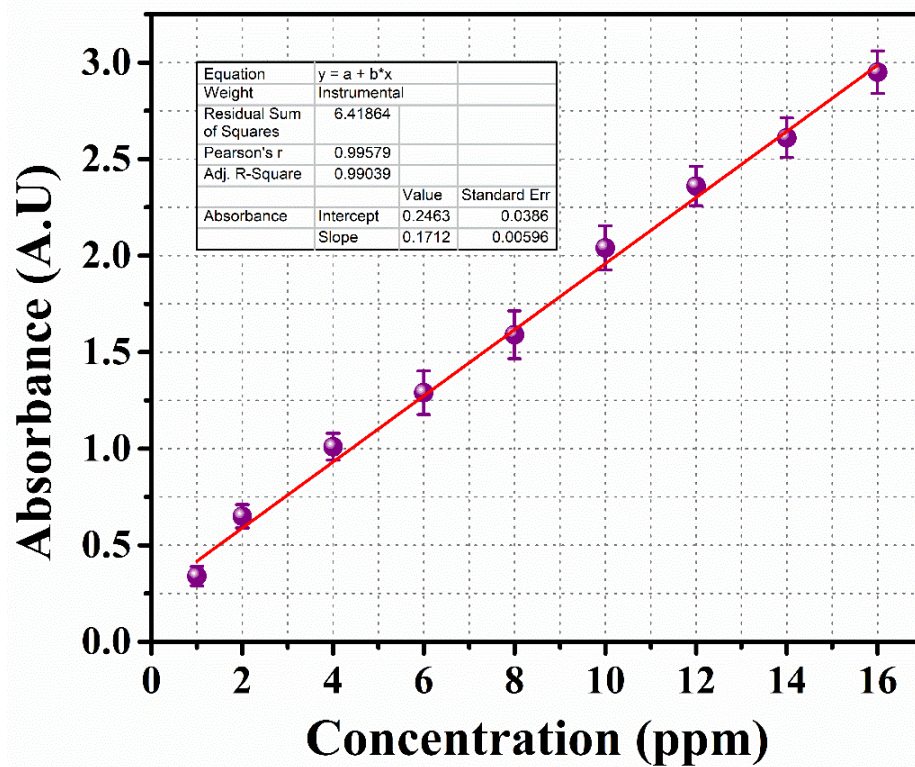
Fig.3.16. *The calibration curve of Rhodamine B dye.*

Sodium dodecyl sulfate and phosphate ions cannot be directly identified using UV-visible spectroscopy, as they lack characteristic peaks in the 200 nm to 900 nm range. Instead, these ions are detected using indirect spectroscopic methods by forming complexes with other active materials, which are then analysed. The absorbance of these complexes is proportional to the concentration of the pollutants in the solution. The estimation of sodium dodecyl sulfate is performed using the Methylene Blue Active Substances (MBAS) method, while phosphate ion estimation is conducted using the Reduced Molybdophosphate Photometric Method. The details of the procedure for these two methods are given below:

Methylene Blue Active Substances (MBAS) method

Calibrating sodium dodecyl sulfate (SDS) using the Methylene Blue Active Substances (MBAS) method involves a series of precise steps to ensure accurate quantification. The MBAS method exploits the formation of a coloured complex between methylene blue dye and anionic surfactants like SDS. The detailed procedure for the calibration is shown below [31]:

Materials and Reagents:

1. Sodium dodecyl sulfate (SDS) standard solution: Prepare a series of known concentrations of SDS in deionised water.
2. Methylene blue reagent: Prepare a methylene blue solution in deionised water.
3. Chloroform: High-purity chloroform for extraction.
4. Buffer solution: pH-adjusted buffer to maintain the appropriate pH during the reaction.
5. Deionised water: For all dilutions and preparations.

Calibration Procedure:

1. Preparation of SDS Standard Solutions:

    - Prepare a series of SDS standard solutions with known concentrations (e.g., 2.0, 4.0, 6.0, 8.0, 10.0, 12.0, 14.0 mg/L) by diluting a stock SDS solution in deionised water.

2. Addition of SDS Standards and Reagent:

    - In separate volumetric flasks, add 1 mL of each SDS standard solution.

- Add 0.5 mL of methylene blue reagent to each flask.

3. Buffer Solution Addition:

    - Add a buffer solution to maintain the pH at around 7-8 to ensure optimal complex formation.

4. Extraction Procedure:

    - Transfer the reaction mixtures to separatory funnels.

    - Add 3 mL of chloroform to each funnel.

    - Shake the funnels vigorously for a fixed time (e.g., 2 minutes) to allow the methylene blue-SDS complex to extract into the chloroform layer.

    - Allow the mixture to settle and separate into two distinct layers (aqueous and organic).

5. Collection of Chloroform Layer:

    - Carefully drain the chloroform layer (containing the methylene blue-SDS complex) into clean cuvettes.

    - Run blank samples (without SDS) to ensure no interference.

6. Measurement of Absorbance:

    - Measure the absorbance of each chloroform extract at the specific wavelength corresponding to the maximum absorbance of the methylene blue-SDS complex (typically around 650-660 nm) using a UV-Vis spectrophotometer.

7. Generation of Calibration Curve:

    - Plot the absorbance values against the known concentrations of SDS to generate a calibration curve.

    - Ensure the calibration curve is a straight line, indicating compliance with the Beer-Lambert law, which shows a direct proportionality between absorbance and SDS concentration.

8. Analysis of Unknown Samples:

    - Follow the same procedure for the unknown sample as described above.

- Measure the absorbance of the chloroform extract of the unknown sample.

- Use the calibration curve to determine the SDS concentration in the unknown sample by comparing its absorbance to the standard curve.

The calibration curve for the estimation of SDS is shown in Fig. 3.17.
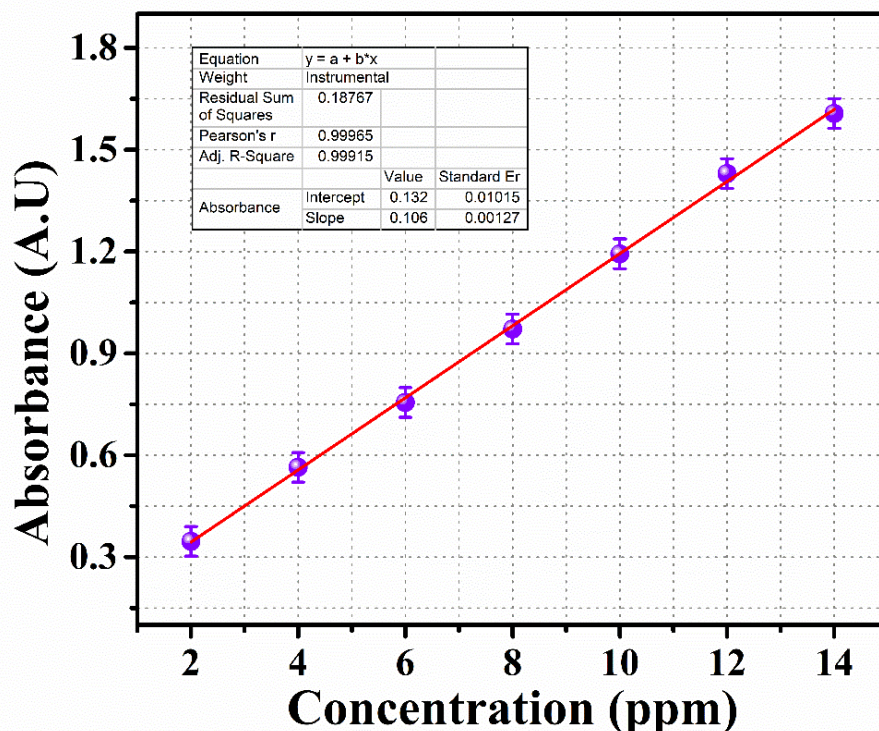
Fig.3.17. *The calibration curve of SDS using the Methylene Blue Active Substances (MBAS) method.*

Ammonium vanadomolybdophosphate color development method

Calibrating phosphate using the ammonium vanadomolybdophosphate colour development method involves a series of steps to determine phosphate concentrations accurately. This method relies on forming a yellow-coloured complex between phosphate ions and ammonium vanadomolybdate, which can be measured spectrophotometrically. The comprehensive procedure is outlined below [32]:

Materials and Reagents:

1. Phosphate standard solutions: Prepare a series of known concentrations of phosphate.

2. Ammonium molybdate reagent: Prepare a solution of ammonium molybdate.

3. Ammonium vanadate reagent: Prepare a solution of ammonium vanadate.

4. Sulfuric acid: For preparing the acidic environment needed for the reaction.

5. Deionised water: For all dilutions and preparations.

Calibration Procedure:

1. Preparation of Phosphate Standard Solutions:

   - Prepare a series of phosphate standard solutions with known concentrations (e.g., 20, 40, 60, 80, 100 mg/L) by diluting a stock phosphate solution in deionised water.

2. Preparation of Ammonium Molybdate Reagent:

   - Dissolve 2.5 g of ammonium molybdate in 50 mL deionised water.

3. Preparation of Ammonium Vanadate Reagent:

   - Dissolve 0.125 g of ammonium vanadate in 1.6 mL nitric acid, then dilute with 50 mL deionised water.

4. Formation of Detection Reagent:

   - Mix the ammonium molybdate and ammonium vanadate solutions together to form the reagent for phosphate detection.

5. Reaction with Phosphate Standards:

   - In separate volumetric flasks, add 5 mL of each phosphate standard solution.

   - Add 1 mL of the prepared reagent to each volumetric flask.

   - Mix well and allow the reaction to proceed for a specified time (typically around 10 minutes) to form the yellow-coloured ammonium vanadomolybdophosphate complex.

6. Preparation for Spectrophotometry:

   - Transfer the reaction mixtures to clean cuvettes.

   - Run blank samples (without phosphate) to ensure no interference.

7. Measurement of Absorbance:

- Measure the absorbance of each solution at the wavelength corresponding to the maximum absorbance of the complex (typically around 400-420 nm) using a UV-Vis spectrophotometer.

8. Generation of Calibration Curve:

   - Plot the absorbance values against the known concentrations of phosphate to generate a calibration curve.

   - Ensure the calibration curve is a straight line, indicating compliance with the Beer-Lambert law, which shows a direct proportionality between absorbance and phosphate concentration.

9. Analysis of Unknown Samples:

   - Follow the same procedure for the unknown sample as described above.

   - Measure the absorbance of the complex formed with the unknown sample.

   - Use the calibration curve to determine the phosphate concentration in the unknown sample by comparing its absorbance to the standard curve.

The calibration curve for estimating phosphate ion is shown in Fig. 3.18.
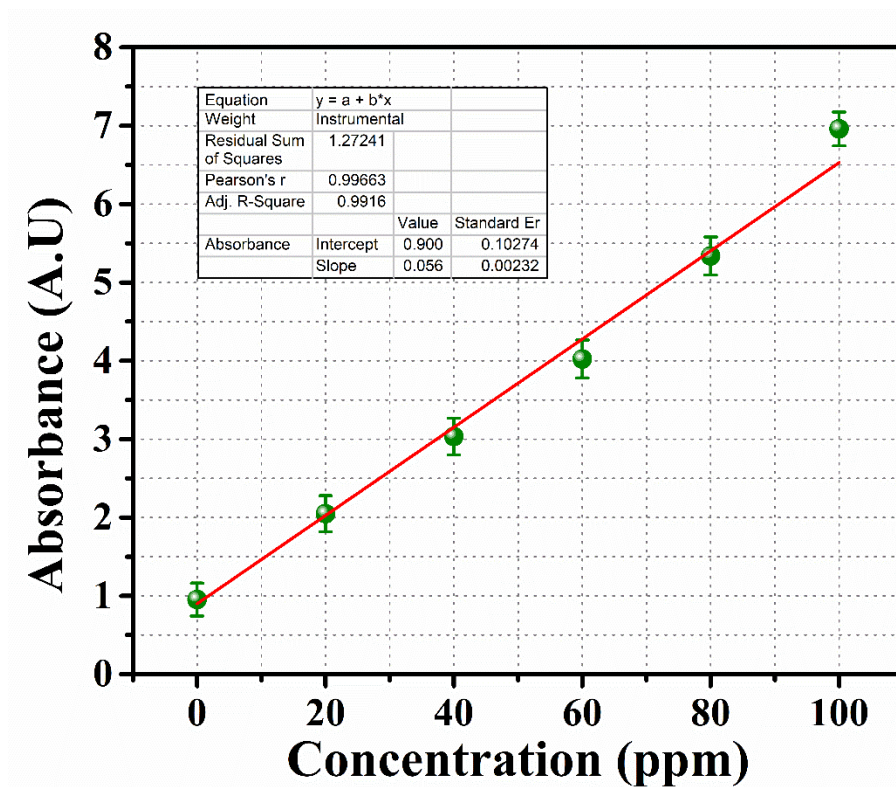
Fig.3.18. *The calibration curve of phosphate ions using the ammonium vanadomolybdophosphate color development method.*

Fig.3.19. *The image of UV-Visible spectrometer-Jasco-750 spectrophotometer-Department of Physics, University of Calicut.*

Specifications of the instrument used for the characterisation:

- Model   : **JascoV-750 spectrophotometer**

  Laboratory for mesoscopic science and devices,

  Department of Physics, University of Calicut.

- Source   : Tungsten filament and deuterium arc lamp

- Wavelength range   : 200 nm – 900 nm

- Band width   : 2 nm

- Optical system   : Czerny-Turner mount Single monochromator Fully

  symmetrical double beam type.

3.6.2. UV-Visible-DRS analysis

When light is focused onto a powdered sample, two types of reflection occur on its surface: specular and diffuse reflection. Specular reflection follows Snell's law, where the angle of incidence equals the angle of reflection. In diffuse reflection, light penetrates the sample and undergoes scattering. Due to the nanostructured material, the light experiences multiple processes such as refraction, reflection, and diffraction in all directions, depending on the wavelength. Consequently, light exits the sample in all directions. This is termed as diffuse reflectance. Diffuse reflectance is defined by the condition that the angular distribution of the reflected radiation is independent of the angle of incidence. This type of reflectance is commonly measured in the UV-Vis-NIR and mid-IR regions to obtain molecular spectroscopic information [33].
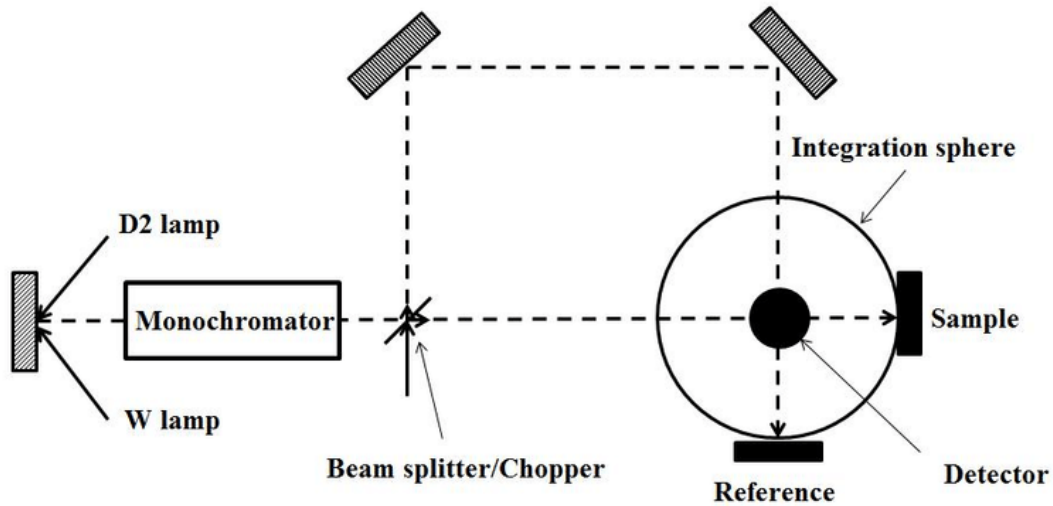
Fig.3.20. *The schematic representation of UV-visible DRS spectrometer instrumentation. The figure is adapted from [34].*

During measurement, samples that exhibit diffuse reflectance simultaneously absorb and scatter radiation. Like an integrating sphere with a spherical surface, a diffuse reflector accessory collects the diffused reflection and directs it to a photodetector. A schematic representation of the integrating sphere and UV-visible DRS spectrometer is shown in Fig.3.20. The light source typically covers a wavelength range of 200-900 nm, with BaSO$_4$ used as the reference. The Kubelka-Munk theory is often used to describe and analyse the diffuse reflectance spectra of powdered samples [33].

The Kubelka-Munk model (1931) is commonly employed in Diffuse Reflectance Spectroscopy to determine the optical bandgap. The Kubelka-Munk function, F(R), is used for infinitely deep samples and is derived from reflectance data. It is defined as [35]:

$$F(R) = \frac{(1-R)^2}{2R} = \frac{k}{S} \qquad R = \frac{(R)_{sample}}{(R)_{reference}}$$

In this context, R represents the reflectance of a thick scattering layer, k is the molar extinction coefficient, and s is the scattering coefficient dependent on particle size. The spectrum is highly sensitive to particle size, influencing radiation scattering. If the particle size is not uniformly fine, spectral distortion may occur compared to a transmission spectrum. This technique can be applied to black, strongly scattering materials like coal [36].

By utilising the Kubelka-Munk function, the optical band gap of the powdered sample can be calculated.

$$[h\nu F(R)]^{1/n} = A(h\nu - E_g)$$

Where h is Planck's constant, ν is the vibration frequency, E_g is the band gap, and A is the proportional constant. The parameter n indicates the nature of the electronic transition, with values of 1/2 for direct allowed, 3/2 for direct forbidden, 2 for indirect allowed, and 3 for indirect forbidden transitions [35].

Plotting the left-hand side of this equation versus hν and drawing a tangent line at the point of inflexion on the curve allows for determining the bandgap value E_g from the corresponding hν value on the horizontal axis.

The UV-visible DRS analysis is employed in this research to estimate the optical bandgap of the materials and to determine their absorbance in the UV and visible regions. This analysis is crucial for understanding the excitation and photocatalytic activity of the catalysts. The optical bandgaps of the bismuth oxyhalide solid solutions and bismuth vanadate nanomaterials are estimated using this technique, and their UV-visible light absorption is examined. A detailed description of the UV-visible DRS analysis for these catalysts is provided in Chapters 6 and 7.

Specifications of the instrument used for the characterisation:

- Model : **JascoV-750 spectrophotometer**

  Laboratiry for Mesoscopic Science and Devices,

  Department of Physics, University of Calicut.

- Source : Tungsten filament and deuterium arc lamp

- Wavelength range : 200 nm – 900 nm

- Band width : 5 nm

3.6.3. Photoluminescence (PL) spectroscopy.

Photoluminescence spectroscopy is a non-destructive and versatile optical technique for investigating the electronic structure of materials. When the sample is irradiated with light, the molecules are excited to higher energy states, and the energy is then dissipated through an emission process. The energy of the emitted light corresponds

to the energy difference between two electronic states involved in the optical transition. This emitted light can be collected and analysed both spectrally and spatially to obtain detailed information about the electronic states of the sample. The instrument used for measuring photoluminescence is called a spectrofluorometer [37].

A photoluminescence (PL) spectrometer consists of several key components designed to measure the photoluminescent properties of samples accurately. The primary light source, typically a Xenon lamp emitting light across the 200-900 nm range, is directed by an elliptical mirror onto the entrance slit of the excitation monochromator, with a quartz window separating the lamp from the monochromator to minimise heat and spherical aberration. The spectrometer includes two monochromators (excitation and emission) utilising reflective optics to reduce diffraction and spherical irregularities. Gratings with vertical grooves disperse light, and the spectrum is acquired by rotating the grating. Adjustable entrance and exit slits on both monochromators allow control over signal intensity and resolution. Excitation and emission shutters protect the sample from photodegradation and photobleaching by preventing continuous exposure to the light source. The sample cell holds the specimen, with optical fibres directing light to and from the sample. The detection system includes a signal detector that counts the photons emitted from the sample and a reference detector that monitors the source lamp to correct for any wavelength variations, ensuring accurate measurements [37].
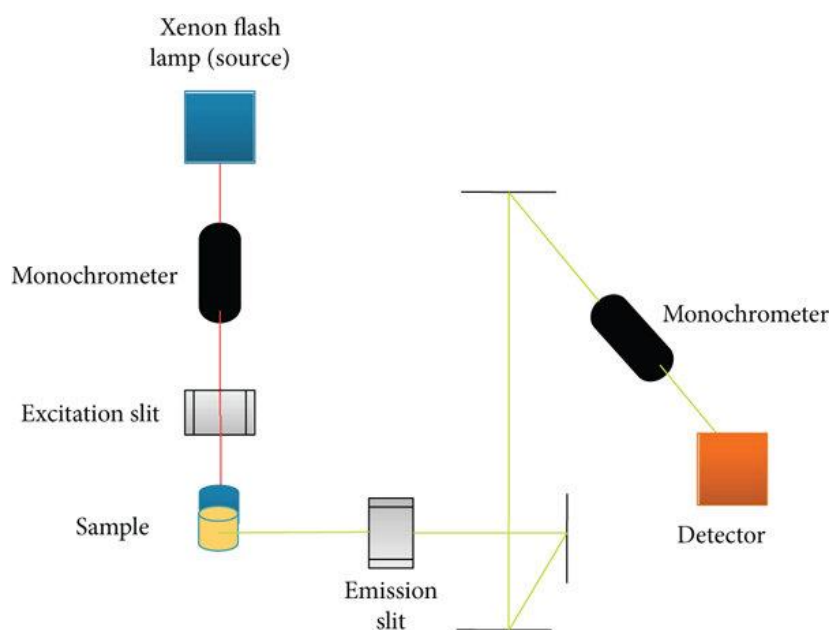
Fig.3.21. *The schematic diagram of Photoluminescence spectrophotometer. This image is adapted from [38].*

Photoluminescence (PL) measurement is scientifically relevant in explaining charge carrier recombination in photocatalysts in photocatalytic applications. By analysing the emitted light from a photocatalyst when irradiated, PL spectroscopy provides insights into the electronic structure and recombination processes of charge carriers (electrons and holes). High PL intensity indicates significant recombination, suggesting inefficient charge separation and lower photocatalytic activity. Conversely, lower PL intensity implies reduced recombination, indicating better charge separation and higher photocatalytic efficiency. Thus, PL measurements are crucial for optimising photocatalyst performance by understanding and controlling charge carrier dynamics. The schematic diagram of Photoluminescence spectrophotometer is shown in Fig.3.21.

The PL measurement is conducted on bismuth oxyhalide solid solutions and bismuth vanadate nanomaterials to understand the recombination rate of electrons and holes and to study their photoluminescence properties. These results are crucial for explaining the efficient photocatalytic and sonophotocatalytic activities. A detailed description of the PL analysis for these catalysts is provided in Chapters 6 and 7.

Fig.3.22. *The image of Horiba Fluromax-4c Fluorescent spectrophotometer. This image is adapted from [39].*

Specifications of the instrument used for the characterisation:

- Model : **Horiba Fluromax-4c Fluorescent spectrophotometer**

    Department of Chemistry, University of Calicut.

- Source : 150W Xe arc lamp.

- Wavelength range : 185 nm – 850 nm.

- Detector : R928P photon counting PMT detector.

3.7. FOURIER TRANSFORM INFRARED SPECTROSCOPY

Fourier Transform Infrared (FTIR) spectroscopy is a widely accepted technique for the structural analysis and identification of chemical compounds. The IR spectrum of a compound serves as its "fingerprint" because the peaks correspond to the excitation of vibrational modes of the molecules, which are associated with various functional groups and chemical bonds present in the molecules. FTIR examines the interaction between the vibrating dipole moments of molecules and infrared radiation. For a molecule to exhibit an IR spectrum, the vibrating motion of the bond must result in a time-dependent change in its dipole moment. In FTIR, the sample is subjected to a single pulse of radiation encompassing a specific frequency range, producing a rapidly decaying composite signal of all possible frequencies. At resonance conditions, certain frequencies will dominate and can be Fourier transformed to obtain the final spectrum. The Fourier transform converts the signal from the time domain to the frequency domain, mathematically represented as:

$$F(\omega) = \int\limits_{-\infty}^{+\infty} f(x)\, e^{i\omega x} dx$$

where $F(\omega)$ is the spectrum, $f(x)$ is the interferogram, ω is the angular frequency, and x is the optical path difference. The experimentally obtained interferogram $f(x)$ is converted into the spectrum $F(\omega)$ using the Fourier transform [40].

The main components of an FTIR spectrometer include the IR radiation source, Michelson interferometer, sample cells, and detector. Common IR radiation sources are the Globar, consisting of electrically heated rods of SiC; the Nernst glower, constructed of rare earth oxides such as Er, Ce, Zr, Th, and Y; and the Nichrome coil. The Michelson interferometer features a mid-IR range emitting broadband light source, a beam splitter, and dual front surface-coated mirrors (one moving and one fixed) along with a detector. When infrared radiation is directed at the beam splitter, half of the light is reflected at a 90-degree angle to a fixed mirror, while the other half transmits to a moving mirror. The beams reflected back to the detector have a phase difference, causing constructive or destructive interference depending on the moving mirror's position. Scanning the moving mirror across a range generates a sinusoidal signal for each frequency, known as an interferogram, which plots the detector signal versus optical path difference. The final

spectrum is obtained from the interferogram through Fourier transformation [40]. The schematic representation of FTIR spectrometer is shown in Fig.3.23.
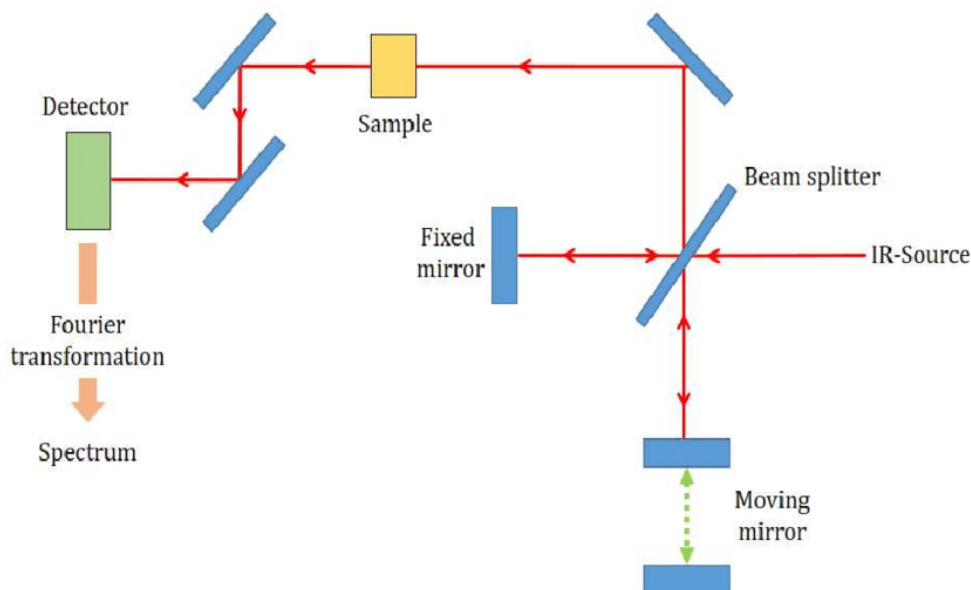
Fig.3.23. *The schematic representation of FTIR spectrometer. The figure is adapted from [41].*

For sample analysis, materials used must be transparent to IR, such as KBr. The sample handling technique varies with the sample's state. Gaseous samples are placed in a gas cell with IR-transparent windows. Liquid samples are pressed as thin films between IR-transparent windows. Solid samples often utilize the KBr disc method, where 20 mg of the sample is ground with 200 mg of KBr and pelletized under high pressure. This study employed the KBr disc method. Finally, detectors in FTIR spectrometers are usually pyroelectric detectors, photodetectors, or liquid-cooled phonon detectors.

Fig.3.24. *The image of Cary 660 FTIR Spectrometer. The image is adapted from [42].*

Specifications of the instrument used for the characterisation:

- Model   : **Cary 660 FTIR Spectrometer, Agilent**

  Technologies, CSIF, University of Calicut.

- Spectral range for spectrometer   : 8500 to 50 cm^{-1}

- Spectral Resolution of spectrometer : 0.06 cm^{-1}

- Sampling method   : KBr Disc Method

3.8. HIGH PERFORMANCE LIQUID CHROMATOGRAPHY

High-Performance Liquid Chromatography (HPLC) is an analytical technique used to separate, identify, and quantify components in a mixture. The basic principle of HPLC relies on the differential partitioning of compounds between a mobile phase (a liquid solvent) and a stationary phase (a solid adsorbent material). Compounds in the sample mixture interact with both phases to varying degrees, leading to different migration rates through the column. These differences in interaction result in the separation of the compounds as they elute at various times, known as retention times, which can be detected and quantified [43].
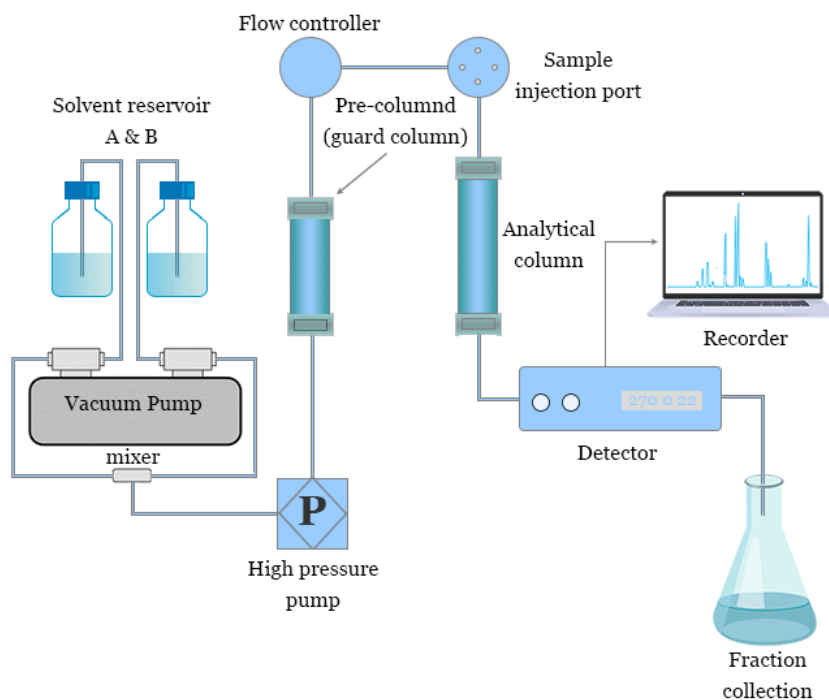
Fig.3.25. *The schematic diagram of the High-Performance Liquid Chromatography (HPLC) analyser. This figure is adapted from [44].*

High-Performance Liquid Chromatography (HPLC) instrumentation consists of several key components working in tandem to achieve the separation, identification, and quantification of analytes. The system begins with solvent reservoirs holding the mobile phase solvents, delivered at a precise and consistent flow rate by a high-pressure pump. The sample is introduced into the mobile phase stream through an injector, which can be manual or automated, allowing precise sample volumes to enter the system. The mobile phase carrying the sample then passes through the column, the core of the HPLC system, packed with a stationary phase material. The stationary phase, typically composed of silica particles with specific chemical modifications, facilitates the separation of compounds based on their interactions with the stationary and mobile phases. As the separated compounds elute from the column, they are detected by a sensitive detector, such as a UV-Vis absorbance detector, fluorescence detector, or mass spectrometer. The detector's signal is processed by a data system, which records the data and generates a chromatogram. The chromatogram displays retention times and peak areas, enabling the qualitative and quantitative analysis of the sample components. This integrated setup allows HPLC to provide precise and reliable analytical results. The schematic representation of the HPLC analyser is shown in Fig.3.25 [45].

Detection of Intermediates in the Degradation Reaction:

High-Performance Liquid Chromatography (HPLC) plays a vital role in detecting intermediate products during the catalytic degradation of pollutants in water remediation. This process begins with collecting and preparing water samples at various intervals during the degradation reaction. The samples are injected into the HPLC system, where they undergo chromatographic separation in a column designed to optimise the resolution of intermediate compounds based on their distinct chemical properties. As the separated intermediates elute from the column, they are detected by sensitive detectors such as UV-visible absorbance, fluorescence, or mass spectrometry, providing qualitative and quantitative data. The resulting chromatograms display peaks corresponding to the intermediates, whose identities and concentrations are determined by comparing retention times and spectral data with known standards. This detailed analysis enables researchers to elucidate degradation pathways, optimise catalytic conditions, and ensure the formation of non-toxic byproducts, thereby validating the efficacy and safety of the water remediation process [46].

In this research, various intermediates of the degradation reactions are identified using HPLC analysis. These include the sonocatalytic degradation of Congo Red in Chapter 5, the photocatalytic degradation of Ciprofloxacin and Tetracycline Hydrochloride in Chapter 6, and the sonophotocatalytic degradation of Rhodamine B in Chapter 7. Detailed analyses of the degradation reactions are also included in the respective chapters.

Fig.3.26. The image of High-Performance Liquid Chromatography analyser- Agilent 6100 Series Quadrupole LC / MS systems- CSIF, University of Calicut.

Specifications of the instrument used for the characterisation:

- Model   : **Agilent 6100 Series Quadrupole LC / MS systems**

    CSIF, University of Calicut.

- Mass range   : m/z 10–1500

- Mass accuracy   : ± 0.13 u within the calibrated mass range in scan mode

- Scan Speed   : 2500 u/s

3.9. TOTAL ORGANIC CARBON ANALYSER.

The Total Organic Carbon (TOC) analyser measures the amount of organic carbon in a water sample by oxidising the organic compounds to carbon dioxide (CO_2), which is then quantified. The process involves the conversion of all organic carbon present in the sample to CO_2, which is measured using various detection methods such as infrared (IR) detection or conductivity measurement. The principle relies on the difference between the total carbon (TC) and inorganic carbon (IC) in the sample, where TOC = TC – IC [47].

A Total Organic Carbon (TOC) analyser consists of a sample injection system, an oxidation reactor, an acidification unit, a gas-liquid separator, a detector, and a data processing unit. In operation, a water sample is injected and acidified to convert inorganic carbonates to CO_2, which is removed by sparging with an inert gas. The remaining organic carbon in the sample is then oxidised in the reactor via high-temperature combustion with a catalyst or UV light with a chemical oxidant. The CO_2 gas is separated from the liquid and measured by the detector, commonly using non-dispersive infrared (NDIR) detection or conductivity measurement. The data processing unit calculates the TOC concentration by analysing the detector signals and displays the result [48]. The schematic diagram of TOC analyser is shown in Fig.3.27.
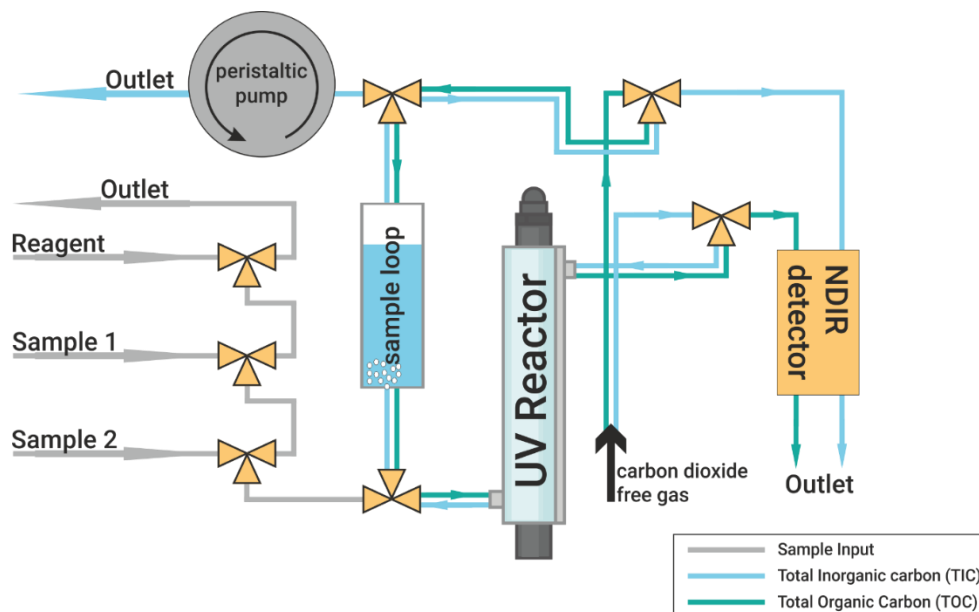
Fig.3.27. *The schematic diagram of the TOC analyser. This figure is adapted from [49].*

TOC analysis is conducted throughout this thesis, which focuses primarily on water remediation applications. Water samples are analysed using a Shimadzu TOC-L CPH Analyzer to estimate total organic carbon concentration before and after the catalytic reactions. During catalytic degradation, pollutants decompose into intermediate compounds and eventually CO_2 and H_2O. However, organic pollutants may not completely decompose into water; some intermediates form less complex organic molecules, which are less polluting. We can estimate the percentage of mineralisation achieved by measuring the TOC value of the water sample. Each section calculates and presents the mineralisation percentages for all catalytic processes. Detailed TOC analysis is included in Chapters 4, 5, 6, and 7.

Fig.3.28. *The image of Total Organic Carbon analyser-Shimadzu TOC-L CPH- Department of Chemical Engineering, NIT Calicut. The figure is adapted from [50].*

Specifications of the instrument used for the characterisation:

- Model   : **Shimadzu TOC-L CPH**

    Department of Chemical Engineering, NIT Calicut.

- Measurement method : 680°C catalytic combustion oxidation – non-dispersive

    infrared detection (NDIR) method.

- Measurement items   : TO, IC, TOC, NPOC (Optional: POC, TN)

- Measurement range TC: TC 0 to 30,000 mg/L.

3.10. CATALYTIC REACTOR

A catalytic reactor is a specialised setup designed for conducting catalytic degradation experiments. The catalytic reactions in this research are mainly focused on sonocatalysis, photocatalysis and sonophotocatalysis. Thus, a brief description of the various catalytic reactor used in this study is described below.

3.10.1. Sonocatalytic reactor

The sonocatalytic reactor used in this work is primarily an ultrasonicator, a device that uses high-frequency sound waves (ultrasound) to agitate particles in a solution. It is widely used in various scientific and industrial applications for cleaning, mixing, and accelerating chemical reactions. An ultrasonicator consists of an ultrasonic generator, a transducer, and an ultrasonic probe or bath, with a control panel for setting parameters like frequency, power, and duration. The generator converts electrical energy into high-frequency sound waves, which the transducer, typically made of piezoelectric materials, transforms into mechanical vibrations. These vibrations are transmitted to the probe or bath, where they are applied to the sample. In this work, we used a GT Sonic ultrasonic cleaner for the sonocatalytic reaction, which produces ultrasonic sound waves at a frequency of 40 kHz. The temperature of the water bath can also be controlled. The sonicator can produce ultrasonic sound waves in three different modes. The image of the GT Sonic ultrasonic cleaner is shown in Fig.3.29.

Fig.3.29. *The image of GT Sonic cleaner- sonocatalytic reactor – Laboratory for Mesoscopic Science and Devices, Department of Physics, University of Calicut.*

3.10.2. Photoreactor

The photoreactor used in this work is equipped with a Xenon arc lamp designed to replicate the solar spectrum for photocatalytic experiments. This setup includes a light source, typically a 300 W Xenon arc lamp, which emits a broad spectrum of light similar to natural sunlight. The photoreactor also features a cooling system to maintain optimal temperatures during experiments and a magnetic stirrer to thoroughly mix the reaction solution. The Xe arc lamp provides a controlled and intense light source, allowing precise studies of photocatalytic activity. The detailed spectrum of the Xenon arc lamp used in our experiments is shown in Fig.3.30, and the experimental setup is illustrated in Fig.3.31. This photoreactor setup ensures consistent and reliable results for photocatalytic performance evaluations.
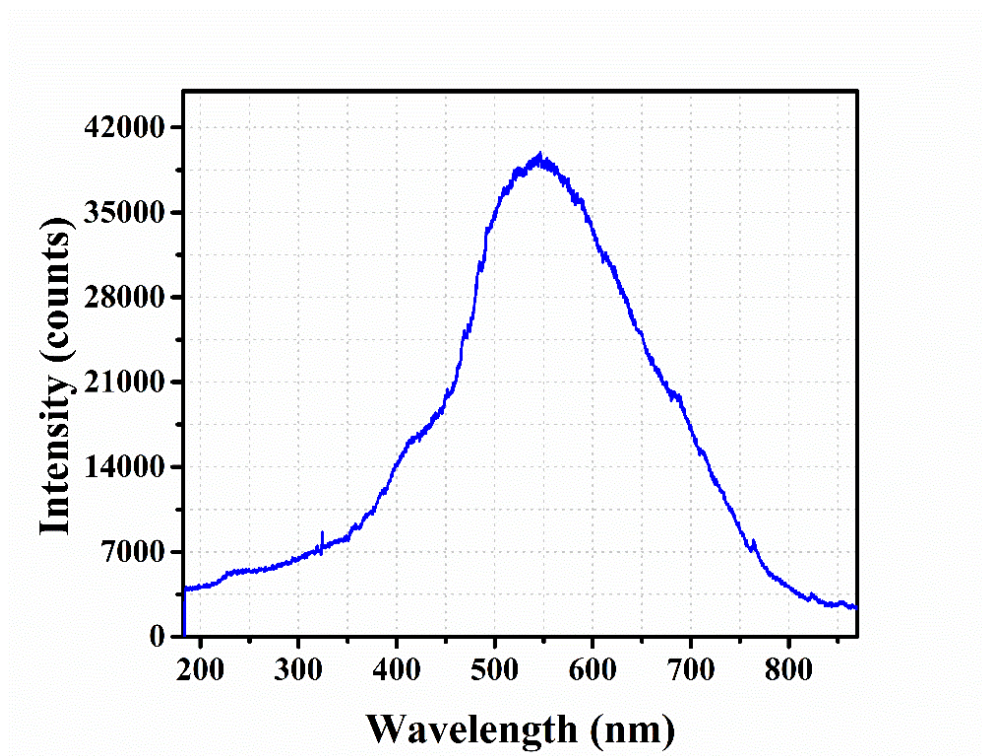
Fig.3.30. *The intensity spectra of Xe-arc lamp used in this research.*

Fig.3.31. *The photoreactor setup with Xe arc lamp source- Laboratory for Mesoscopic Science and Devices Department of Physics, University of Calicut.*

3.10.3. Sonophotoreactor

In the sonophotocatalytic process, ultrasound and visible light are simultaneously irradiated into the reaction medium. To achieve this, we combined an Xe arc lamp photoreactor with a GT ultrasonicator, allowing for the concurrent irradiation of light and sound. This combined setup, termed a sonophotoreactor, can perform sonophotocatalytic reactions. The image of sonophotocatalytic reactor is shown in Fig.3.32.

Fig.3.32. *The image of sonophotocatalystic reactor-Laboratory for Mesoscopic Science and Devices, Department of Physics, University of Calicut.*

3.11. CONCLUSION

In conclusion, the chapter on 'Experimental Techniques' has comprehensively outlined the various synthesis methods and characterisation techniques employed in this study. Detailed descriptions of the synthesis processes, including traditional and advanced methods, have been provided to provide a thorough understanding of the material preparation. The characterisation techniques, ranging from structural and morphological analysis to optical and electronic property measurements, have been meticulously discussed. These techniques are crucial for accurately assessing and understanding the synthesised materials. By integrating these methodologies, the study ensures a robust framework for systematically investigating the materials, thereby laying a solid foundation for the subsequent research findings presented in this thesis.

3.12. REFERENCES.

[1]   Brown, M. E., Dollimore, D., & Galwey, A. K. (Eds.). (1980). *Reactions in the solid state*. Elsevier.

[2]   Cohn, G. (1948). Reactions in the solid state. *Chemical Reviews*, *42*(3), 527-579.

[3]   Kumar, A., Dutta, S., Kim, S., Kwon, T., Patil, S. S., Kumari, N., ... & Lee, I. S. (2022). Solid-state reaction synthesis of nanoscale materials: strategies and applications. *Chemical Reviews*, *122*(15), 12748-12863.

[4]   Wang, L., Xu, J. B., Gao, B., Chang, A. M., Chen, J., Bian, L., & Song, C. Y. (2013). Synthesis of $BiFeO_3$ nanoparticles by a low-heating temperature solid-state precursor method. *Materials Research Bulletin*, *48*(2), 383-388.

[5]   Gan, Y. X., Jayatissa, A. H., Yu, Z., Chen, X., & Li, M. (2020). Hydrothermal synthesis of nanomaterials. *Journal of Nanomaterials*, *2020*. DOI:10.1155/2020/8917013

[6]   Singh, A. K., Pandey, S. K., Vishwakarma, P. K., Pratap, R., Verma, R., Pandey, A., ... & Srivastava, A. (2023). Catalyst-free biphasic orthorhombic/hexagonal tungsten oxide system with enhanced photocatalytic response under visible light. *Oxford Open Materials Science*, *3*(1), itad009.

[7]   Petcharoen, K., & Sirivat, A. J. M. S. (2012). Synthesis and characterisation of magnetite nanoparticles via the chemical co-precipitation method. *Materials Science and Engineering: B*, *177*(5), 421-427.

[8]   Ba-Abbad, M. M., Benamour, A., Ewis, D., Mohammad, A. W., & Mahmoudi, E. (2022). Synthesis of Fe3O4 nanoparticles with different shapes through a co-precipitation method and their application. *Jom*, *74*(9), 3531-3539.

[9]   Bhandari, H., Ruhi, G., Gaba, R., Chaudhary, A., Johar, R., Singh, T., ... & Chadha, Y. (2020). Eco-friendly magnetic biopolymer nanocomposites for removal of organic dye/heavy metals from waste water. *Vantage: J. Themat. Anal*, *1*, 17-31.

[10]   Cullity, B. D., & Smoluchowski, R. (1957). Elements of X-ray Diffraction. *Physics Today*, *10*(3), 50-50.

[11]   Britannica, The Editors of Encyclopaedia. "X-ray diffraction". Encyclopedia Britannica, 31 Mar. 2023, https://www.britannica.com/science/X-ray-diffraction. Accessed 14 July 2024.

[12]   Chatterjee, S. K. (2010). *X-ray diffraction: Its theory and applications*. PHI Learning Pvt. Ltd.

[13]   Termtanun, Mutsee. (2013). Photocatalytic degradation of pesticides using TiO2 nanoparticles. PhD thesis, University of Nottingham, Access from the University of Nottingham repository: http://eprints.nottingham.ac.uk/13827/2/Thesis_MUTSEE2.pdf

[14]   Patterson, A. L. (1939). The Scherrer formula for X-ray particle size determination. *Physical review*, *56*(10), 978.

[15]   McCreery, R. L. (2005). *Raman spectroscopy for chemical analysis*. John Wiley & Sons.

[16]   https://www.edinst.com/blog/what-is-raman-spectroscopy/

[17]   Jimenez-Sandoval, S. (2000). Micro-Raman spectroscopy: a powerful technique for materials research. *Microelectronics Journal*, *31*(6), 419-427.

[18]   Bonales, L. J., Elorrieta, J. M., Lobato, Á., & Cobos, J. (2016). Raman spectroscopy, a useful tool to study nuclear materials. *Applications of Molecular spectroscopy to current research in the chemical and biological sciences*.

[19]   Mohan, V. B., Jayaraman, K., & Bhattacharyya, D. (2020). Brunauer–Emmett–Teller (BET) specific surface area analysis of different graphene materials: a comparison to their structural regularity and electrical properties. *Solid State Communications*, *320*, 114004.

[20]   Brame, J. A., & Griggs, C. S. (2016). Surface area analysis using the Brunauer-Emmett-Teller (BET) method: scientific operation procedure series: SOP-C.

[21]   Villarroel-Rocha, J., Barrera, D., & Sapag, K. (2014). Introducing a self-consistent test and the corresponding modification in the Barrett, Joyner and Halenda method for pore-size determination. *Microporous and Mesoporous Materials*, *200*, 68-78.

[22]   Králik, M. (2014). Adsorption, chemisorption, and catalysis. *Chemical Papers*, *68*(12), 1625-1638.

[23]   Niwa, M., & Katada, N. (2013). New method for the temperature-programmed desorption (TPD) of ammonia experiment for characterisation of zeolite acidity: a review. *The Chemical Record*, *13*(5), 432-455.

[24]   Zhou, W., Apkarian, R., Wang, Z. L., & Joy, D. (2007). Fundamentals of scanning electron microscopy (SEM). *Scanning microscopy for nanotechnology: techniques and applications*, 1-40.

[25]   Ali, A. S. (2020). Application of nanomaterials in environmental improvement. *Nanotechnology and the Environment*, 17-36.

[26]   Kaech, A. (2013). An introduction to electron microscopy instrumentation, imaging and preparation. *Center for Microscopy and Image Analysis, University of Zurich*.

[27] Perkampus, H. H. (2013). *UV-VIS Spectroscopy and its Applications*. Springer Science & Business Media.

[28] Swinehart, D. F. (1962). The beer-lambert law. *Journal of chemical education*, *39*(7), 333.

[29] Rocha, F. S., Gomes, A. J., Lunardi, C. N., Kaliaguine, S., & Patience, G. S. (2018). Experimental methods in chemical engineering: Ultraviolet visible spectroscopy—UV-Vis. *The Canadian Journal of Chemical Engineering*, *96*(12), 2512-2517.

[30] Passos, M. L., & Saraiva, M. L. M. (2019). Detection in UV-visible spectrophotometry: Detectors, detection systems, and detection strategies. *Measurement*, *135*, 896-904.

[31] Dehghani, M. H., Zarei, A., & Yousefi, M. (2019). Efficiency of ultrasound for degradation of an anionic surfactant from water: Surfactant determination using methylene blue active substances method. *MethodsX*, *6*, 805-814.

[32] Ribeiro, M. F., Couto, C. M., Conceicao, P. M., & Santos, J. L. (2013). An automated multi-pumping pulsed flow system with spectrophotometric detection for the determination of phosphate in natural waters. *Analytical Letters*, *46*(11), 1769-1778.

[33] Blitz, J. P. (1998). Diffuse reflectance spectroscopy. *Modern techniques in applied molecular spectroscopy*, *14*, 185-219.

[34] Jiulong, S. (2014). *Development of Inorganic-Organic Hybrid Materials for Waste Water Treatment* , Doctoral dissertation, National University of Singapore (Singapore).

[35] Murphy, A. B. (2006). Modified Kubelka–Munk model for calculation of the reflectance of coatings with optically-rough surfaces. *Journal of Physics D: Applied Physics*, *39*(16), 3571.

[36] Colthup, N. (2012). *Introduction to infrared and Raman spectroscopy*. Elsevier.

[37] Li, Q., Anpo, M., You, J., Yan, T., & Wang, X. (2023). Photoluminescence (PL) Spectroscopy. In *Springer Handbook of Advanced Catalyst Characterization* (pp. 295-321). Cham: Springer International Publishing.

[38] Fornaguera, C., & Solans, C. (2018). Analytical methods to characterise and purify polymeric nanoparticles. *International Journal of Polymer Science*, *2018*(1), 6387826.

[39] https://www.horiba.com/int/scientific/products/detail/action/show/Product/fluoromax-1576/

[40] Bintu Thomas (2020), Surface modified magnetic nanoparticles for photocatalytic applications, Doctoral Thesis, University of Calicut

[41]   Makhdoom, Atif. (2018). Low Temperature Processing Route of Silicon Nanoparticle Layers for Solar Cell Application. Doctoral thesis,

[42]   https://www.torontomu.ca/analytical-centre/instrumentation/spectroscopy/

[43]   Belanger, J. M., Paré, J. J., & Sigouin, M. (1997). High performance liquid chromatography (HPLC): principles and applications. In *Techniques and instrumentation in analytical chemistry* (Vol. 18, pp. 37-59). Elsevier.

[44]   Lozano-Sánchez, J., Borrás-Linares, I., Sass-Kiss, A., & Segura-Carretero, A. (2018). Chromatographic technique: high-performance liquid chromatography (HPLC). In *Modern techniques for food authentication* (pp. 459-526). Academic Press.

[45]   Lozano-Sánchez, J., Borrás-Linares, I., Sass-Kiss, A., & Segura-Carretero, A. (2018). Chromatographic technique: high-performance liquid chromatography (HPLC). In *Modern techniques for food authentication* (pp. 459-526). Academic Press.

[46]   Vaněrková, D., Sakalis, A., Holčapek, M., Jandera, P., & Voulgaropoulos, A. (2006). Analysis of electrochemical degradation products of sulphonated azo dyes using high-performance liquid chromatography/tandem mass spectrometry. *Rapid Communications in Mass Spectrometry: An International Journal Devoted to the Rapid Dissemination of Up-to-the-Minute Research in Mass Spectrometry*, *20*(19), 2807-2815.

[47]   Shetty, A., & Goyal, A. (2022). Total organic carbon analysis in water–A review of current methods. *Materials Today: Proceedings*, *65*, 3881-3886.

[48]   Visco, G., Campanella, L., & Nobili, V. (2005). Organic carbons and TOC in waters: an overview of the international norm for its measurements. *Microchemical journal*, *79*(1-2), 185-191.

[49]   https://membrapure.de/toc-analyzers/unitoc/

[50]   https://www.swanenviron.com/water-laboratory-total-organic-carbon-analyzer.html

CHAPTER 4

Adsorptive Removal and Decomposition of Sodium Dodecyl Sulfate using CuS Nanoflower
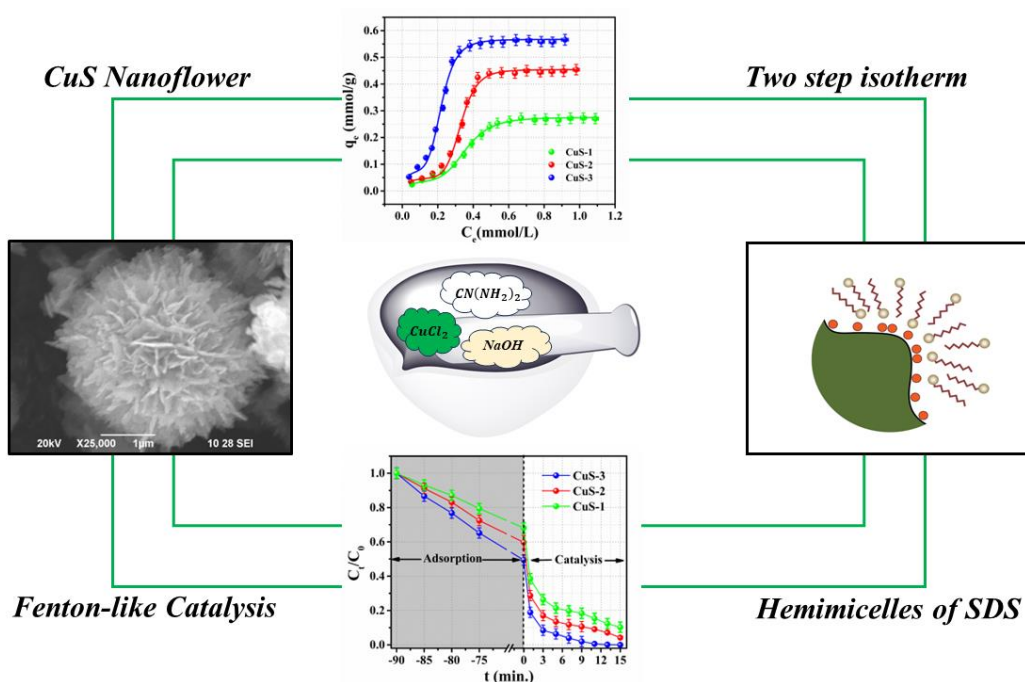
Highlights

> ➤ *We combined the adsorption and Fenton-like catalytic activity of CuS for the complete removal of SDS from wastewater.*

> ➤ *Firstly, we report the metal chalcogenides used for the removal of surfactants.*

> ➤ *Enhanced adsorption of SDS on CuS nanostructures could be explained using the hemimicellization phenomenon.*

> ➤ *Establishing kinetic, thermodynamic and catalytic studies of SDS and CuS.*

ABSTRACT

The untreated surfactant in industrial effluents is a burgeoning environmental concern. This study demonstrates that CuS nanoflowers are highly effective as both adsorbents and catalysts for removing and decomposing sodium dodecyl sulfate (SDS) in water. The efficient decomposition of surfactants from effluents can be achieved through adsorption and advanced oxidation process. The fast catalytic decomposition of SDS into CO_2 and water is demonstrated to be led by (i) hemi-micelle driven enhanced adsorption (maximum adsorption capacity of 0.56 ± 0.02 mmol/g) and (ii) synergetic action of H_2O_2. The mechanism of surfactant adsorption on CuS nanoflowers is understood through the Dubinin-Radushkevich, Fowler-Guggenheim, Sips, Hill, and two-step adsorption isotherm models. Pseudo-first-order kinetics and intraparticle diffusion mechanism govern the adsorption kinetics. The adsorption thermodynamics is endothermic and enthalpy-driven. The catalytic activity is approximated to a Fenton-like process-a rarity in chalcogenides. Industrially scalable, energy-efficient catalytic remediation of surfactants using copper chalcogenides holds vast significance for industrial effluent treatment.

Keywords*: catalytic degradation; surfactant; adsorption; hemi-micellization; Fenton process.*

4.1. INTRODUCTION

Surface active agents, or surfactants, are the active components in detergents and cleaning products for household and industrial applications [1]. Globally, the production of surfactants is growing because of the increasing areas of industrial application. Surfactants are widely used in the agrochemical, pharmaceutical, oil, paper, mining, and textile industries [2,3]. It is a major organic pollutant with a very high potential to affect the ecosystem via effluent discharges from industries [4]. The quantity discharged from large-scale industrial units varies depending on the pollution regulations of the region. Degradation products of surfactants can build up in the body, causing irreversible pathological consequences [5]. It delays carcinogen breakdown and limits oxygen intake and nitrification [6]. For commercial reasons, replacing those low-biodegradable surfactants in all household and industrial applications is impractical. Therefore, it is necessary to develop pre-treatment methods for surfactant effluent that allow for the secure application of low-biodegradable surfactants [3]. Sodium Dodecyl Sulfate (SDS) is a low-biodegradable anionic surfactant component of detergents and associated products. Even below the toxic level, the presence of SDS in the water can lead to biochemical alterations in aquatic life [7]. Moreover, the low biodegradability of SDS makes its impact long-lasting [8].

Removing surfactants from wastewater is a significant problem at the industrial level [9]. Because conventional physiochemical and biological treatment methods produce foam beds in water treatment plants, they are difficult to remove from wastewater [10]. Proposed techniques for removing SDS from wastewater include reverse osmosis, chemical oxidation, coagulation, biological degradation methods, membrane separations, and adsorption [11]. Adsorption has drawn wide attention as a technologically promising research topic for eliminating organic and inorganic wastewater contaminants [12]. Thus, removing surfactants from wastewater can be employed through adsorption and is considered a popular, straightforward, inexpensive, and cost-effective strategy.

Management of the exhausted adsorbent material and the adsorbed pollutant is a crucial environmental concern with attached commercial implications. The improper disposal of exhausted adsorbent material may result in a more extensive ecological hazard. In addition, the reuse of the absorbent is also limited. To win this conflict, we must consider not only filtering out contaminants but also degrading them- keeping the

adsorbent ready for reuse. The advanced oxidation process (AOP) is a reliable technique for degrading organic contaminants, including disintegrating surfactant molecules [13,14]. Therefore, the attempt is to incorporate advanced oxidative decomposition and adsorption within the same material to remove pollutants effectively from the effluent water.

Nowadays, transition metal sulfides are employed for the catalytic decomposition of organic pollutants present in wastewater [15]. A detailed account of the metal chalcogenides was provided in Chapter 1, section 1.7. Among the inorganic metal chalcogenides, CuS is reported as one of the most attractive catalysts - especially as a functional component in nanocomposites. CuS is recognized as a crucial p-type semiconductor owing to its versatility, availability, and non-toxic nature [16]. Recent studies reveal that reducing the size of CuS to the nanoscale induces substantial changes in its physical and chemical properties. Consequently, significant efforts have been directed towards creating nanostructured copper sulfides with diverse sizes, shapes, and morphologies. The morphology of the CuS plays a vital role in the adsorption and catalytic processes [17].

Herein, we report a quick, simple, and efficient solid-state route for synthesizing CuS nanoflowers at room temperature. These CuS nanostructures can be utilized to remove SDS from water efficiently. In this chapter, we propose an adsorption mechanism for the enhanced adsorption activity of the CuS nanostructure. The paradoxical situation of having an adsorption capacity comparable to activated carbon but a low surface area suggested by BET analysis made the elucidation of the adsorption mechanism interesting.

Moreover, the CuS nanostructures exhibit high efficiency in degrading SDS as a Fenton-like catalyst, capable of rapidly catalyzing H_2O_2 to decompose SDS. Consequently, effluents from industries containing a high concentration of SDS, contributing to water contamination, can be effectively removed and degraded by using CuS as a catalytic adsorbent. We now report, for the first time, the direct catalytic SDS degradation of CuS in the dark.

Furthermore, this work introduces a nature-abundant and environmentally friendly nanomaterials for efficiently removing surfactants from industrial effluents. In contrast to other adsorbents, this study proposes a chalcogenide capable of completely

decomposing surfactants. The enhanced adsorption is attributed to hemimicellization and morphology, with the distinctive feature being the complete breakdown of surfactants through Fenton-like catalytic activity.

4.2. EXPERIMENTAL

4.2.1. Reagents and chemicals

The analytical reagents used for this study were Copper chloride dihydrate $(CuCl_2.2H_2O \geq 98\%$ Avra), Sodium hydroxide $(NaOH, \geq 98\%$ Qualigen), Thiourea $(CH_4N_2S \geq 98\%$ Avra), Sodium Dodecyl Sulfate $(NaC_{12}H_{25}SO_4 \geq 96\%$ *Spectrochem*), and Hydrogen peroxide $(H_2O_2, 30\%$ *Merk*) . Deionized water was used as a solvent in all synthesis and adsorption experiments.

4.2.2. Synthesis of CuS nanoflower

CuS nanostructures were synthesized at room temperature via a simple solid-state reaction route using $CuCl_2.2H_2O$, thiourea, and NaOH as starting materials [18]. CuCl.2H₂O was evenly mixed with thiourea in the molar ratio of 1:2 by grinding in an agate mortar for 2 minutes. Then, 4 mmol NaOH was added to the mortar, and another grinding process was operated for another 2 minutes. The resulting black mash was collected and settled in water for half an hour. Then, the precipitate was filtered and washed with deionized water and absolute ethanol several times. The powder was dried at 60 °C in a vacuum oven; dark green powders were obtained. Three different samples were prepared by changing the reaction time to 5 and 10 minutes; we denoted these three samples as CuS-1, CuS-2 and CuS-3, respectively, for the reaction times 2,5 and 10 minutes. The schematic representation of the synthesis of CuS nanoflower is shown in Fig.4.1.
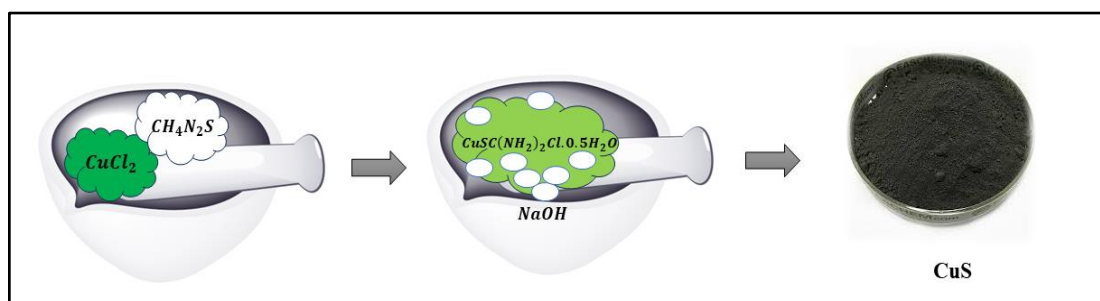
Fig.4.1. *Schematic representation of synthesis of CuS nanomaterials using solid-state reaction route.*

The reaction process is described in the following reactions:

Step 1. Reactions during the first grinding step:

$$2CuCl_2.2H_2O + 2CH_4N_2S \rightarrow [CuSC(NH_2)_2].0.5H_2O \dots\dots (4.1)$$
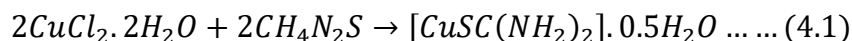
Step 2. Reaction occurred after adding NaOH into the ground mixture:

$$4[CuSC(NH_2)_2].0.5H_2O + 4NaOH + O_2 + 4H_2O$$
$$\rightarrow 4CuS + 8NH_3 + 4H_2O + 4CO_2 + 4NaCl \dots\dots (4.2)$$
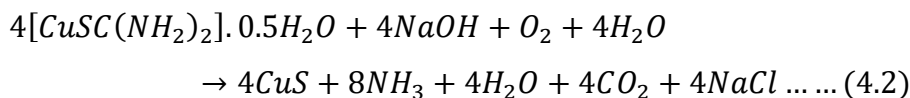
4.2.3. Adsorption experiments

As mentioned above, CuS nanostructures were used as the absorbent to remove SDS from water. Batch adsorption studies were conducted to examine the effect of initial concentrations of SDS on the adsorption process. The initial concentration of the SDS solution varies from 0.07 mmol/L (20 ppm) to 1.18 mmol/L (340 ppm), and the dosage of the adsorbent was 0.6 g/L. The initial and equilibrium concentrations of the SDS solutions were estimated by the Methylene Blue Active Substances (MBAS) method [19] using a UV-Vis spectrophotometer (JASO V-750). All experiments were conducted at a temperature of 303 K, under ambient atmospheric pressure, and at the inherent pH (7-8) of the SDS solution.

The amount of SDS adsorbed on the CuS surface at adsorption equilibrium (adsorption density, $q_e\ mmol/g$), can be calculated using the formula,

$$q_e = \frac{(C_0 - C_e)V}{m} \dots\dots (4.3)$$

where C_0 and C_e are the initial and residual concentration of the SDS solution in mmol/L, V is the volume of the SDS solution in L, and m is the weight of the adsorbent in g.

In the kinetic studies of adsorption, an aliquot was examined every 5 minutes using the previous method. The experiments were also conducted at different temperatures, ranging from 303 K to 333 K, to study the thermodynamics of adsorption. All kinetic and thermodynamic adsorption experiments were performed at 0.07 mmol/L (20 ppm) of SDS solution and the adsorbent dosage of 0.6 g/L.

4.2.4. Catalytic experiments

The catalytic activity of different as-synthesized CuS nanostructures was studied using SDS degradation. For a typical experiment, 60mg of catalyst is dispersed in 100 mL of 0.14 mmol/L (40 ppm) SDS solution. After the catalyst and SDS mixture were stirred for 60 minutes in the dark to achieve complete SDS adsorption and desorption on

the catalyst surface, 1 mL of H_2O_2 was added to the above catalyst and SDS mixed solution for the decomposition of SDS. The SDS solution was collected after predetermined intervals, and the Methylene Blue Active Substances (MBAS) method was used to determine the SDS concentration. [19]

The degree of mineralization in the SDS solution was assessed by measuring the oxygen equivalent of the organic matter in each sample, i.e., total organic carbon (TOC), using a Shimadzu TOC L-CPH Analyzer. The percentage of mineralization was calculated using a specific equation.

$$\% \ mineralization = \frac{TOC_0 - TOC_f}{TOC_0} \times 100 \ ... ... \ (4.4)$$

where TOC_0 and TOC_f refer to the initial and the final total organic carbon, respectively.

4.3. RESULTS AND DISCUSSION

4.3.1. Structural characterizations

The X-ray diffraction patterns of the synthesized samples are shown in Fig.4.2. The XRD pattern agrees with the reported hexagonal covellite phase of CuS (JCPDS Card 06-0464) [20]. The characteristic peaks of the samples are located at 2θ around $29.3^0, 31.8^0$, 47.9^0 and 59.3^0, which are attributed to the diffraction peaks from (102), (103), (110) and (116) planes respectively. The average crystalline size of the nanoparticle is calculated using the Scherer formula $D = K\lambda/\beta cos\theta$; where d is the crystallite size, K is dimensionless shape factor (here taken to be 0.94), λ is the wavelength of X-ray used and β is the full width at half maximum corresponding to the Bragg's angle. The average crystallite size was estimated to be $9.86 \pm 0.25 \ nm, \ 6.80 \pm 0.24 \ nm$ and 8.98 ± 0.42 nm for CuS-1, CuS-2, and CuS-3 samples, respectively.

Fig.4.3. Displays the Raman spectrum of CuS nanoparticles. The Raman peaks appear at about 468 cm^{-1} and 267 cm^{-1}. Among these two peaks, the strongest and characteristic peak of CuS at 468 cm^{-1} can be attributed to the stretching mode of vibration of the S-S bond (A$_{1g}$ symmetry), while the weak band at 267 cm^{-1} corresponds to vibration of the Cu-S bond (A$_{1g}$ TO mode) [21]. These bands are, according to the S2 groups, the acknowledged crystal structure of copper sulfide, and these peaks are associated with the covellite phase of CuS [21]. No pronounced impurity peaks can be observed in XRD patterns and Raman spectra, indicating the successful formation of

uniform and pure covellite phase of CuS nanoparticles under our experimental conditions.
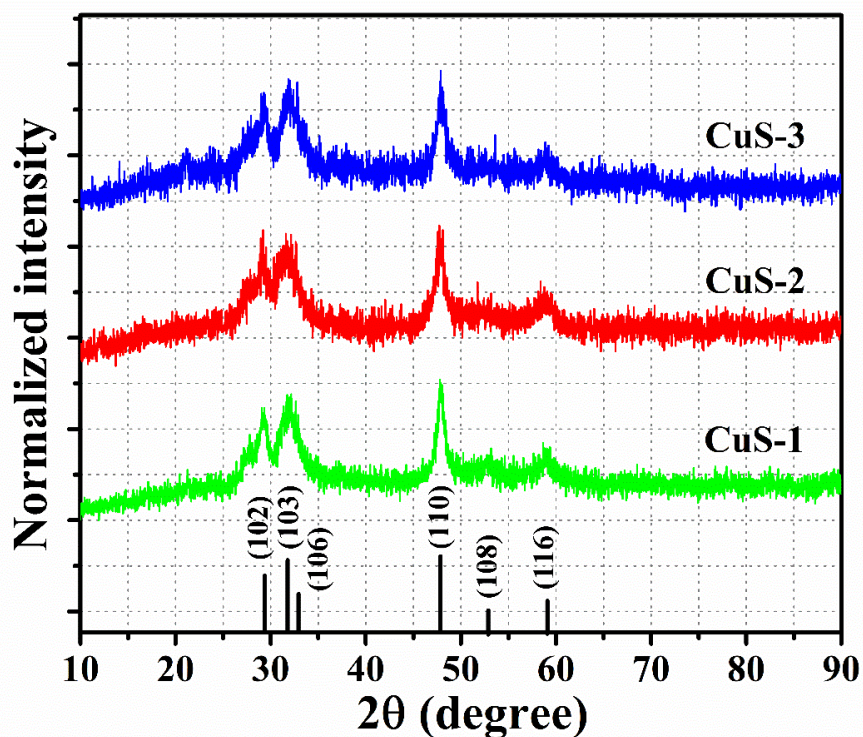
Fig.4.2. *The XRD patterns of the synthesized CuS nanostructures. XRD pattern agrees with the reported hexagonal covellite phase of CuS.*
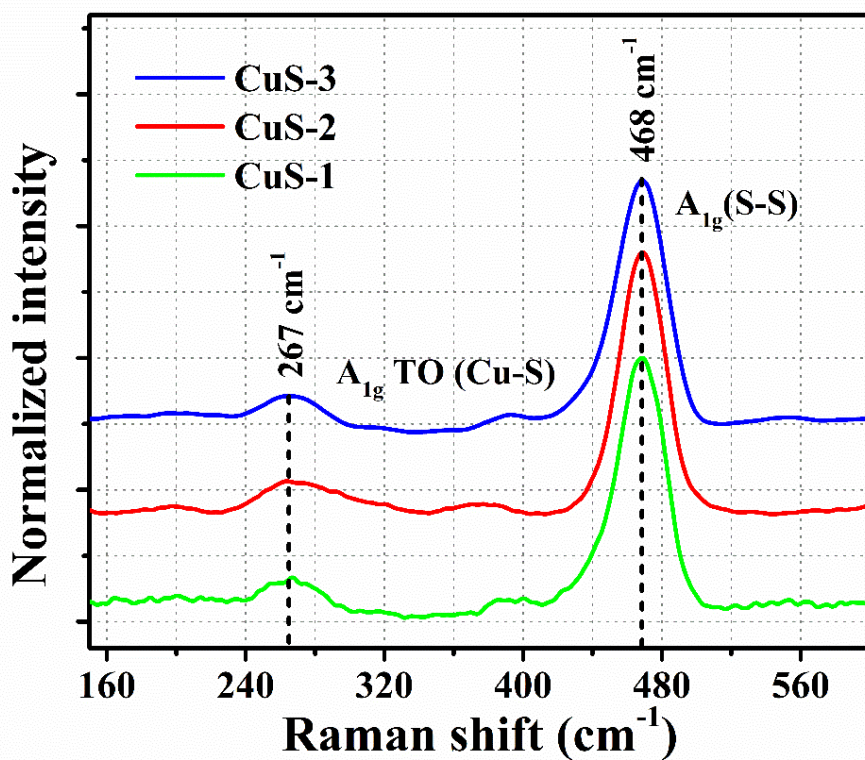
Fig.4.3. Raman spectra of the synthesized CuS nanostructures.

4.3.2. Morphological characterization

The morphology and shape of the adsorbent are significant in the field of adsorption. FE-SEM images of synthesized CuS nanostructures are shown in Fig.4.4, 4.5 and 4.6. Sample CuS-1 had a quick synthesis time, which prevented the proper nucleation of CuS particles, as shown in Fig.4.4, which shows an agglomerated CuS. Fig.4.5 depicts the shape of the CuS-2 nanostructure, which has enormous folds and resembles flower buds. The CuS-3 shows a flower-like morphology (Fig.4.6). Thus, the morphology of the synthesized samples alters with reaction time, evolving from a random form to a flower-like one.
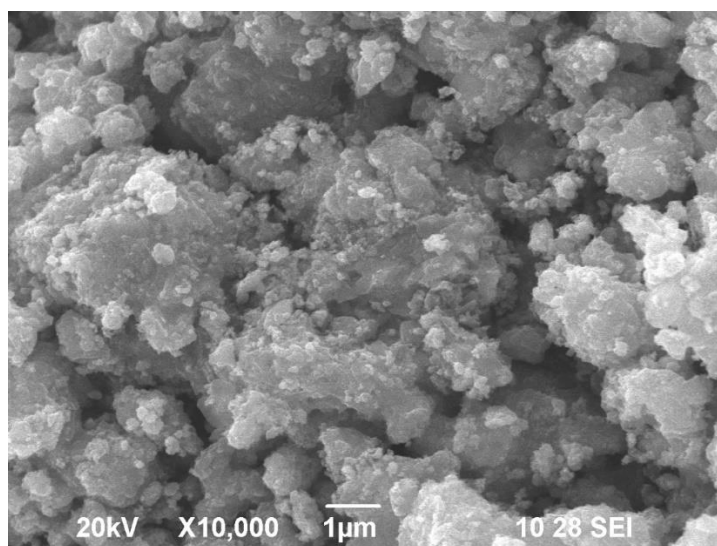
Fig.4.4. *The FESEM images of CuS-1, which shows an agglomerated structures.*
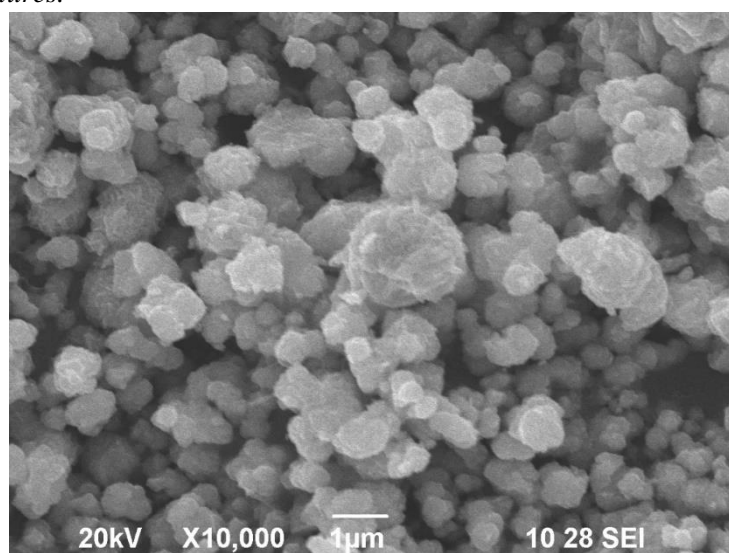
Fig.4.5. *The FESEM images of CuS-2, shows a flower bud like morpholohy.*
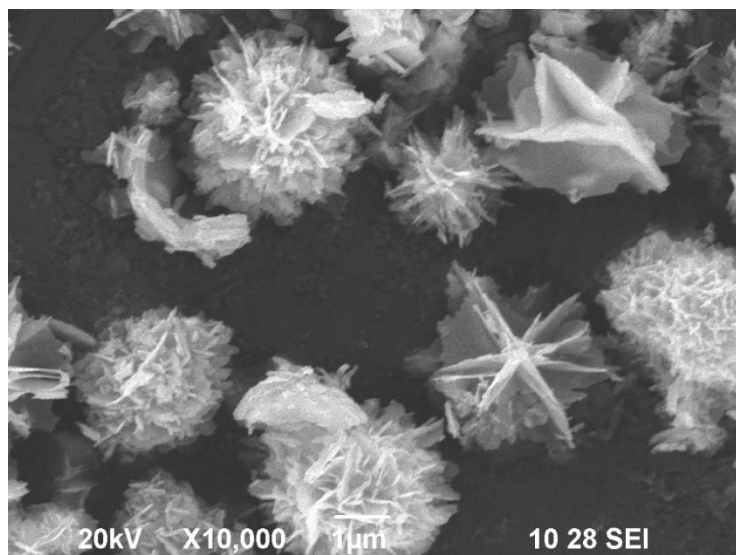
Fig.4.6. *The FESEM images of CuS-3, shows a flower-like morphology with many petals.*

4.3.3. Surface area and porosity analysis

Nitrogen gas adsorption-desorption isotherm measurements were carried out to gain insight into the surface features. Fig.4.7 shows the N_2 adsorption-desorption isotherms of CuS nanostructures closely match the type II isotherm with a type H3 hysteresis loop [22]. The H3-type hysteresis loop suggests slit-like pores in the samples.

The BJH pore distribution curve of the synthesized samples is shown in Fig.4.8. The pore distribution is almost the same in all synthesized samples and ranges from 1 nm to 50 nm in the BJH curve, indicating micro-meso pore formation in the synthesized CuS samples [23]. The porosity profile of synthesized samples was self-formed without any templating agents, including surfactants.

The specific surface area of the synthesized samples is estimated using the linear fit of the $P/V_a(P_0-P)$ versus P/P_0 data points, as shown in Fig. 4.9. The estimated specific surface area is found to be 9.36 ± 0.01 m^2/g 12.26 ± 0.02 m^2/g 19.04 ± 0.03 m^2/g for CuS-1, CuS-2, and CuS-3 respectively. It is worth mentioning that CuS-3 has a larger BET surface area than the other CuS nanostructures. Compared to other samples, the CuS-3 sample exhibits a more pronounced hysteresis loop of the isotherm, indicating capillary condensation of the N_2 gas on the sample
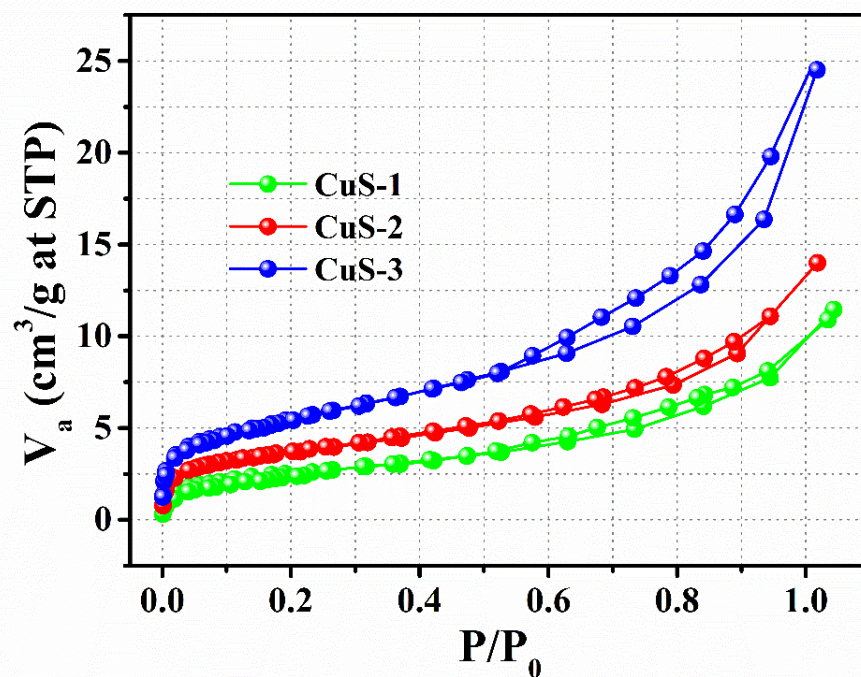
Fig.4.7. *N₂ Adsorption-desorption isotherms which closely match the type II isotherm (S-shaped isotherm) with a type H3 hysteresis loop.*
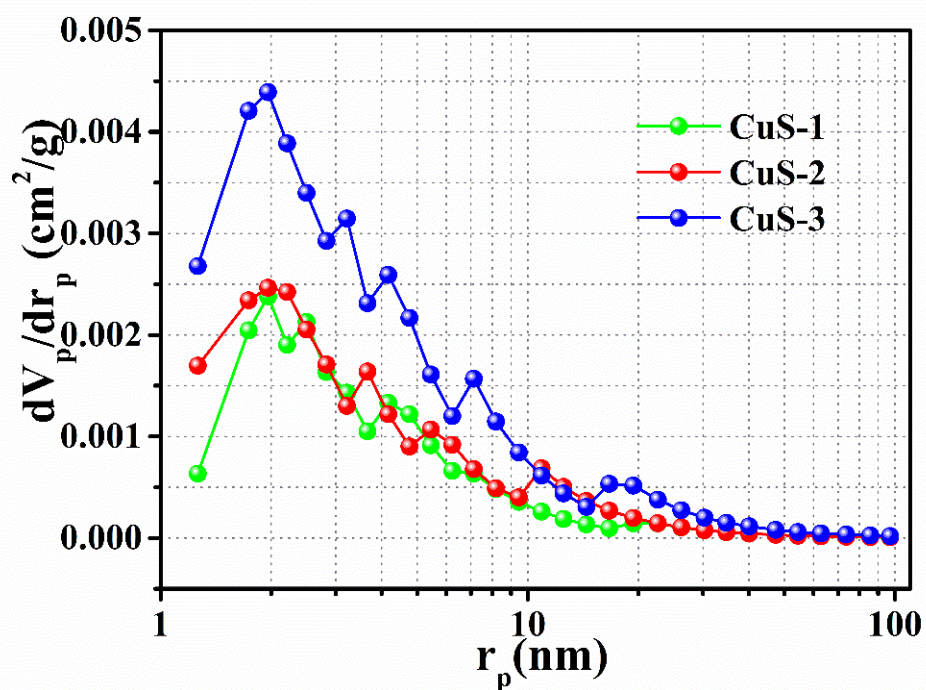
Fig.4.8. *The BJH pore distribution curve indicating the micro-meso pore formation was self-formed without any templating agents, including surfactants.*
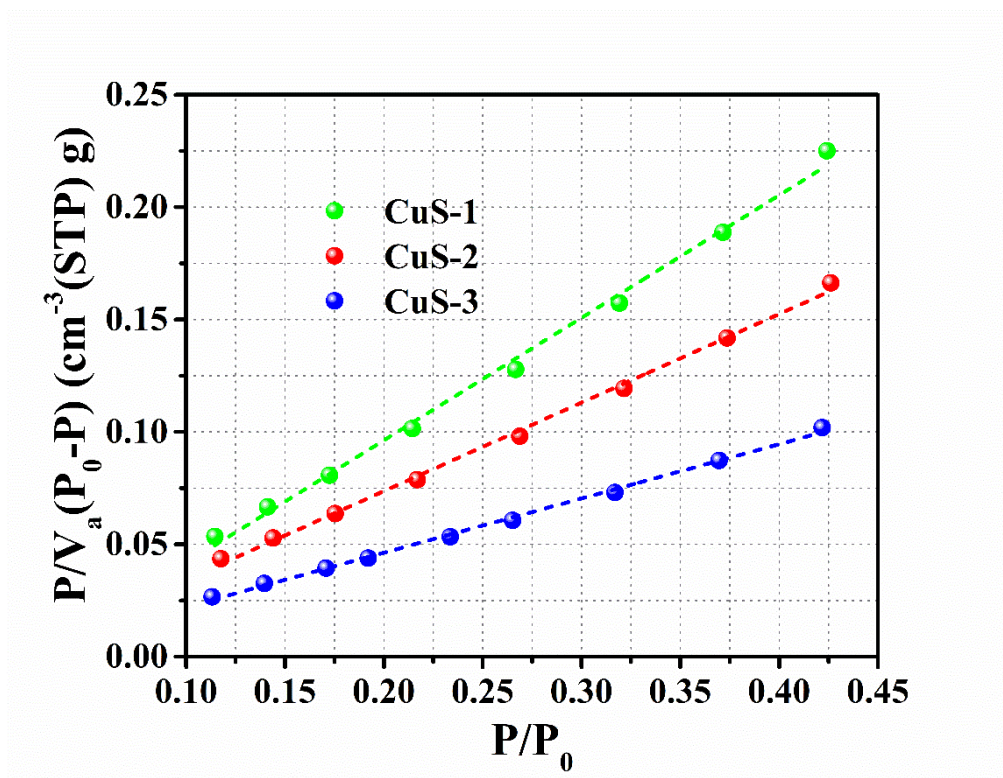
Fig.4.9. *The linear fit of P/V$_a$ (P$_0$-P) versus P/P$_0$ data points to estimate BET surface area.*

4.3.4. Adsorption isotherms

The adsorption properties of the synthesized CuS nanostructures were investigated using SDS as a pollutant. Fig.4.10. depicts the SDS adsorption isotherms on various CuS nanostructures. All isotherms are identical to the type V isotherm of the IUPAC classification [24]. At a high concentration, the adsorption density reaches a plateau called the maximum adsorption density. The maximum adsorption densities of the three nanostructures are estimated as 0.27 ± 0.01 mmol/g, 0.45 ± 0.01 mmol/g and 0.56 ± 0.02 mmol/g for CuS-1, CuS-2, and CuS-3 respectively. Thus, all the isotherms have sigmoid shapes and originated from forming multilayers of adsorbate molecules on the adsorbent surface. Notably, the isotherms do not follow the commonly reported Langmuir and Freundlich adsorption models. This kind of sigmoidal adsorption isotherm is often seen in the adsorption of surfactants at the interface between a solid and a liquid, and it is thought to be caused by lateral interactions between the adsorbed species [25].
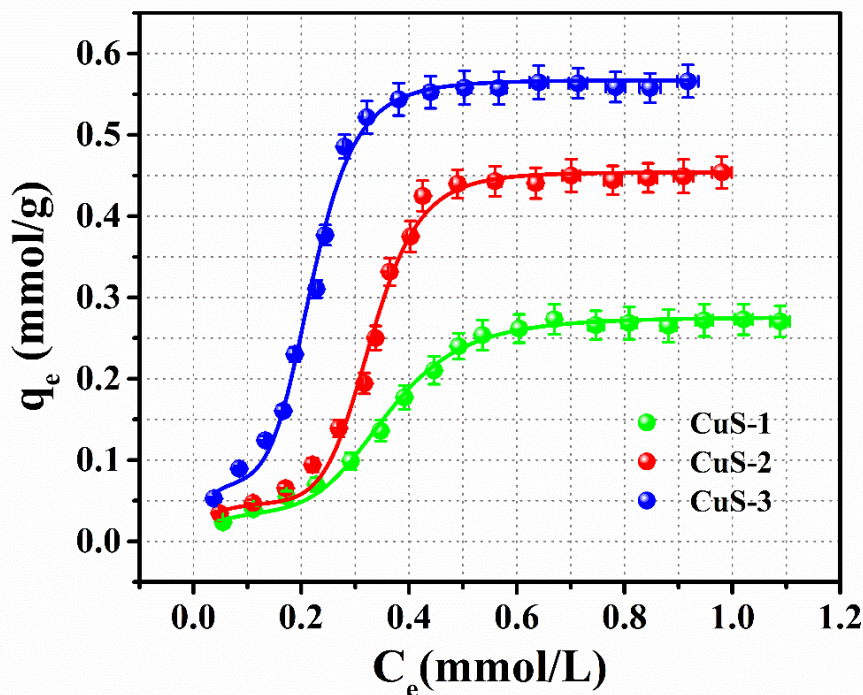
Fig.4.10. *Adsorption isotherms of SDS on CuS nanostructures. All isotherms are identical to the type V isotherm of the IUPAC classification.*

To examine the nature of adsorption as well as the interaction between the adsorbate and the adsorbent molecules at equilibrium, the adsorption data were tested using two isotherm models, *viz.* Dubinin–Radushkevich (D–R) and Fowler-Guggenheim (F-G) models. The linearized form of the D–R model is represented by equation (3) [26]:

$$\ln q_e = \ln q_{max} - \beta \varepsilon^2 \ldots \ldots (4.5)$$

where β is the Dubinin-Radushkevich constant, R is the universal gas constant ($8.314 \, JK^{-1}mol^{-1}$), T is the absolute temperature, and ε is Polanyi potential and is defined as $\varepsilon = RT \ln \left(1 + \frac{1}{C_e}\right)$. And the F-G model is represented by

$$\ln \left[\frac{C_e(1-\theta)}{\theta}\right] = -\ln K_{FG} + \frac{2\theta\omega}{RT} \ldots \ldots (4.5)$$

where K_{FG} is Fowler-Guggenheim equilibrium constant ($L/mmol$), θ is fractional coverage, and ω is interaction energy between adsorbed molecules $kJmol^{-1}$[27]. The isotherm models and their significance are thoroughly explained in Section 2.2.3 of Chapter 2.
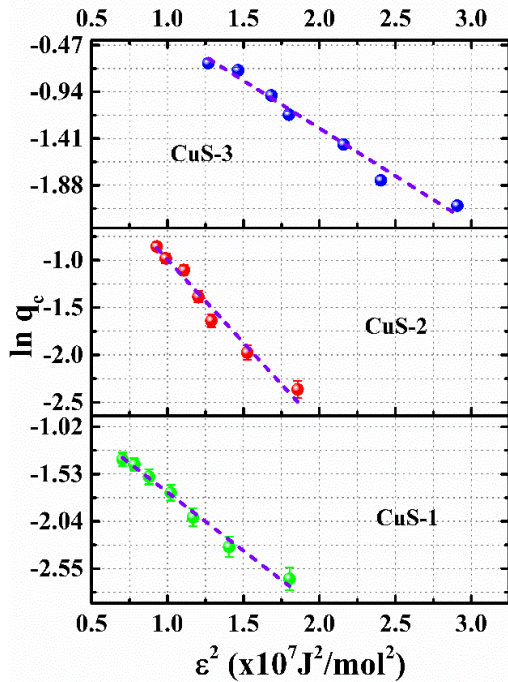
Fig.4.11. *Linear fit of D-R model.*   **Fig.4.12.** *Linear fit of F-G model.*
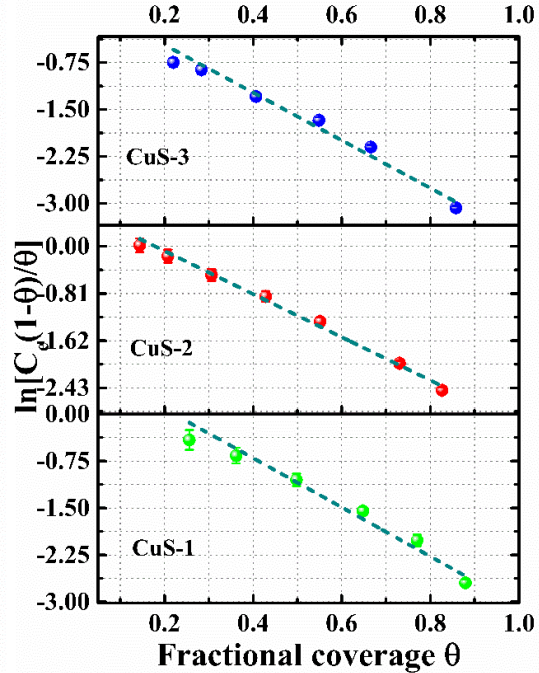
The adsorption isotherms are fitted to the D-R and F-G models, as shown in Fig.4.11. and 4.12. and the various parameters of the isotherm models are listed in Table.4.1. The mean free energy of adsorption (E), designated as the free energy change when 1 mole of SDS is transported to the surface of the solid from infinity in a solution, can be computed from the equation as $E = \frac{1}{\sqrt{2\beta}}$ [28]. The quantity of E is beneficial for reasoning the type of adsorption, and if E values less than $8\ kJ/mol$, the adsorption process is physical adsorption [28]. The mean free energy of adsorption for three isotherms is less than $3\ kJ/mol$, indicating the adsorption process involved in this study is nothing but physisorption. The adsorbent (CuS) is chemically stable during this process of adsorption because the plausibility of chemical reactions or bonds between the adsorbent and adsorbate molecules, in this case, is very low.

In the F-G model, lateral interaction energy ω is physically relevant. It has been determined that the lateral interaction energy of each isotherm is negative. This leads to the fact that the interaction between adsorbed molecules is repulsive. Then, the heat of adsorption will decrease with loading because of increased repulsion between adsorbed molecules as loading increases [27]. The interaction between the hydrophobic tails of the SDS molecules may contribute to the repulsion between the adsorbed molecules. The enhanced adsorption seen in this solution is mainly attributable to what we refer to as the

122

tail-tail interactions between the adsorbed SDS molecules. The SDS molecules at the adsorbent surface produce a unique two-dimensional shape due to interactions between their tails. Consequently, these two models imply that CuS and SDS molecules have negative lateral interaction energy, which leads to tail-tail interaction of the SDS molecules and may physically adsorb one another.

Table 4.1. The fitted parameters of D-R and F-G isotherm models.

Isotherm model	Fitted parameter	CuS-1	CuS-2	CuS-3
D-R model	q_m $(mmol/g)$	0.62 ± 0.03	2.12 ± 0.31	1.84 ± 0.22
	β $(\times 10^{-7} mol^2/J^2)$	1.26 ± 0.05	1.75 ± 0.12	0.95 ± 0.06
	E (kJ/mol)	1.99 ± 0.04	1.68 ± 0.06	2.28 ± 0.07
	R^2	0.9866	0.9696	0.9753
F-G model	ω (kJ/mol)	-4.67 ± 0.36	-4.53 ± 0.15	-4.48 ± 0.31
	K_{FG} $(L/mmol)$	2.02 ± 0.40	1.82 ± 0.11	1.15 ± 0.14
	R^2	0.9677	0.9930	0.9690

To gain insight into the adsorption process and related mechanisms, we analysed the isotherm with three prominent isotherm models, viz. the Sips, Hill, and Two-step adsorption models - typically used for fitting sigmoid-type isotherms. The isotherm models and their significance are thoroughly explained in Section 2.2.3 of Chapter 2. The Sips isotherm model makes it possible to rigorously calculate the distribution of adsorption energies on a catalyst surface (surface heterogeneity) [29]. The Hill adsorption isotherm model explains the binding of various species onto homogeneous substrates. This isotherm model assumes that adsorption is a cooperative process in which the ability of the adsorbates to bind at one site on the adsorbent may impact other binding sites on the same adsorbent [30]. The 'two-step isotherm model' is defined primarily for surfactant adsorption on soil/water interfaces, as proposed by Bu-Yao Zhu and Tiren Gu [31]. The

nonlinear fit of these isotherm models on CuS-1, CuS-2 and CuS-3 is shown in Fig.4.13,4.14 and 4.15, respectively, and the obtained parameters are listed in Table 4.2.
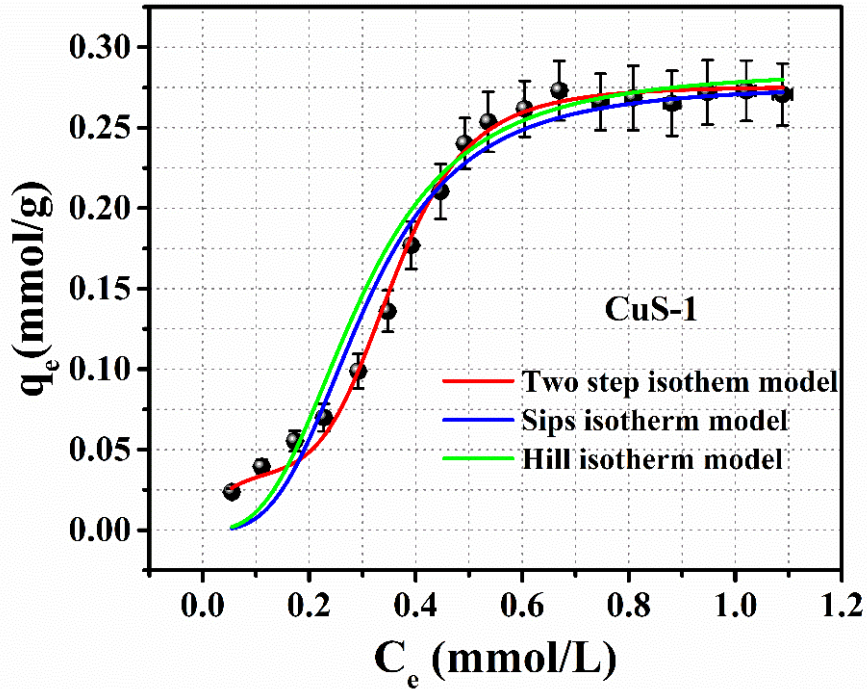
Fig.4.13. *Non-linear fitting of the Sips, Hill, and Two-step adsorption models, typically used for sigmoid-type isotherms, for the sample CuS-1.*
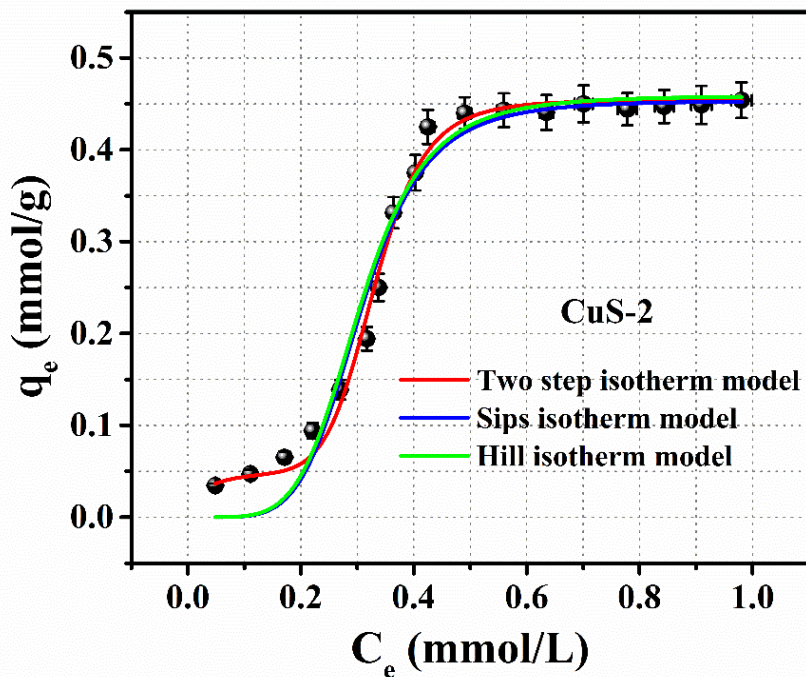
Fig.4.14. *Non-linear fitting of the Sips, Hill, and Two-step adsorption models, typically used for sigmoid-type isotherms, for the sample CuS-2.*
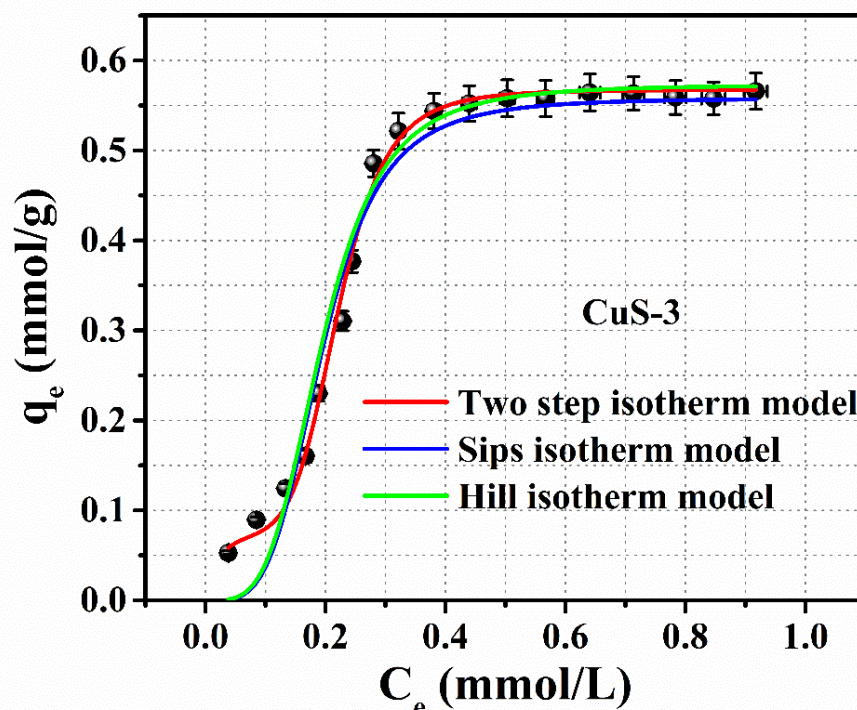
Fig.4.15. *Non-linear fitting of the Sips, Hill, and Two-step adsorption models, typically used for sigmoid-type isotherms, for the sample CuS-3.*

The parameter n_S in the Sips isotherm is regarded as surface heterogeneity; the bigger the parameter, the more heterogeneous the system is [29]. For all the isotherms, the estimated value of n_S is greater than one, which shows that all the synthesized catalysts have heterogeneous active sites on their surfaces. For all isotherms, the estimated value of the Hill exponent factor n_H is positive and greater than 1. The estimate indicates the positive, cooperative ability of the SDS molecules to adhere to the CuS nanostructure. That is, the ability of the adsorbates to bind at one site on the adsorbent may positively affect other binding sites on the same adsorbent [30].

The two-step adsorption model (TSA model) provides the best fit for all regions of the isotherm. The high level of agreement between the TSA model and our experimental data predicts that the adsorption of SDS molecules on the CuS nanostructure takes place in two steps (according to the TSA model). The first step is the monolayer adsorption of SDS molecules on the CuS nanostructure due to the electrostatic interaction between the charged surface of CuS and the head group of SDS molecules. The second step depends on the concentration of the SDS molecule. At a critical concentration, the surfactant molecules begin associating with each other, forming a two-

dimensional micelle-like structure called hemi-micelles [32]. This association considerably enhances the adsorption of sulfonate ions and, hence, the rapid rise in the adsorption of isotherms.

Table 4.2. The fitted parameters of Sips, Hill and Two-step model.

Isotherm model	Expression	Fitted parameter	CuS-1	CuS-2	CuS-3
Sips	$q_e = \dfrac{A_S B_S C_e^{n_s}}{1 + B_S C_e^{n_s}}$	A_s $(mmol/g)$	0.27 ± 0.02	0.45 ± 0.03	0.555 ± 0.05
		B_s $(L/mmol)^{n_s}$	46.19 ± 5.46	552.67 ± 65.61	651.37 ± 75.45
		n_s	3.22 ± 0.42	5.35 ± 0.73	3.96 ± 0.42
		R^2	0.8850	0.8918	0.8467
Hill	$q_e = \dfrac{A_H C_e^H}{B_H + C_e^{n_H}}$	A_H (mmol/g)	0.27 ± 0.02	0.45 ± 0.03	0.55 ± 0.05
		$B_H \times 10^{-3}$ $(mmol/L)^{n_H}$	21.70 ± 7.20	1.81 ± 0.65	1.54 ± 0.48
		n_H	2.94 ± 0.15	5.23 ± 0.22	3.85 ± 0.12
		R^2	0.8851	0.8918	0.8467
Two step adsorptions model	$q = \dfrac{q_\infty k_1 C \left(\frac{1}{n} + k_2 C^{n-1}\right)}{1 + k_1 C (1 + k_2 C^{n-1})}$	q_∞ $(mmol/g)$	0.27 ± 0.01	0.45 ± 0.01	0.56 ± 0.04
		k_1 $(L/mmol)$	24.37 ± 3.74	41.19 ± 9.31	51.58 ± 10.33
		$k_2 \times 10^3$ $(L/mmol)^{n-1}$	0.18 ± 0.02	3.45 ± 0.39	3.89 ± 0.42
		n	6.04 ± 0.15	8.31 ± 0.15	6.43 ± 0.29
		R^2	0.9929	0.9935	0.9916

The Hemi-micelle concentration (H.M.C.) is defined as the concentration above which the adsorption increases dramatically as hemimicelle forms on the solid/liquid interface [32]. It can be determined from the inflection of the adsorption density versus

concentration curve, i.e. adsorption isotherm. For the mathematical analysis, the H.M.C. is the concentration at which the straight line with the maximum $\left(\frac{\partial q}{\partial c}\right)$ on the adsorption isotherm intersects the line of $q = 0$ or & $\frac{q - q_{\infty}}{n} = 0$.

$$H.M.C = \left(\frac{n-1}{n+1}\right)^{\frac{n+1}{n}} K^{-\frac{1}{n}} \dots \dots (4.6)$$

where $K = k_1 k_2$ in the equation of the Two-step adsorption isotherm model. The Hemimicelle concentration (H.M.C) for the three isotherms is estimated using equation 4.6. These values are summarized in Table 4.3. The estimated values of H.M.C are in good agreement with the experimental results.

Table.4.3. *The estimated values of hemi-micelle concentration for different adsorption isotherms.*

System	n	K $(L/mmol)^n$	H.M.C $(mmol/L)$
CuS-1	6.04 ± 0.15	$(0.45 \pm 0.10) \times 10^4$	0.20 ± 0.02
CuS-2	8.31 ± 0.15	$(1.42 \pm 0.28) \times 10^5$	0.18 ± 0.08
CuS-3	6.43 ± 0.29	$(2.00 \pm 0.61) \times 10^5$	0.11 ± 0.09

4.3.5. Surface chemistry and adsorption behaviour of CuS nanostructures

The surface chemistry of adsorbents is determined by the acidic and basic character of the surface, which can be tuned by the pH of the solution [33]. The pH_{PZC}, is a fundamental parameter in adsorption studies that informs researchers about the electrostatic characteristics of the adsorbent surface and how pH conditions can affect adsorption processes [34]. It plays a critical role in optimizing adsorption conditions and understanding adsorption mechanisms, mainly when dealing with solid-liquid interfaces and the behaviour of adsorbent materials. The pH_{PZC}, represents the pH at which the adsorbent's net charge becomes neutral [35]. When the solution's pH is below the pH_{PZC}, the adsorbent surface carries a positive charge, promoting the adsorption of anionic species. Conversely, when the solution's pH exceeds the pH_{PZC}, the adsorbent surface becomes negatively charged, facilitating the adsorption of cationic species [36]. The drift

method [37] is used to estimate the point of zero charge of the CuS nanostructures, as depicted in Fig.4.16. It is found that CuS-1 and CuS-3 have a value of $pH_{pzc} = 9.89 \pm 0.20$, whereas CuS-2 has a value of $pH_{pzc} = 9.73 \pm 0.20$. Thus, we can conclude that, the surface charge of all the CuS nanostructures was entirely protonated and shows positively charged at $pH < 9.9$. In the adsorption studies, the natural pH of the SDS solution stayed between 7 and 8 (up to 2 mmol/L). Therefore, the surface of the CuS nanostructure is highly protonated and positively charged during our adsorption experiments. Although SDS is an anionic surfactant, the negative head group of SDS molecules could interact significantly with the positively charged CuS nanostructures. The surface protonation of the CuS nanostructure in the SDS solution aids the monolayer adsorption of SDS molecules on the adsorbent. On the other hand, at solution $pH > 9.9$, the surface becomes deprotonated and negatively charged, causing electrostatic repulsion with negatively charged anions and deprotonated CuS nanostructure surface- decreasing adsorption efficiency.
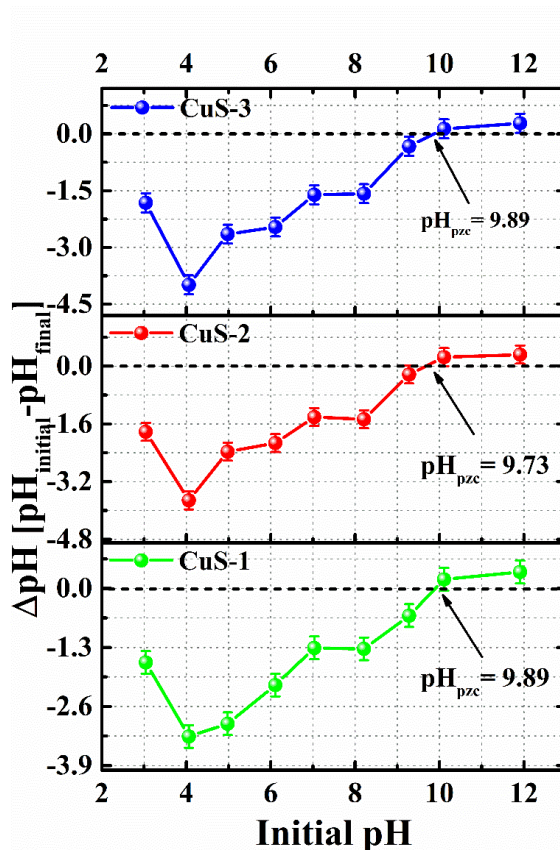
Fig.4.16. *The graphical variation of the initial pH of the solution with ΔpH- using the Drift method to find the pH$_{pzc}$ of the adsorbent. It is inferred that the surface of the CuS nanostructures was protonated at $pH < pH_{pzc} = 9.9$, and its surface charge becomes positive under this pH.*

The effect of the initial pH of the SDS solution on adsorption is shown in Fig. 4.17. The percentage of SDS removal from water is significantly reduced if the pH is greater than 9, a trend observed consistently with two different SDS concentrations. At pH 2, a similar decrease in removal efficiency is noted. This is due to the high concentration of hydrogen ions (H^+) at low pH, leading to partial protonation of the sulfate groups of SDS, which reduces its negative charge and affinity for adsorption onto the CuS surface [38]. Additionally, the CuS surface becomes positively charged due to the adsorption of H^+ ions, repelling the protonated SDS molecules and further decreasing adsorption capacity. These findings confirm the impact of surface protonation of CuS nanostructures on SDS adsorption.
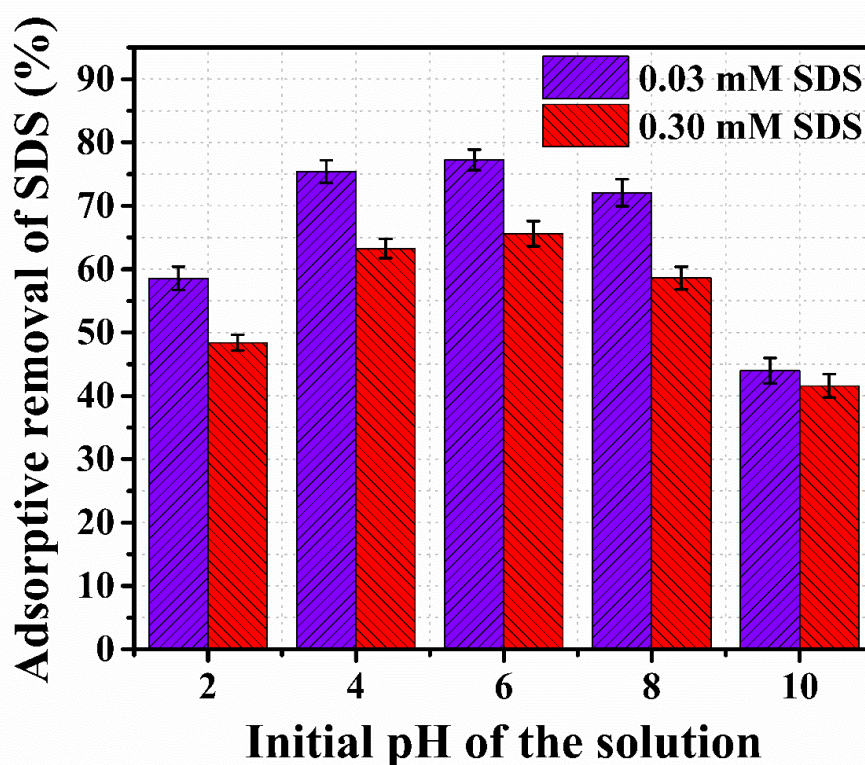
Fig.4.17. *Percentage of removal of SDS from water with pH of the solution.*
(C_0= 0.07 mM, Dosage = 0.6 g/L, T= 303 K).

4.3.6. Adsorption kinetics

Modelling the adsorption rate and understanding the system's dynamic behaviour is vital for practical applications such as process design and control. The rate of adsorption is determined by fitting the adsorption kinetic data to the Pseudo-first-order (PFO), Pseudo-second-order (PSO), and Intra-particle diffusion (IPD) models [39]. The adsorption kinetic models and their significance are thoroughly explained in Section

2.2.4 of Chapter 2. The non-linear fit of PFO and PSO is shown in Fig.4.18, and the fitted parameters are shown in the Table. 4.4. the correlation coefficients of pseudo-first order is observed to be higher than those of pseudo-second order for all CuS nanostructures. Furthermore, the equilibrium adsorption capacity q_e values computed by the PFO are comparable to the q_e values gathered by experiment. Thus, the kinetic adsorption of SDS onto CuS is in excellent agreement with PFO.
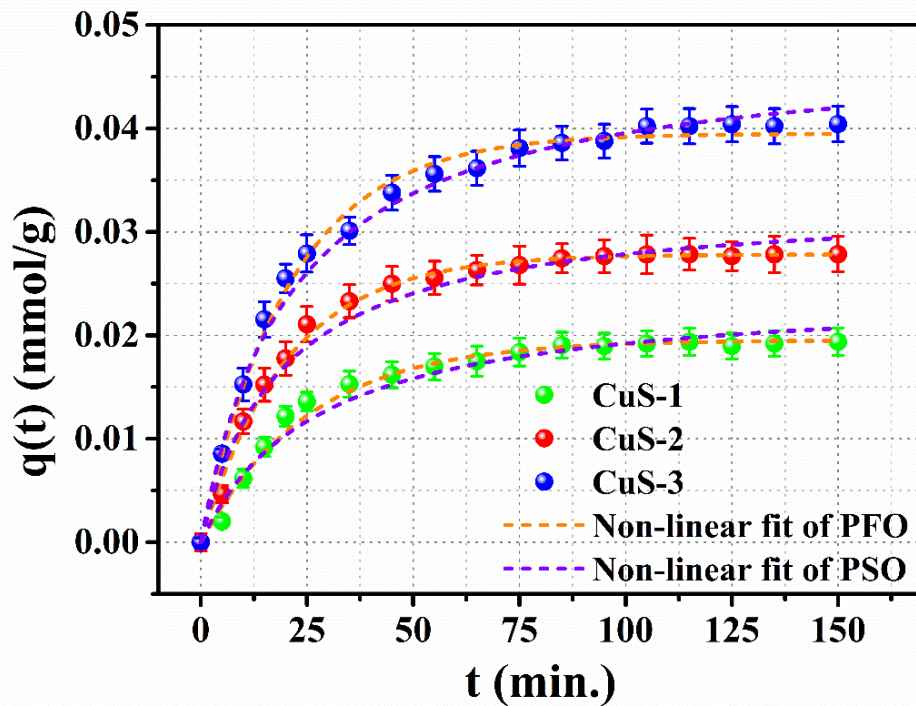
Fig.4.18. Nonlinear fit of Pseudo First Order (PFO) and Pseudo Second Order (PSO) kinetics. Our results reveal that the kinetic adsorption of SDS onto CuS was in good agreement with Pseudo First Order kinetics. (C_0= 0.07 mM, Dosage = 0.6 g/L, T= 303 K, pH ~ 7).

The sorption kinetics may alternatively be described from a mechanistic point of view. The adsorption process on sorbents can be divided into four phases, each of which can affect the rate and quantity of adsorption on the solid surface. The steps involved are bulk diffusion, film diffusion, intraparticle diffusion, and solute adsorption on the surface [40]. The enhanced adsorption capacity for all the adsorbents in the initial stage indicated the diffusion-based interaction between the adsorbate and adsorbent during adsorption. To see whether the intraparticle diffusion phenomena play a role in the adsorption process, we consider the Weber-Morris equation for the intra-particle diffusion model as

$$q(t) = k_{id}\sqrt{t} + C \ldots \ldots (4.7)$$

where k_{id} ($mmole$ g^{-1} $min^{1/2}$) is the intra-particle diffusion rate constant, and C is related to the boundary layer thickness [41].

Table.4.4. *The fitted parameters of kinetic models.*

Kinetic Model	Parameters obtained by fitting	CuS-1	CuS-2	CuS-3
Pseudo-First Order Kinetics $q(t) = q_e(1 - e^{-k_1 t})$	q_e $(mmol/g)$	0.019 ± 0.001	0.027 ± 0.001	0.039 ± 0.001
	k_1 $(min.^{-1})$	0.039 ± 0.003	0.049 ± 0.002	0.047 ± 0.001
	R^2	0.9861	0.9956	0.9980
Pseudo-Second Order Kinetics $q(t) = \dfrac{k_2 q_e^2 t}{1 + k_2 q_e t}$	q_e $(mmol/g)$	0.024 ± 0.001	0.033 ± 0.001	0.047 ± 0.001
	k_2 $(g/min.mmol)$	1.49 ± 0.30	1.62 ± 0.21	1.00 ± 0.06
	R^2	0.9758	0.9861	0.9974

Fig.4.19. displays the regression of $q(t)$ versus $t^{1/2}$ for all the adsorbents. In Fig.4.19, the data points are related by two straight lines for CuS-1 and CuS-2, while CuS-3 shows three distinct linear portions. The multilinearity (like in the present case) in curves drawn between $q(t)$ and $t^{1/2}$ has often been attributed to the involvement of two or more steps in adsorption kinetics. The adsorption process consists of two stages for CuS-1 and CuS-2. First, the SDS molecules are transported from the bulk solution to the external surface of the adsorbent by boundary layer diffusion: this is represented by the first sharper portion. The second linear portion (plateau) is the gradual adsorption stage, representing equilibrium [42]. As shown in Fig.4.19., CuS-3 produced a three-stage plot of $q(t)$ and $t^{1/2}$, with three distinct sections: the initial plot or steep-sloped portion represents bulk diffusion or a very high exterior adsorption rate, the subsequent linear portion represents intraparticle diffusion, and the plateau portion represents equilibrium [43]. It is to be noted that the intraparticle diffusion process is distinctly seen in CuS-3. The list of fitted parameters in the intraparticle diffusion model is shown in Table 4.5.
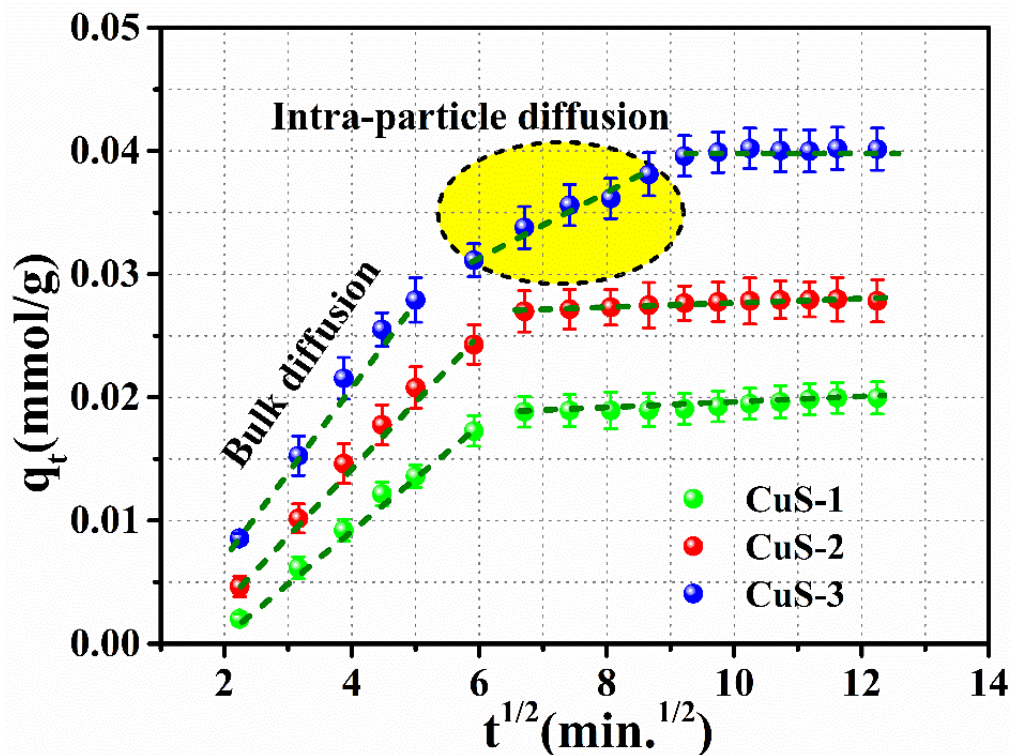
Fig.4.19. *The Weber-Morris plot. Kinetics of SDS adsorption onto CuS according to the intraparticle diffusion model. The adsorption of CuS-1 and CuS-2 consists of two steps: boundary layer diffusion and gradual equilibrium stage. However, CuS-3 shows three distinct sections: bulk diffusion, intraparticle diffusion, and equilibrium stage. (C$_0$ = 0.07 mM, Dosage = 0.6 g/L, T= 303 K, pH ~ 7).*

Table 4.5*. List of fitted parameters in Intraparticle Diffusion Model.*

Adsorbent	Stages	k_{id} $(\times 10^{-3})$ $(mmol\ g^{-1}\ min^{1/2})$	C $(mmol\ g^{-1})$
CuS-1	Stage-I	4.21 ± 0.01	0
	Stage-II	2.34 ± 0.02	0.017 ± 0.003
CuS-2	Stage-I	4.17 ± 0.02	0
	Stage-II	2.14 ± 0.02	0.017 ± 0.002
CuS-3	Stage-I	7.35 ± 0.02	0
	Stage-II	2.44 ± 0.02	0.016 ± 0.002
	Stage-III	0.15 ± 0.01	0.038 ± 0.003

4.3.7. Thermodynamics of adsorption

Adsorption thermodynamic studies have a significant role in forecasting reaction feasibility. The adsorption studies were conducted at five different temperatures, and Gibb's free energy change of the reaction (ΔG) was calculated using the Van't Hoff equation for each temperature [44].

$$\Delta G = -RT \ln(1000 \times K_d) \dots \dots (4.8)$$

where K_d is the solute distribution co-efficient between the solid and liquid phases at different temperatures; $K_d = \frac{q_e}{C_e}$. In this study, the ΔG for SDS adsorption on CuS nanostructure was found to be in the range of $-18 \, kJ/mol - 21 \, kJ/mol$ at all temperatures, indicating that the adsorption is physisorption [45]. Moreover, the adsorption was thermodynamically feasible and spontaneous in the defined temperature ranges.

Comparing the Van't Hoff equation with the equation for Gibbs free energy change as $\Delta G = \Delta H - T\Delta S$, we get

$$\ln(1000 \times K_d) = -\frac{\Delta H}{RT} + \frac{\Delta S}{R} \dots \dots 4.9$$

Thus, the thermodynamic parameters like enthalpy change and entropy change of the adsorption reaction can be estimated from the slope and intercept of $\ln(1000 \times K_d)$ versus $\frac{1}{T}$ graph, and this is shown in the Fig.4.20. The estimated values of the thermodynamic parameters of the adsorption processes are shown in Table 4.6. The detailed description of the thermodynamics of adsorption is thoroughly explained in Section 2.2.5 of Chapter 2.

It is found that all CuS nanostructures exhibit a negative enthalpy change during the reaction, signifying an exothermic process. For this exothermic process, the energy released in bond formation between adsorbate and adsorbent is greater than the energy absorbed for desorbing previously adsorbed solvent (water) molecules [46]. The affinity of CuS for the adsorbate species is indicated by a positive value for ΔS. It suggests increased randomness at the solid/solution interface during the adsorption of SDS on the CuS nanostructure [47,48]. Additionally, this adsorption process is enthalpy-driven from a thermodynamic point of view. The Gibb's free energy change of the reaction with temperature is shown in Fig.4.21.
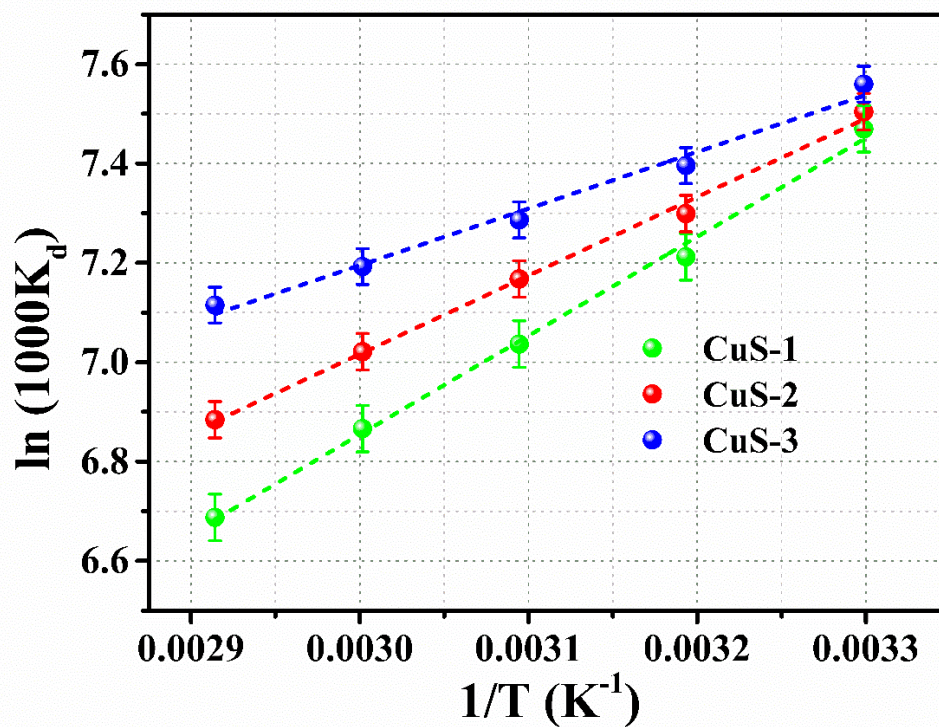
Fig.4.20. *Variation of ln(1000K$_d$) versus 1/T. The linear fit of this graph gives the values of ΔH and ΔS of the reaction. (C$_0$= 0.07 mM, Dosage=0.6 g/L, pH ~ 7).*
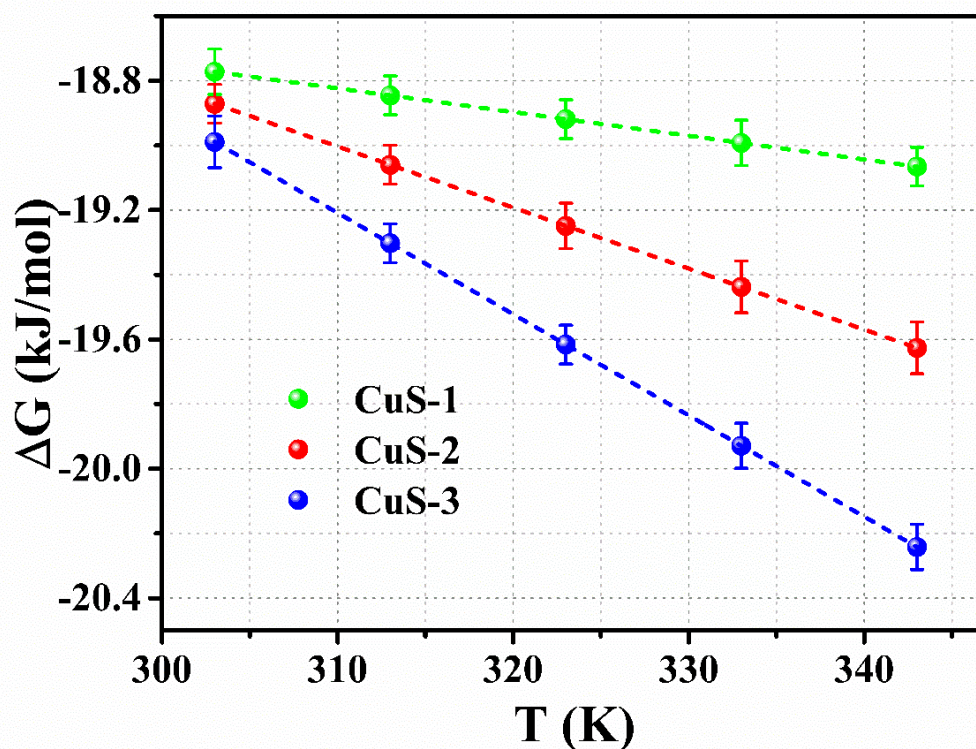
Fig.4.21. *The variation of Gibb's free energy change of the reaction with temperature. (C$_0$= 0.07 mM, Dosage=0.6 g/L, pH ~ 7).*

Table 4.6. *Summary of estimated thermodynamic parameters- standard enthalpy change of the reaction for all CuS nanostructures is negative, indicating an exothermic process and positive standard entropy changes indicate the spontaneous process.*

Adsorbent	Temperature (K)	ΔG (kJ/mol)	ΔH (kJ/mol)	ΔS (J/mol)
CuS-1	303	−18.77 ± 0.05	−16.55 ± 0.56	+ 7.33 ± 0.44
	313	−18.84 ± 0.06		
	323	−18.91 ± 0.06		
	333	−18.99 ± 0.05		
	343	−19.02 ± 0.04		
CuS-2	303	−18.87 ± 0.04	−13.15 ± 0.44	+18.88 ± 1.38
	313	−19.05 ± 0.04		
	323	−19.24 ± 0.05		
	333	−19.43 ± 0.04		
	343	−19.62 ± 0.03		
CuS-3	303	−18.98 ± 0.04	−9.49 ± 0.62	+31.33 ± 1.93
	313	−19.30 ± 0.03		
	323	−19.61 ± 0.04		
	333	−19.92 ± 0.04		

4.3.8. Adsorption mechanism

Based on the physicochemical and isotherm analyses of the adsorption process, the adsorption of the SDS at the solid/liquid interface should involve two main stages with radically different features. In the first step, surfactant molecules are adsorbed through the interactions between the molecules and the solid surface; the second is

through the hydrophobic interaction between the adsorbed surfactant molecules. For adsorption to occur, the molecules of SDS and the solid surface must be attracted to one another. Specifically, the Coulomb attraction between the anionic head group of SDS molecules and the protonated CuS nanostructures in the SDS solution plays a role in this process. Sip's isotherm model clearly shows the adsorbent's surface heterogeneity, which allows us to predict the random adsorption of SDS on the CuS surface. When the number of sulfonate ions, the head group of SDS molecules, is equal to the number of surface sites, the contribution from electrostatic attraction diminishes. It results in the formation of monolayer adsorption [49].

The second stage comes from the characteristics of the surfactant, which leads to an interfacial phenomenon. Suppose the SDS molecules are adsorbed at the solid/liquid interface. In that case, they should also exhibit the hydrophobic effect, forming aggregates at the solid-liquid interface with other SDS molecules. Above a particular concentration, the conspicuous increase in adsorption signifies the beginning of interfacial surfactant association due to lateral interaction between hydrocarbon chains. This phenomenon is classically referred to as 'hemi-micellization' [32]. The surface aggregates are referred to as hemi-micelles in this context. Each molecule adsorbed in the first step provides a potential active centre for hemi-micellization, leading to a dramatic increase in adsorption. The remaining adsorption is attributable only to the interaction between the hydrocarbon chains, reaching its maximum as the concentration of SDS increases. As a result, the slope of the adsorption isotherm falls, and the isotherm curve flattens. The graphical representation of the adsorption mechanism is demonstrated in Fig.4.22.
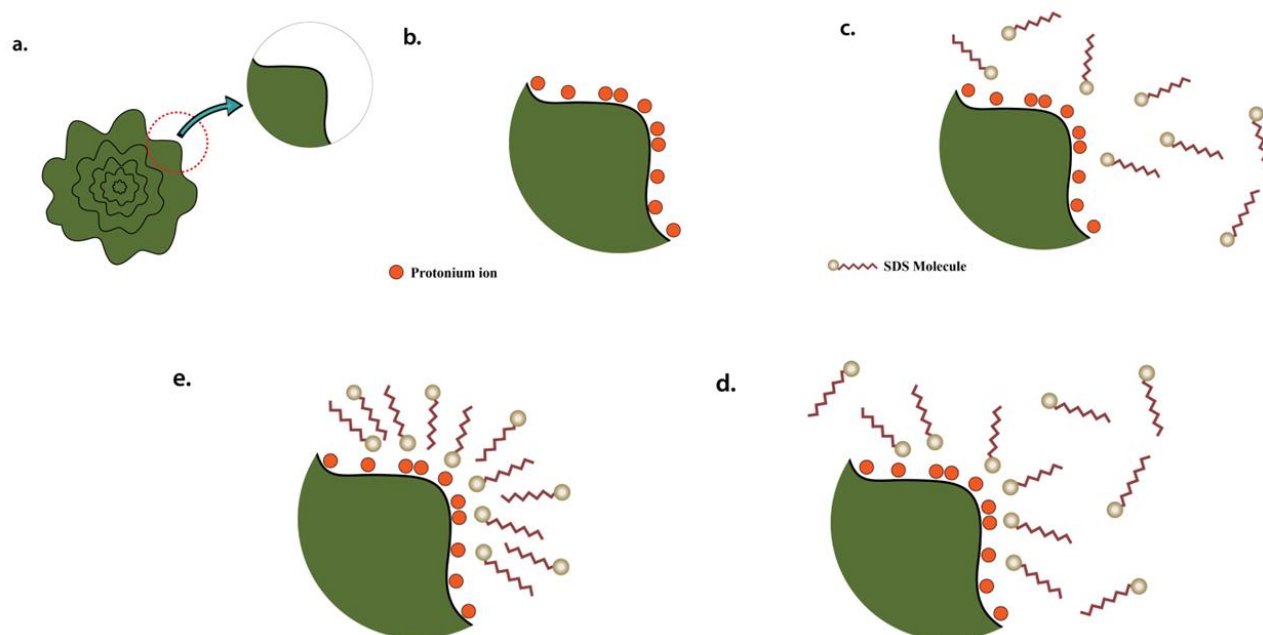
Fig.4.22. *The mechanism of SDS adsorption on the CuS nanostructures. a) the enlarged position of CuS nanostructures; b) protonated CuS surface; c) the interaction of the SDS head group with the protonated CuS surface; d) Monolayer adsorption of CuS nanostructure; e) hemi-micellization takes place due to the tail-tail interaction of the SDS molecules.*

4.3.9. Relevance of CuS adsorbent

Table.4.7. summarises the reported SDS adsorption capacities of various adsorbents. The most often employed adsorbents in these processes are activated carbon, mineral adsorbents, and biomass. The Table shows that the synthesized CuS nanostructure has a higher adsorption capacity for SDS than other published natural and synthetic adsorbents, and it considerably outperforms reported metal oxides and their composites. As an outcome, the CuS nanostructure can be considered a promising candidate for wastewater management, paving the way for metal chalcogenides to be exploited as an adsorbent and a catalyst in environmental remediation research.

Table 4.7. Summary of different adsorbents used for the removal of SDS from wastewater. Note that the adsorbents in the given list, except CuS (present study), are incapable of degrading SDS molecules post-adsorption.

Name of the adsorbent	Adsorption capacity q_{max} $(mmol/g)$	Reference
Alumina	0.006	Koopal *et al.* [49]
Dolochar	0.02	Pham *et al.* [50]
$\gamma - Al_2O_3$	0.08	Nguyen *et al.* [51]
Waste Activated Carbon	0.21	Shami *et al.* [52]
Magnetic MWCNT	0.21	Gupta *et al.* [53]
Chitosan beads	0.26	Rahmani *et al.* [54]
Fe_2O_3	0.22	Pal *et al.* [55]
Pine cone mass	0.36	Gao *et al.* [56]
Activated coconut shell	0.38	Sen *et al.* [57]
CuS nanoflower	**0.56**	**Present study**
Standard Activated Carbon	0.61	Bhandari *et al.* [58]

4.3.10. Catalytic decomposition of SDS

During the adsorption process, the contaminant SDS is successfully removed from the water; nevertheless, the procedure does not destroy the contaminants. The catalytic activity of CuS in the presence of H_2O_2 is utilized for the complete degradation of SDS molecules present in the water and adsorbed on the CuS nanostructures. The time-dependent degradation of SDS on the catalytic activity of CuS and H_2O_2 is depicted in Fig.4.23. Catalytic reactions were carried out after achieving the adsorption-desorption equilibrium of SDS and CuS. The introduction of H_2O_2 markedly initiated the catalytic dissociation of SDS molecules adsorbed on the CuS surface. Furthermore, there was no

notable change in the degradation rate of the reaction under visible light irradiation. This indicates that the adsorbent does not undergo photocatalytic decomposition of SDS. The catalytic decomposition of SDS was performed in the dark.
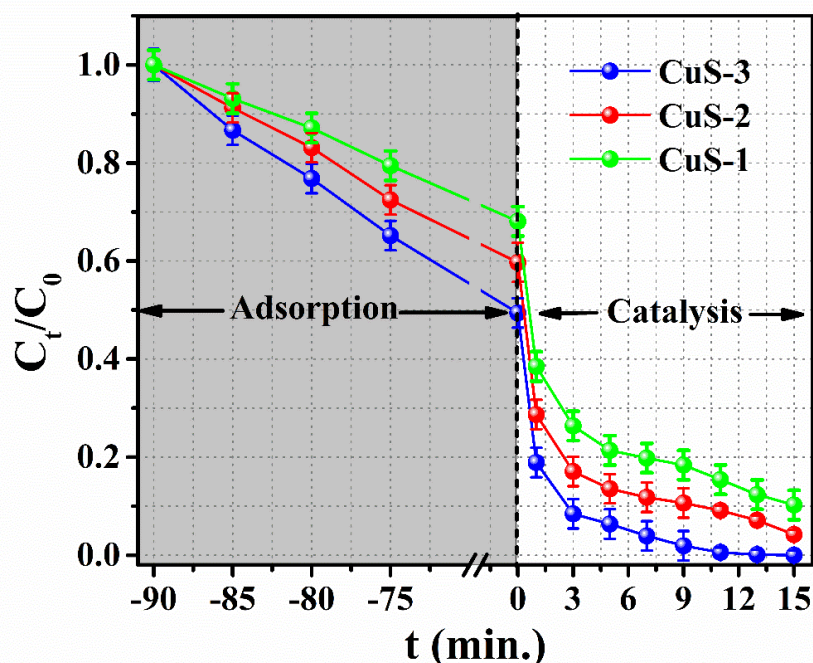
Fig.4.23. *Catalytic degradation of SDS- The SDS molecules were degraded entirely in the catalytic reaction of CuS-3 and H_2O_2. The experiment involved a 100 mL, 0.14 mM SDS solution with a catalyst dosage of 0.6 g/L. After 60 minutes of stirring in the dark to achieve adsorption-desorption equilibrium, the catalytic reaction was initiated by adding H_2O_2 to the solution.*

To quantify the rate of the decomposition reaction, the experimental data can be fitted to the pseudo-first-order kinetic equation as $C_t/C_0 = e^{-kt}$ where k is the rate constant of the pseudo-first-order kinetic reaction [56]. The rate constant of the reaction is estimated by using the linear fit of the $\ln\left(\frac{C_0}{C_t}\right)$ versus time graph. The slope of the graph gives the rate constant of the reaction. The details of this kinetic model and its significance are thoroughly explained in Section 2.6 of Chapter 2. Fig. 4.24 shows the aforementioned linear fit, and Table 4.8 presents the reaction rates for SDS and various CuS structures.
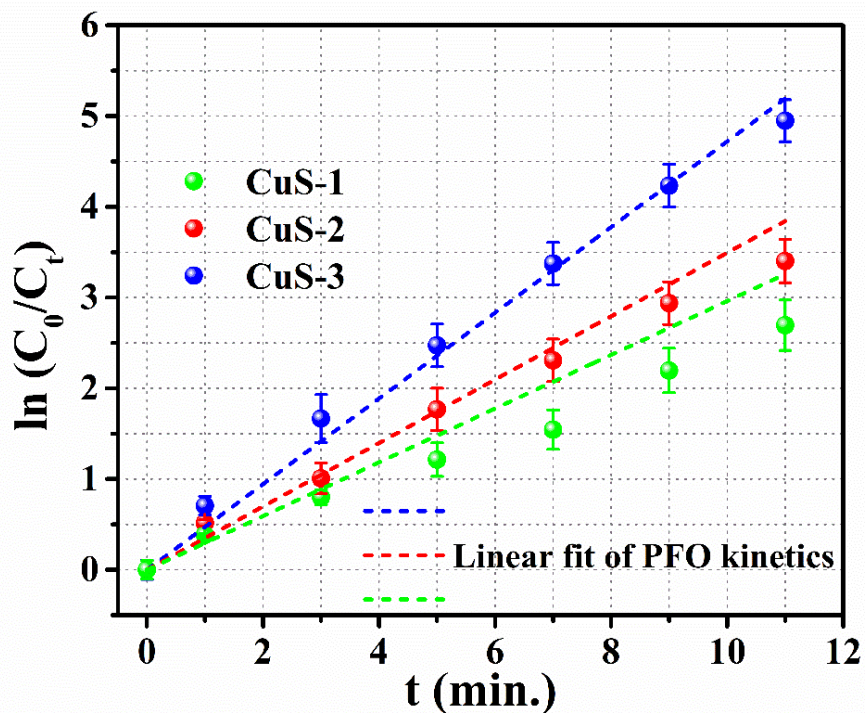
Fig.4.24. *The linear fit of Pseudo First Order kinetic model for catalytic decomposition of SDS. (C_0= 0.14 mM, Dosage=0.6 g/L, T=303 K, pH ~ 7).*

Table 4.8. *The list of the catalytic decomposition's rate constant and mineralization efficiency.*

Catalyst	Rate constant of the reaction ($min.^{-1}$)	Mineralization efficiency %
CuS-1	0.50 ± 0.01	64.3
CuS-2	0.61 ± 0.01	78.5
CuS-3	0.78 ± 0.02	90.8

The mineralization efficiency of CuS in catalytically decomposing SDS was assessed through total organic carbon analysis. CuS-3 exhibited a notably higher mineralization efficiency, reaching 90.8%. For CuS-1 and CuS-2, the estimated mineralization efficiencies are 64.3% and 78.5%, respectively, within an 11-minute catalytic process.

4.3.11. Effect of pH on catalysis

The catalytic decomposition of SDS in the presence of CuS and H_2O_2 was conducted under both acidic and basic conditions of the solution. It was observed that the catalytic decomposition of SDS occurred more rapidly at pH level 4 compared to neutral pH, while it proceeded more slowly at pH = 12. The temporal progression of SDS degradation is illustrated in Fig.4.25. The acidic environment provided by H^+ ions facilitate the catalytic degradation initiation, aiding in the protonation of hydrogen peroxide [60]. This protonation step enhances the reactivity of hydrogen peroxide, rendering it more susceptible to subsequent reactions [61].
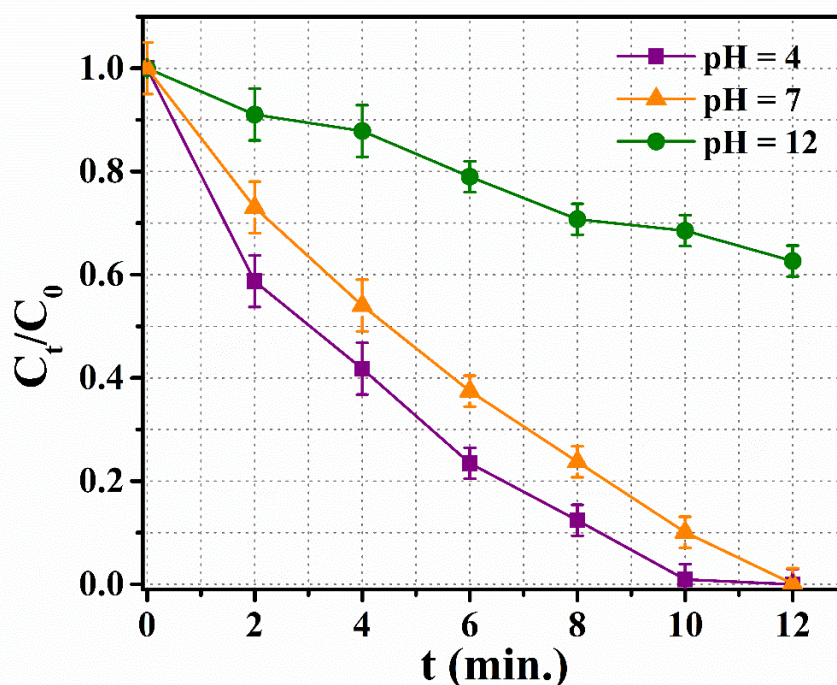
Fig.4.25. *The temporal variation of catalytic decomposition of SDS under various pH of the solution. (C_0= 0.14 mM, Dosage=0.6 g/L, T = 303 K).*

4.3.12. Mechanism of catalytic decomposition of SDS

The SDS degradation mechanism can be ascribed to the formation of hydroxide radicals in the presence of CuS and H_2O_2. The rate of degradation of SDS was negligible in the presence of H_2O_2 without the assistance of the catalyst. Thus, H_2O_2 cannot produce sufficient hydroxyl radicals without the CuS catalyst. This is shown in Fig.4.26
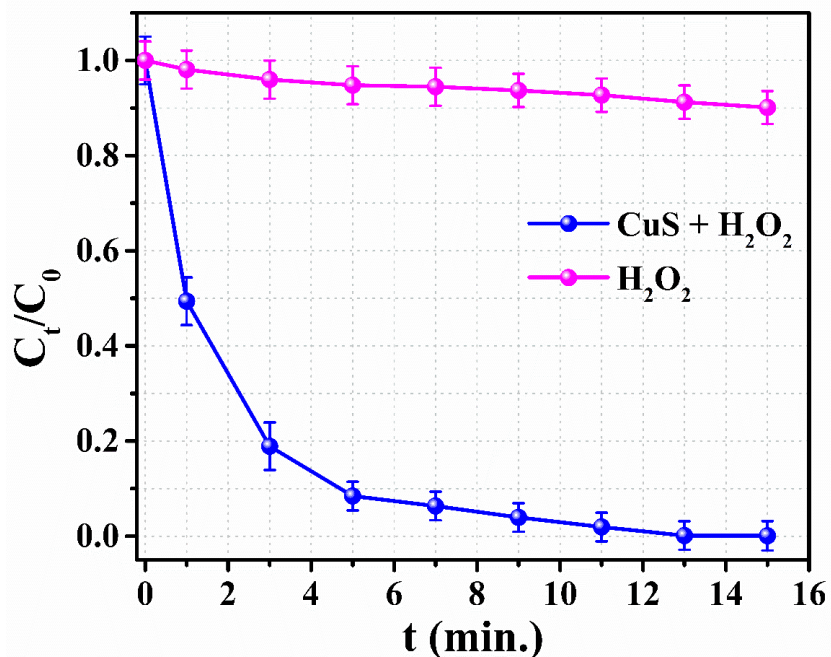
Fig.4.26. *Catalytic decomposition of SDS in the presence of H_2O_2 alone and H_2O_2+CuS. It is evident that the catalytic decomposition is drastically enhanced in the presence of CuS. (C_0= 0.14 mM, Dosage=0.6 g/L, T=303 K, pH ~ 7).*

A brief description of the formation of hydroxyl radicals in the presence of CuS is given as follows [62].

$$Cu^{2+} + H_2O_2 \rightarrow H^+ + CuOOH^+ \dots \dots (5a)$$

$$CuOOH^+ \rightarrow HOO^{\bullet} + Cu^+ \dots (5b)$$

$$Cu^+ + H_2O_2 \rightarrow Cu^{2+} + HO^{\bullet} + OH^- \dots \dots (5c)$$
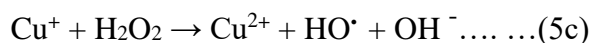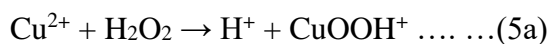
These $HO^{\bullet}$ radicals can attack the SDS molecules present in the solution. It is reported that hydroxyl radicals can attack methyl groups at the ends of the hydrocarbon chain as well as CH_2- groups in the middle position of such long-chain hydrocarbons. It can generate alkyl radicals by the abstraction reaction (or dehydrogenation) [63], represented as:

$$RH + HO^{\bullet} \rightarrow R^{\bullet} + H_2O \dots \dots (6)$$

Further, these alkyl radicals can react with other hydroxyl radicals and dissolved oxygen in the water to alcohol and peroxy radicals [60].

$$R^{\bullet} + HO^{\bullet} \rightarrow R\text{-}OH \dots \dots (7a)$$

142

$$R^{\bullet} + O_2 \rightarrow R\text{-}O\text{-}O \dots \dots (7b)$$
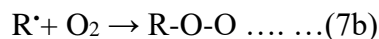
Then these organic radicals undergo oxidative chain reactions, leading to the formation of aldehydes and carboxylic acids. This aldehyde and carboxylic acid can be further reduced to form CO_2 and H_2O [64].

4.3.13. Effect of dosage of the catalyst

In the experiment, the relationship between the amount of catalyst used and its effectiveness in decomposing SDS was investigated. The results indicated that changing the dosage of the catalyst did not significantly affect the efficiency of SDS degradation. This finding is visually represented in Fig.4.27.
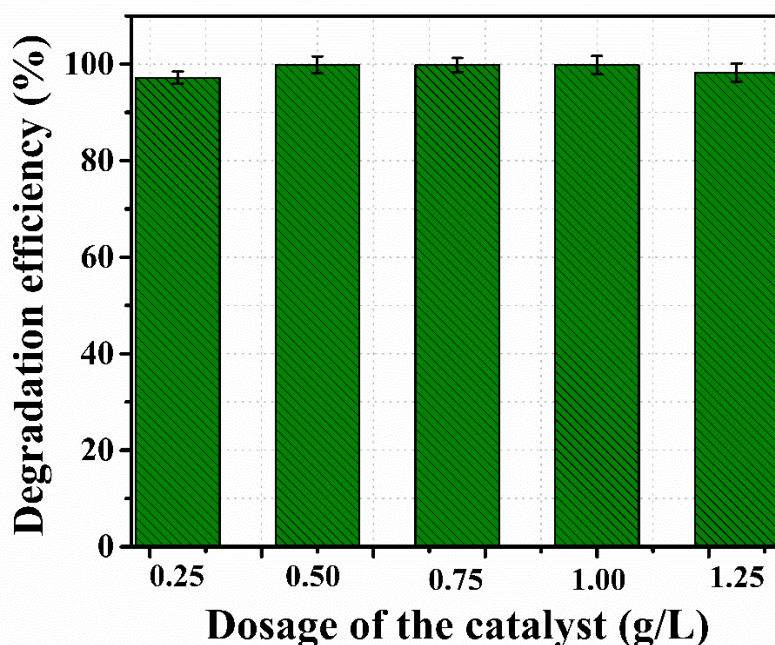
Fig.4.27. *The effect of dosage of the catalyst on the decomposition of SDS.*
(C_0= 0.14 mM, T =303 K, pH ~ 7).

4.3.14. Reusability of the catalyst

The reusability test of the catalyst was conducted as follows: 30 mg of the catalyst was introduced into 50 mL of SDS solution with an initial concentration of 0.14 mM and stirred for 60 minutes to establish adsorption-desorption equilibrium. Subsequently, 0.5 mL of H_2O_2 was added to the solution to initiate the catalytic reaction, which was allowed to proceed for 15 minutes. The SDS concentrations in the initial and final solutions were determined using the Methylene Blue Active Substances (MBAS) method.

At the end of each cycle, the residual solution was drained, and the catalyst was retained in the reaction medium. The catalyst was washed twice with distilled water to remove any residual reaction by-products. Fresh SDS solution (50 mL, 0.14 mM) was then added to the reaction medium, and the experiment was repeated under identical conditions. This process was carried out for five consecutive cycles. In each cycle, the initial and final SDS concentrations were measured using the MBAS method to evaluate the catalytic efficiency and stability.

The percentage of degradation was calculated using the equation.

$$\% \ of \ degradadtion = \frac{C_0 - C_f}{C_0} \times 100$$

where C_0 and C_f are the initial and final concentration of SDS solution.
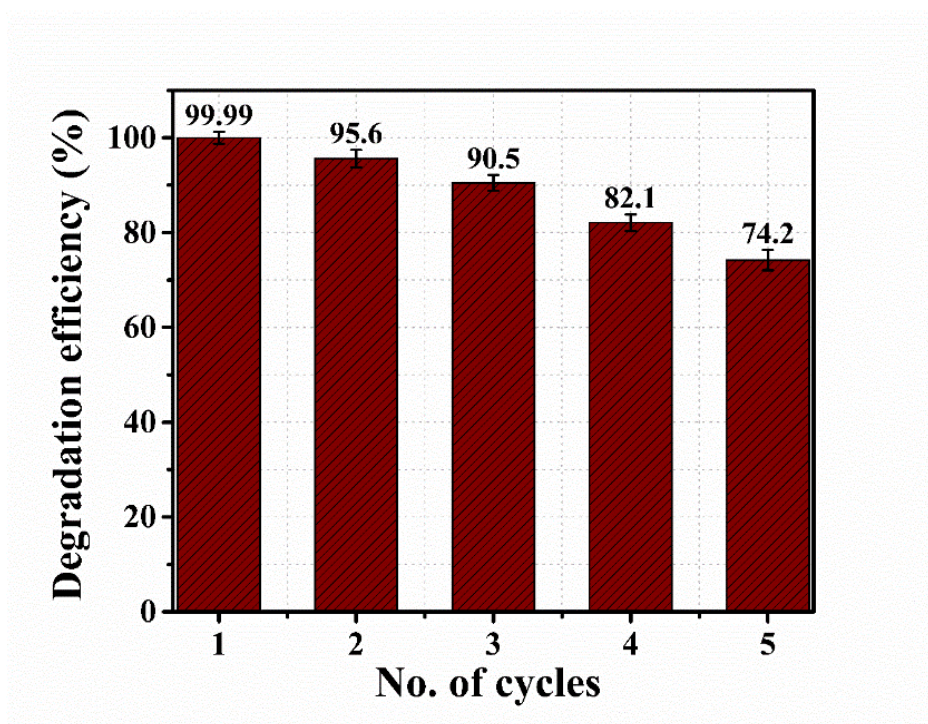
Fig.4.28. *The effect of reusability of the catalyst. (C_0= 0.14 mM, Dosage = 0.6 g/L, T =303 K, pH ~ 7).*

This study examined the reusability of the catalyst, determining how many times it could be effectively used before its performance started to decline. It was found that the catalyst maintained its efficiency for up to four cycles of use, with only a slight reduction in its ability to decompose SDS after each cycle. This gradual decrease in efficiency is depicted in Fig.4.28., showing that while the catalyst remains functional over multiple uses, there is a minor loss in effectiveness with each reuse.

144

The primary goals of this research were to improve the adsorption of SDS from water and to develop an effective method for degrading SDS in water. Degradation of SDS molecules in wastewater can be accomplished *via* various physiochemical techniques. The removal efficiencies of various degradation processes for SDS molecules in water are tabulated in Table 4.9. The catalytic degradation of SDS in the presence of CuS and H_2O_2 is an excellent strategy for effectively removing SDS from wastewater.

Table 4.9. Summary of different AOP methods for decomposing SDS- It is evident that the catalytic degradation of SDS in the presence of CuS and H_2O_2 is an efficient method for completely removing SDS in the wastewater.

Name of the method	Degradation efficiency	Time required for the degradation	Reference
Photo-Fenton oxidation	80%	30 min.	Kıran, *et al.*[65]
Photo-oxidative degradation	80%	6 hrs.	Panich *et al.* [66]
Photocatalytic degradation using TiO2/layered double hydroxide materials	90%	50 min.	Aoudjit *et al.* [67]
Biodegradation using Staphylococus aureusWAWI (bacteria)	36%	88 hrs.	Yeldho *et al.* [68]
Photo-electrochemical oxidation	90%	60 min.	Nguyen *et al.* [69]
Electrochemical dark oxidation	90%	60 min.	Nguyen *et al.* [69]
Sonochemical oxidative reaction	83%	120 min.	Dehghani *et al.* [70]
Fenton like oxidation using CuS/H2O2	**100%**	**11 min.**	**Present study**

4.4. CONCLUSION

The work demonstrated the fast-catalytic decomposition of a significant pollutant surfactant, sodium dodecyl sulphate. The catalytic environmental remediation activity is achieved via (i) interface hemi-micelle driven enhanced adsorption and (ii) synergetic action of the (a). characteristics of CuS, (b). nanoflower morphology, and (c) the presence of H_2O_2.

The CuS nanoflower is synthesized using a facile single solid-state synthesis route. The XRD and Raman results confirmed the formation of a pure hexagonal covellite phase of CuS. FE-SEM images suggest tunable morphologies for CuS nanostructures. The CuS nanoflower shows a high maximum adsorption capacity of 0.56 ± 0.02 mmol/g. All isotherms display type V sigmoidal structures. The two-step adsorption model for surfactants can reasonably represent the adsorption isotherms of SDS onto CuS nanostructures. The kinetics of SDS adsorption followed pseudo-first-order kinetics and intraparticle diffusion mechanisms. The thermodynamic studies suggested that the adsorption reaction is an endothermic and enthalpy-driven process. The kinetic and thermodynamic studies confirmed that the adsorption of SDS molecules on CuS nanostructures is based on physisorption. A fundamental understanding of the enhanced adsorption of SDS on CuS is developed based on hemi-micellization.

Here, the CuS is demonstrated as an adsorbent that is on par even with activated carbon (AC), as compared in Table.4.7 - but the AC cannot decompose SDS. The CuS in the presence of H_2O_2 shows fast-catalytic activity to decompose the SDS molecules into carbon dioxide and water. The catalyst is stable under various pH conditions of the solution and can be recycled for up to 3 usage cycles. Almost 90% of SDS mineralisation occurs within 11 minutes of the catalytic process. The outcome of the work promises a reliable and industrially scalable chalcogenide for the environmental remediation of typical surfactants in effluents from chemical industries.

4.5. REFERENCES

[1]   Arora, U., Khuntia, H. K., Chanakya, H. N., & Kapley, A. (2023). Surfactants: combating the fate, impact, and aftermath of their release in the environment. *International Journal of Environmental Science and Technology*, *20*(10), 11551-11574.

[2]   Ali, S., Shaukat, M. A., Shakeel, Q., Raheel, M., Ullah, M. I., & Tariq, K. (2022). Application of biosurfactants as a replacement to synthetic surfactants used in pesticide industries. In *Applications of biosurfactant in agriculture* (pp. 29-44). Academic Press.

[3]   Esteban García, A. B., Szymański, K., Mozia, S., & Sánchez Pérez, J. A. (2021). Treatment of laundry wastewater by solar photo-Fenton process at pilot plant scale. *Environmental Science and Pollution Research*, *28*(7), 8576-8584.

[4]   Bolan, S., Padhye, L. P., Mulligan, C. N., Alonso, E. R., Saint-Fort, R., Jasemizad, T., ... & Bolan, N. (2023). Surfactant-enhanced mobilization of persistent organic pollutants: potential for soil and sediment remediation and unintended consequences. *Journal of Hazardous Materials*, *443*, 130189.

[5]   Nunes, R. F., & Teixeira, A. C. S. C. (2022). An overview on surfactants as pollutants of concern: Occurrence, impacts and persulfate-based remediation technologies. *Chemosphere*, *300*, 134507.

[6]   Sarkar, S., Gill, S. S., Das Gupta, G., & Kumar Verma, S. (2022). Water toxicants: a comprehension on their health concerns, detection, and remediation. *Environmental Science and Pollution Research*, *29*(36), 53934-53953.

[7]   Asio, J. R. G., Garcia, J. S., Antonatos, C., Sevilla-Nastor, J. B., & Trinidad, L. C. (2023). Sodium lauryl sulfate and its potential impacts on organisms and the environment: A thematic analysis. *Emerging Contaminants*, 29,100205.

[8]   Jena, G., Dutta, K., & Daverey, A. (2023). Surfactants in water and wastewater (greywater): Environmental toxicity and treatment options. *Chemosphere*, *341*, 140082.

[9]   Dai, H., Zhang, H., Sun, Y., Abbasi, H. N., Guo, Z., Chen, L., ... & Zhang, S. (2023). An integrated process for struvite recovery and nutrient removal from ship domestic sewage. *Water Research*, *228*, 119381.

[10]   Kumar, L., Chugh, M., Kumar, S., Kumar, K., Sharma, J., & Bharadvaja, N. (2022). Remediation of petrorefinery wastewater contaminants: A review on physicochemical and bioremediation strategies. *Process Safety and Environmental Protection*, *159*, 362-375.

[11]   Vijayalakshmi, K., Florence, J. A. K., & Arunachalam, P. (2023). Industrial Wastewater Sources and Treatment Strategies by using Bionanomaterials. In *Nanobiomaterials* (pp. 255-266). CRC Press.

[12]   Qiu, B., Shao, Q., Shi, J., Yang, C., & Chu, H. (2022). Application of biochar for the adsorption of organic pollutants from wastewater: Modification strategies, mechanisms and challenges. *Separation and Purification Technology*, 300,121925.

[13]   Kumari, P., & Kumar, A. (2023). ADVANCED OXIDATION PROCESS: A remediation technique for organic and non-biodegradable pollutant. *Results in Surfaces and Interfaces*,11, 100122.

[14] Yu, T., Chen, H., Hu, T., Feng, J., Xing, W., Tang, L., & Tang, W. (2024). Recent advances in the applications of encapsulated transition-metal nanoparticles in advanced oxidation processes for degradation of organic pollutants: A critical review. *Applied Catalysis B: Environmental*, *342*, 123401.9

[15] Priya, G. H., Shaly, A. A., Evangelin, G., & Linet, J. M. (2022). Fabrication and characterization of TiO2/CuS nanocomposites (Cu= 0.25, 0.50, and 0.75 M) utilized for the photocatalytic degradation of crystal violet dye. *Journal of Materials Research*, *37*(23), 4182-4199.

[16] Huang, Z., Wang, L., Wu, H., Hu, H., Lin, H., Qin, L., & Li, Q. (2022). Shape-controlled synthesis of CuS as a Fenton-like photocatalyst with high catalytic performance and stability. *Journal of Alloys and Compounds*, *896*, 163045.

[17] Sudhaik, A., Raizada, P., Rangabhashiyam, S., Singh, A., Nguyen, V. H., Van Le, Q., ... & Singh, P. (2022). Copper sulfides based photocatalysts for degradation of environmental pollution hazards: A review on the recent catalyst design concepts and future perspectives. *Surfaces and Interfaces*, 33,102182.

[18] Qin, Y., Kong, X., Lei, D., & Lei, X. (2018). Facial grinding method for synthesis of high-purity CuS nanosheets. *Industrial & Engineering Chemistry Research*, *57*(8), 2759-2764.

[19] Jurado, E., Fernández-Serrano, M., Nunez-Olea, J., Luzon, G., & Lechuga, M. (2006). Simplified spectrophotometric method using methylene blue for determining anionic surfactants: applications to the study of primary biodegradation in aerobic screening tests. *Chemosphere*, *65*(2), 278-285.

[20] Deb, S., & Kalita, P. K. (2021). Green synthesis of copper sulfide (CuS) nanostructures for heterojunction diode applications. *Journal of Materials Science: Materials in Electronics*, *32*(19), 24125-24137.

[21] Isik, M., Terlemezoglu, M., Gasanly, N., & Parlak, M. (2022). Structural, morphological and temperature-tuned bandgap characteristics of CuS nano-flake thin films. *Physica E: Low-dimensional Systems and Nanostructures*, *144*, 115407.

[22] Thomas, B., & Alexander, L. K. (2019). Nanoreactor based enhancement of photocatalysis with Co0. 7Zn0. 3Fe2O4@ SrTiO3 core-shell nanocomposites. *Journal of Alloys and Compounds*, *788*, 257-266.

[23] Thomas, B., & Alexander, L. K. (2018). Enhanced synergetic effect of Cr (VI) ion removal and anionic dye degradation with superparamagnetic cobalt ferrite meso–macroporous nanospheres. *Applied Nanoscience*, *8*(1), 125-135.

[24] Buttersack, C. (2019). Modeling of type IV and V sigmoidal adsorption isotherms. *Physical Chemistry Chemical Physics*, *21*(10), 5614-5626.

[25] Vuorte, M., Kuitunen, S., Van Tassel, P. R., & Sammalkorpi, M. (2023). Equilibrium state model for surfactants in oils: Colloidal assembly and adsorption. *Journal of Colloid and Interface Science*, *630*, 783-794.

[26] Rajabi, M., Keihankhadiv, S., Suhas, Tyagi, I., Karri, R. R., Chaudhary, M., ... & Singh, P. (2023). Comparison and interpretation of isotherm models for the adsorption of dyes, proteins, antibiotics, pesticides and heavy metal ions on different nanomaterials and non-

nano materials—a comprehensive review. *Journal of Nanostructure in Chemistry*, *13*(1), 43-65.

[27]   Samadi, A., Kong, L., Guo, W., Sillanpää, M., Boztepe, I., Song, C., ... & Zhao, S. (2024). Standardized methodology for performance evaluation in using polyaniline-based adsorbents to remove aqueous contaminants. *Journal of Environmental Chemical Engineering*, 112650.

[28]   Mudhoo, A., & Pittman Jr, C. U. (2023). The Dubinin-Radushkevich Models: Dissecting the ps/p to cs/ce Replacement in Solid-aqueous Interfacial Adsorption and Tracking the Validity of E= 8 kJ mol–1 for Assigning Sorption Type. *Chemical Engineering Research and Design*.

[29]   Hu, Q., Lan, R., He, L., Liu, H., & Pei, X. (2023). A critical review of adsorption isotherm models for aqueous contaminants: Curve characteristics, site energy distribution and common controversies. *Journal of Environmental Management*, *329*, 117104.

[30]   Mohamed, L. A., Aniagor, C. O., Aly, A. A., & Hashem, A. (2023). Removal of chromium (VI) and acid orange 142 dye from contaminated wastewater using bio-waste mycelium of Aspergillus ustus: extraction, isotherms and kinetics studies. *Water Conservation Science and Engineering*, *8*(1), 31.

[31]   Zhu, B. Y., & Gu, T. (1989). General isotherm equation for adsorption of surfactants at solid/liquid interfaces. Part 1. Theoretical. Journal of the Chemical Society, Faraday Transactions 1: Physical Chemistry in Condensed Phases, 85(11), 3813-3817.

[32]   Fuerstenau, D. W. (2002). Equilibrium and nonequilibrium phenomena associated with the adsorption of ionic surfactants at solid–water interfaces. *Journal of colloid and interface science*, *256*(1), 79-90.

[33]   Aragaw, T. A., & Alene, A. N. (2022). A comparative study of acidic, basic, and reactive dyes adsorption from aqueous solution onto kaolin adsorbent: Effect of operating parameters, isotherms, kinetics, and thermodynamics. *Emerging Contaminants*, *8*, 59-74.

[34]   Abumelha, H. M., Alzahrani, S. O., Alrefaee, S. H., Al-bonayan, A. M., Alkhatib, F., Saad, F. A., & El-Metwaly, N. M. (2023). Evaluation of tetracycline removal by magnetic metal organic framework from aqueous solutions: Adsorption isotherm, kinetics, thermodynamics, and Box-Behnken design optimization. *Journal of Saudi Chemical Society*, 27,101706.

[35]   Umeh, A. C., Hassan, M., Egbuatu, M., Zeng, Z., Al Amin, M., Samarasinghe, C., & Naidu, R. (2023). Multicomponent PFAS sorption and desorption in common commercial adsorbents: Kinetics, isotherm, adsorbent dose, pH, and index ion and ionic strength effects. *Science of The Total Environment*, *904*, 166568.

[36]   Boushara, R. S. H., Rahim, A. R. A., Johari, K., Rabat, N. E., Khan, A. S., & Saman, N. (2023). Effect of various solvents on the structure of silica nanocapsules synthesised for anionic and cationic dyes adsorption from aqueous solution. *Journal of Environmental Chemical Engineering*, *11*(5), 110981.

[37]   Wibowo, N., Setyadhi, L., Wibowo, D., Setiawan, J., & Ismadji, S. (2007). Adsorption of benzene and toluene from aqueous solutions onto activated carbon and its acid and

heat-treated forms: influence of surface chemistry on adsorption. *Journal of hazardous materials*, *146*(1-2), 237-242.

[38]   Shah, A., Shahzad, S., Munir, A., Nadagouda, M. N., Khan, G. S., Shams, D. F., ... & Rana, U. A. (2016). Micelles as soil and water decontamination agents. *Chemical reviews*, *116*(10), 6042-6074.

[39]   Mirzaee, E., & Sartaj, M. (2022). Activated carbon-based magnetic composite as an adsorbent for removal of polycyclic aromatic hydrocarbons from aqueous phase: Characterization, adsorption kinetics and isotherm studies. *Journal of Hazardous Materials Advances*, *6*, 100083.

[40]   Wang, J., & Guo, X. (2020). Adsorption kinetic models: Physical meanings, applications, and solving methods. *Journal of Hazardous materials*, *390*, 122156.

[41]   López-Luna, J., Ramírez-Montes, L. E., Martinez-Vargas, S., Martínez, A. I., Mijangos-Ricardez, O. F., González-Chávez, M. D. C. A., ... & Vázquez-Hipólito, V. (2019). Linear and nonlinear kinetic and isotherm adsorption models for arsenic removal by manganese ferrite nanoparticles. *SN Applied Sciences*, *1*(8), 1-19.

[42]   Randhawa, N. S., Das, N. N., & Jana, R. K. (2014). Adsorptive remediation of Cu (II) and Cd (II) contaminated water using manganese nodule leaching residue. *Desalination and Water Treatment*, *52*(22-24), 4197-4211.

[43]   Yakar, A., Ünlü, A., Yeşilçayır, T., & Bıyık, İ. (2020). Kinetics and thermodynamics of textile dye removal by adsorption onto iron oxide nanoparticles. *Nanotechnology for Environmental Engineering*, *5*(1), 1-12.

[44]   Lima, E. C., Gomes, A. A., & Tran, H. N. (2020). Comparison of the nonlinear and linear forms of the van't Hoff equation for calculation of adsorption thermodynamic parameters (Δ S° andΔ H°). *Journal of Molecular Liquids*, *311*, 113315.

[45]   Al-Harby, N. F., Almutairi, R. S., Elmehbad, N. Y., & Mohamed, N. A. (2023). A novel O-carboxymethyl chitosan-based hydrogel of an outstanding adsorption performance for removal of cationic Basic Red 12 dye from its aqueous solution. *Polymer Engineering & Science*, *63*(8), 2336-2353.

[46]   Myers, A. L. (2002). Thermodynamics of adsorption in porous materials. *AIChE journal*, *48*(1), 145-160.

[47]   Saha, P., & Chowdhury, S. (2011). Insight into adsorption thermodynamics. *Thermodynamics*, *16*, 349-364.

[48]   Lombardo, S., & Thielemans, W. (2019). Thermodynamics of adsorption on nanocellulose surfaces. *Cellulose*, *26*(1), 249-279.

[49]   Koopal, L. K., Lee, E. M., & Böhmer, M. R. (1995). Adsorption of cationic and anionic surfactants on charged metal oxide surfaces. *Journal of colloid and interface science*, *170*(1), 85-97.

[50]   Pham, T. D., Kobayashi, M., & Adachi, Y. (2015). Adsorption of anionic surfactant sodium dodecyl sulfate onto alpha alumina with small surface area. *Colloid and Polymer Science*, *293*(1), 217-227.

[51]   Nguyen, T. M. T., Do, T. P. T., Hoang, T. S., Nguyen, N. V., Pham, H. D., Nguyen, T. D., ... & Pham, T. D. (2018). Adsorption of anionic surfactants onto alumina: characteristics,

mechanisms, and application for heavy metal removal. *International Journal of Polymer Science*, 2018(11), *2018*.

[52]   Shami, S., Dash, R. R., Verma, A. K., Dash, A. K., & Pradhan, A. (2020). Adsorptive removal of surfactant using dolochar: A kinetic and statistical modelling approach. *Water Environment Research*, *92*(2), 222-235.

[53]   Gupta, S., Pal, A., Ghosh, P. K., & Bandyopadhyay, M. (2003). Performance of waste activated carbon as a low-cost adsorbent for the removal of anionic surfactant from aquatic environment. *Journal of Environmental Science and Health, Part A*, *38*(2), 381-397.

[50]   Rahmani, Z., & Samadi, M. T. (2017). Preparation of magnetic multi-walled carbon nanotubes to adsorb sodium dodecyl sulfate (SDS). *Avicenna Journal of Environmental Health Engineering*, *4*(1), 61902-61902.

[54]   Pal, A., Pan, S., & Saha, S. (2013). Synergistically improved adsorption of anionic surfactant and crystal violet on chitosan hydrogel beads. *Chemical Engineering Journal*, *217*, 426-434.

[55]   Gao, X., & Chorover, J. (2010). Adsorption of sodium dodecyl sulfate (SDS) at ZnSe and α-Fe2O3 surfaces: Combining infrared spectroscopy and batch uptake studies. *Journal of colloid and interface science*, *348*(1), 167-176.

[56]   Sen, T. K., Thi, M. T., Afroze, S., Phan, C., & Ang, M. (2012). Removal of anionic surfactant sodium dodecyl sulphate from aqueous solution by adsorption onto pine cone biomass of Pinus Radiate: equilibrium, thermodynamic, kinetics, mechanism and process design. *Desalination and Water Treatment*, *45*(1-3), 263-275.

[57]   Bhandari, P. S., & Gogate, P. R. (2019). Adsorptive removal of sodium dodecyl sulfate using activated coconut shell-based adsorbent: Kinetic and thermodynamic study. *Desalin. Water Treat*, *165*, 111-123.

[58]   Moussavi, G., Shekoohiyan, S., & Mojab, S. (2016). Adsorption capacity of NH4Cl-induced activated carbon for removing sodium dodecyl sulfate from water. *Desalination and Water Treatment*, *57*(24), 11283-11290.

[59]   Vidyarajan, N., & Alexander, L. K. (2018). Strain induced optical properties of perovskite LaFeO3. *Materials Research Express*, *6*(1), 015610.

[60]   Han, M., Wang, H., Jin, W., Chu, W., & Xu, Z. (2023). The performance and mechanism of iron-mediated chemical oxidation: Advances in hydrogen peroxide, persulfate and percarbonate oxidation. *Journal of Environmental Sciences*, *128*, 181-202.

[61]   Tian, Y., Deng, D., Xu, L., Li, M., Chen, H., Wu, Z., & Zhang, S. (2023). Strategies for Sustainable Production of Hydrogen Peroxide via Oxygen Reduction Reaction: From Catalyst Design to Device Setup. *Nano-Micro Letters*, *15*(1), 1-45.

[62]   Mi, L., Wei, W., Zheng, Z., Gao, Y., Liu, Y., Chen, W., & Guan, X. (2013). Tunable properties induced by ion exchange in multilayer intertwined CuS microflowers with hierarchal structures. *Nanoscale*, *5*(14), 6589-6598.

[63]   Li, Z., Mi, L., Chen, W., Hou, H., Liu, C., Wang, H., ... & Shen, C. (2012). Three-dimensional CuS hierarchical architectures as recyclable catalysts for dye decolorization. *CrystEngComm*, *14*(11), 3965-3971.

[64]   Hussain, S., Aneggi, E., & Goi, D. (2021). Catalytic activity of metals in heterogeneous Fenton-like oxidation of wastewater contaminants: a review. *Environmental Chemistry Letters*, *19*(3), 2405-2424.

[65]   Kıran, I., Bektaş, N., Cengiz Yatmaz, H., & Tekbaş, M. (2013). Photocatalytic Fenton oxidation of sodium dodecyl sulfate solution using iron-modified zeolite catalyst. *Desalination and Water Treatment*, *51*(28-30), 5768-5775.

[66]   Panich, N. M., Seliverstov, A. F., & Ershov, B. G. (2008). Photooxidative decomposition of sodium dodecyl sulfate in aqueous solutions. *Russian Journal of Applied Chemistry*, *81*(12), 2104-2107.

[67]   Aoudjit, F., Cherifi, O., & Halliche, D. (2019). Simultaneously efficient adsorption and photocatalytic degradation of sodium dodecyl sulfate surfactant by one-pot synthesized TiO2/layered double hydroxide materials. *Separation Science and Technology*, *54*(7), 1095-1105.

[68]   Yeldho, D., Rebello, S., & Jisha, M. S. (2011). Plasmid-mediated biodegradation of the anionic surfactant sodium dodecyl sulphate, by Pseudomonas aeruginosa S7. *Bulletin of environmental contamination and toxicology*, *86*(1), 110-113.

[69]   Nguyen, H. M., Phan, C. M., & Sen, T. (2016). Degradation of sodium dodecyl sulfate by photoelectrochemical and electrochemical processes. *Chemical Engineering Journal*, *287*, 633-639.

[70]   Dehghani, M. H., Zarei, A., & Yousefi, M. (2019). Efficiency of ultrasound for degradation of an anionic surfactant from water: Surfactant determination using methylene blue active substances method. *MethodsX*, *6*, 805-814.

CHAPTER 5

Phosphate Removal and Degradation of Congo Red using MnS.
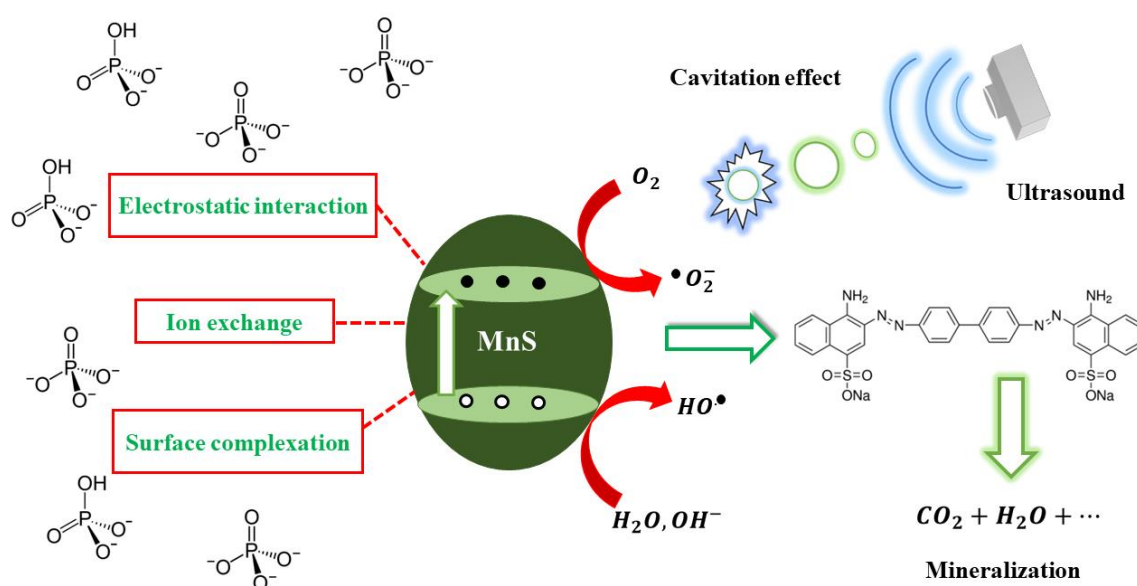
Highlights

- *MnS adsorbent: demonstrated as a replacement for La-based phosphate removal.*

- *Studying the effect of polymorphism on adsorption properties and efficiency.*

- *γ-MnS showed superior phosphate removal, with a capacity of 160.73 mg P/g.*

- *Piolet report on efficient sonocatalytic degradation of Congo red dye.*

- *MnS nanomaterials synthesized for dual functionality: adsorption and sonocatalysis.*

ABSTRACT

Naturally abundant, environmentally friendly alternatives for replacing the expensive lanthanum-based phosphate removal technique are sought after. Solocatalysis is an emerging area for water remediation. This study introduces a dual-functional MnS nanomaterial for removing phosphate ions and Congo Red textile dye. MnS nanomaterials were synthesized via a hydrothermal route. Batch adsorption experiments revealed a phosphate adsorption capacity of 160.73 mg P/g, commendable for adsorbent in its bare form. Thermodynamic parameters of the process indicated a spontaneous, exothermic process, confirming favourable adsorption. FTIR analysis confirmed the adsorption mechanism, which includes electrostatic attraction, surface complexation, and ion exchange. MnS maintained its adsorption capacity despite competing ions, demonstrating a selective affinity for phosphate ions. MnS showed high sonocatalytic efficiency, degrading Congo Red dye within 10 minutes of ultrasonic irradiation. The degradation mechanism of Congo Red dye in the sonocatalytic process is proposed. This novel metal chalcogenide material exhibits exceptional affinity for phosphate ions and Congo Red dye molecules, surpassing La-based adsorbents in efficacy. The results suggest that MnS nanomaterials are promising for practical applications in phosphate removal and textile dye degradation from wastewater.

Keywords: *phosphate removal; congo red; sonocatalysis; polymorphic adsorbents; chalcogenide.*

5.1. INTRODUCTION

Rapid industrialization and population growth have caused severe water pollution, particularly from the food, textile, cosmetics, rubber, drug, and pharmaceutical industries, with inorganic phosphate ions and textile dyes being especially concerning due to their high concentrations and significant environmental impact [1,2,3]. Technologies like reverse osmosis, chemical precipitation, ion exchange, electrocoagulation, and membrane filtration effectively remove phosphorus and dyes but are costly, chemical-intensive, inefficient, and complex [4]. In contrast, adsorption and catalysis based on advanced oxidation processes (AOP) offer low operational costs, minimal energy consumption, high efficiency, and easy regeneration in water remedial applications [5]. Modified adsorption carriers with lanthanides are frequently used for phosphate removal due to the strong affinity between lanthanum and phosphorus [6]. Despite their effectiveness, La-based adsorbents are costly and scarce and pose environmental and health risks due to potential ion leaching, making large-scale applications challenging [7].

Common wastewater treatment materials and methods usually target single contaminants due to their specific chemical affinities [8]. A comprehensive approach for simultaneous multi-pollutant removal would enhance treatment systems. Developing materials with a broad affinity for pollutants, especially phosphate ions and dyes simultaneously, can significantly improve efficiency, streamline processes, and potentially revolutionize wastewater remediation.

Metal chalcogenides, known for their high adsorption capacity and catalytic efficiency, are ideal for environmental remediation. Manganese sulfide (MnS), with natural abundance, light-absorbing capabilities, excellent charge separation properties and eco-friendly synthesis, is a promising alternative to La-based adsorbents [9,10]. MnS's catalytic properties can degrade textile dyes in wastewater [11]. However, its adsorptive properties and sonocatalytic performance have been underexplored. Mn^{2+} ions can act as active species in advanced oxidation processes, making MnS a promising material for catalytic and adsorptive systems [12,13].

MnS exists in three crystal phases: α-MnS, β-MnS, and γ-MnS. Crystal phases probably influence the morphology, active sites, and charge separation in advanced oxidation processes (AOPs), affecting catalytic and adsorptive performance [14,15]. Understanding the relationship between crystalline phase changes and adsorptive activity

is crucial for improving water remediation [16]. In this study, we demonstrate how the crystalline phase of MnS affects adsorption and catalytic degradation activity.

In this study, we report our investigations on two crystalline phases of MnS: cubic α-MnS and hexagonal γ-MnS. The objective is to assess the utility of MnS for removing phosphate ions and the textile dye Congo red from an aqueous medium. Selective adsorption of MnS towards phosphate ions is explored. We examined the catalytic activity of polymorphic forms of MnS in degrading Congo red under ultrasound irradiation. Experimental evidence and insights into the significance of crystal phases and the effect of ultrasound-induced electron-hole pairs and active radicals in catalysis are provided. Our study elucidates the mechanism by which MnS effectively removes phosphate from aqueous solutions, offering theoretical and practical support for future research on transition metal chalcogenides.
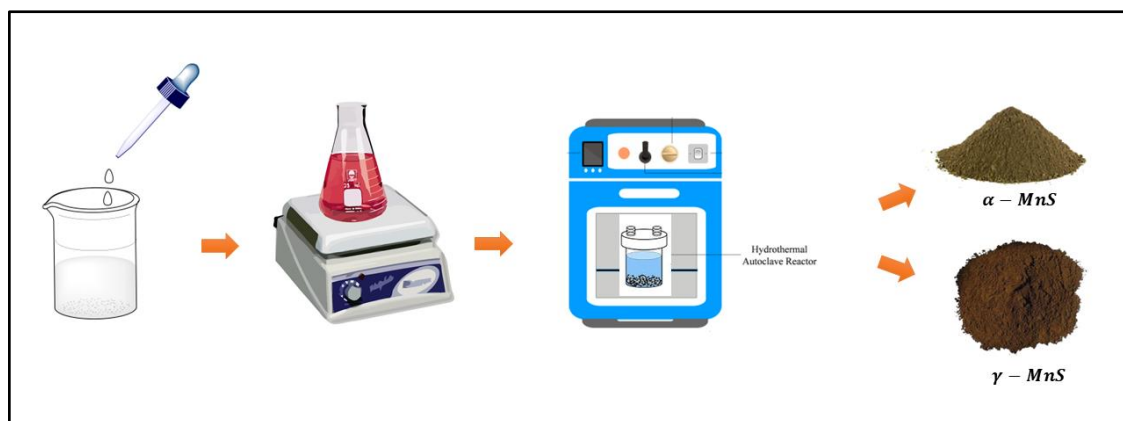
5.2. EXPERIMENTAL

5.2.1. Reagents and chemicals

Manganese chloride (MnCl$_2$ > 97%, Alfa Aesar), Sodium sulphide (Na$_2$S > 97%, Fisher Scientific), Potassium phosphate dibasic anhydrite (K$_2$HPO$_4$ > 99%, SRL), Congo Red (C$_{32}$H$_{22}$N$_6$Na$_2$O$_6$S$_2$, > 99%, Spectrochem). All chemicals used were of analytical grade. Deionized water was used as a solvent in all synthesis and other experiments.

5.2.2. Synthesis of MnS nanomaterials

The MnS nanostructures were synthesized using the facile hydrothermal method by varying the reaction temperature and time. Typically, MnCl$_2$ and Na$_2$S were dissolved in 30 mL of deionized water in the same molar ratio. The Na$_2$S aqueous solution was then added dropwise into the MnCl$_2$ solution. The solution was vigorously stirred for 2 hours. Next, the mixture was hydrothermally treated in an autoclave at 180°C for 8 hours and then allowed to cool naturally into room temperature. The precipitate was collected by centrifugation, then washed, and dried at 50°C for 12 hours to obtain α-MnS. For the synthesis of γ-MnS, the experiment was repeated at 180°C for 16 hours. The schematic representation of synthesis of MnS nanostructures are shown in Fig.5.1.

Fig.5.1. *The schematic representation of synthesis of MnS nanostrutcures.*

5.2.3. Batch adsorption study

The adsorption of phosphate onto MnS nanostructures was evaluated through a series of batch experiments. In each experiment, 15 mg of MnS nanomaterials were added to 30 mL of phosphate solution in a 100 mL conical flask. This flask was then placed on a mechanical shaker at 150 rpm for a predetermined time at a specified temperature. To control the competitive anionic strength, a specific amount of four common anions (Cl^-, NO_3^- , SO_4^{2-}, and HCO_3^-) was added as needed. Once adsorption reached equilibrium, the suspensions were separated, and the phosphate concentration in the residues was measured using the ammonium vanadomolybdophosphate color development method.

5.2.4. Sonocatalytic activity of MnS

The sonocatalytic activity of the synthesized MnS was studied through the degradation of Congo Red (CR). For each experiment, 25 mg of catalyst was added to a 50 mL CR solution (80 ppm). Before irradiation, the suspension was stirred in the dark for 10 minutes to achieve adsorption–desorption equilibrium. The suspension was then irradiated with ultrasonic waves. Approximately 3 mL of the solution was removed from the reaction medium at successive intervals and centrifuged to remove the catalyst. The supernatant solution was examined using UV–visible spectroscopy to estimate the concentration of Congo Red, utilizing a JASCO V-750 spectrophotometer.

5.3. RESULTS AND DISCUSSION

5.3.1. Structural characterization

The X-ray diffraction pattern in Fig.5.2. shows the synthesized MnS nanostructures. The XRD peaks of α-MnS predict a cubic structure (space group: Fm-3m), and γ-MnS show a hexagonal phase (space group: P63mc) [17, 18, 19]. The

crystallite size of the samples was calculated using Scherer's equation $D = 0.9\lambda/(\beta \cos\theta)$ where λ is the X-ray wavelength ($\lambda = 1.5418$ Å for Cu-Kα radiation), β is the full width at half maximum (FWHM) and θ the Bragg's angle. The average crystallite size of the samples was estimated as 40.2 ± 2.8 nm and 38.6 ± 5.6 nm respectively, for α-MnS and γ-MnS.
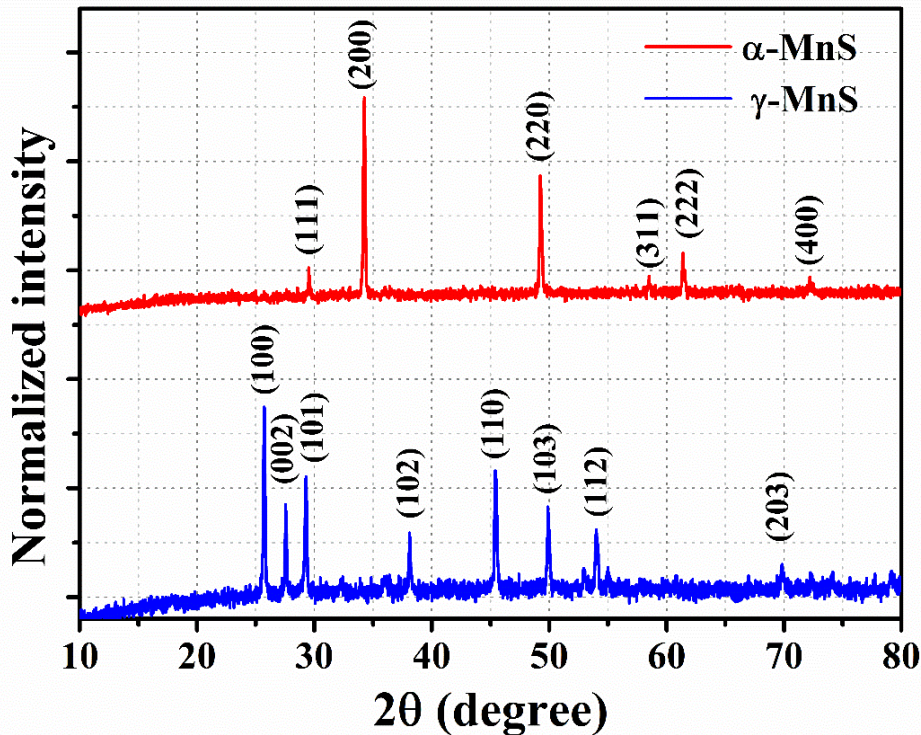
Fig.5.2. *XRD pattern of synthesized samples. α-MnS exhibits a cubic crystal system (space group: Fm-3m-JCPDS No.06-0518), γ-MnS exhibits a hexagonal phase (space group: P63mc- (JCPDS No. 40-1289).*

5.3.2. Morphological analysis

The morphology of the synthesized samples was characterized using FE-SEM. Fig.5.3 show the FE-SEM images of α-MnS, revealing a nano-almond-like morphology with a uniform size of about 50 nm. Fig.5.4. display the FE-SEM images of γ-MnS, which exhibit a hexagonal nano-tile-like morphology with a width of approximately 3 μm and a thickness in the nanometer range.
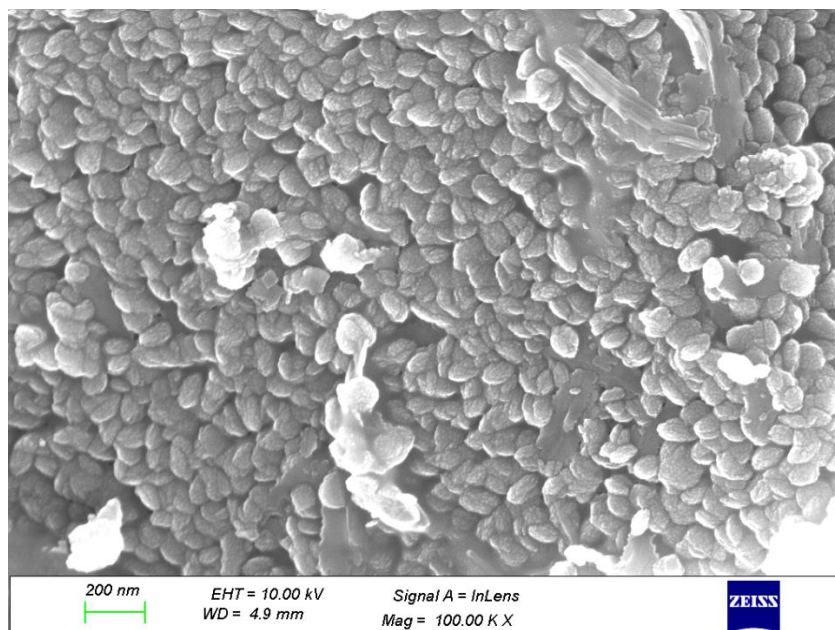
Fig.5.3. *The FESEM images of α-MnS reveal a nanostructure structure resembling nano almond, showcasing their unique morphology.*

Fig.5.4. *The FESEM image of γ-MnS unveils an array of hexagonal nano-tiles, creating a mosaic-like morphology.*
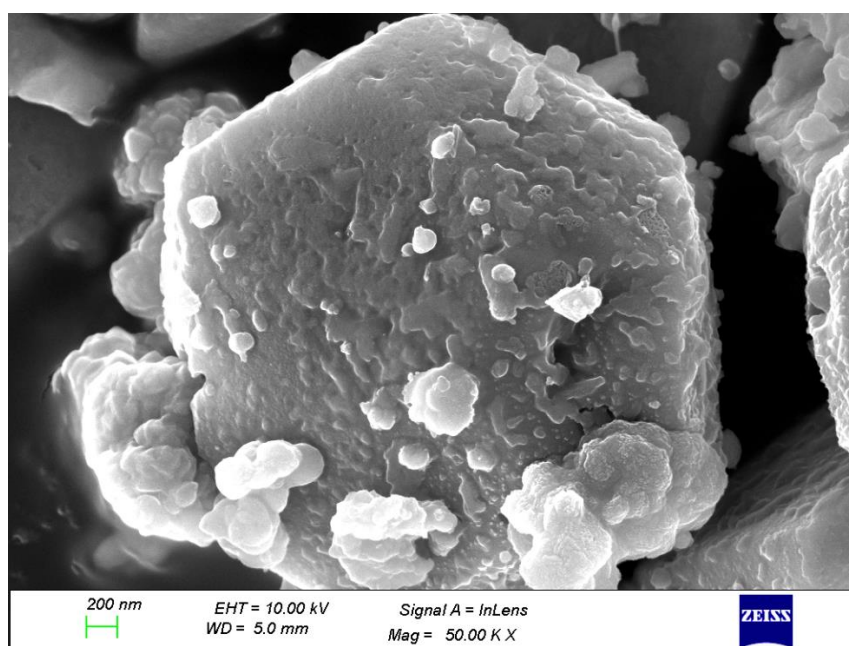
5.3.3. Surface area and porosity analysis.

Nitrogen adsorption–desorption measurements were carried out to determine specific surface area, pore volume and pore diameter, and the results are illustrated in Fig.5.5. The isotherms for the samples exhibit a classical type II pattern with a hysteresis loop observed in the relative pressure (P/P_0) range of 0.8-1.0, indicating the presence of

surface mesopores and interparticle pores of significant size due to the composite nature of the material [20]. The linear fit of $P/V_a(P_0-P)$ versus P/P_0 data points for the estimation of BET surface area is shown in Fig.5.6. The surface area of the sample is estimated as 1.61 ± 0.11 m^2/g and 10.71 ± 0.12 m^2/g for α-MnS and γ-MnS respectively. The pore size distribution is examined using a BJH analysis. The mesoporous pore distribution is observed in both samples. This is shown in Fig.5.6.
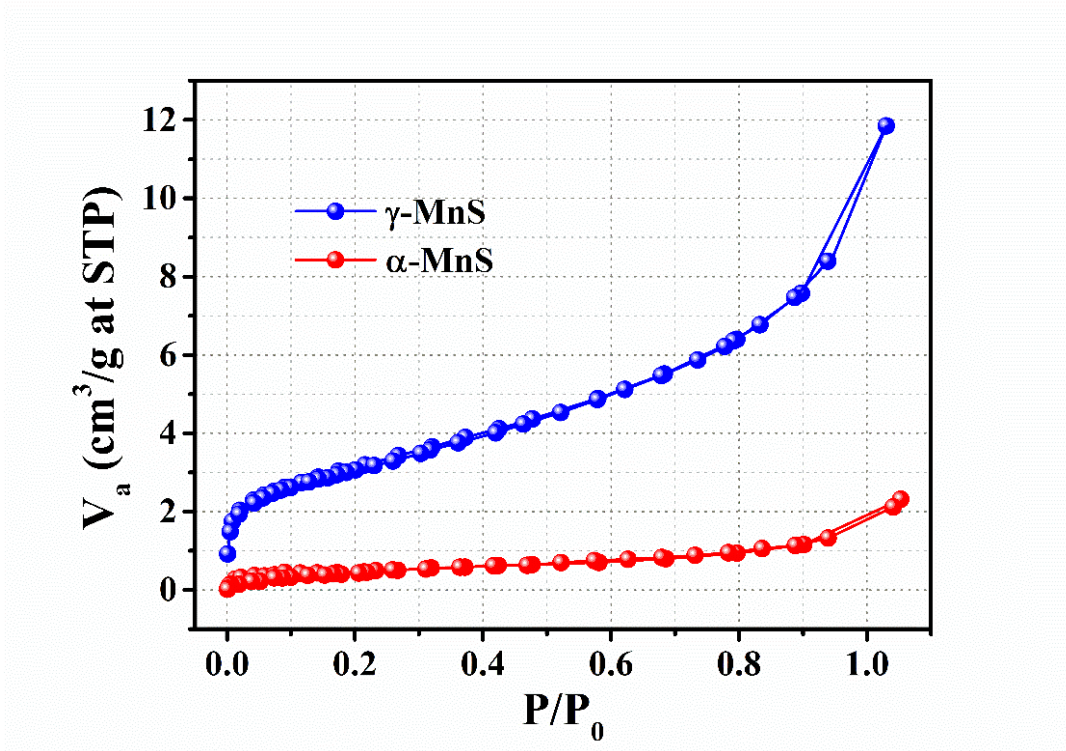
Fig.5.5. *N$_2$ adsorption-desorption isotherms display a type II pattern with a hysteresis loop at P/P$_0$ = 0.8-1.0, signifying surface mesopores and substantial interparticle pores from the composite material.*
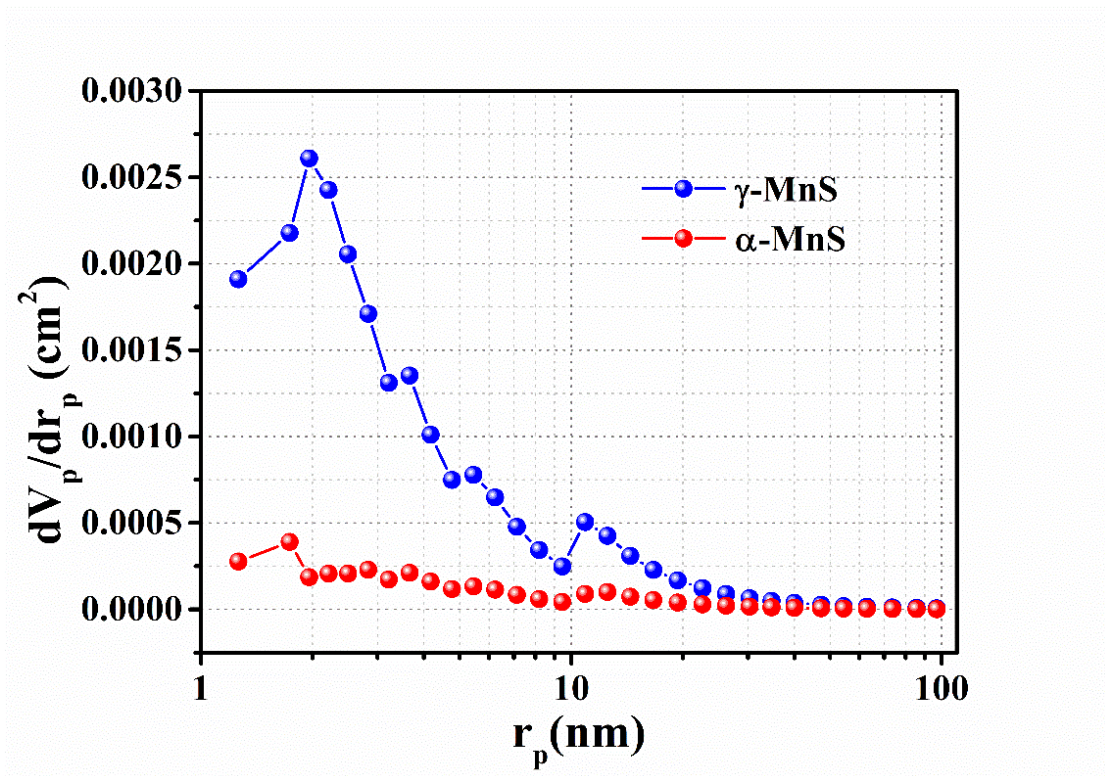
Fig.5.6. *The BJH pore distribution curve, indicating mesoporous pore distribution.*
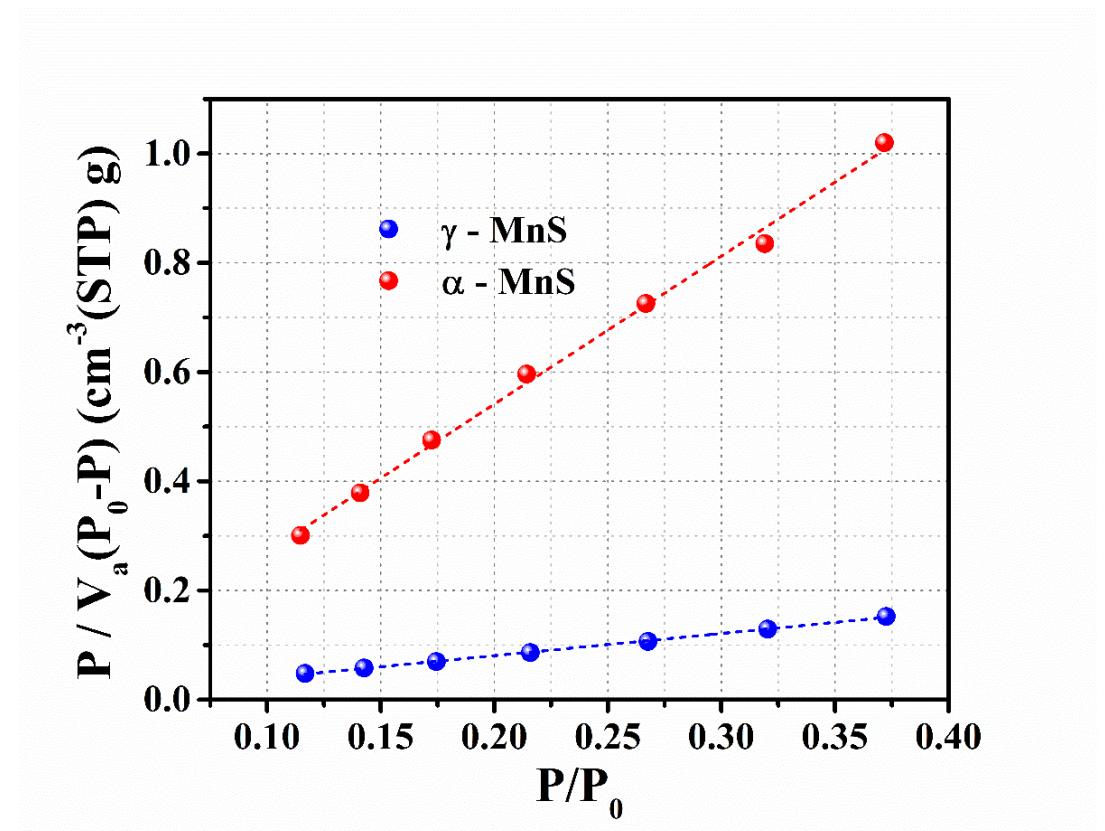
Fig.5.7. *The linear fit of $P/V_a(P_0-P)$ versus P/P_0 data points for the estimation of BET surface area.*

The surface acidity of the catalysts was studied using temperature-programmed desorption of NH₃ (NH₃-TPD), and the results are shown in Fig.5.8. The α-MnS desorption profile exhibits a weak peak around 525 K, a broad high-temperature shoulder up to 660 K, and an intense peak near 811 K. The peaks near 525 K and 660 K indicate weaker acid sites. In comparison, the high-temperature shoulder up to 811 K suggests a range of stronger acid sites, reflecting the heterogeneous nature of the catalyst surface with varying acid site strengths.

In contrast, the γ-MnS TPD profile reveals distinct peaks at approximately 514 K, 562 K, and 704 K, along with intense high-temperature peaks around 809 K and shoulder peaks near 783 K and 860 K. This indicates a complex distribution of both weak and strong acid sites, attributed to the heterogeneous surface, varied surface species, and specific preparation and treatment conditions. Consequently, γ-MnS has a higher number of active acid sites than α-MnS, with estimated values presented in Table.5.1.
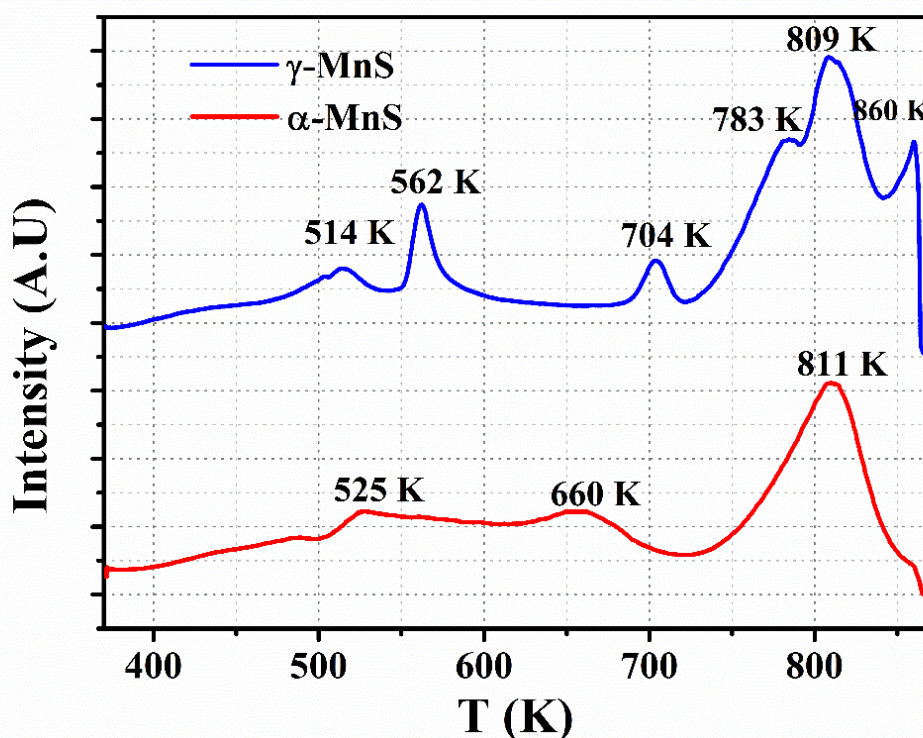
Fig.5.8*. NH₃-temperature-programmed desorption (TPD) profiles were obtained for the samples.*

Table.5.1. *The table shows the estimated values of acid sites on MnS nanostructures.*

Sample	Peak position (K)	Active sites (mmol/g)
$\gamma - MnS$	514	1.41 ± 0.11
	562	1.19 ± 0.08
	704	0.58 ± 0.03
	783	2.30 ± 0.12
	809	3.31 ± 0.13
	860	1.27 ± 0.10
$\alpha - MnS$	525	1.71 ± 0.09
	660	0.89 ± 0.05
	811	2.03 ± 0.13

5.3.4. Adsorption studies

The batch adsorption experiments were carried out to study the affinity of phosphate on MnS and to estimate its maximum adsorption capacity. The phosphate adsorption capacities of as-synthesized MnS nanostructures were investigated by varying the initial phosphate ion concentration. The adsorption capacities of both adsorbents showed a rapid increase with initial phosphate concentrations from 10 mg P/L to 100 mg P/L, followed by a plateau. The maximum adsorption densities were estimated as 160.73 ± 8.37 mg P/g for γ-MnS and 128.31 ± 6.12 mg P/g for α-MnS. Compared to the adsorption densities of various adsorbents used for phosphate ion removal (Table.5.2), the values obtained for MnS are relatively high, making it highly suitable for water remediation applications.

Langmuir, Freundlich, and Temkin models were employed to describe the isotherm data, aiming to further understand the adsorption behaviour and mechanism of phosphate adsorption onto MnS nanostructures. Their non-linear fitting curves and

parameters are summarised in Fig.5.9. & Fig.5.10. and Table.5.2, respectively. The Langmuir model indicated homogeneous monolayer chemisorption without lateral or vertical competing forces among adsorbed molecules, while the Freundlich model suggested multilayer physisorption on a heterogeneous surface [21]. The high non-linear correlation coefficients ($R^2 > 0.947$) for Langmuir and Freundlich models demonstrated that phosphate adsorption involved multiple mechanisms. The Temkin model, which assumes uniformly distributed binding energy and decreasing adsorption energy with increased surface coverage, also fits the data well, indicating the involvement of chemical forces in the adsorption process [22]. The positive Temkin constant A_T for both isotherms suggests that the adsorption process is exothermic [23].

Table5.2. *The estimated parameters of the various isotherm models using the non-linear curve fitting.*

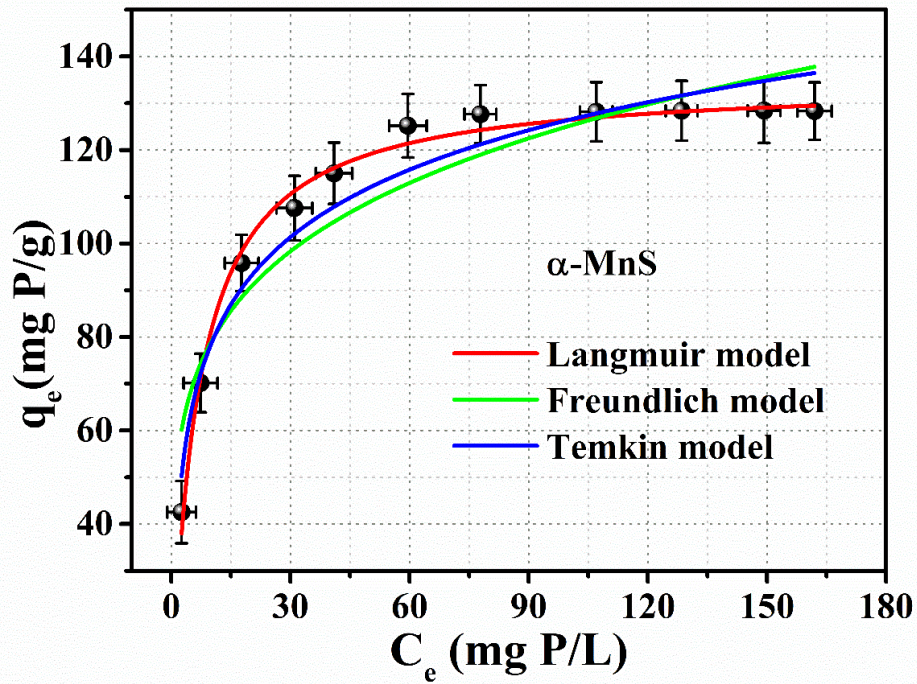| Isotherm model	Fitted parameters	$\alpha - MnS$	$\gamma - MnS$
Langmuir model $$q_e = \frac{q_m K_L C_e}{1 + K_L C_e}$$	$q_m \ (mg\,g^{-1})$	134.72 ± 1.38	201.78 ± 4.91
	$K_L (\times 10^{-2} \mathrm{L}\,mg^{-1})$	2.99 ± 0.17	15.24 ± 0.93
	R^2	0.9958	0.9914
Freundlich model $$q_e = K_F C_e^{\frac{1}{n}}$$	$K_F (L mg^{-1})$	49.78 ± 5.91	18.25 ± 3.26
	n	4.99 ± 0.68	2.19 ± 0.21
	R^2	0.9437	0.8836
Temkin model $$q_e = \left(\frac{RT}{b_T}\right) \ln(A_T C_e)$$	b_T	121.05 ± 8.89	59.58 ± 2.32
	A_T	4.33 ± 1.70	0.33 ± 0.02
	R^2	0.9859	0.9479

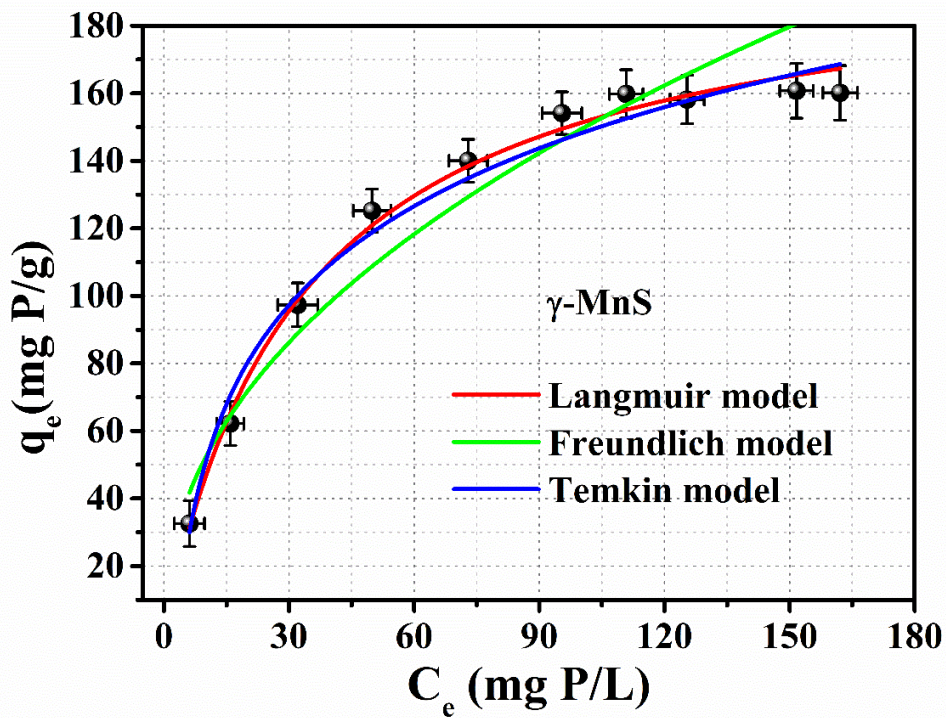**Fig.5.9.** *The non-linear fit of Langmuir, Freundlich and Temkin isotherm model on the sample α-MnS.*

Fig.5.10. *The non-linear fit of Langmuir, Freundlich and Temkin isotherm model on the sample γ-MnS.*

5.3.5. Adsorption kinetics

Fig. 5.11. illustrates the amount of phosphate adsorbed on MnS nanostructures over time, showing that γ-MnS had a significantly higher adsorption capacity than α-MnS regardless of contact time. The adsorption kinetics were analysed using pseudo-first-order and pseudo-second-order models. The fitting curves Fig.5.11. indicated that the pseudo-first-order model better matched the experimental data with higher correlation coefficients (R^2 = 0.98 and 0.96). This result suggests that chemisorption, involving electron exchange or sharing to form covalent bonds or new complexes between MnS and phosphate, governed the adsorption process [24]. The estimated parameters of the various kinetic models are shown in Table.5.3.
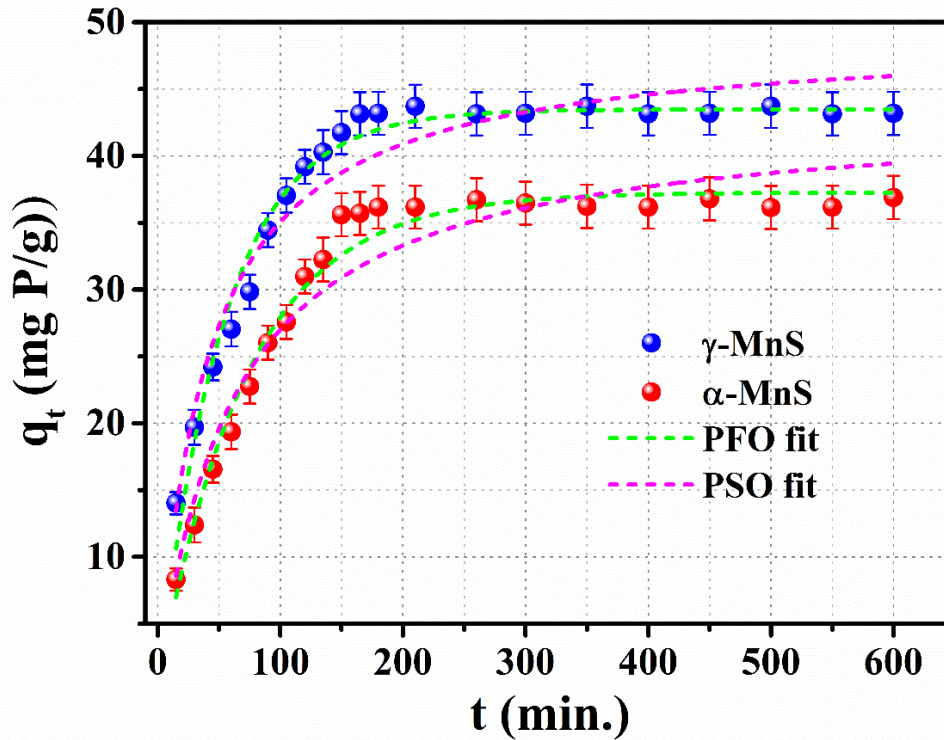
Fig.5.11. *Non-linear fit of PFO and PSO kinetic models. (C_0 = 20 ppm, dosage = 0.5g/L, pH= ~7, T = 303 K).*

The intraparticle and film diffusion models were also applied to fit the kinetics data of phosphate adsorption by MnS nanostructure [25]. Fig.5.12. shows the linear fit of the intraparticle diffusion model for phosphate adsorption onto MnS nanostructures, divided into two stages: (i) liquid diffusion, where phosphate ions transfer from the solution to the outer surfaces of MnS, and (ii) adsorption equilibrium, where phosphate ions bind to the active sites of MnS.
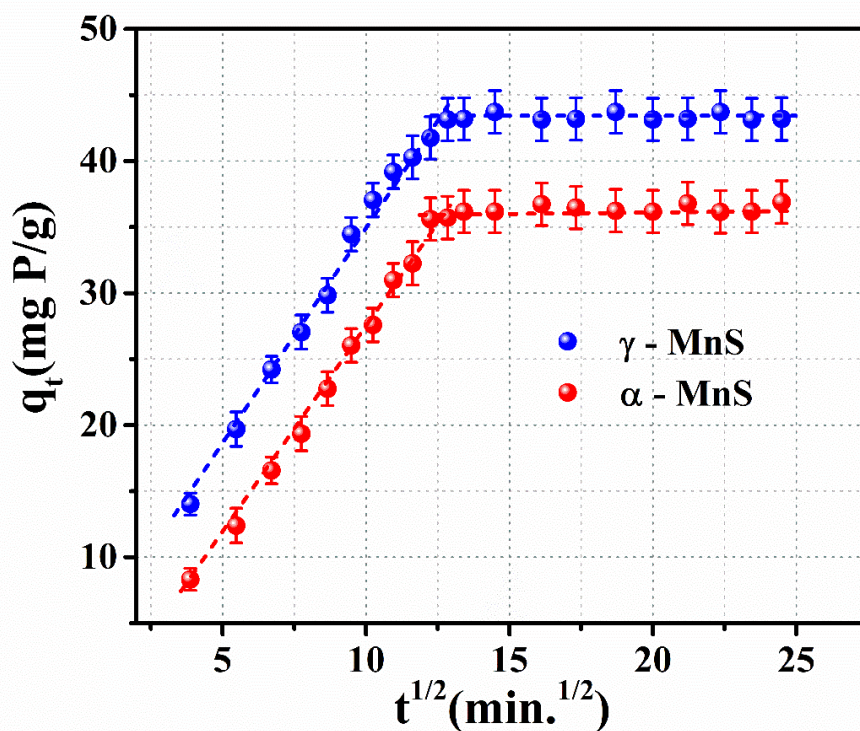
Fig.5.12. *The linear fit of intra-particle diffusion model. (C₀ = 20 ppm, dosage = 0.5g/L, pH= ~7, T = 303 K).*
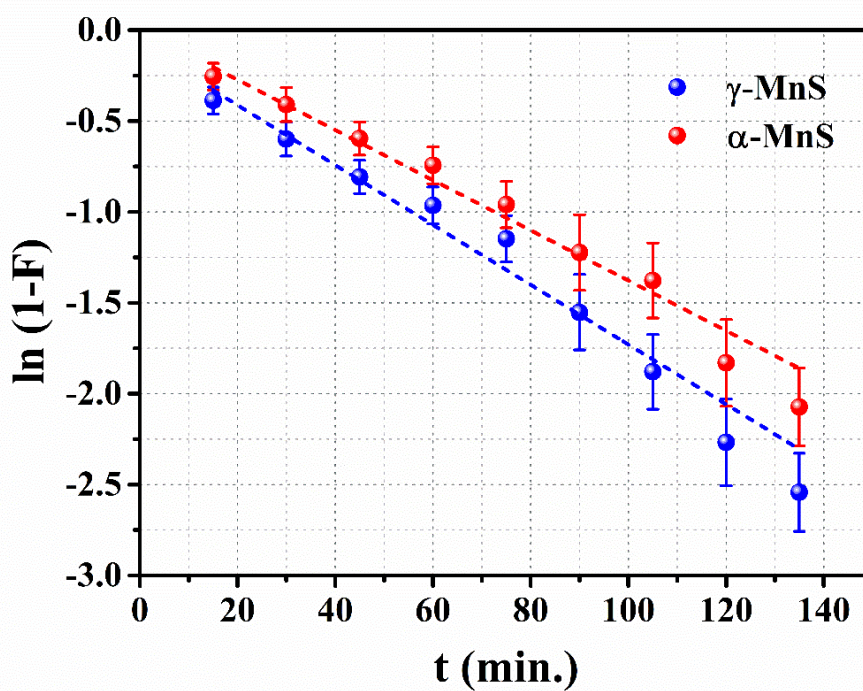

Fig.5.13. *The linear fit of film diffusion model. (C₀ = 20 ppm, dosage = 0.5g/L, pH= ~7, T = 303 K).*

The kinetic data were also examined using the liquid film model, with the linear fit shown in Fig.5.13. This model suggests that the rate-determining step is the diffusion of adsorbate molecules through the liquid film surrounding the adsorbent particles [27]. The rate constants obtained from the linear fit are 0.013 ± 0.001 min^{-1} and 0.016 ± 0.001 min^{-1}, with corresponding reduced square values of 0.9754 and 0.9654, indicating a strong fit. Compared to the intraparticle diffusion model, this superior fit underscore the significance of the liquid film boundary layer in controlling the adsorption rate under the given experimental conditions.

Table.5.3. The estimated parameters of the various adsorption kinetic models using the linear curve fitting.

Kinetic model	Fitted parameters	$\alpha - MnS$	$\gamma - MnS$
Pseudo-first-order kinetics $$q_t = q_e(1 - e^{-k_1 t})$$	$q_e \ (mg g^{-1})$	37.26 ± 0.51	43.48 ± 0.61
	k_1 $(\times 10^{-2} min.^{-1})$	1.38 ± 0.05	1.86 ± 0.01
	R^2	0.9858	0.9756
Pseudo-second-order kinetics $$q_t = \frac{k_2 q_e^2 t}{1 + k_2 q_e t}$$	$q_e (mg g^{-1})$	43.43 ± 1.41	49.02 ± 1.08
	k_2 $(\times 10^{-4} g /min. \ mg)$	3.78 ± 0.52	5.13 ± 0.55
	R^2	0.9576	0.9649
Liquid Film Diffusion model $$\ln(1 - F) = -k_{fd}t,$$ $$F = \frac{q_t}{q_e}$$	k_{fd} $(min.^{-1})$	0.013 ± 0.001	0.016 ± 0.001
	R^2	0.9724	0.9654

5.3.6. Thermodynamics of adsorption

The effect of temperature on the adsorption behaviour of phosphate onto MnS was studied by varying the temperature from 303 K to 353 K. Thermodynamic parameters were calculated using the Van't Hoff equation: $\ln(1000 \times K_d) = -\frac{\Delta H}{RT} + \frac{\Delta S}{R}$ determine the enthalpy change (ΔH) and entropy change (ΔS) [27]. The linear fit of $\ln(1000 \times K_d)$ vs. $1/T$ shown in Fig.5.14. allows for the estimation of the thermodynamic parameters governing the adsorption process from the slope and intercept of the graph. The negative ΔH value indicated an exothermic process, while the negative ΔG values at different temperatures demonstrated the spontaneity of phosphate adsorption onto MnS. Higher temperatures favoured phosphate adsorption (Fig.5.15.), as the decreasing ΔG with increasing temperature suggested enhanced spontaneity [28]. The positive ΔS value also indicated an increase in randomness at the solid-liquid interface. Thus, phosphate adsorption onto MnS was a spontaneous, exothermic process with increasing randomness.
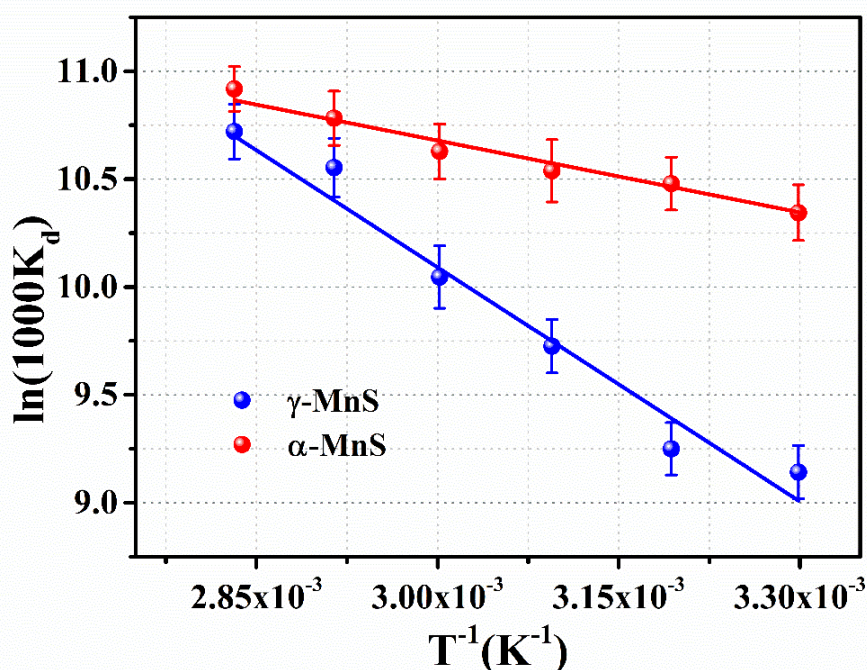
Fig.5.14. *The linear fit of $\ln(1000 \times K_d)$ vs. 1/T for estimating the thermodynamic parameters (C_0 = 20 ppm, dosage = 0.5g/L, pH= ~7).*
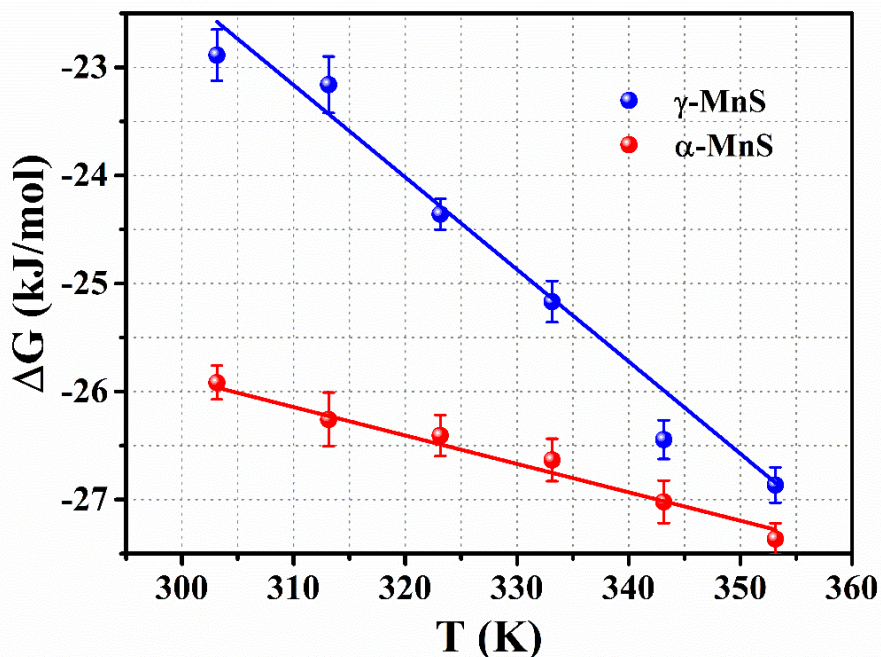
Fig.5.15. *Temperature variation of Gibb's free energy change of the adsorption.*

5.3.7. Effect of pH on adsorption

pH significantly impacts adsorption outcomes by altering the surface charge of MnS and the speciation of phosphate in the solution. As shown in Fig. 5.16, the adsorption capacity was measured under various pH conditions, remaining high between pH level 3 and 8 but decreasing beyond pH = 8. MnS demonstrated significantly higher adsorption capacity in acidic and neutral environments than alkaline ones. This is likely due to the main phosphorus species being $H_2PO_4^-$ and HPO_4^{2-} at pH values of 2.5–7.2 and 7.2–11.5, respectively, with $H_2PO_4^-$ having lower adsorption energy than HPO_4^{2-}, making it more readily adsorbed by MnS [29].

At extreme pH levels (pH = 2 or 12), MnS adsorption capacity significantly decreased. At pH 2, the high concentration of H^+ ions could disrupt MnS adsorption sites, with most phosphate existing as H_3PO_4, which is less readily adsorbed by MnS. At pH 12, the high OH^- concentration competes with phosphate for adsorption sites, and the dominant species PO_4^{3-} experiences electrostatic repulsion from the negatively charged MnS surface, negatively affecting adsorption [30].
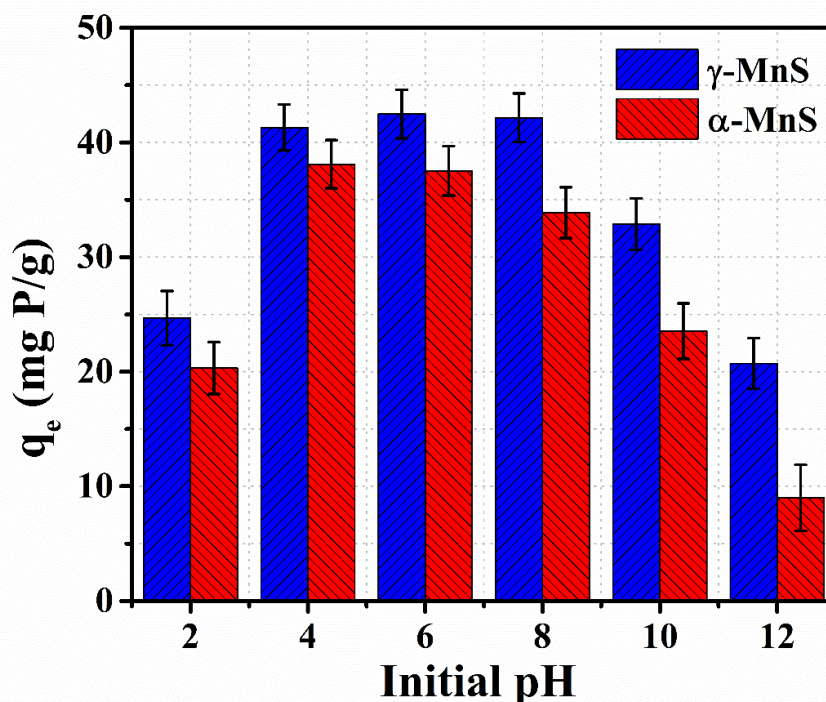
Fig.5.16. *The variation of the adsorption density with the initial pH of the solution. (C_0 = 20 ppm, dosage = 0.5g/L, T = 303 K).*

The pH-dependent adsorption can be explained by understanding the surface characteristics of the adsorbent. The surface features of MnS are significantly influenced by the pH of the solution, which alters the surface charge of the MnS nanostructures. The point of zero charge (pH_{pzc}) or the neutral charge of the adsorbent can be estimated using the drift method [31]. Fig.5.17. illustrates the variation in pH difference of the solution with its initial pH, showing the pH_{pzc} value of the two adsorbents. The pH_{pzc} value for both adsorbents is nearly 8, indicating that below pH 8, the adsorbent surface is highly protonated and positively charged, which is favourable for the adsorption of negatively charged phosphate ions onto MnS nanostructures. Above pH 8, the adsorbent surface becomes negatively charged, hindering phosphate adsorption.
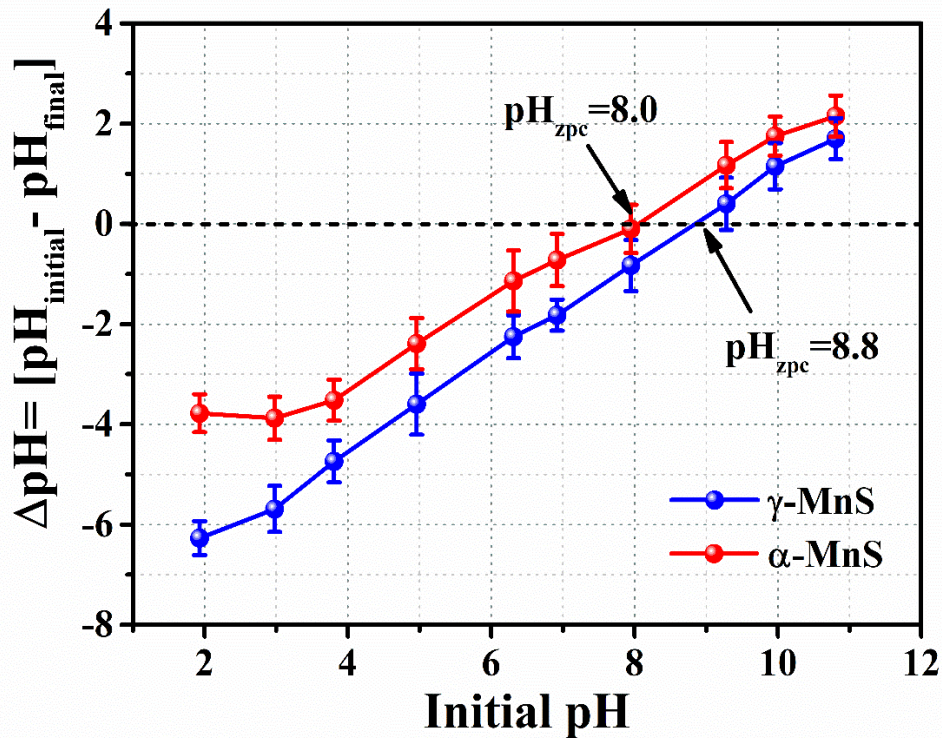
Fig.5.17. *The graphical variation of the initial pH of the solution with ΔpH- using the Drift method to find pH$_{pzc}$ of the adsorbent.*

5.3.8. Effect of co-existing ions and analysing selectivity.

Various anions are frequently found in aqueous environments and can affect the efficiency of phosphorus removal by the adsorbent. The influence of five anions on the phosphorus removal performance of MnS is shown in Fig.5.18. There is no considerable decrease in the adsorption density of the MnS adsorbent in the presence of other competing ions, demonstrating its ability to selectively adsorb phosphate ions from the solution. Only a slight decrease in adsorption density is observed in the presence of other co-existing ions, indicating the adsorbent's versatility and suitability for industrial applications.
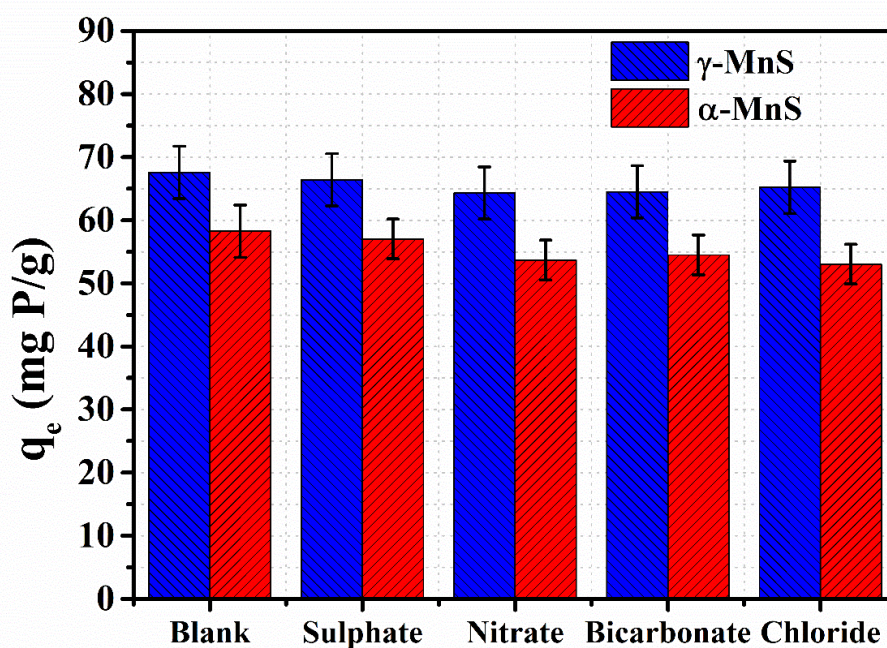
Fig.5.18. *The effect of co-existing ions on phosphate adsorption by MnS. (Initial concentration of phosphate solution C_0 = 20 ppm, concentration of competing ions = 20 ppm, dosage = 0.5g/L, T = 303 K).*

5.3.9. FTIR studies of the adsorbent

To elucidate the mechanism of phosphate adsorption by MnS, FTIR spectra of two adsorbents, α-MnS and γ-MnS, were recorded before and after adsorption in phosphate solutions. Fig.5.19. shows peaks near 501 cm⁻¹ and 609 cm⁻¹, corresponding to the stretching vibrations of the Mn-S bonds in γ-MnS and α-MnS, respectively [32]. A peak near 520-541 cm⁻¹ is attributed to the S-S bond vibration in MnS nanostructures. After phosphate adsorption, these peaks weakened, indicating that MnS played a crucial role in the phosphorus adsorption process. Notably, MnS exhibited a distinct and fluctuating vibrational band within the range of 1119–1037 cm⁻¹, primarily due to the P–O bond vibrations. Stronger peaks at 541, 612, and 1054 cm⁻¹ are associated with PO_4^{3-} vibrations, while the peak around 3467 cm⁻¹ is ascribed to the –OH stretching vibrations and H–O–H bending vibrations of H_2PO_4 [33]. These results confirm that the adsorbent has successfully adsorbed phosphate, forming the absorbent-phosphate structure.
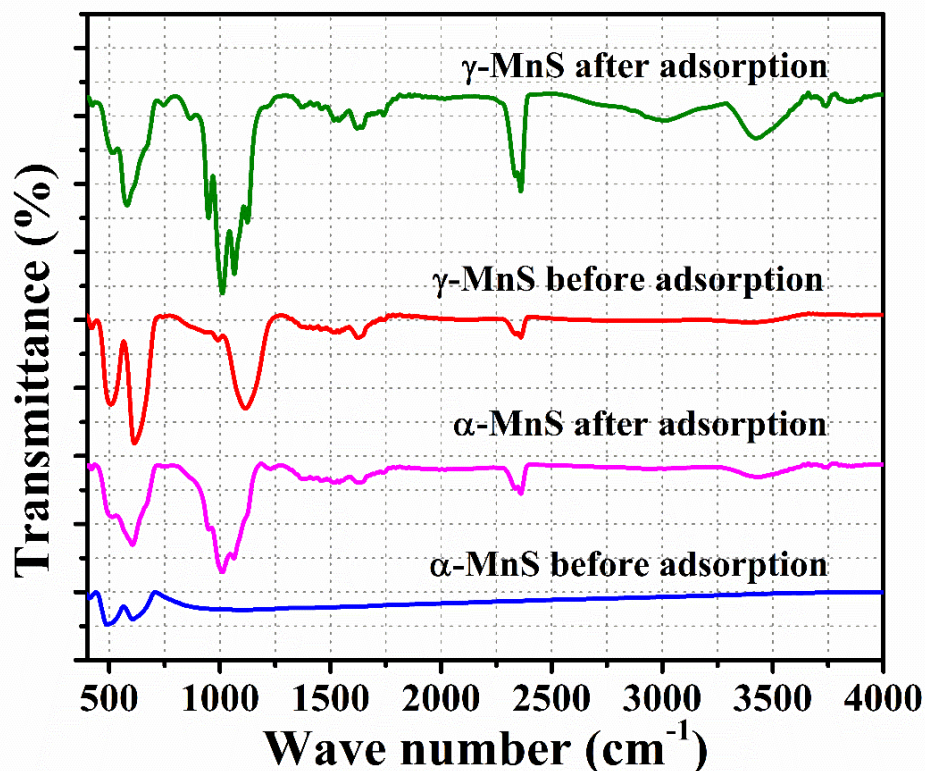
Fig.5.19. *FTIR spectra of the adsorbents before and after phosphate adsorption. The figure shows significant changes in the spectrum after adsorption, indicating the incorporation of phosphate ions into the MnS nanostructures.*

5.3.10. Mechanism of adsorption

The isotherm data for phosphate adsorption onto MnS fit well with both Langmuir and Freundlich models, indicating that the process involves monolayer homogeneous chemisorption and multilayer heterogeneous physisorption. The large surface area and porosity of MnS create more accessible binding sites and pore channels for phosphate adsorption and transport. Experiments on solution pH demonstrated that near-acidic and neutral environments promote phosphate adsorption onto MnS nanostructures. The detection of the zero-point charge revealed that the MnS surface is positively charged in natural phosphate solutions, highlighting the significant role of electrostatic attraction in phosphate ion adsorption. When the initial pH of the adsorption solution was between 2 and 8, the pH of the water sample at adsorption equilibrium significantly increased, likely due to ligand exchange between hydroxyl and phosphate ions, releasing OH^- into the water. This exchange occurs as Mn^{2+} is replaced by $H_2PO_4^-$ and HPO_4^{2-} (depending on the initial pH) on the adsorbent surface, forming inner-sphere surface complexes via

Lewis's acid-base interactions [34]. When the initial pH was 8–11, the pH of the solution only slightly decreased after phosphate adsorption, suggesting inhibition of ligand exchange. However, MnS maintained adsorption capacity, indicating that complexation is also essential for phosphate ion adsorption. The FTIR spectrum of the phosphate-loaded adsorbent confirms these findings. Based on the experimental investigation, we propose that phosphate adsorption on MnS occurs through three primary mechanisms: electrostatic attraction, ion exchange, and surface complexation.

Electrostatic Attraction: Electrostatic forces play a significant role due to the ionic nature of both phosphate and MnS surfaces. Phosphate ions (PO_4^{3-}) are attracted to the positively charged sites on the MnS surface (e.g., Mn^{2+} ions.

Ion Exchange: Here, MnS can exchange its surface-bound ions with phosphate ions in the solution. The Mn^{2+} ions on the MnS surface can be partially or fully replaced by phosphate ions (PO_4^{3-}) through reactions such as:

$$MnS\ (s) + H_2PO_4^-\ (aq) \rightarrow Mn(H_2PO_4)\ (s) + S^{2-}(aq)$$

$$MnS\ (s) + HPO_4^{2-}\ (aq) \rightarrow Mn(HPO_4)\ (s) + S^{2-}(aq)$$
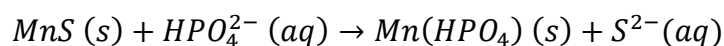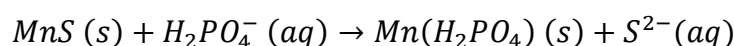
In these reactions, phosphate ions replace surface-bound sulfide ions (S^{2-}), forming manganese phosphate $\left(Mn(H_2PO_4)\ /Mn(HPO_4)\right)$ on the MnS surface.

Surface Complexation: This mechanism involves the formation of chemical bonds or complexes between phosphate ions and specific sites on the MnS surface. The surface complexation enhances the adsorption capacity and stability of phosphate on MnS. Reactions include [34]:

$$Mn^{2+} + OH^- + H_2PO_4^- \rightarrow Mn(OH)(H_2PO_4)$$

$$Mn^{2+} + OH^- + HPO_4^{2-} \rightarrow Mn(OH)(HPO_4^-)$$
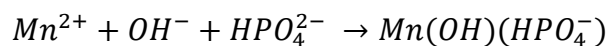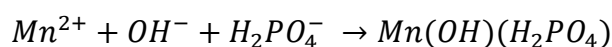
These reactions indicate the formation of inner-sphere surface complexes through Lewis's acid-base interactions, where phosphate ions replace water or hydroxyl groups on the MnS surface. Surface complexation can involve the formation of mono-, bi-, or polydentate complexes, depending on the coordination geometry and available surface sites.

The summary of the adsorption mechanism process is illustrated in the Fig.5.20.
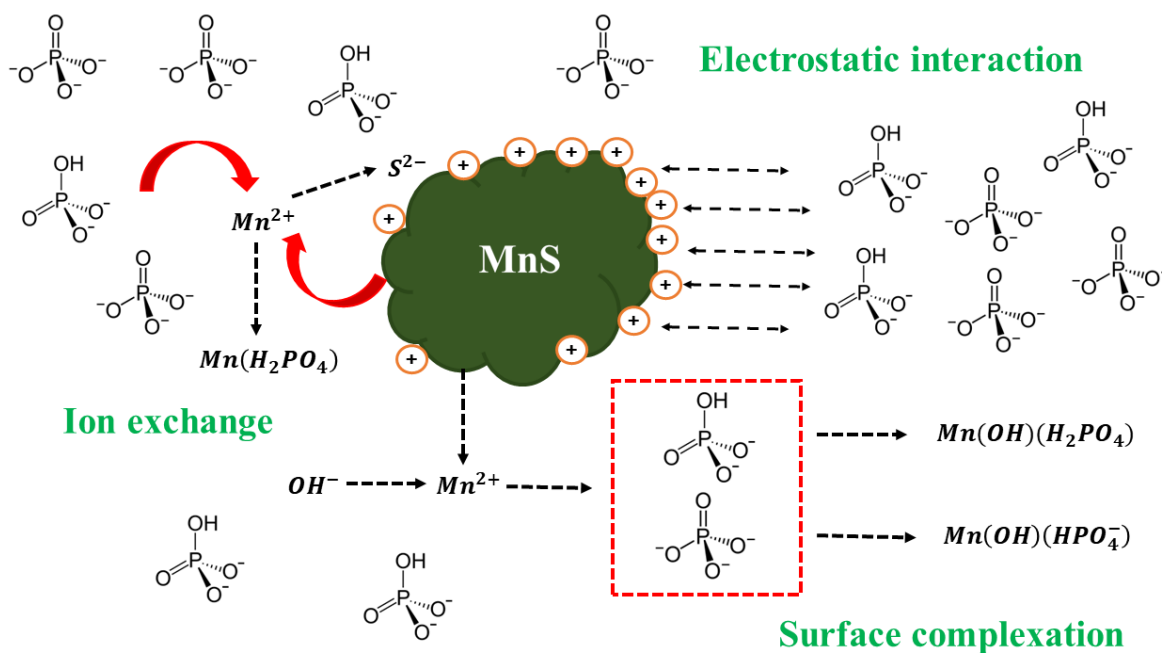
Fig.5.20. *The schematic representation of the adsorption process. The adsorption of phosphate on MnS occurs through three primary mechanisms: electrostatic attraction, ion exchange, and surface complexation.*

### 5.3.11. Sonocatalytic activity of MnS

The synthesized MnS nanostructures serve as an effective adsorbent for phosphate removal from water and exhibit sonocatalytic activity for the degradation of textile dyes. Congo red (CR) dye was used to demonstrate this sonocatalytic degradation. CR dye molecules show a strong affinity for MnS nanostructures, enabling degradation experiments at an initial concentration of 80 ppm. In the dark reaction, 11.5% and 31.6% of CR dyes were removed by adsorption within 10 minutes for α-MnS and γ-MnS, respectively, achieving adsorption-desorption equilibrium. A 100% adsorptive removal of CR is attained for a 50-ppm solution, demonstrating the strong affinity of CR dye molecules for MnS. This strong affinity can be explained as follows: The molecular structure of Congo red includes functional groups such as amino ($-NH_2$) and azo ($-N=N-$) groups, which can form hydrogen bonds with MnS surface atoms. Additionally, the aromatic rings in Congo red participate in π-π interactions with the MnS surface, where electron-rich π systems of the dye molecules interact with the MnS surface, enhancing adsorption affinity.

Upon exposure to ultrasonic sound waves, sonocatalytic degradation resulted in the degradation of 91.8% of CR dyes with α-MnS and 99.8% with γ-MnS within 10

minutes (for 80 ppm initial concentration of dye solution). The kinetic degradation reaction follows pseudo-first-order kinetics given as $\ln\left(\frac{C_0}{C_t}\right) = kt$ where C_0 and C_t are the initial concentration and concentration at time t of the dye solution k is the rate constant of the reaction [35]. The temporal variation of the degradation reactions and the linear fit of pseudo-first-order kinetics are shown in Fig.5.21. and Fig.5.22. respectively. The rate constants were estimated to be 0.15 ± 0.05 min^{-1} for α-MnS and 0.31 ± 0.01 min^{-1} for γ-MnS. TOC analysis of the initial and final dye solution samples revealed mineralization rates of approximately 83.5% for γ-MnS and 78.2% for α-MnS. The effect of catalyst dosage and reusability was also examined, as illustrated in Fig.5.23. MnS catalysts performed degradation reactions effectively at dosages starting from 0.25 g/L, with increased efficiency at higher dosages. The catalysts maintained their degradation efficiency for five cycles without significant decline, as shown in Fig.5.24. The TOC mineralization efficiency of the catalytic degradation is shown in Fig.5.25.
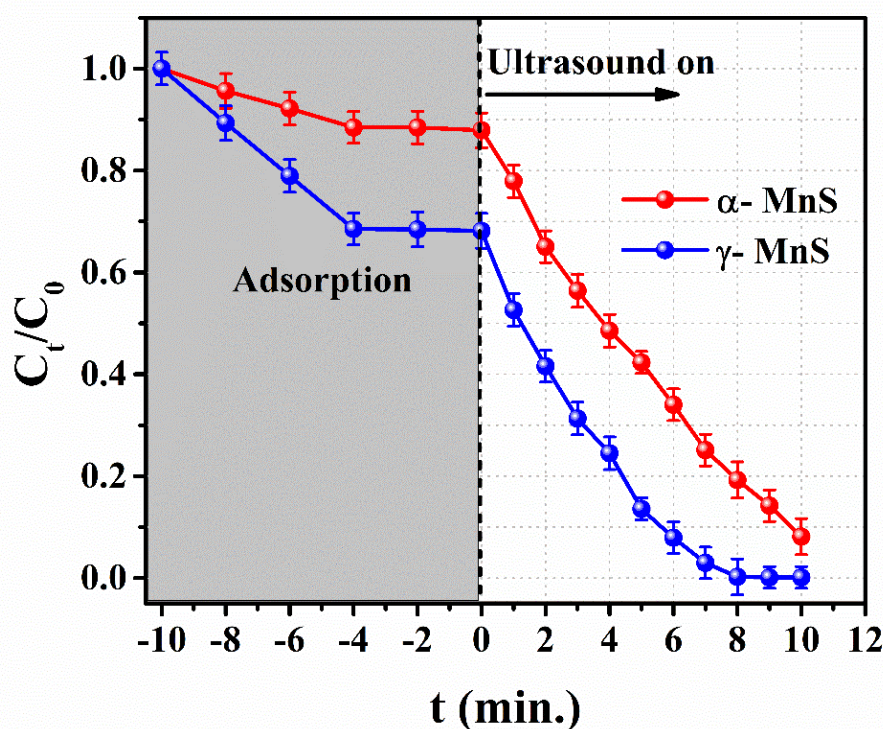
Fig.5.21. *Temporal variation of the concentration of the CR dye under dark reaction and sonocatalytic degradation. Sonocatalytic degradation resulted in 91.8% degradation with α-MnS and 99.8% with γ-MnS within 10 minutes.*
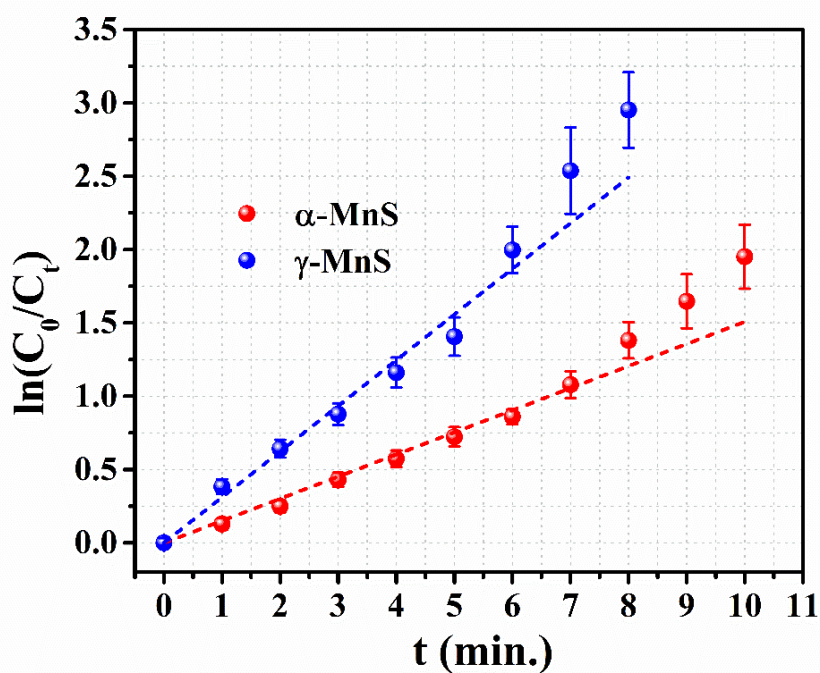
Fig.5.22. *The linear fit of pseudo-first order kinetic model - the rate constants were estimated to be 0.15 ± 0.05 min⁻¹ with α-MnS and 0.31 ± 0.01 min⁻¹ with γ-MnS. (C₀ = 80 ppm, dosage = 0.5g/L, pH= ~7, T = 303K).*
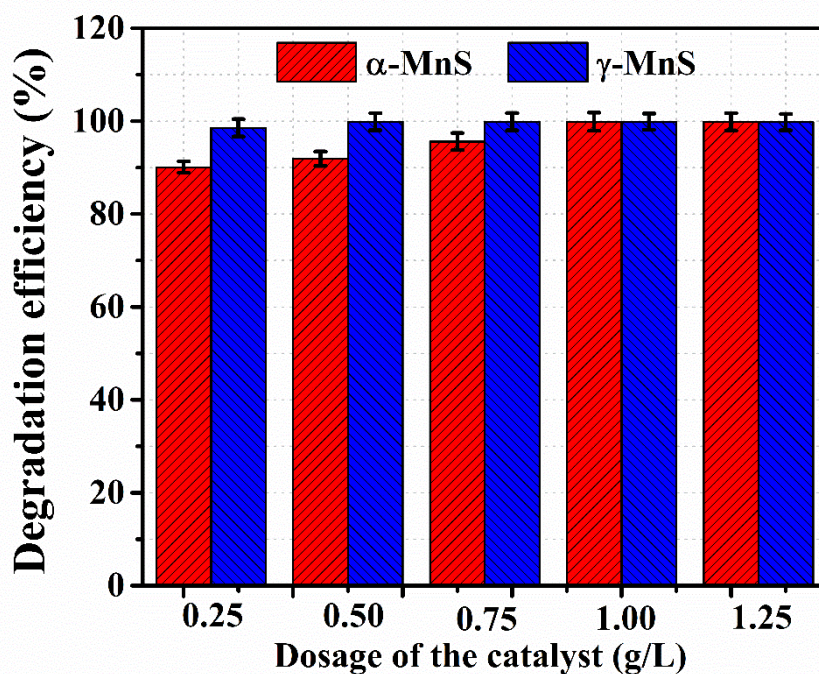
Fig.5.23. *Variation of degradation with the dosage of the sonocatalysts. The degradation efficiency is independent of the dosage of the sonocatalysts. (C₀ = 80 ppm, pH= ~7, T = 303K).*
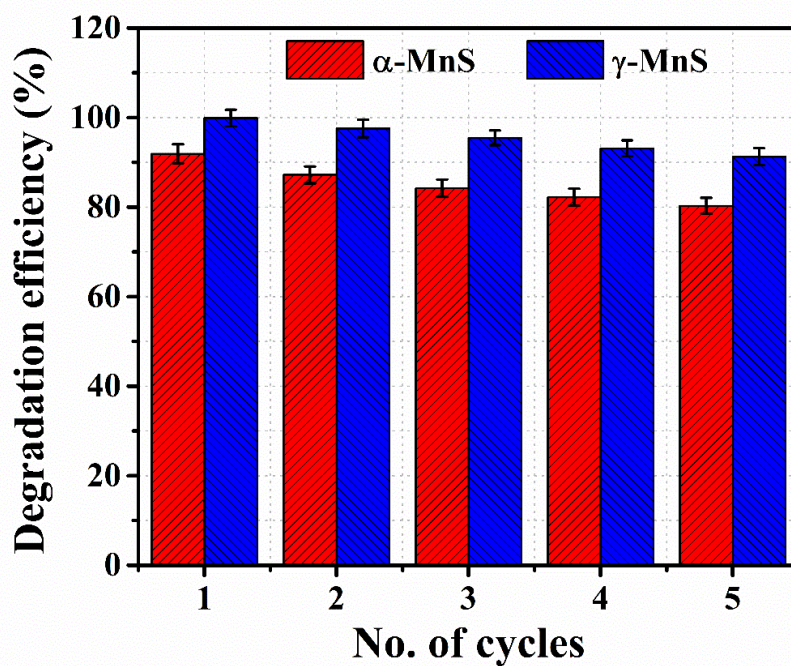
Fig.5.24. *The reusability of the sonocatalysts. The sonocatalysts can be reused up to 5 cycles without any considerable decrease in its efficiency. (C₀ = 80 ppm, dosage = 0.5g/L, pH= ~7, T = 303K).*
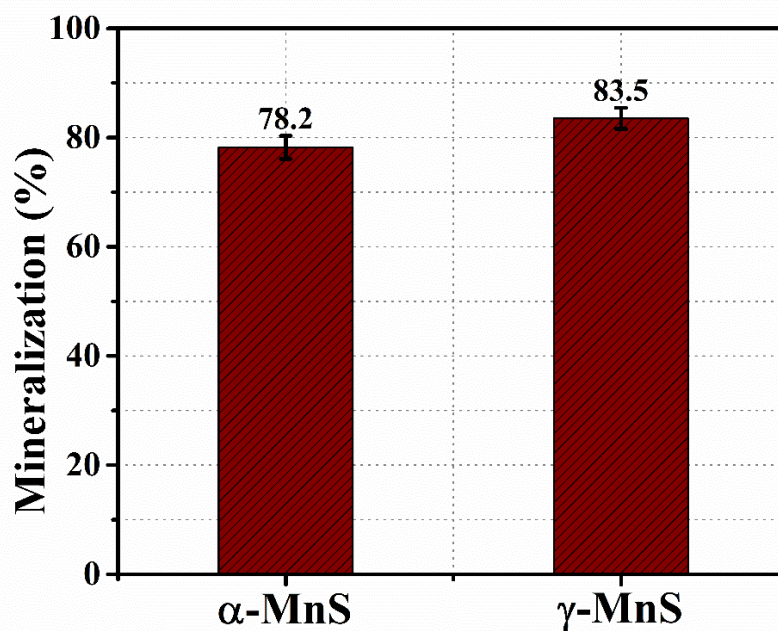
Fig.5.25. *TOC mineralization of the sonocatalysis of CR. (C₀ = 80 ppm, dosage = 0.5g/L, pH= ~7, T = 303K).*

5.3.12. Mechanism of sonocatalytic degradation of CR

The degradation mechanism of sonocatalytic processes is primarily based on the hot-spot theory and the sonoluminescence phenomenon. According to the hot-spot theory, most physical and chemical effects of ultrasonic (US) waves are related to cavitation, which involves the formation, growth, and collapse of microbubbles in an aqueous solution [36]. When these bubbles collapse, they produce shock waves that create localized high temperatures and pressures. These extreme conditions can lead to the pyrolysis of water molecules, forming hydrogen and hydroxyl radicals ($H\cdot$ and $\cdot OH$), and the thermal excitation of electrons from the valence band (VB) to the conduction band (CB) of the semiconductor catalyst [36]. Additionally, the collapse of the bubbles generates picosecond flashlights known as sonoluminescence, which can create electron-hole (e^-/h^+) pairs by light stimulation of the semiconductor. The dye molecules are adsorbed onto the catalyst surface and degraded by the free radicals generated from water pyrolysis and photo-thermal catalysis [37].

$$H_2O +)))) \rightarrow \cdot H + \cdot OH$$

$$MnS + SL/Heat \rightarrow MnS\,(h^+) + MnS\,(e^-)$$

$$h^+ + H_2O \rightarrow \cdot OH + H^+$$

$$h^+ + OH^- \rightarrow \cdot OH$$

$$e^- + O_2 \rightarrow \cdot O_2^-$$

$$CR + \cdot OH \rightarrow Intermediates + CO_2 + H_2O$$

$$CR + \cdot O_2^- \rightarrow Intermediates + CO_2 + H_2O$$
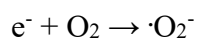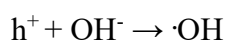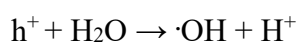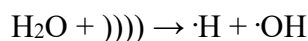
These highly active oxidative species *viz.* $\cdot OH$ and $\cdot O_2^-$ radicals can attack the CR molecules present in the water - forming various intermediate products and finally mineralized into CO_2 and H_2O. The mechanism of sonocatalytic degradation is shown in the Fig.5.26.

To investigate the sonocatalytic mechanism, the influence of radical scavengers (benzoquinone for O_2 and tert-butanol for $\cdot OH$) was studied under optimized conditions. The addition of benzoquinone slightly reduced sonocatalytic efficiency, while tert-butanol significantly hindered the process. These results indicate that hydroxyl radicals play a crucial role in the sonocatalytic degradation of CR using MnS.
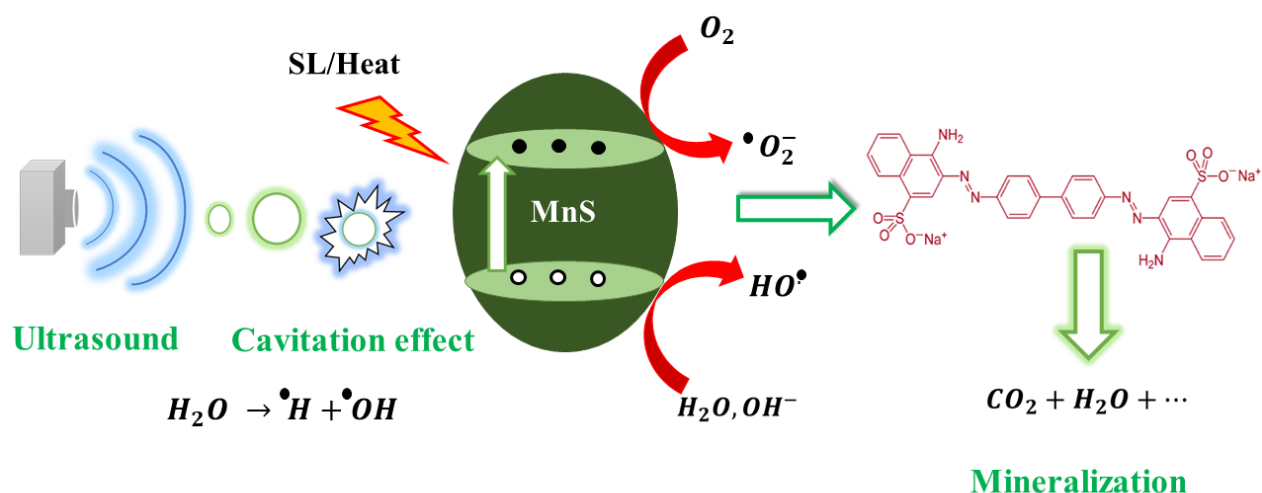
Fig.5.26. *Mechanism of sonocatalytic degradation of CR using MnS. The mechanism of sonocatalytic processes is based on the hot-spot theory and sonoluminescence phenomenon, where cavitation from ultrasonic waves leads to the formation of radicals and thermal excitation of electrons in the catalyst. These radicals degrade dye molecules adsorbed on the catalyst surface through water pyrolysis and photo-thermal catalysis.*

5.3.16. Degradation pathway of CR

High Performance Liquid Chromatography-Mass Spectrometry (HPLC-MS) analyzed the intermediate products of CR dye at various time intervals. Fig.5.25. illustrates a possible degradation pathway derived from the HPLC-MS data. The degradation process involves the removal of the amine group and oxygenation of the CR dye, forming a new compound with a mass-to-charge (m/z) value of 680. The cleavage of the benzene ring, NQN, and C–N bonds in the CR dye generates compounds with m/z ratios 224 (4-hydroxynaphthalene-1-sulfonic acid) and 207 (4-aminobiphenyl-4'-sulfonic acid) [38]. Further oxidation, nitrification, desulfonation, or deamination along with hydroxylation by OH radicals, lead to the formation of 4-carboxybutanoate (m/z = 138) and naphthalene (m/z = 122) [38]. Subsequent oxidation causes the cleavage of amino, nitro, hydroxyl, and/or sulfonic groups attached to the benzene ring, resulting in low molecular weight intermediates such as 3-carboxypropanoate (m/z = 120), malonic acid (m/z = 108), and malonate (m/z = 101) [39]. These short linear intermediates are further mineralized into CO_2 and H_2O upon light irradiation. The HPLC-MS analysis indicated the complete removal of higher mass fragments of the CR dye, leaving only lower mass fragments, which explains the less than 100% mineralization observed in the TOC

analysis shown in Fig.5.27. The list of intermediate products and their details are provided in the Table.5.4.
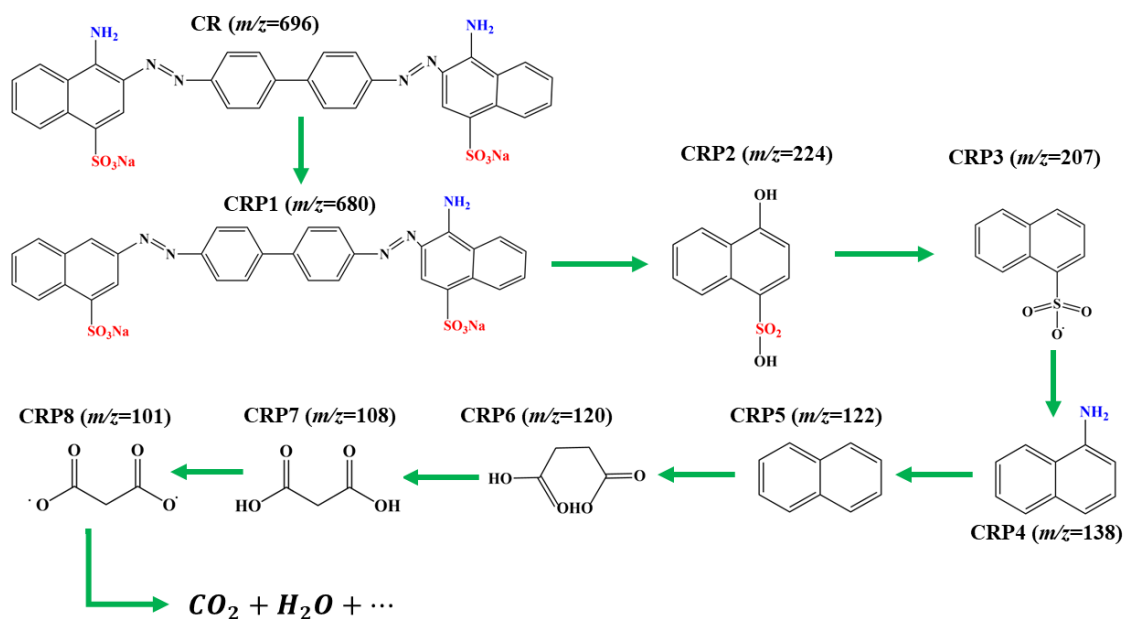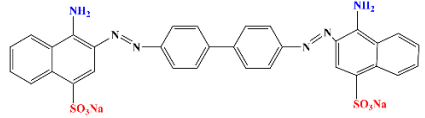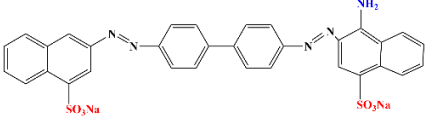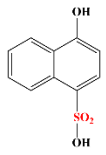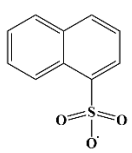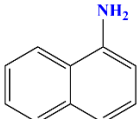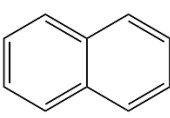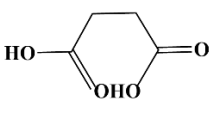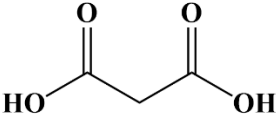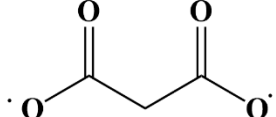
Fig.5.27. *Proposed sonocatalytic degradation pathway of the CR dye based on the HPLC-MS results.*

In this study, we introduce MnS as a promising candidate for the efficient adsorptive removal of phosphate from water - a new role for metal chalcogenide. Numerous studies have focused on removing phosphate using lanthanum (La) and zirconium (Zr) based adsorbents, known for their strong affinity towards phosphate ions. Our findings reveal that MnS exhibits a similar affinity for phosphate ions as these established adsorbents. Furthermore, MnS can be integrated with other commercially available adsorbents to enhance their adsorption capacity. Table.5.5. summarises the reported phosphate adsorption capacities of various adsorbents.

Table.5.4. *List of intermediates formed in the sonocatalytic degradation of Congo Red.*

Intermediates	t_R (min)	m/z	Chemical structure
CR	-	696	
CRP1	3.57	680	
CRP2	3.24	224	
CRP3	4.95	207	
CRP4	2.95	138	
CRP5	2.63	122	
CRP6	1.06	120	
CRP7	1.95	108	
CRP8	2.84	101	

Table.5.5. *Summary of different adsorbents used to remove phosphate from wastewater. La and Zr based adsorbents are known for their high phosphate affinity. Our findings show that MnS similarly adsorbs phosphate ions effectively and can enhance the capacity of commercial adsorbents.*

Adsorbent	Maximum adsorption capacity (mg P/g)	Reference
La-modified herbal residues	52.00	Caigao Zhou *et al*. [40]
calcium modified biochar	70.26	Ying Liu *et al.* [41]
Layered double hydroxide loaded pinecone biochar	36.00	Wei-Hao Huang *et al.* [42]
biogenic calcium carbonate	4.57	Andreia F. Santos *et al.* [43]
La-modified natural zeolite	122.70	Qingyue Luo *et al.* [44]
Fe-Mg co-modified water hyacinth-based biochar	114.00	Xianguo Ji *et al.* [45]
Zr-modified Merlinoite	67.72	Youness Abdellaoui *et al.* [46]
Hydrated Zr-loaded resin	47.22	Huanhuan Xu *et al.* [47]
Zr-chitosan-soyabean husk	154.71	Banu H T *et al.* [48]
MnS	**160.73**	**Present study**

Beyond its role as an adsorbent, MnS also serves as an effective sonocatalyst for degrading textile dyes in water, showcasing rapid sonocatalytic activity. This dual functionality highlights the versatile application potential of MnS nanoparticles in environmental remediation, particularly in wastewater treatment. The selective activity and high removal efficiency of MnS for both phosphate ions and Congo red dye in single

and binary mixture studies demonstrate its effectiveness as a viable candidate for wastewater treatment. This is illustrated in Fig.5.28. in the supplementary session.
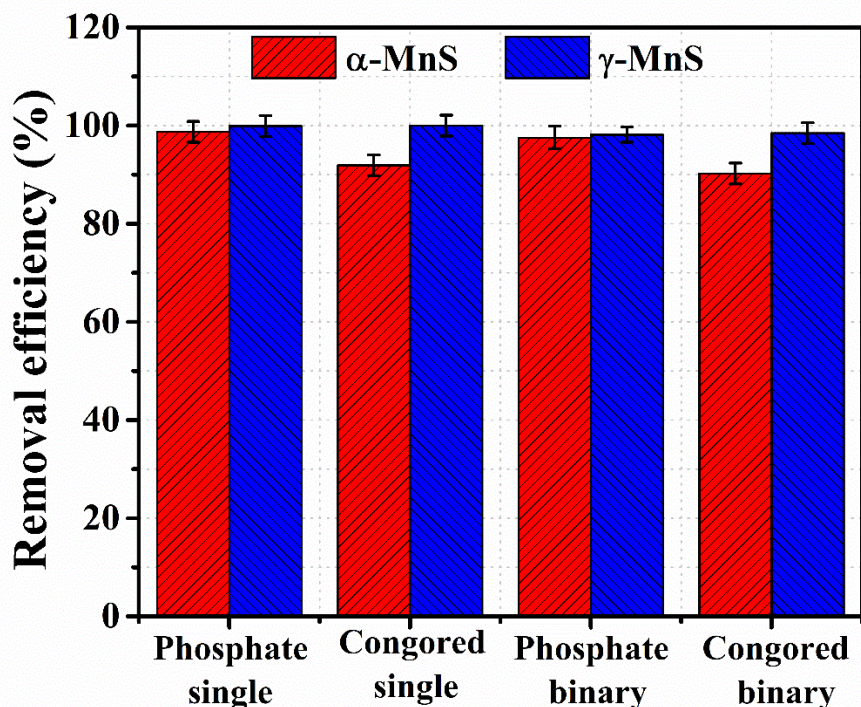
Fig.5.28. *Effect of removal efficiency of MnS nanomaterials in the single and binary mixture of phosphate ions and congo red dye solutions.*

5.4. CONCLUSION

MnS nanomaterials with distinct crystal phases (α-MnS and γ-MnS) were successfully synthesized using a straightforward hydrothermal method. γ-MnS exhibited superior adsorption properties for phosphate removal, attributed to its larger active sites, higher surface area, and surface heterogeneity. Thermodynamic analyses confirmed that phosphate adsorption onto MnS is a spontaneous, exothermic process that increases randomness at the solid-liquid interface. The adsorption mechanism, supported by FTIR and other characterization techniques, involves electrostatic attraction, surface complexation, and ion exchange. MnS maintained its adsorption capacity in the presence of competing ions, demonstrating a selective affinity for phosphate ions. This study introduces MnS as the first metal chalcogenide effective for phosphate removal from water, more efficient than the established lanthanum and zirconium-based adsorbents, with the potential to enhance the adsorption capacity of other commercial adsorbents. Additionally, MnS functioned as a potent sonocatalyst, efficiently degrading textile dyes

in water, notably achieving Congo red dye degradation within 10 minutes of ultrasonic irradiation. The proposed mechanism for Congo red degradation elucidates the sonocatalytic process facilitated by MnS nanoparticles.

In conclusion, MnS nanoparticles exhibit dual functionality as effective sonocatalysts for rapid textile dye degradation and highly efficient non-La or Zr-based adsorbent for phosphate ions. This versatile capability underscores MnS's promising role in environmental remediation, particularly in wastewater treatment, where it demonstrates selective activity and high removal efficiency for both contaminants in various environmental conditions.

5.5. REFERENCES

[1]   Sahu, A. K., Mir, S., Nayak, B., & Baitharu, I. (2024). Sustainable management of eutrophication and problems associated with the algal toxin in ponds and lakes of rural areas. In *Water Resources Management for Rural Development* (pp. 155-170). Elsevier.

[2]   Dutta, S., Adhikary, S., Bhattacharya, S., Roy, D., Chatterjee, S., Chakraborty, A., ... & Rajak, P. (2024). Contamination of textile dyes in aquatic environment: Adverse impacts on aquatic ecosystem and human health, and its management using bioremediation. *Journal of Environmental Management*, *353*, 120103.

[3]   Sajjad, M., Huang, Q., Khan, S., Nawab, J., Khan, M. A., Ali, A., ... & Sajjad, M. (2024). Methods for the removal and recovery of nitrogen and phosphorus nutrients from animal waste: A critical review. *Ecological Frontiers*, *44*(1), 2-14.

[4]   Adhikari, S., Mandal, S., Kim, D. H., & Mishra, A. K. (2019). An overview of treatment technologies for the removal of emerging and nanomaterials contaminants from municipal and industrial wastewater. *Emerging and Nanomaterial Contaminants in Wastewater*, 3-40.

[5]   Mukherjee, J., Lodh, B. K., Sharma, R., Mahata, N., Shah, M. P., Mandal, S., ... & Bhunia, B. (2023). Advanced oxidation process for the treatment of industrial wastewater: A review on strategies, mechanisms, bottlenecks and prospects. *Chemosphere*, 140473.

[6]   Yang, Y., Yu, H., Shen, T., Wang, N., & Wang, P. (2024). Critical review of La (III)-based absorbents toward phosphate adsorption from aqueous solutions: mechanisms, adsorbent design, and prospects. *Journal of Environmental Chemical Engineering*, 112571.

[7]   Luo, H., Liu, B., Zhang, M., Wei, C., Long, Q., Pan, S., ... & Rong, H. (2024). Efficient adsorption of phosphorus by macroscopic MOF/chitosan composites and preliminary investigation of subsequent phosphorus recovery through electrochemically-driven struvite precipitation. *International Journal of Biological Macromolecules*, *257*, 128707.

[8]   Mishra, R. K., Mentha, S. S., Misra, Y., & Dwivedi, N. (2023). Emerging pollutants of severe environmental concern in water and wastewater: A comprehensive review on current developments and future research. *Water-Energy Nexus*.

[9]   Farooq, N., ur Rehman, Z., Khan, M. I., Asghar, S., Saleem, M., Irshad, R., ... & Khan, Z. U. (2024). Nanomaterial-based energy conversion and energy storage devices: a comprehensive review. *New Journal of Chemistry*.

[10]   Wang, Y., He, Y., Chi, Y., Yin, P., Wei, L., Liu, W., ... & Song, H. (2023). Construction of S-scheme pn heterojunction between protonated g-C3N4 and α-MnS nanosphere for photocatalytic H2O2 production and in situ degradation of oxytetracycline. *Journal of Environmental Chemical Engineering*, *11*(3), 109968.

[11]   Sun, B. C., Zhao, W. K., Han, C. B., Zheng, J. Y., Yan, H., Yang, Z. C., ... & Song, X. (2023). Oxygen vacancies modified MnS/MnO2 heterostructure anode catalyst for efficiently electrocatalytic removal of dye wastewater. *Journal of Alloys and Compounds*, *942*, 169037.

[12]   Ali, J., Guo, S., Chen, Y., Shahzad, A., Ullah, M. W., & Chen, F. (2024). Metal sulfides as emerging materials for advanced oxidation of wastewater: Recent developments, challenges, and prospects. *Coordination Chemistry Reviews*, *509*, 215765.

[13]   Shim, K., Seo, K. D., & Kim, H. J. (2023). Synthesis of MnS/MnO Decorated N, S-Doped Carbon Derived from a Mn (II)-Coordinated Polymer for the Catalytic Oxidation of H2O2 and Bisphenol A. *Advanced Functional Materials*, *33*(22), 2210549.

[14]   Yu, H., Liu, Y., Cong, S., Xia, S., & Zou, D. (2023). Review of Mo-based materials in heterogeneous catalytic oxidation for wastewater purification. *Separation and Purification Technology*, *312*, 123345.

[15]   Xie, Z. H., Zhou, H. Y., He, C. S., Pan, Z. C., Yao, G., & Lai, B. (2021). Synthesis, application and catalytic performance of layered double hydroxide-based catalysts in advanced oxidation processes for wastewater decontamination: A review. *Chemical Engineering Journal*, *414*, 128713.

[16]   Luo, J., Zhang, S., Sun, M., Yang, L., Luo, S., & Crittenden, J. C. (2019). A critical review on energy conversion and environmental remediation of photocatalysts with remodeling crystal lattice, surface, and interface. *ACS nano*, *13*(9), 9811-9840.

[17]   Luo, H., Liu, B., Zhang, M., Wei, C., Long, Q., Pan, S., ... & Rong, H. (2024). Efficient adsorption of phosphorus by macroscopic MOF/chitosan composites and preliminary investigation of subsequent phosphorus recovery through electrochemically-driven struvite precipitation. *International Journal of Biological Macromolecules*, *257*, 128707.

[18]   Menaka, V., Geetha, D., & Ramesh, P. S. (2024). Effect of MnS/rGO nanocomposites on enhancing the removal efficiency of organic dyes and electrochemical applications. *Journal of Materials Science: Materials in Electronics*, *35*(17), 1146.

[19]   Zhu, Y., Zhong, W., Chen, W., Hu, Z., Xie, Y., Deng, W., ... & Ji, X. (2024). Crystallographic types depended energy storage mechanism for zinc storage. *Nano Energy*, *125*, 109524.

[20]   Karuppaiyan, J., Mullaimalar, A., & Jeyalakshmi, R. (2023). Adsorption of dyestuff by nano copper oxide coated alkali metakaoline geopolymer in monolith and powder forms: Kinetics, isotherms and microstructural analysis. *Environmental Research*, *218*, 115002.

[21]   Jain, M., Sahoo, A., Mishra, D., Khan, S. A., Pant, K. K., Ziora, Z. M., & Blaskovich, M. A. (2024). Modelling and statistical interpretation of phenol adsorption behaviour of 3-Dimensional hybrid aerogel of waste-derived carbon nanotubes and graphene oxide. *Chemical Engineering Journal*, *490*, 151351.

[22]   Hu, Q., Lan, R., He, L., Liu, H., & Pei, X. (2023). A critical review of adsorption isotherm models for aqueous contaminants: Curve characteristics, site energy distribution and common controversies. *Journal of Environmental Management*, *329*, 117104.

[23]   Rahmani, M., Mabrouki, J., Regraguy, B., Moufti, A., El'Mrabet, M., Dahchour, A., & El Hajjaji, S. (2023). Adsorption of (methylene blue) onto natural oil shale: kinetics of adsorption, isotherm and thermodynamic studies. *International Journal of Environmental Analytical Chemistry*, *103*(18), 6495-6509.

[24]   Omo-Okoro, P. N., Adeiga, O. I., Velempini, T., Prabakaran, E., Curtis, C. J., & Pillay, K. (2023). Nickel ion removal from aqueous media using polyaniline–macadamia

nutshells and its reuse for photodegradation of orange dye. *International Journal of Environmental Science and Technology*, *20*(8), 8655-8672.

[25] Sravandas, P., & Alexander, L. K. (2024). Isotype BiVO4 Heterostructure and the Effect of Photo-Sono Induced Electron-Hole Pair. *Journal of Environmental Chemical Engineering*, 113240.

[26] Isiuku, B. O., Ochule, B. I., Enedoh, M. C., & Ebosie, N. P. (2023). Application of kinetic models in batch adsorption processes–A review. *World Scientific News*, *186*, 67-93.

[27] Sravandas, P., & Alexander, L. K. (2024). Fast catalytic degradation of an industrial surfactant driven by Hemi-micellization on facile synthesized CuS nanoflower. *Emergent Materials*, *7*(1), 209-220.

[28] Khan, Z. H., Li, Z., Gao, M., Islam, M. S., Xiao, L., Qiu, W., & Song, Z. (2023). Simultaneous and efficient removal of Cd (II) and As (III) by a magnesium-manganese codoped biochar composite: Sorption performance and governing mechanisms. *Journal of Environmental Chemical Engineering*, *11*(3), 109919.

[29] Ji, X., Liu, Y., Gao, Z., Lin, H., Xu, X., Zhang, Y., ... & Duan, J. (2024). Efficiency and mechanism of adsorption for imidacloprid removal from water by Fe-Mg co-modified water hyacinth-based biochar: Batch adsorption, fixed-bed adsorption, and DFT calculation. *Separation and Purification Technology*, *330*, 125235.

[30] Zou, X., Zhang, H., Xiang, L., Huang, C., & Li, J. (2024). Designing a dual-functional ultrathin ZIF-L@ GO adsorbent for simultaneous removal of phosphate and tetracycline hydrochloride: Adsorption capacity and mechanism. *Colloids and Surfaces A: Physicochemical and Engineering Aspects*, *683*, 132851.

[31] Sayed, N. S., Ahmed, A. S., Abdallah, M. H., & Gouda, G. A. (2024). ZnO@ activated carbon derived from wood sawdust as adsorbent for removal of methyl red and methyl orange from aqueous solutions. *Scientific Reports*, *14*(1), 5384.

[32] Heiba, Z. K., Mohamed, M. B., Farag, N. M., & Ahmed, S. I. (2021). Influence of synthesis temperature on the phases developed and optical properties of manganese sulfide and zinc sulfide. *Crystal Research and Technology*, *56*(6), 2000201.

[33] Ma, Y., Yao, Y., Deng, Z., Tang, J., Liu, Y., Ma, J., & Zhang, Z. (2024). Ball milling and phosphoric acid hydrothermally co-functionalized sludge biochar for efficiently adsorptive removal of environmental concentration sulfamethoxazole: Experimental, characterization and DFT study. *Separation and Purification Technology*, *328*, 125051.

[34] Santos, A. F., Lopes, D. V., Alvarenga, P., Gando-Ferreira, L. M., & Quina, M. J. (2024). Phosphorus removal from urban wastewater through adsorption using biogenic calcium carbonate. *Journal of Environmental Management*, *351*, 119875.

[35] Sravandas, P., & Alexander, L. K. (2021). Facile hydrothermal synthesis and sonophotocatalytic performance of novel Bi2WO6 structure on the degradation of rhodamine B. *Materials Today: Proceedings*, *46*, 2925-2929.

[36] Wu, T. Y., Guo, N., Teh, C. Y., Hay, J. X. W., Wu, T. Y., Guo, N., ... & Hay, J. X. W. (2013). Theory and fundamentals of ultrasound. *Advances in ultrasound technology for environmental remediation*, 5-12.

[37] Qiu, P., Park, B., Choi, J., Thokchom, B., Pandit, A. B., & Khim, J. (2018). A review on heterogeneous sonocatalyst for treatment of organic pollutants in aqueous phase based on catalytic mechanism. *Ultrasonics sonochemistry*, *45*, 29-49.

[38] Kumar, A., Mittal, H., Nagar, R., & Khanuja, M. (2022). The synergistic effect of acid-etched gC 3 N 4 nanosheets and polyaniline nanofibers for the adsorption and photocatalytic degradation of textile dyes: a study of charge transfer mechanism and intermediate products. *Materials Advances*, *3*(13), 5325-5336.

[39] Krishnamoorthy, R., Jose, P. A., Ranjith, M., Anandham, R., Suganya, K., Prabhakaran, J., ... & Kumutha, K. (2018). Decolourization and degradation of azo dyes by mixed fungal culture consisted of Dichotomomyces cejpii MRCH 1-2 and Phoma tropica MRCH 1-3. *Journal of environmental chemical engineering*, *6*(1), 588-595.

[40] Zhou, C., Chen, Z., Lv, G., Xu, C., Wang, G., Zhang, S., ... & Xu, X. (2024). Optimization of the adsorption performance of herbal residues as lanthanide ion-modified carriers for phosphate by fly ash and its application. *Chemosphere*, *348*, 140704.

[41] Liu, Y., Wang, S., Huo, J., Zhang, X., Wen, H., Zhang, D., ... & Ngo, H. H. (2024). Adsorption recovery of phosphorus in contaminated water by calcium modified biochar derived from spent coffee grounds. *Science of the Total Environment*, *909*, 168426.

[42] Huang, W. H., Chang, Y. J., & Lee, D. J. (2024). Layered double hydroxide loaded pinecone biochar as adsorbent for heavy metals and phosphate ion removal from water. *Bioresource Technology*, *391*, 129984.

[43] Santos, A. F., Lopes, D. V., Alvarenga, P., Gando-Ferreira, L. M., & Quina, M. J. (2024). Phosphorus removal from urban wastewater through adsorption using biogenic calcium carbonate. *Journal of Environmental Management*, *351*, 119875.

[44] Luo, Q., Wei, J., Guo, Z., & Song, Y. (2024). Adsorption and immobilization of phosphorus from water and sediments using a lanthanum-modified natural zeolite: Performance, mechanism and effect. *Separation and Purification Technology*, *329*, 125187.

[45] Ji, X., Liu, Y., Gao, Z., Lin, H., Xu, X., Zhang, Y., ... & Duan, J. (2024). Efficiency and mechanism of adsorption for imidacloprid removal from water by Fe-Mg co-modified water hyacinth-based biochar: Batch adsorption, fixed-bed adsorption, and DFT calculation. *Separation and Purification Technology*, *330*, 125235.

[46] Abdellaoui, Y., Abou Oualid, H., Hsini, A., El Ibrahimi, B., Laabd, M., El Ouardi, M., ... & Gamero-Melo, P. (2021). Synthesis of zirconium-modified Merlinoite from fly ash for enhanced removal of phosphate in aqueous medium: Experimental studies supported by Monte Carlo/SA simulations. *Chemical Engineering Journal*, *404*, 126600.

[47] Xu, H., Zeng, W., Li, S., Wang, B., Jia, Z., & Peng, Y. (2020). Hydrated zirconia-loaded resin for adsorptive removal of phosphate from wastewater. *Colloids and Surfaces A: Physicochemical and Engineering Aspects*, *600*, 124909.

[48] Banu, H. T., Karthikeyan, P., & Meenakshi, S. (2019). Zr4+ ions embedded chitosan-soya bean husk activated bio-char composite beads for the recovery of nitrate and phosphate ions from aqueous solution. *International journal of biological macromolecules*, *130*, 573-583.

CHAPTER 6

Decomposition of Antibiotics Using 3D-Micro-Flower like $BiOBr_{(1-x)}Cl_x$ Solid Solution
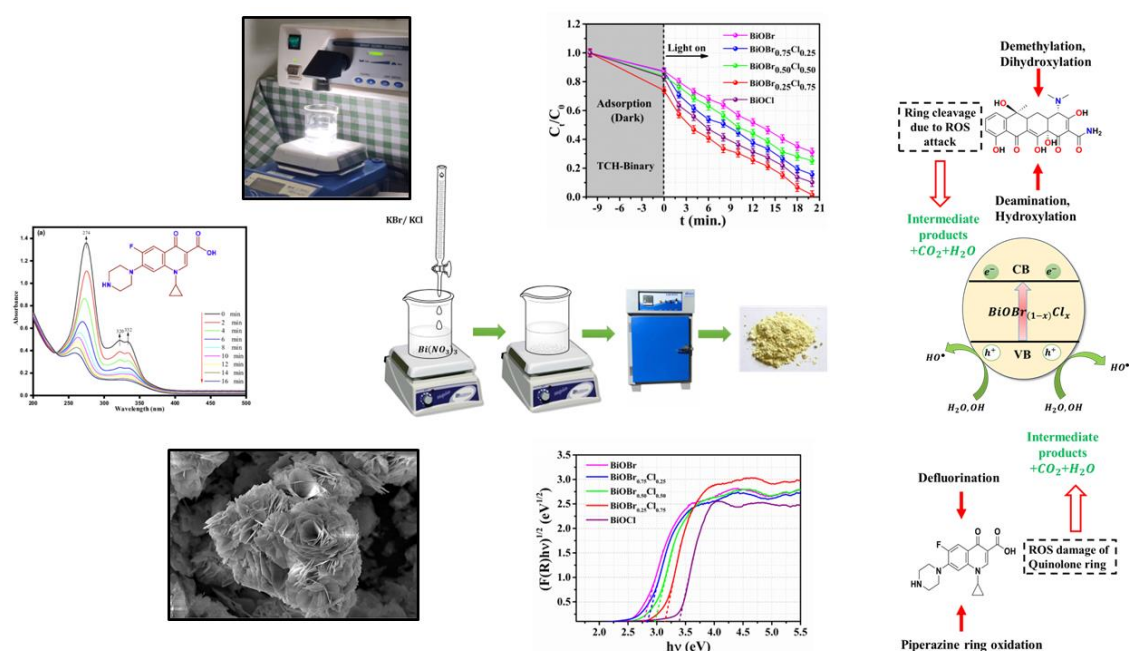
Highlights

- *Fabrication of 3D-mesoporous-flower like $BiOBr_{(1-x)}Cl_x$ nanoplate solid solutions.*

- *Eminent antibiotics photodegradation via heterogeneous photocatalysts*

- *Exploring the interplay between Br/Cl content and photocatalytic proficiency.*

- *Proposing the intricate mechanism and pathway for excellent photocatalytic efficacy*

ABSTRACT

This research addresses the environmental threat posed by residual antibiotics in water and explores the potential of the photocatalytic process as an eco-friendly solution for antibiotic wastewater treatment. Here in, a series of $BiOBr_{(1-x)}Cl_x$ nanosheet solid solutions with varied Br:Cl molar ratios were synthesized through a simple co-precipitation method. Morphological, optical, and structural analyses revealed successful tuning of the optical bandgap from 3.39 eV to 2.75 eV in the samples for light harvesting, facilitated by halide alloying. These solid solutions exhibited superior visible-light-driven photocatalytic activity compared to pristine BiOCl and BiOBr. Notably, the $BiOBr_{0.25}Cl_{0.75}$ sample demonstrated exceptional performance, achieving 89% and 99% degradation efficiency for ciprofloxacin (CIP) and tetracycline hydrochloride (TCH), respectively, within 20 minutes under optimum conditions. The outstanding performance is attributed to factors such as a large specific surface area, suitable morphology and band gap, effective separation of photo-generated electron-hole pairs, and the presence of meso-size pores in the structure. Thermodynamic studies confirmed the exothermic and spontaneous nature of the photocatalytic reactions. The proposed degradation pathway of CIP and TCH, along with the photocatalytic mechanism, is elucidated. The solid solution, $BiOBr_{(1-x)}Cl_x$, exhibits facile recyclability, robust stability, and excellent adaptability to actual aquatic environments, establishing its potential as a promising eco-friendly photocatalyst for antibiotic pollution control.

Keywords: *solid solution, antibiotics, photocatalysis, ciprofloxacin and tetracycline hydrochloride*

6.1. INTRODUCTION

Antibiotics are widespread due to their health benefits, which have led to the growth of pharmaceutical manufacturing units. Improper effluent management from the manufacturing units has led to sewage plants discharging antibiotic components into aquatic environments [1,2]. This persistent pollution threatens ecosystems and promotes antibiotic resistance in living beings. The remains and degraded products of antibiotics in the environment underscore the urgency of their removal to protect the environment and human well-being [3].

Various methods, including adsorption, biological treatment, filtration, coagulation, and advanced oxidation, are used for antibiotic removal. However, they face limitations like limited capacity, incomplete removal, high costs, and harmful byproducts requiring further treatment. [4]. Photocatalytic degradation technology, with its high efficiency, non-toxicity, low cost, and reusability, is gaining prominence in environmental water remediation [5]. Despite its advantages, challenges like wide band gaps and high rates of photoinduced carrier recombination limit its applications [6]. Therefore, developing efficient photocatalysts for improved visible-light absorption and enhanced electron-hole separation is crucial.

Bismuth-based compounds, with their unique layered structure and suitable band gap, are efficient photocatalysts due to the effective separation of photogenerated electron-hole pairs. [7, 8]. However, pure BiOX (X=Cl, Br, I) exhibits limited absorption in the visible-light range, necessitating improvements for practical use. In contrast, mixed solid solutions offer a promising strategy for enhancing photocatalyst properties. The scientific relevance of solid solution photocatalysts lies in their ability to deliver tailored properties for enhanced photocatalytic activity, improved stability, and versatile applications in addressing environmental challenges [9]. Researchers continue to explore and refine these materials to unlock their full potential for sustainable and efficient photocatalysis.

To date, various strategies, including the design of heterojunctions, doping of elements, and the fabrication of solid solutions, have been explored to enhance the photocatalytic performance of bare bismuth oxyhalide [10,11]. It has been demonstrated that the solid solution strategy is an efficient method in this pursuit. The solid solution structure can absorb a broad range of the light spectrum due to its appropriate band gap,

crystal structure, and local electronic structure of photocatalysts [12]. Bismuth oxyhalide-based solid solutions (BiOXY, where X and Y can be Br, Cl, or I) are promising photocatalysts due to their unique layered structure. This structure consists of [Bi_2O_2] layers and double halogen atom layers arranged in a staggered manner. Notably, these solid solution materials maintain the typical layered structure and intrinsic internal electric field of BiOX materials, which promotes charge separation. BiOXY photocatalysts can achieve flexible and adjustable band positions compared to single BiOX materials by modifying the halogen atoms and their proportions. The band position was optimized by adjusting the atomic ratio of Br and Cl atoms, which extended the light response range of pure BiOCl material from UV to visible light. Despite the successful synthesis of BiOX solid solutions using hydrolysis, sol-gel, mechanochemical synthesis, and hydrothermal processes, developing simple, reproducible methods for controlled synthesis remains challenging. [13]. Given the high inclination of Bi^{3+} cations to hydrolysis in water, solvent-based synthesis methods, such as co-precipitation, appear suitable for preparing photocatalysts.

Regarding the above-aforesaid, herein, a series of 3D mesoporous flowerlike $BiOBr_{(1-x)}Cl_x$ solid solutions with varying Br: Cl molar ratios were successfully synthesized through a straightforward one-pot co-precipitation method. The aim was to employ these solid solutions in the hetero photocatalytic degradation of ciprofloxacin (CIP) and tetracycline hydrochloride (TCH) antibiotics under simulated solar light irradiation. The primary objectives included the fabrication of sunlight-activated 3D mesoporous flowerlike Cl–Br bismuth oxides nanosheet solid solutions using an in-situ co-precipitation approach, investigating the impact of different Br to Cl molar ratios, and assessing the photocatalytic activity of these solid solutions in the degradation of CIP and TCH antibiotics.

6.2. EXPERIMENTAL

6.2.1. Reagents and chemicals

Bismuth nitrate pentahydrate $(Bi(NO_3)_3.5H_2O > 99\% \, Alfa \, Aesar)$, Potassium chloride $(KCl > 98\% \, Qualigens)$, Potassium bromide $(KBr > 98\% \, Qualigens)$ Glacial acetic acid $(CH_3COOH, Merk)$, Ciprofloxacin (> 99% Alfa Aesar), Tetracycline hydrochloride (SRL), anhydrous ethanol (99% Merk), deionized water.

6.2.2. Synthesis of the photocatalysts

The $BiOBr_{(1-x)}Cl_x$ microflowers were successfully prepared by the co-precipitation method. Dissolving 2 mmol of $Bi(NO_3)_3 \cdot 5H_2O$ in 10 mL of glacial acetic acid, followed by adding 30 mL of deionized water, allowed for magnetic stirring for 15 minutes. Similarly, 2 mmol of KBr was dispersed uniformly in 30 mL of deionized water, and stirring for 15 minutes was done. The resultant KBr solution was gradually added drop by drop into the Bi precursor solution, forming a white precipitate. After thorough mixing, the mixture underwent continuous stirring for 2 hours and was subsequently washed using deionized water and ethanol. Finally, the obtained products were dried at 60 °C for 12 hours to yield BiOBr powder. The synthesis method of BiOCl is similar to BiOBr; just KCl was replaced by KBr. The $BiOBr_{(1-x)}Cl_x$ solid can be synthesized by varying the molar ratio of KBr and KCl, used in the previous method. The schematic representation of the synthesis of $BiOBr_{(1-x)}Cl_x$ solid solutions microflowers are shown in the Fig.6.1.
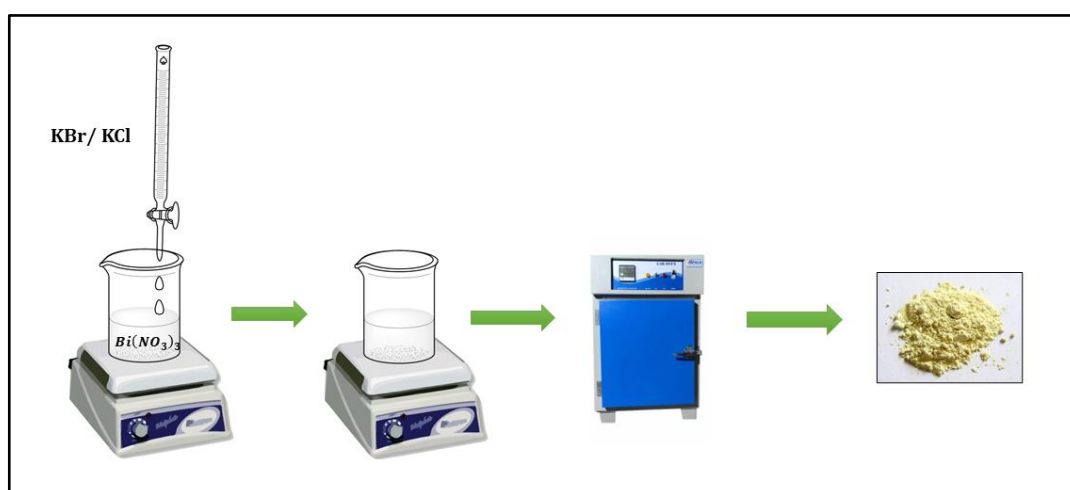
Fig.6.1. *Schematic representation of synthesis of $BiOBr_{(1-x)}Cl_x$ micro flowers.*

6.2.3. Photocatalytic decomposition of antibiotics.

The photocatalytic activities of the as-prepared materials were studied by the decomposition of CIP and TCH single and binary mixtures under simulated sunlight illumination. The photocatalytic experiments were performed at the catalyst dosage of 0.5 g/L and an initial concentration of 20 ppm. A 300W Xe arc lamp was used as the light source for the photocatalytic decomposition of antibiotics in wastewater. The 100.0 mL CIP solution (10.0 mg/L) was first mixed with 50.0 mg of photocatalysts before the photocatalytic process, and the resulting suspension was then stirred for 30 minutes in

the dark to reach adsorption-desorption equilibrium. 2.5 mL of the solution was sampled regularly throughout the photocatalytic process. The sample was centrifuged to facilitate additional analysis and remove the solid material. A Jasco 750 S UV-vis spectrophotometer was used to measure the concentration of CIP at its characteristic wavelength of 276 nm (Lai et al., 2019). Through four adsorption-degradation-regeneration runs, the optimal photocatalyst's recyclability was evaluated.

6.3. RESULTS AND DISCUSSION

6.3.1. Structural characterization.

Fig.6.2. shows the X-ray diffraction (XRD) patterns of photocatalysts comprising $BiOBr_{(1-x)}Cl_x$ solid solutions. The diffraction peaks of both BiOBr and BiOCl agreed with the tetragonal structures of BiOBr (JCPDS No. 00-009-0393) and BiOCl (JCPDS No. 00-006-0249), characterized by the p4/nmm space group [14].
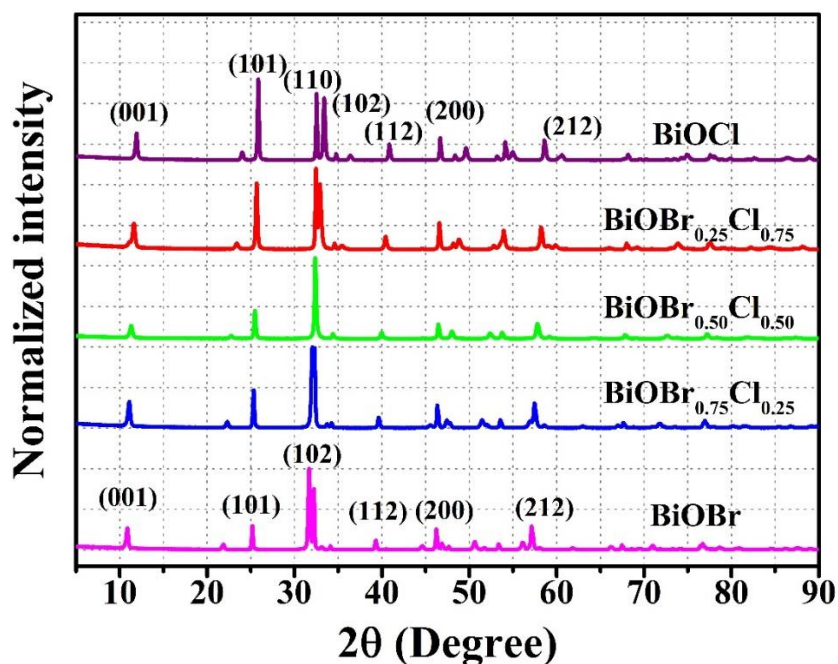
Fig.6.2. *The XRD pattern of synthesized samples. The diffraction peaks of both BiOBr and BiOCl corresponded precisely to the tetragonal arrangements found in BiOBr (JCPDS No. 00-009-0393) and BiOCl (JCPDS No. 00-006-0249), each possessing the p4/nmm space group.*

The XRD patterns of BiOBr, BiOCl and their solid solutions are strikingly similar, underscoring their identical crystal structure and space group. Nevertheless, discernible shifts in peak positions are evident, indicating the substitution of smaller Cl- ions with larger Br- ions [9]. This ionic replacement induces strain within the crystal lattice,

manifesting as observable peak shifts. The enlarged XRD patterns (Fig.6.3) visually elucidate these shifts, offering compelling evidence for the formation of $BiOBr_{(1-x)}Cl_x$ solid solutions. Table 6.1 presents the estimated crystallite size and micro-strain values for the catalysts, providing additional insights into their structural characteristics.
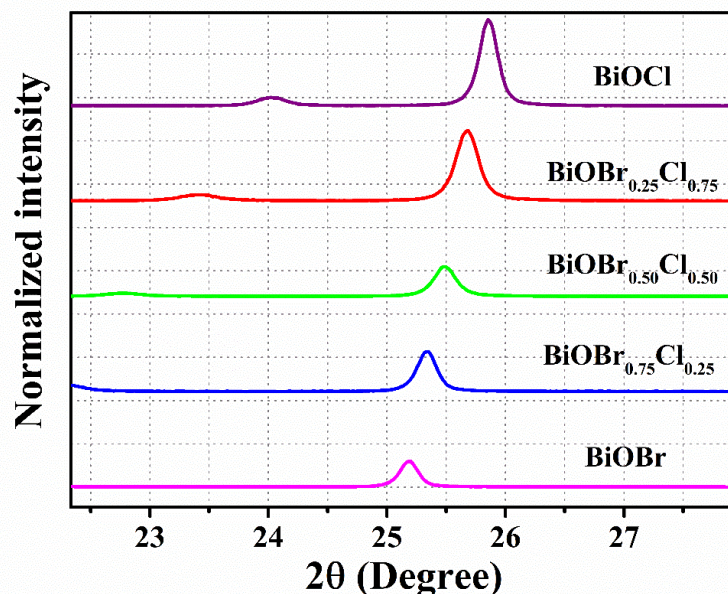
Fig.6.3. *The enlarged portion of the XRD pattern of the sample in the range 23^0-27^0 demonstrates the shift in peak originating from the strain due to ion replacement.*

Table 6.1. *The estimated crystallite size and micro-strain value in the crystal lattice of the photocatalysts.*

Sample	Crystallite size (nm)	Micro-strain (ε) ($\times 10^{-3}$)
$BiOBr$	33.16 ± 2.37	5.50 ± 0.56
$BiOBr_{0.75}Cl_{0.25}$	27.27 ± 2.30	6.75 ± 0.85
$BiOBr_{0.50}Cl_{0.50}$	28.08 ± 1.32	6.53 ± 0.26
$BiOBr_{0.25}Cl_{0.75}$	28.68 ± 1.79	6.67 ± 0.12
$BiOCl$	35.52 ± 2.44	4.71 ± 0.66

6.3.2. Raman analysis

In Fig. 6.4, the Raman spectra of synthesized samples unveil two Raman active modes in both BiOBr and BiOCl. The intense peak at around 130 cm^{-1} is ascribed to the stretching vibrations A$_{1g}$ mode of Bi-Br and Bi-Cl, while the 201 cm^{-1} peak corresponds to the E$_g$ mode of internal Bi–Cl stretching [15]. Notably, the BiOBr sample exhibits only the A$_{1g}$ mode, with the E$_g$ peak being less prominent. Furthermore, compared to the BiOCl sample, the dominant peak undergoes a lower wavenumber shift, likely attributed to the lighter atoms in BiOCl altering the bond length and resulting in a higher wavenumber for the A$_{1g}$ mode in BiOCl. Notably, the significant peaks in all other solid solutions fall between the Raman shifts of BiOBr and BiOCl, aligning with literature reports and underscoring the high quality of both BiOCl and BiOBr [16,17].
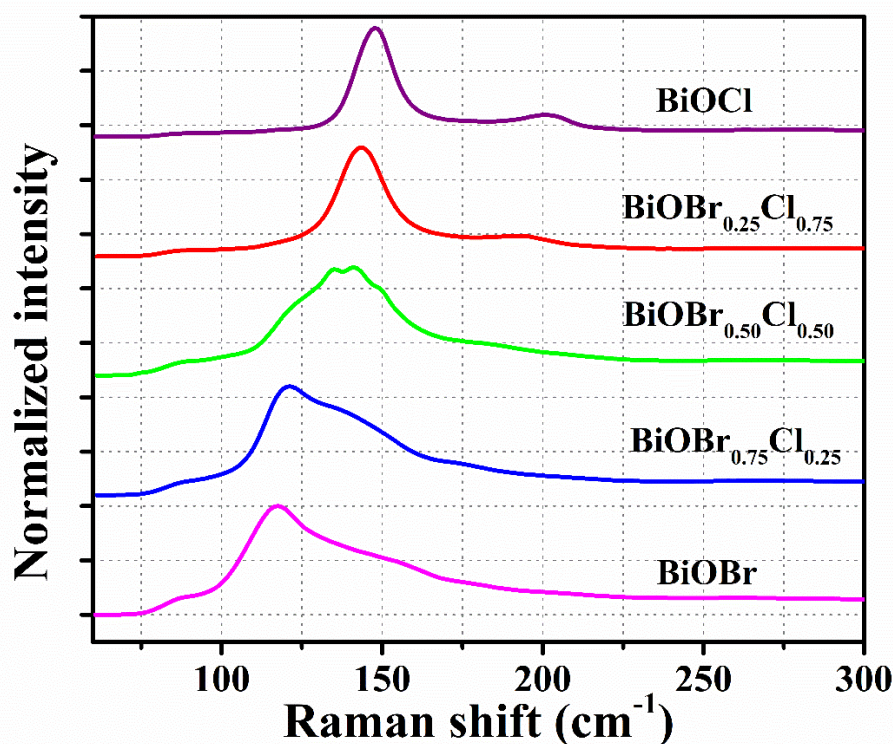
Fig.6.4. *The Raman spectrum of the synthesized samples displays a dominant peak at 147 cm^{-1}, associated with the A$_{1g}$ Bi–Cl internal stretching mode and 201 cm^{-1} originating from the E$_g$ Bi–Cl internal stretching mode.*

6.3.3. Morphological analysis

FESEM analysis was used to evaluate the morphology of samples. As is evident from Fig.6.5. to Fig.6.9., all of the samples have a sheet-like structure with a thickness of several nanometres. As depicted in Fig.6.9., a pristine BiOCl photocatalyst is

composed of stacking small nanoplates, which is a significant result of its unique synthesis conditions. The surface of the nanoplates is smooth; the morphology of these nanoplates can increase their light-harvesting capacity. These nanosheets can provide increased surface area and active sites for the photocatalytic reaction, resulting in enhanced photocatalytic performance. Careful analysis of the FESEM images reveals that the nanoplates are oriented in a regular manner to achieve the micro flower morphology as the Cl : Br ratio increases. The well-oriented micro flower morphology is obtained for the photocatalyst $BiOBr_{0.25}Cl_{0.75}$.For the photocatalyst BiOCl, the micro flower morphology shows a slightly altered, withered flower-like appearance. Thus, we can conclude that the Cl : Br ratio in the solid solution significantly influences both the crystal structure and the morphology of the photocatalysts. This fine-tuning of the morphology through solid solution is achieved using halide alloying, and it is notable that this is accomplished via a simple co-precipitation method, highlighting a unique aspect of this work.
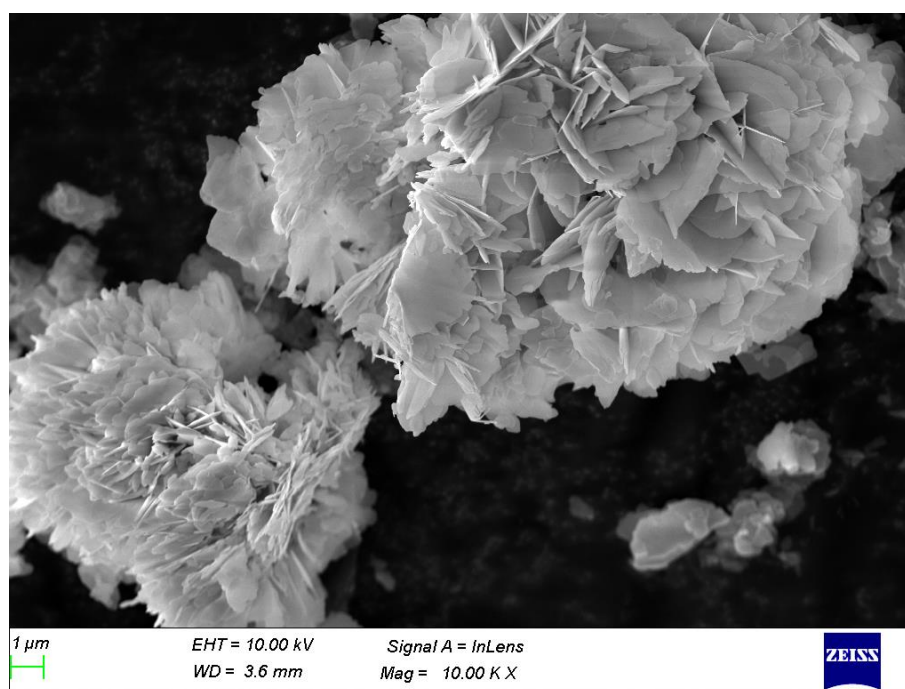
Fig.6.5. *FESEM images of BiOBr*
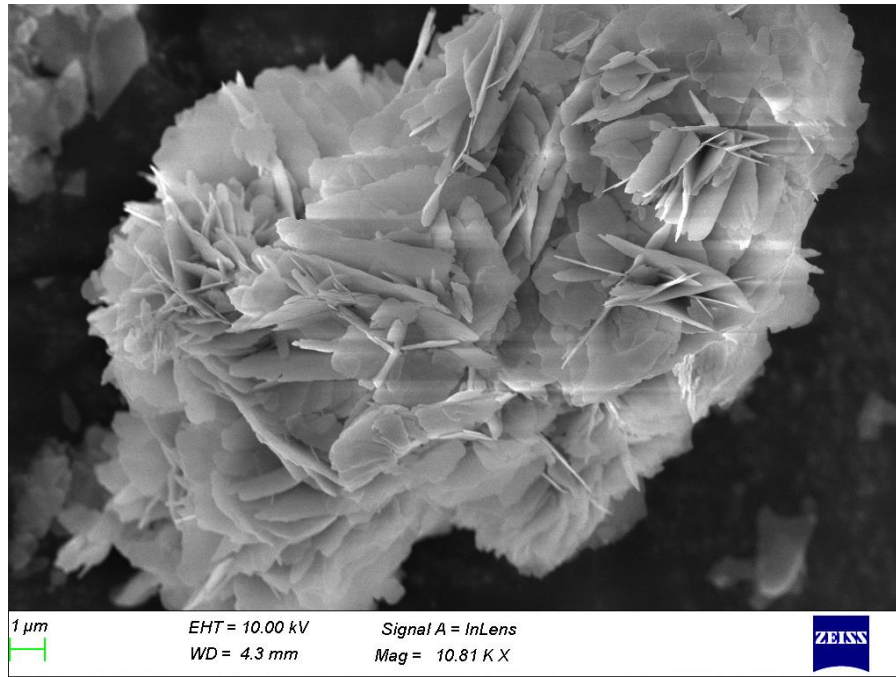
Fig.6.6. *FESEM images of $BiOBr_{0.75}Cl_{0.25}$*
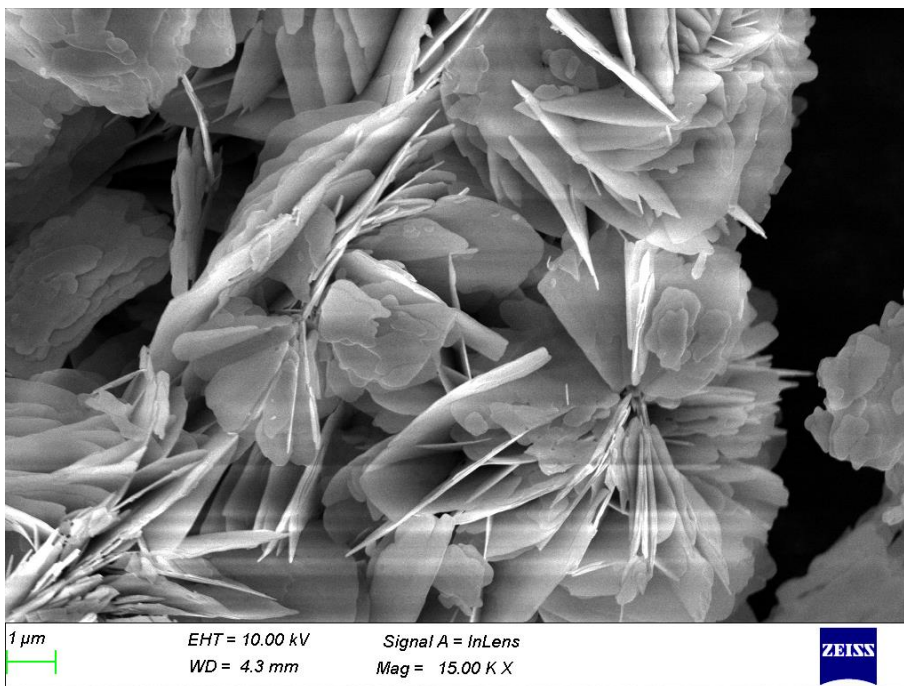
Fig.6.7. *FESEM images of $BiOBr_{0.50}Cl_{0.50}$*
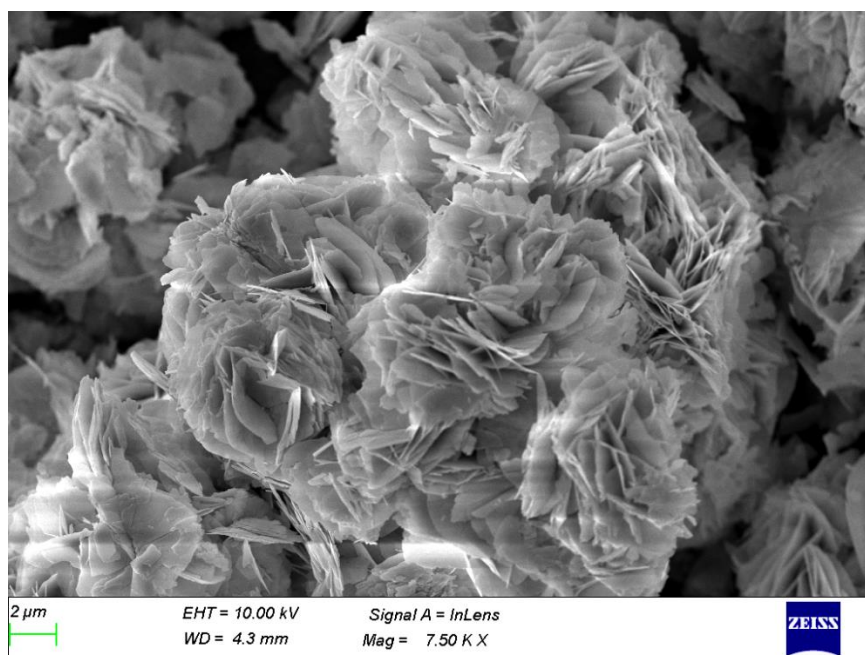
Fig.6.8. *FESEM images of* $BiOBr_{0.25}Cl_{0.75}$
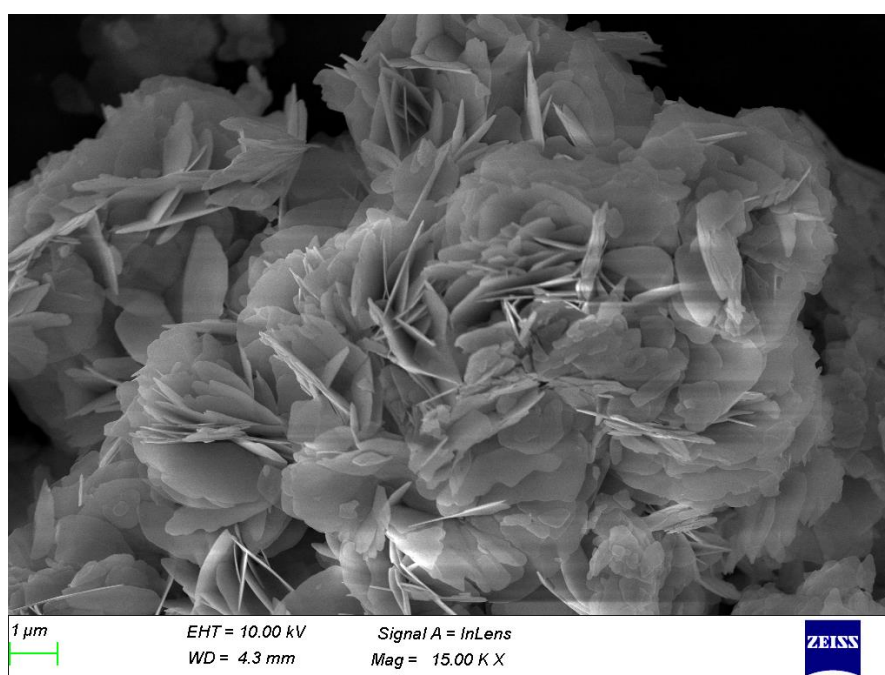
Fig.6.9. *FESEM images of BiOCl.*

6.3.4. Surface area and porosity analysis

The BET-BJH technique was employed to examine the $BiOBr_{(1-x)}Cl_x$ solid solution samples, providing insights into the specific surface area (S_{BET}), pore-size distribution, pore volume (V_p), and pore diameter (d_p). The adsorption-desorption isotherms for all samples, depicted in Fig. 6.10, exhibit a distinctive type IV classification according to IUPAC, characterized by pronounced hysteresis, indicating the mesoporous structure of the as-prepared samples [18]. The BJH distribution of the samples is shown in Fig. 6.11. The pore-size distributions further validate the presence of mesopores within the size range of 6–35 nm in the synthesized samples. The BET surface area of the samples was estimated using the linear fit of P/V_a(P_0-P) versus P/P_0 data points. The estimated surface area, monolayer volume, and mean pore diameter of the samples are shown in Table 6.2.

Table.6.2. *The estimated values of surface area, monolayer volume, mean pore diameter of the sample.*

Sample	Surface area (S_{BET}) m^2/g	Monolayer Volume (V_m) cm^3/g	Mean pore diameter (d_p) (nm)
$BiOBr$	5.80 ± 0.10	1.33 ± 0.01	25.02
$BiOBr_{0.75}Cl_{0.25}$	5.17 ± 0.08	1.18 ± 0.02	26.23
$BiOBr_{0.50}Cl_{0.50}$	6.01 ± 0.15	1.36 ± 0.03	23.50
$BiOBr_{0.25}Cl_{0.75}$	7.15 ± 0.15	1.64 ± 0.03	30.07
$BiOCl$	4.79 ± 0.12	1.02 ± 0.03	25.15
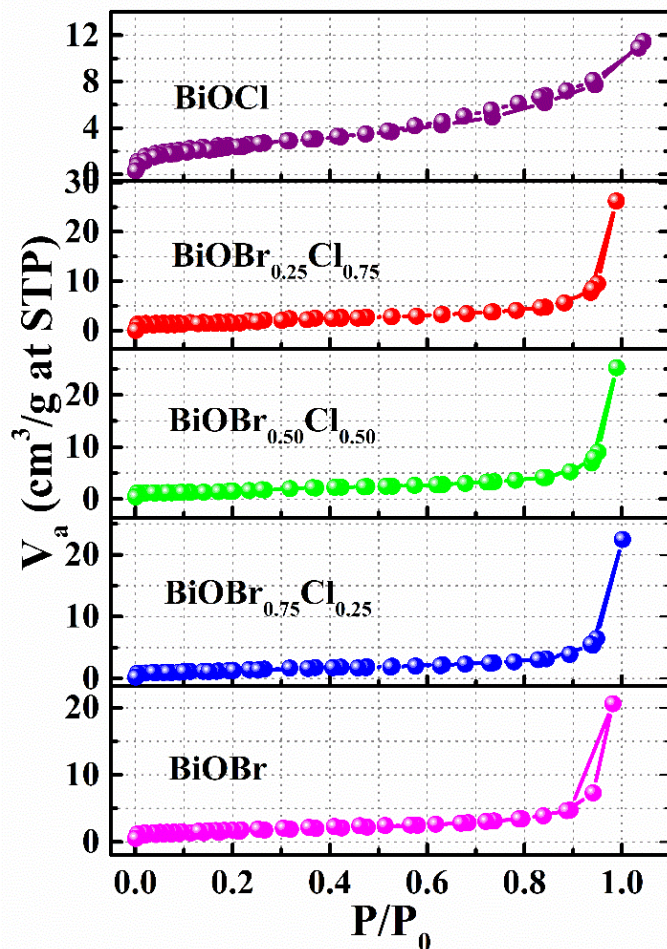
Fig.6.10. *N₂ Adsorption-desorption isotherms which closely match IUPAC classification type IV.*
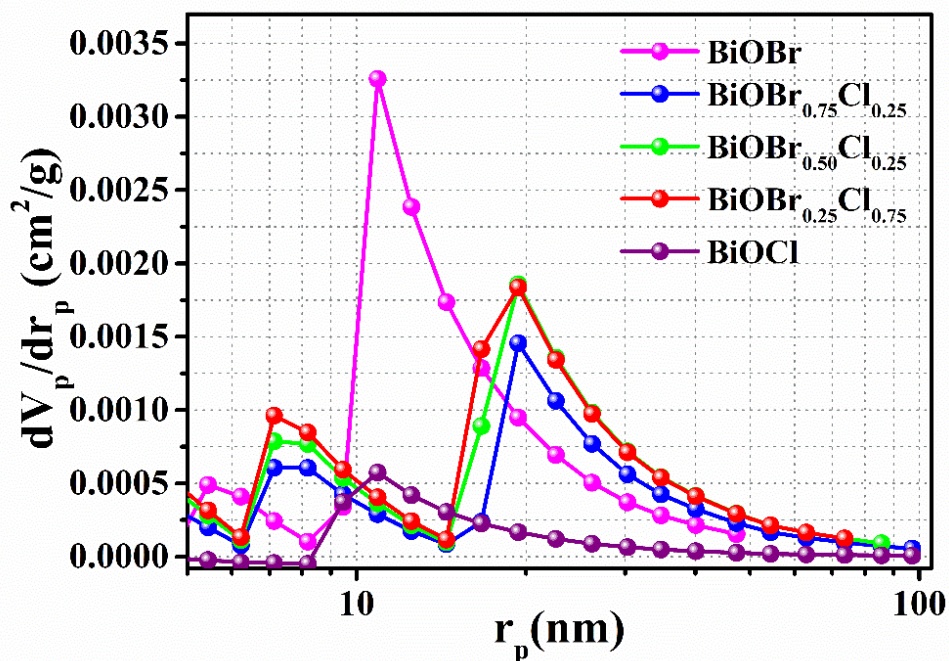
Fig.6.11. *The BJH pore distribution of mesopores within the size range of 6–35 nm.*
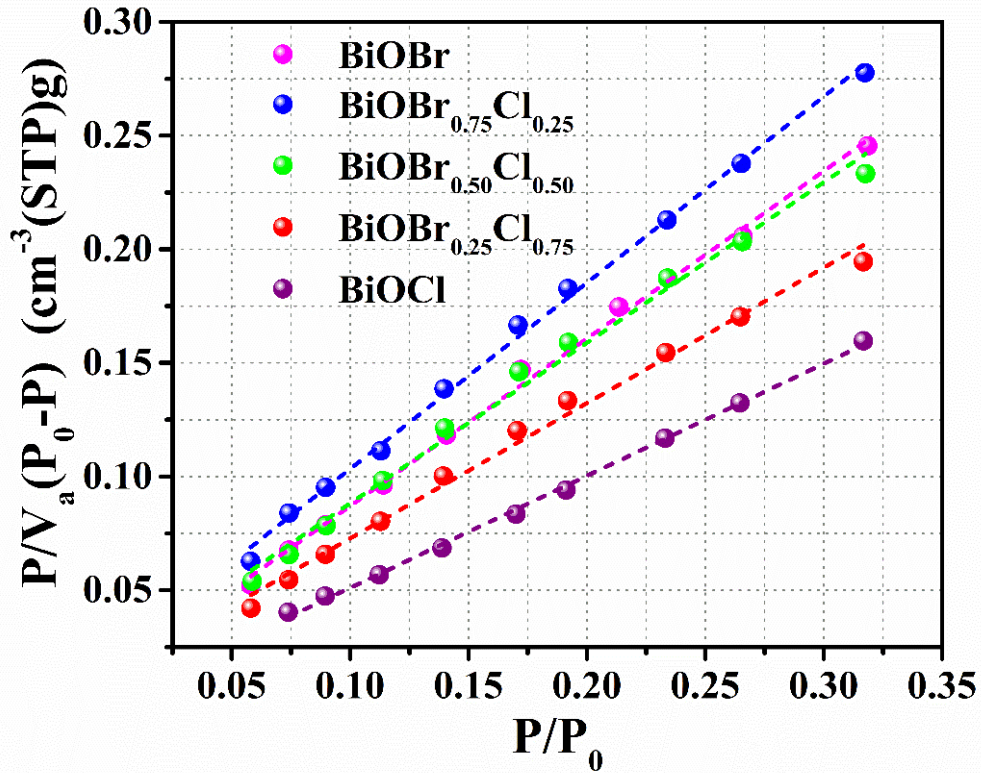
Fig.6.12. *The linear fit of $P/V_a(P_0-P)$ versus P/P_0 data points for the estimation of BET surface area.*

6.3.5. UV-Visible spectroscopic analysis

The light-harvesting ability of the photocatalysts is a crucial factor in determining photocatalytic activity. Fig.6.13. depicts the UV-visible DRS spectrum of the synthesized samples. Notably, the BiOCl sample exhibits a broad UV light response, evident from its absorption edge at approximately 356 nm. In contrast, the $BiOBr_{(1-x)}Cl_x$ solid solution displays a remarkable increase in visible light absorption compared to BiOCl, with its band edge shifting from 356 to 428 nm. The band edge positions of the synthesized samples are provided in Table.6.3.

The determination of the band gap energy for as-synthesized photocatalysts was performed by the Kubelka-Munk equation [19]:

$$(F(R)h\upsilon)^n = k\left(h\upsilon - E_g\right) \dots \dots (6.1)$$

$F(R)$ is the Kubelka-Munk function for the approximation of absorption co-efficient, $h\upsilon$ is the energy of a photon, E_g is the energy band gap of the sample and k is

the proportionality constant. While n is the constant associated with different types of electronic transition, in this study $n = \frac{1}{2}$ implies the indirect transitions.
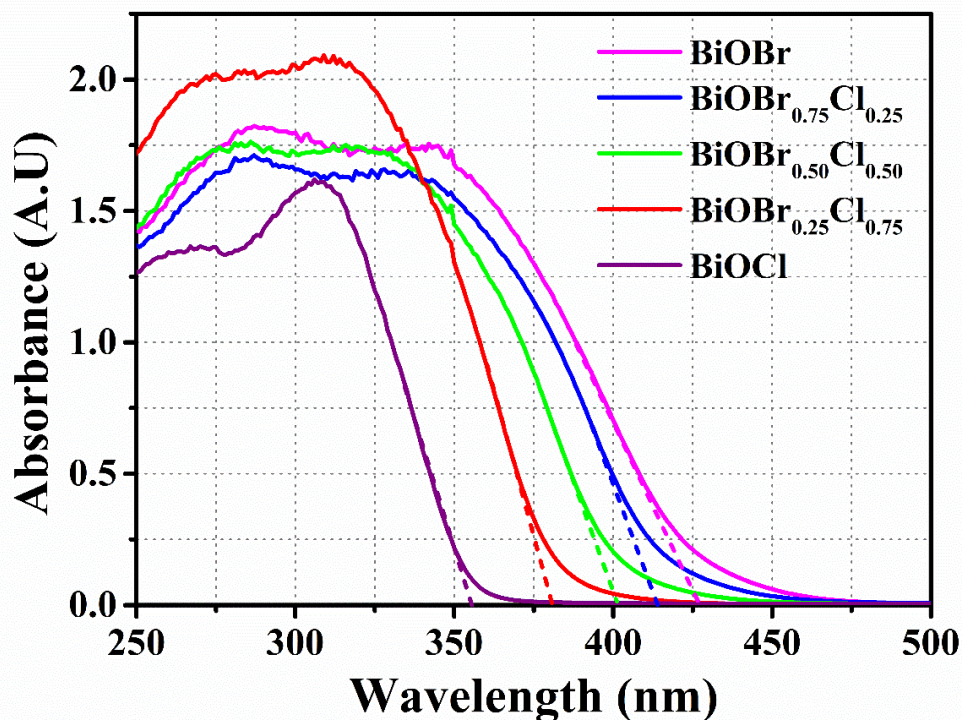
Fig.6.13. *The UV-Visible absorption spectrum of the sample shows a band edge shift from 356 nm to 428 nm (redshift) as the ratio of Cl to Br in the bare BiOCl sample is increased.*

The band gap energy of the synthesized samples can be estimated by extrapolating the linear portion of the $(F(R)h\nu)^{\frac{1}{2}}$ versus $h\nu$ graph. This is shown in 6.14. Table.6.3. represents the estimated band gap values for the samples, revealing the successful tuning of the optical band gap from 3.39 eV to 2.75 eV by increasing the Br : Cl molar ratio. This observation signifies effective halide alloying within the pristine BiOBr crystal lattice.
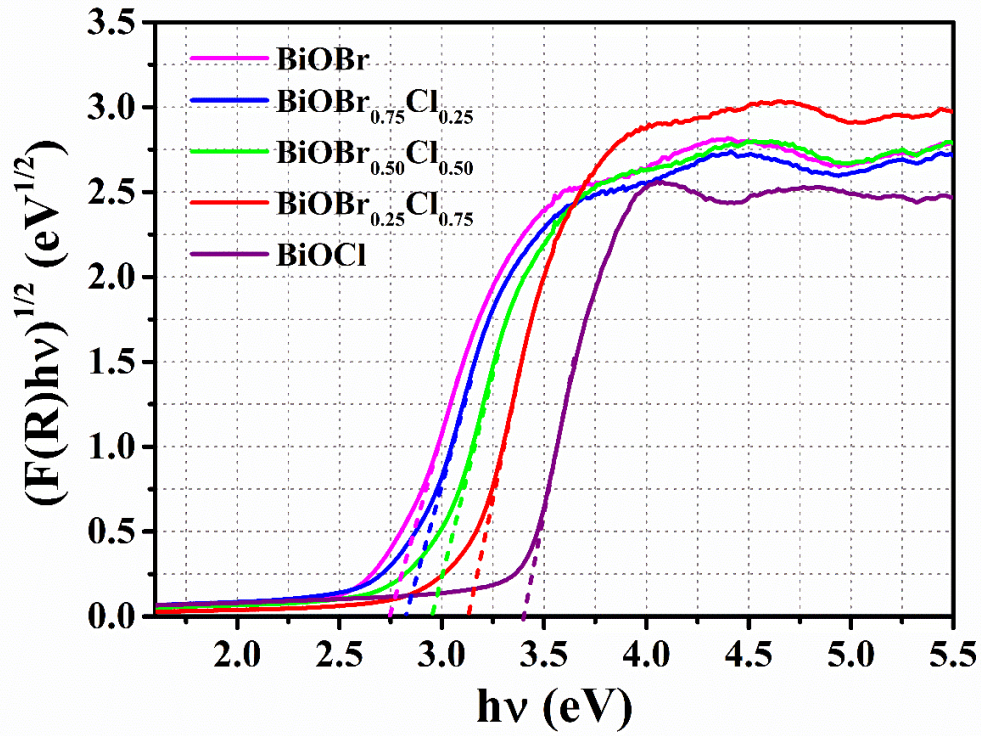
Fig.6.14. *The plot of $(F(R)h\nu)^{\frac{1}{2}}$ versus $h\nu$. The successful tuning of the optical band gap from 3.39 eV to 2.75 eV in the samples is a clear indicator of the effective introduction of halide alloying into the pure BiOBr crystal lattice.*

Table.6.3. *Estimated values bandgap and band edge of the synthesized samples.*

Sample	Band gap (eV)	Band edge (nm)
$BiOBr$	2.75 ± 0.05	428 ± 1
$BiOBr_{0.75}Cl_{0.25}$	2.81 ± 0.05	413 ± 1
$BiOBr_{0.50}Cl_{0.50}$	2.96 ± 0.05	401 ± 1
$BiOBr_{0.25}Cl_{0.75}$	3.13 ± 0.05	381 ± 1
$BiOCl$	3.39 ± 0.05	356 ± 1

6.3.6. Photocatalytic studies

The performance of $BiOBr_{(1-x)}Cl_x$ nano photocatalysts were evaluated for degrading CIP and TCH antibiotics under simulated solar light. Adsorption equilibrium was achieved within 20 minutes prior to illumination. Photolysis experiments in the absence of the photocatalyst, under simulated sunlight, showed negligible degradation. However, significant degradation of CIP and TCH was observed in the presence of the photocatalyst under visible light irradiation. Notably, the $BiOBr_{0.25}Cl_{0.75}$ solid solution, after 20 minutes of irradiation, exhibited superior performance, removing 99% of TCH and 89% of CIP from wastewater. In comparison, pristine BiOBr achieved only 69% of TCH and 58% of CIP removal, and BiOCl achieved approximately 86% of TCH and 82% CIP removal. Additionally, experiments involving a binary mixture of TCH and CIP affirmed the superior photocatalytic activity of $BiOBr_{0.25}Cl_{0.75}$ photocatalysts. These findings underscore the enhanced photocatalytic activity of solid solution samples over their pure counterparts. The time-dependent degradation of the CIP and TCH antibiotics in the single and binary system are shown in Figs.6.15-6.18. The percentage of degradation efficiency in the single and binary mixture is shown in Table 6.4.

Table.6.4. *Summary of degradation efficiency of various photocatalytic decomposition of CIP and TCH. (C₀=10 ppm CIP, Dosage= 0.5 g/L, T=303 K Ph ~ 7, Irradiation time of light =20 min.)*

Sample	Degradation efficiency (%) – Single		Degradation efficiency (%) – Binary	
	TCH	CIP	TCH	CIP
$BiOBr$	69.8 ± 1.7	58.7 ± 1.2	84.4 ± 1.8	58.7 ± 1.1
$BiOBr_{0.75}Cl_{0.25}$	78.5 ± 1.1	68.7 ± 1.2	68.7 ± 1.4	44.5 ± 1.2
$BiOBr_{0.50}Cl_{0.50}$	94.7 ± 1.1	76.5 ± 1.3	74.7 ± 1.8	49.8 ± 1.9
$BiOBr_{0.25}Cl_{0.75}$	99.0 ± 1.1	89.7 ± 1.2	98.4 ± 1.2	63.8 ± 1.5
$BiOCl$	89.7 ± 1.1	83.4 ± 1.2	89.7 ± 2.1	55.7 ± 1.2
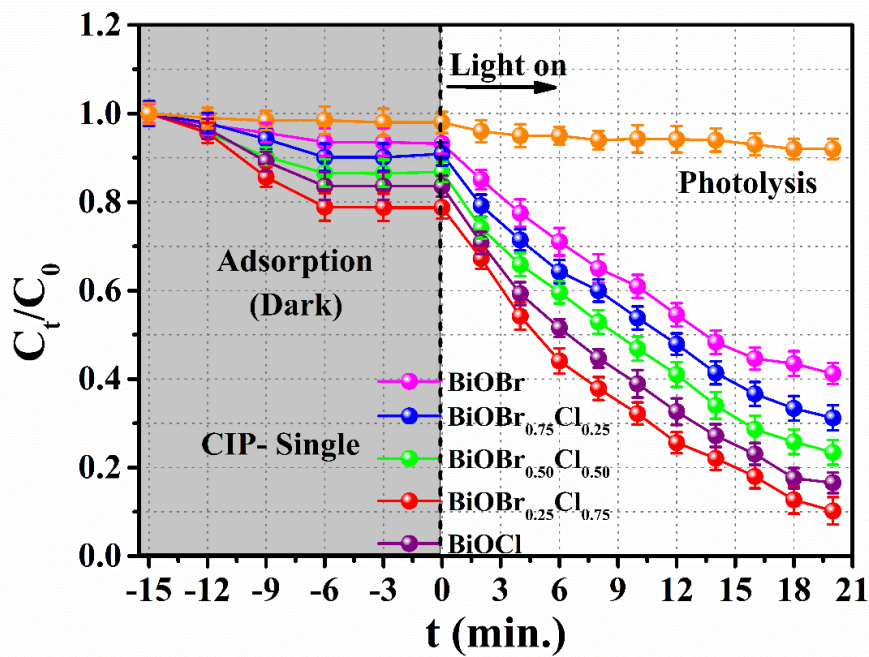
Fig.6.15. *The temporal variation of the degradation of CIP in the single system. (C_0=10 ppm CIP, Dosage= 0.5 g/L, T=303 K pH ~ 7, Irradiation time of light =20 min.)*
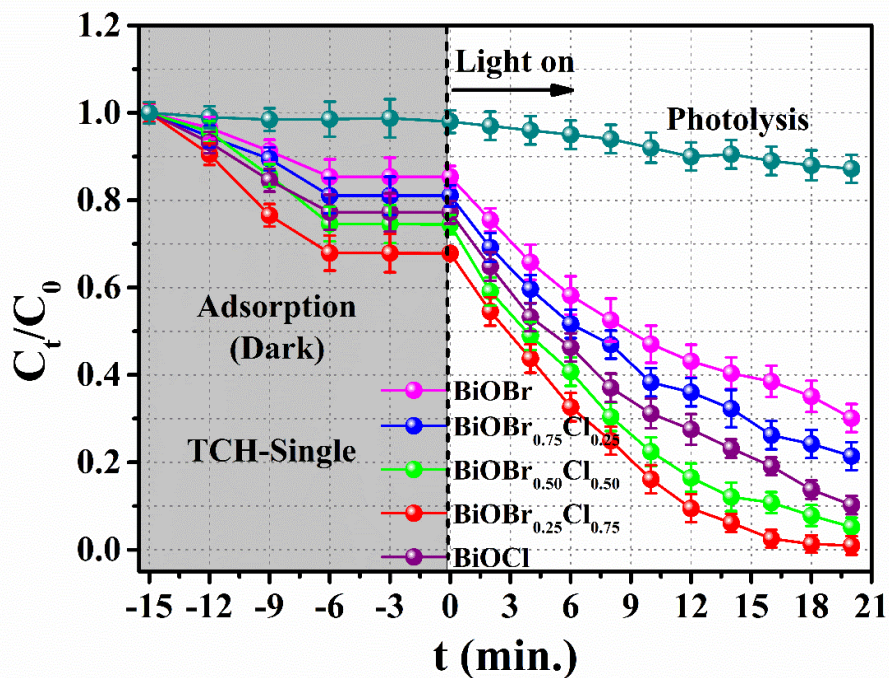
Fig.6.16. *The temporal variation of the degradation of TCH in the single system. (C_0=10 ppm CIP, Dosage= 0.5 g/L, T=303 K pH ~ 7, Irradiation time of light =20 min.)*
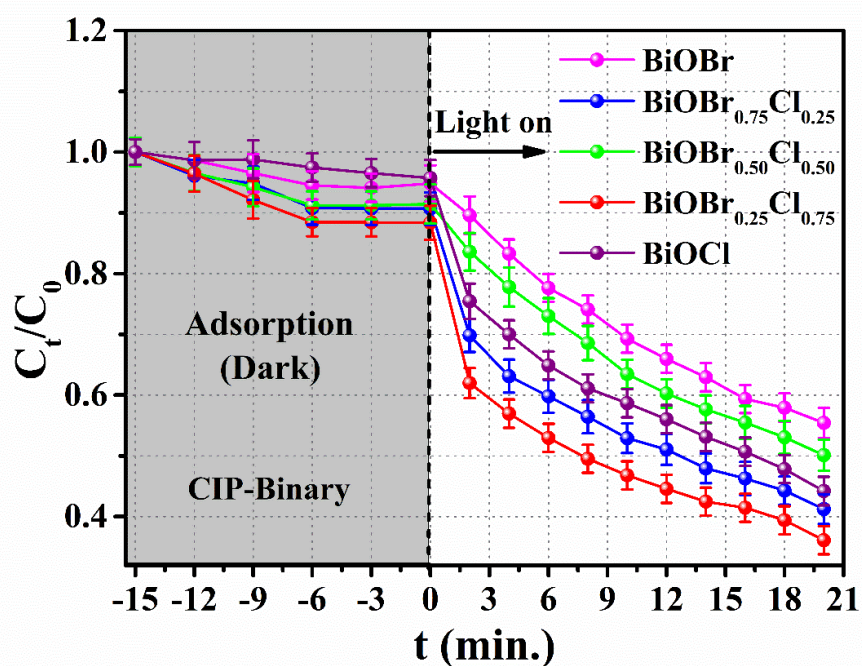
Fig.6.17. *The temporal variation of the degradation of CIP in the binary system. (C_0=10 ppm CIP, Dosage= 0.5 g/L, T=303 K pH ~ 7, Irradiation time of light =20 min.)*
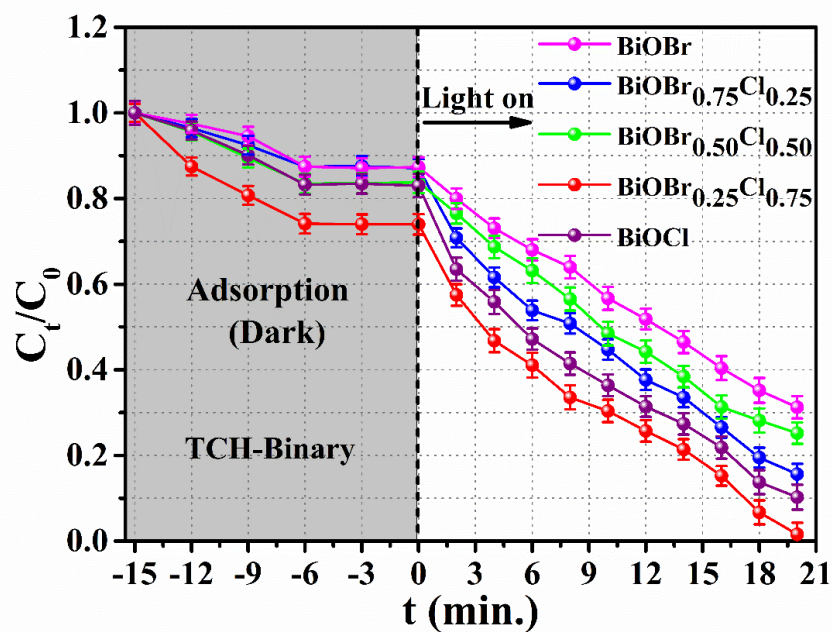
Fig.6.18. *The temporal variation of the degradation of TCH in the binary system. (C_0=10 ppm CIP, Dosage= 0.5 g/L, T=303 K pH ~ 7, Irradiation time of light =20 min.)*

The photodegradation kinetics of the CIP and TCH molecules over the fabricated photocatalysts were investigated by the Pseudo first-order kinetic formula [20]:

$$\ln\left(\frac{C_0}{C_t}\right) = k_{app}t \dots \dots (6.2)$$

The table displays the estimated apparent rate constant for the reaction (refer to Table 6.5.). In comparison to pure BiOCl and BiOBr, $BiOBr_{0.25}Cl_{0.75}$ demonstrated the highest value, exceeding them by 1.1 and 2.2 times, respectively, for CIP degradation and 1.7 and 2.8 times, respectively, for TCH degradation in single and binary systems, respectively. This remarkable improvement can be attributed to the compelling presence of surface-active sites and the efficient separation of photoinduced charge carriers. The linear fit of the binary system, particularly the data points corresponding to the photocatalyst $BiOBr_{0.25}Cl_{0.75}$ shows slight deviations from linear behavior. This implies that the degradation of CIP and TCH in the binary system deviates slightly from pseudo-first-order kinetics. This deviation can arise from factors such as mass transfer limitations, variations in light exposure, surface interactions, and the formation of reaction intermediates. These factors may lead to the exhibition of higher-order kinetic degradation in the binary system. Further studies in this area are being considered for future work.

Table 6.5. *The apparent rate constant of the degradation reaction for the single and binary systems. (C_0=10 ppm CIP, Dosage= 0.5 g/L, T=303 K pH~ 7, Irradiation time of light =20 min.)*

Sample	Rate constant k_{app} ($\times 10^{-3} min.^{-1}$) - Single		Rate constant k_{app} ($\times 10^{-3} min.^{-1}$) - Binary	
	CIP	TCH	CIP	TCH
BiOBr	43.69 ± 0.75	56.77 ± 0.24	28.92 ± 0.07	46.54 ± 0.14
$BiOBr_{0.75}Cl_{0.25}$	53.95 ± 0.10	74.36 ± 0.25	42.17 ± 0.42	70.31 ± 0.25
$BiOBr_{0.50}Cl_{0.50}$	65.32 ± 0.13	122.16 ± 1.33	33.27 ± 0.12	58.88 ± 0.19
$BiOBr_{0.25}Cl_{0.75}$	96.98 ± 0.18	160.83 ± 1.23	50.033 ± 0.61	102.54 ± 0.54
BiOCl	81.58 ± 0.12	93.76 ± 0.25	37.35 ± 0.29	84.30 ± 0.32
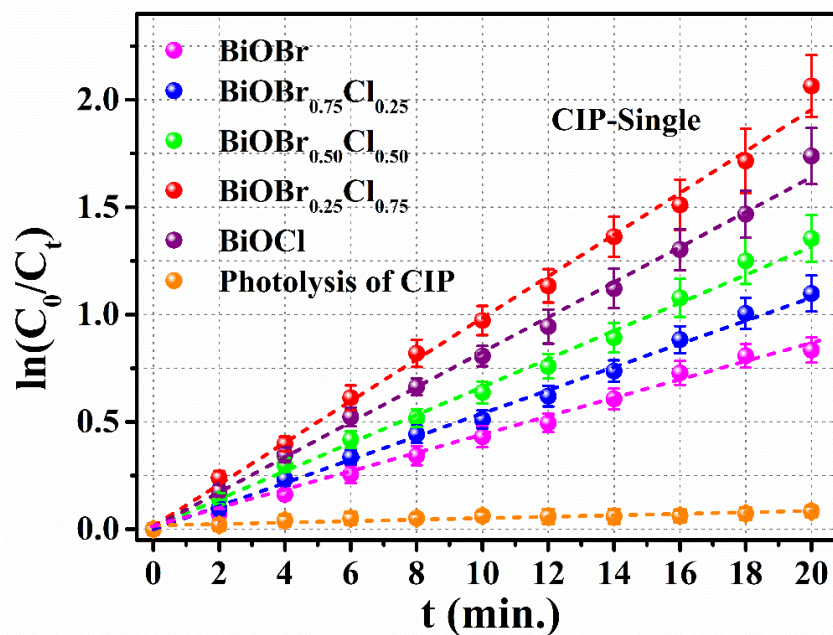
Fig.6.19. *Pseudo First Order kinetic fitting of the photodegradation reaction of CIP single system. (C_0=10 ppm CIP, Dosage= 0.5 g/L, T=303K pH ~ 7, Irradiation time of light =20 min.)*
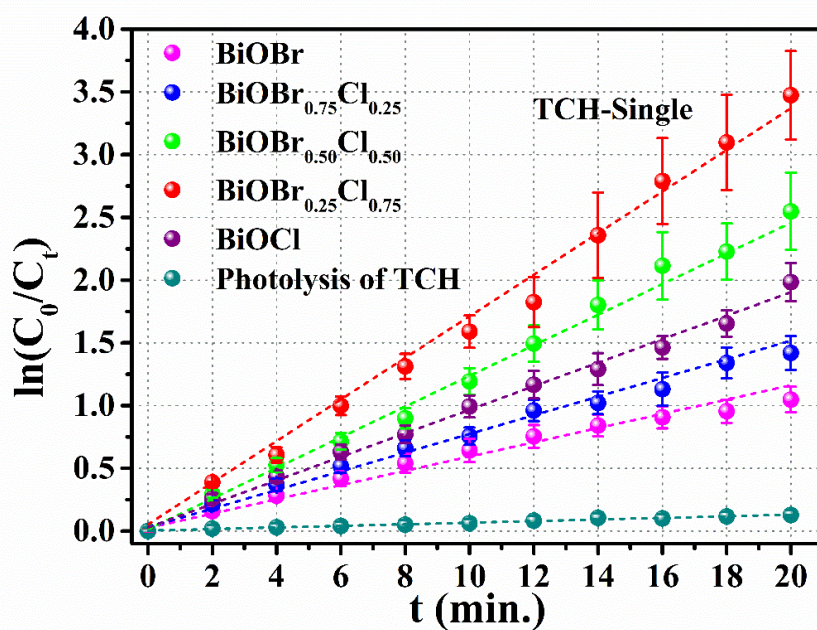
Fig.6.20. *Pseudo First Order kinetic fitting of the photodegradation reaction of TCH single system. (C_0=10 ppm CIP, Dosage= 0.5 g/L, T=303K pH ~ 7, Irradiation time of light =20 min.)*
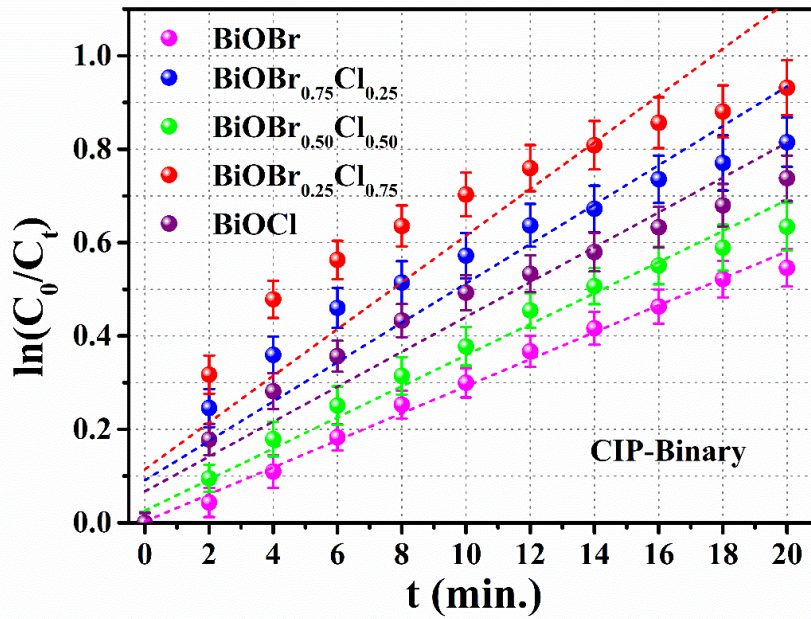
Fig.6.21. *Pseudo First Order kinetic fitting of the photodegradation reaction of CIP binary system. (C_0=10 ppm CIP, Dosage= 0.5 g/L, T=303K pH ~ 7, Irradiation time of light =20 min.)*
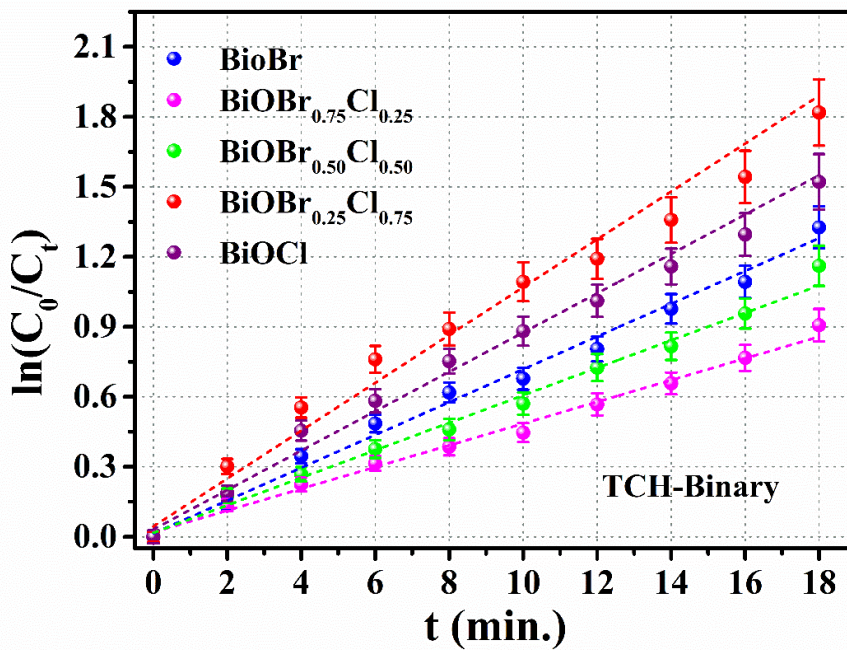
Fig.6.22. *Pseudo First Order kinetic fitting of the photodegradation reaction of TCH binary system. (C_0=10 ppm CIP, Dosage= 0.5 g/L, T=303K pH ~ 7, Irradiation time of light =20 min.)*

The linear fit of PFO kinetics for various photocatalytic reactions are shown in Figs.6.19-6.21.The results indicate that the fabrication of the $BiOBr_{(1-x)}Cl_x$ solid solution significantly enhances photocatalyst activity by developing physicochemical properties during the halide alloying process. Compared to pristine BiOBr and BiOCl, the solid solution demonstrates superior photocatalytic activity in the degradation of antibiotics in both single and binary mixtures. Upon further investigation of the enhanced photocatalytic activity among the three solid solutions, it was found that the one $BiOBr_{0.25}Cl_{0.75}$ exhibits the highest efficiency in degrading CIP and TCH. Now let us investigate how these solid solutions exhibit superior photocatalytic activity over pristine BiOBr and BiOCl. Firstly, the solid solution samples offer a larger specific surface area, providing more reaction sites for the photocatalytic process. Secondly, as confirmed by BET and BJH analysis, the presence of large pores facilitates the diffusion of reactant molecules. Additionally, the solid solution structure aids in efficiently separating charge carriers, further enhancing photocatalytic activity.

The light-harvesting capability of the photocatalysts significantly influences their photocatalytic efficiency. The process of halide alloying tunes the bandgap, enhancing the light-harvesting capability by adjusting the Br:Cl molar ratio in the solid solutions. Specifically, a Br:Cl molar ratio of 1:3 demonstrated the highest efficiency. This enhanced photoactivity at the 1:3 molar ratio, in comparison to the pristine BiOBr photocatalyst, can be attributed to the widened band gap with increasing Cl content. This widening facilitates increased absorption of visible light and the generation of more electron-hole pairs.

6.3.7. Hall measurement studies of the photocatalysts

Charge carrier concentration and transport in the photocatalyst can be investigated with DC field Hall effect measurements. The investigation can provide the samples' carrier mobility (μ) and carrier concentration (n). Conductivity (σ) is evaluated with the equation $\sigma = ne\mu$, where 'e' represents the charge of the electron. Table.6.6. presents the Hall measurement outcomes and calculated conductivity values. All samples exhibit a positive carrier concentration, identifying them as p-type semiconductors. Despite BiOBr having a significantly greater carrier concentration than other photocatalysts, its mobility and conductivity remain relatively low. Upon introducing Cl into the BiOBr solids, an initial decrease in carrier concentration is observed, followed by an increase, reaching a maximum value in the $BiOBr_{0.25}Cl_{0.75}$ sample. Moreover, the

mobility and conductivity of this photocatalyst exhibit significantly larger values than others. The optimal combination of carrier concentration, mobility, and conductivity in $BiOBr_{0.25}Cl_{0.75}$ contributes to its favourable photocatalytic activity.

Table.6.6. *The carrier concentration, mobility and conductivity of the catalysts obtained from DC Hall measurement.*

Sample	Carrier concentration n ($\times 10^{16} cm^{-3}$)	Mobility μ ($cm^2 V^{-1} s^{-1}$)	Conductivity σ ($\Omega^{-1} cm^{-1}$)
$BiOBr$	4.76 ± 0.11	22.54 ± 1.25	0.17 ± 0.01
$BiOBr_{0.75}Cl_{0.25}$	1.76 ± 0.48	122.99 ± 3.12	0.34 ± 0.10
$BiOBr_{0.50}Cl_{0.50}$	0.50 ± 0.04	156.10 ± 3.41	0.13 ± 0.01
$BiOBr_{0.25}Cl_{0.75}$	3.24 ± 0.10	167.38 ± 4.12	0.86 ± 0.04
$BiOCl$	3.06 ± 0.18	140.16 ± 2.15	0.75 ± 0.05

6.3.8. Thermodynamic studies of photocatalysis.

Henry Eyring's Transition State Theory (TST) analyses the thermodynamics of photocatalytic degradation by relating the rate constant of the reaction to thermodynamic parameters, expressed in logarithmic form as [23]:

$$\ln\left(\frac{k_{app}}{T}\right) = -\frac{\Delta H}{R}\left(\frac{1}{T}\right) + \frac{\Delta S}{R} + \ln\left(\frac{k_B}{h}\right) \dots \dots (6.3)$$

where k_{app} is the apparent rate constant of the reaction, R is the universal gas constant $(8.314\ JK^{-1}mol^{-1})$, k_B is the Boltzmann constant $(1.38 \times 10^{-23} JK^{-1})$, ΔH and ΔS are the enthalpy and entropy changes of the reaction. The values of ΔH and ΔS for the photocatalytic degradation reactions were calculated from the slope and intercept of the $\ln\left(\frac{k_{app}}{T}\right) - \frac{1}{T}$ plot, which is shown in Fig.6.23. The estimated values of thermodynamic parameters are shown in Table 6.7.
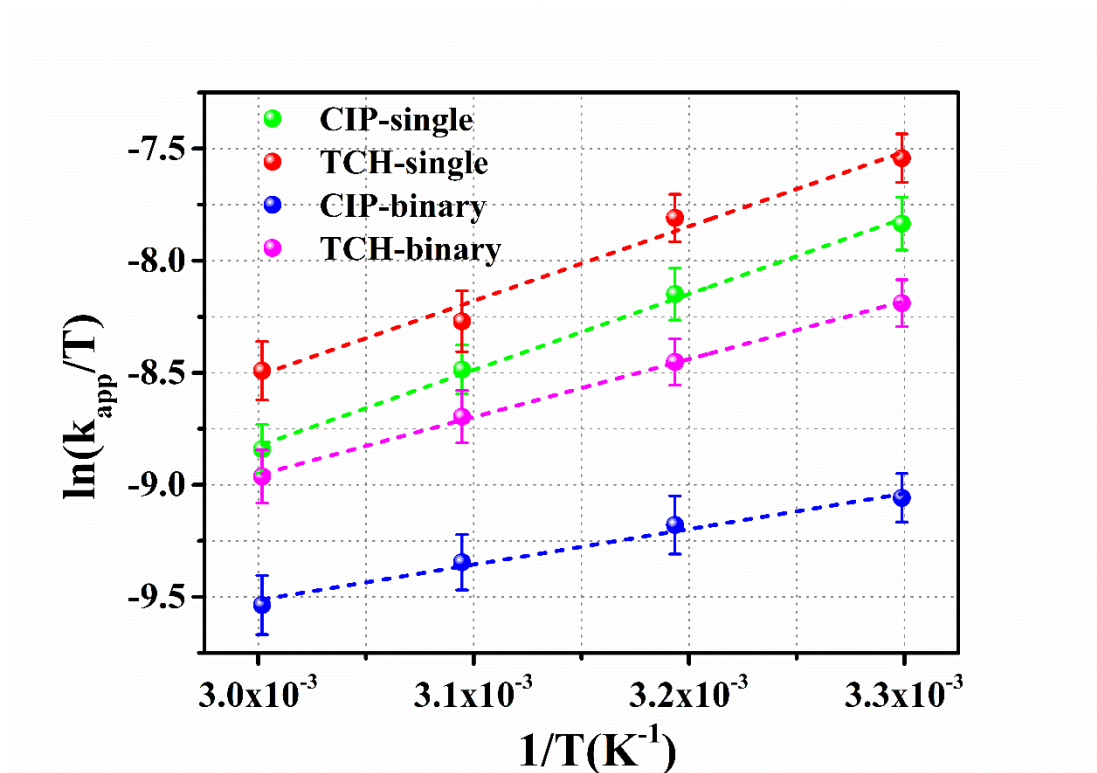
Fig.6.23. *The* $\ln\left(\frac{k_{app}}{T}\right) - \frac{1}{T}$ *plot for estimating the various thermodynamic parameters of the catalytic reactions. (C₀=10 ppm, Dosage= 0.5 g/L, T=303 K pH ~ 7, Irradiation time of light =20 min.)*

In all photocatalytic degradation reactions, a consistently negative enthalpy change (ΔH) signifies the exothermic nature of these processes, indicating the release of heat into the surroundings [24]. Concurrently, a positive entropy change (ΔS) suggests an increase in overall disorder or randomness as the photocatalytic reactions progress [25]. The negative ΔH and positive ΔS combination results in a negative Gibbs free energy change (ΔG) across all temperatures, as depicted in Fig.6.24. This observation underscores the spontaneity and thermodynamic feasibility of the photocatalytic reactions under standard conditions. The negative ΔG values affirm the favourability of these reactions without the need for external energy input, emphasizing their spontaneous nature in the given experimental conditions.
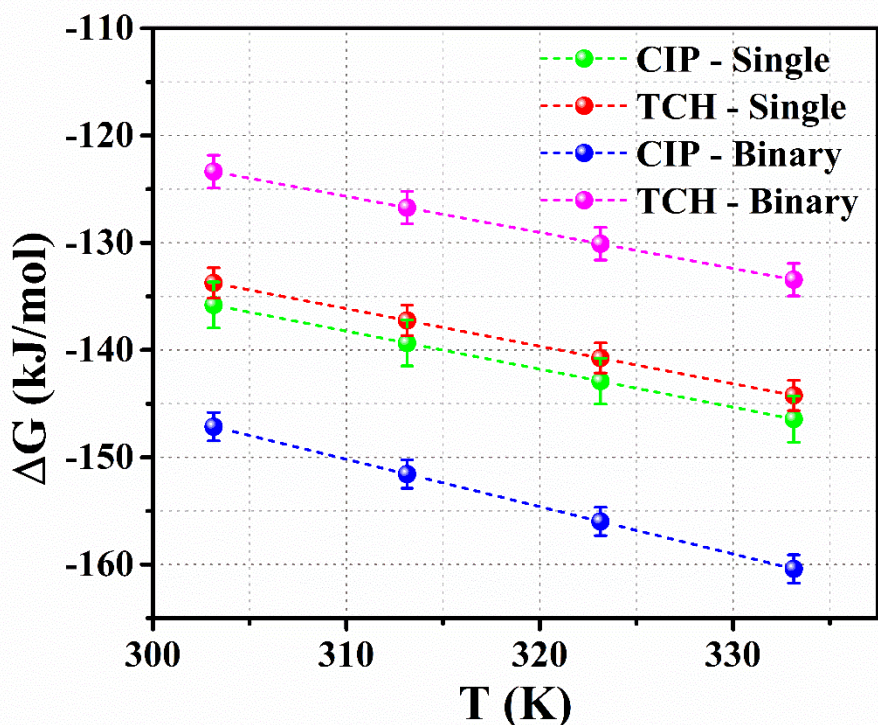
Fig.6.24. *The variation of Gibb's free energy change of the reaction with temperature. (C_0=10 ppm, Dosage= 0.5 g/L, pH ~ 7, Irradiation time of light =20 min.)*

The temperature influence on the reaction rate was investigated through kinetic experiments conducted within the temperature range of 298–318 K. The determination of the activation energy (E_a) for the reaction was carried out using the Arrhenius equation [26].

$$\ln k_{app} = -\frac{E_a}{R}\left(\frac{1}{T}\right) + \ln A \ldots \ldots (6.4)$$

The slope of the $\ln k_{app} - \frac{1}{T}$ plot provided E_a. This is shown in Fig.6.25. A lower activation energy, as seen in Table.6.7. for various photocatalytic processes, signifies higher catalytic activity and effectiveness. In binary systems, activation energy is lower than in single pollutant systems, possibly due to increased molecular collisions from pollutant crowding, leading to decreased activation energy and less pronounced temperature dependence of the reaction rate [27].
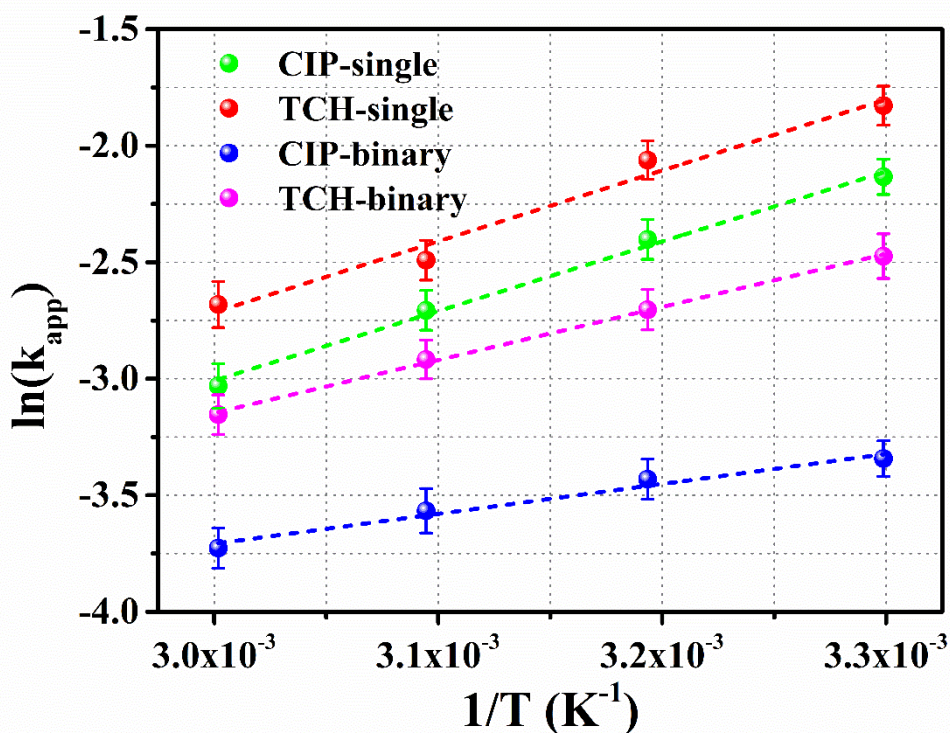
Fig.6.25. *The linear fit for the estimation of activation energy. The* $\ln k_{app} - \frac{1}{T}$ *plot. (C$_0$=10 ppm, Dosage= 0.5 g/L, pH ~ 7, Irradiation time of light =20 min.)*

Table 6.7. *The estimated value of thermodynamic parameters of the photocatalytic reactions.*

Photocatalytic reaction	ΔH $(kJmol^{-1})$	ΔS (JK^{-1})	$E_a(kJmol^{-1})$
CIP-Single	-28.18 ± 1.11	355.13 ± 7.84	-24.84 ± 1.24
TCH-Single	-27.64 ± 2.59	350.89 ± 8.70	-25.29 ± 2.75
CIP-Binary	-13.16 ± 1.15	442.70 ± 4.25	-10.67 ± 1.12
TCH-Binary	-21.51 ± 0.52	336.18 ± 4.02	-18.95 ± 0.55

6.3.9. Effect of dosage of the photocatalysts
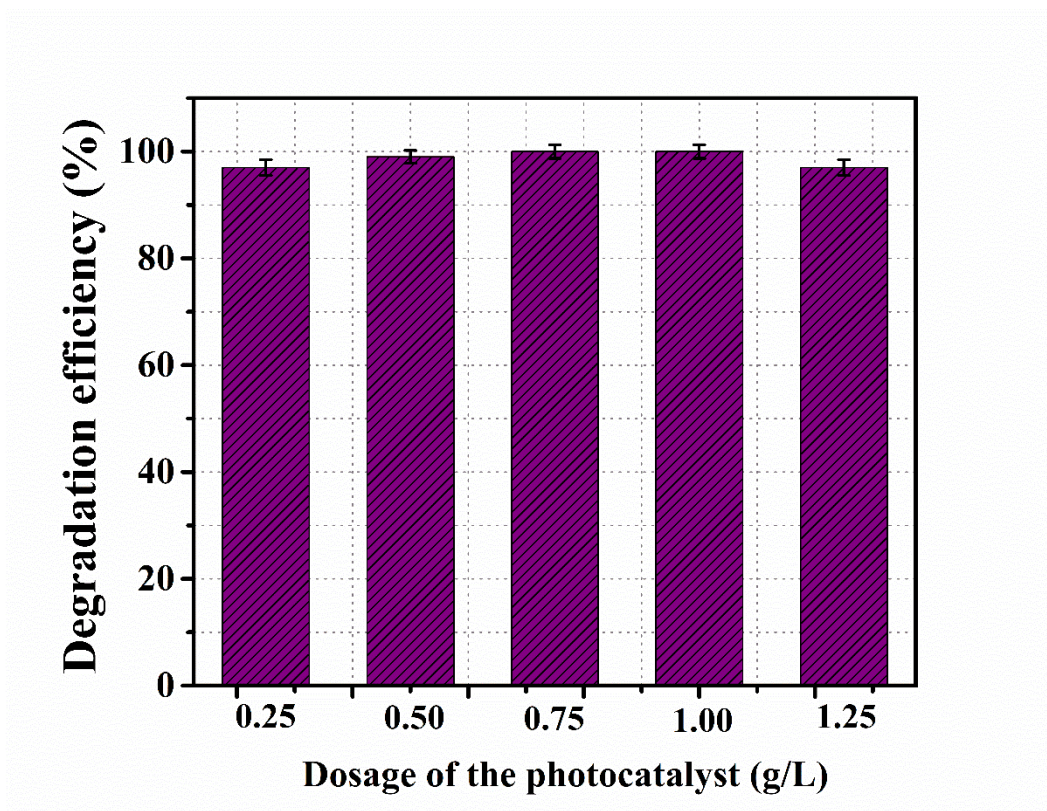
Fig.6.26. *Effect of dosage of the catalyst on catalytic degradation of TCH.*
(C_0=10 ppm, T=303 K pH ~ 7, Irradiation time of light =20 min.)

The amount of catalyst used is not greatly influences the antibiotic degradation, as indicated by changing the dosage from 0.25 g/L to 1.25 g/L. Fig.6.26 shows that higher catalyst amounts create more active sites and species, resulting in improved degradation efficiency in all catalytic processes. This increased dosage minimizes diffusion limitations, allowing pollutant molecules a shorter path to the active sites on the catalyst surface. As a result, more active sites are accessible for adsorption and degradation, raising the likelihood of pollutant molecules interacting with the catalyst and boosting degradation efficiency.

6.3.10. Recyclability of photocatalyst

The $BiOBr_{0.25}Cl_{0.75}$ photocatalyst demonstrated degradation efficiencies of approximately 65.5% and 86.8% for CIP and TCH, respectively, after 4 cycles. These outcomes signify the photocatalyst's stability and absence of photo corrosion during the photocatalytic process. Additionally, XRD patterns of $BiOBr_{0.25}Cl_{0.75}$ photocatalyst after 4 runs showed no significant changes compared to new catalysts, highlighting the excellent stability of the $BiOBr_{0.25}Cl_{0.75}$ solid solution. The marginal deactivation of the

degradation efficiency is attributed to the loss of photocatalyst particles and the leaching of active sites as the photocatalyst is used. The reusability test of the photocatalyst is shown in Fig.6.27.
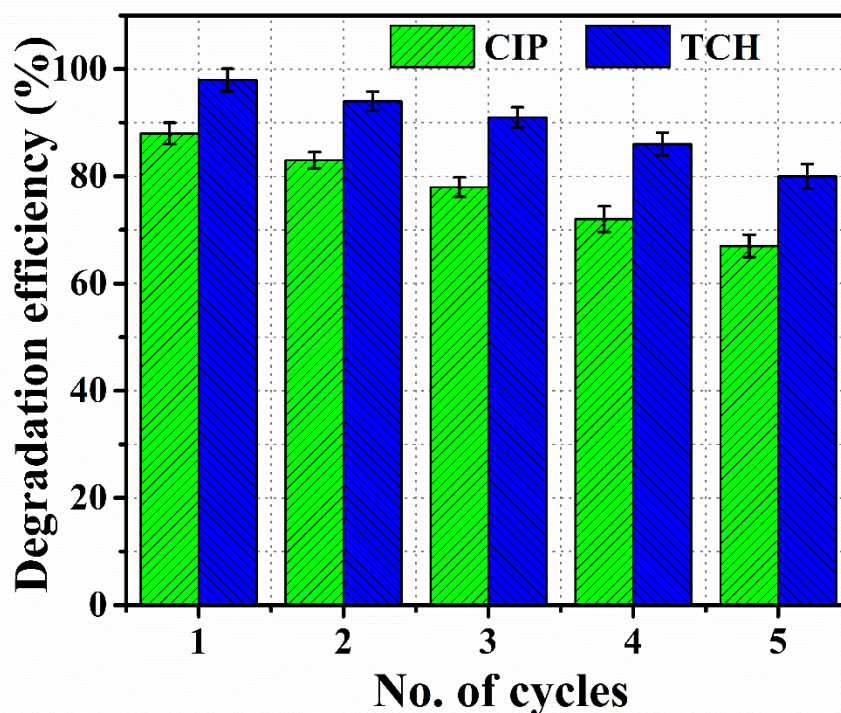
Fig.6.27. *Recyclability test of the catalyst- under photocatalysis. (C₀=10 ppm, Dosage= 0.5 g/L, T=303 K pH ~ 7, Irradiation time of light =20 min.)*

6.3.11. Active species reaction test

Radical quenching experiments were conducted to investigate the potential oxidative species participating in the photocatalytic degradation of CIP and TCH. The presence of dominant oxidative species, namely $\bullet O_2^-$, h^+, $\bullet OH$ and electron, are identified by using silver nitrate ($AgNO_3$), EDTA, isopropanol (IPA), and ascorbic acid, respectively. The results, as depicted in the Fig.6.28. suggest that photogeneration via electrons (e^-), holes (h^+) and $\bullet OH$ radicals play a supporting role in the presence of visible light degradation of CIP and TCH. Meanwhile, photocatalytic CIP and TCH degradation are similar, with or without adding $AgNO_3$, suggesting that $\bullet O_2^-$ only plays a minor role in CIP and TCH removal.
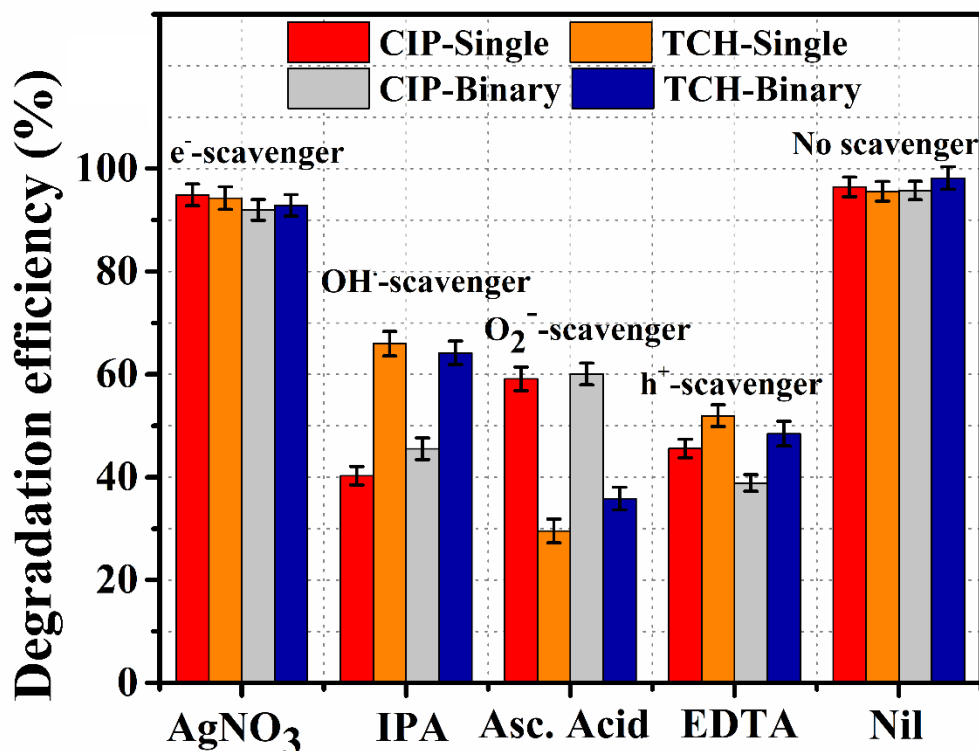
Fig.6.28. *Schematic diagram illustrating the generation and function of dominant reactive species during the photocatalytic degradation of CIP and TCH. (C_0=10 ppm CIP, Dosage= 0.5 g/L, T=303K pH ~ 7, Irradiation time of light =20 min.)*

6.3.12. Mineralization of the reaction using TOC analysis

Furthermore, to assess the photocatalytic activity of $BiOBr_{0.25}Cl_{0.75}$ after 30 minutes of light irradiation, the residual solutions were examined for total organic carbon (TOC) content. The results show that the TOC removal efficiency for CIP and TCH solutions reaches 81.2% and 86.3%, respectively, after 30 minutes of visible light exposure. This substantial TOC removal efficiency suggests that the photocatalyst decomposes antibiotic molecules and mineralizes the majority of organic compound byproducts generated during the photocatalytic reaction. This is illustrated in Fig.6.29.
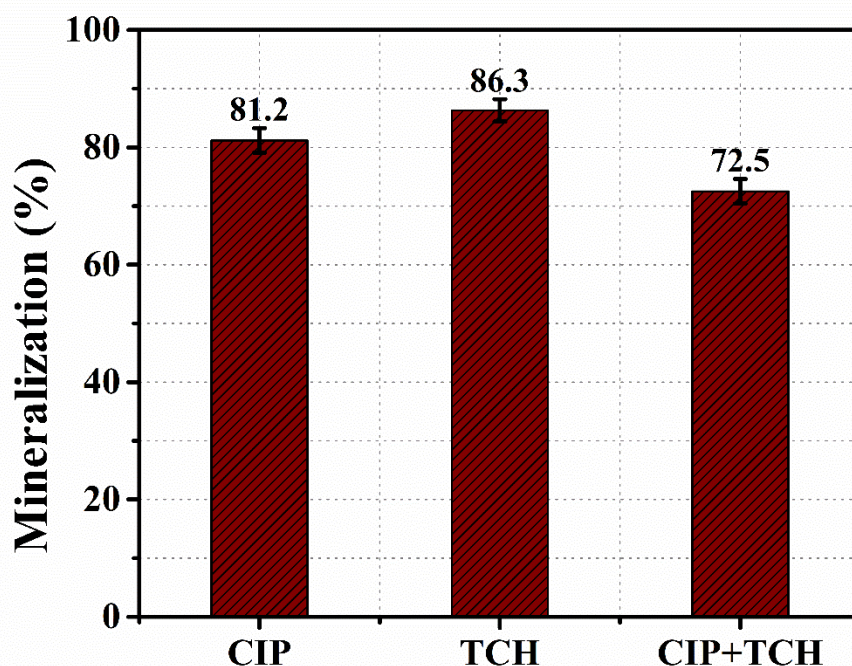
Fig.6.29. *TOC removal efficiency for the photocatalytic decomposition of CIP and TCH in the single and binary mixture. (C_0=10 ppm, Dosage= 0.5 g/L, T=303 K pH ~ 7, Irradiation time of light =20 min.)*

6.3.13. Proposed photocatalytic degradation pathway of CIP and TCH

HPLC-MS was employed to detect intermediate products during the photocatalytic degradation of CIP and TCH to explore degradation pathways. The results indicated two primary CIP photodegradation pathways: defluorination and piperazine ring oxidation. In pathway I, defluorination primarily occurred through hydroxylation substitution. The intermediate with an m/z of 330 (CP6) resulted from the substitution of –F with –OH, confirming the •OH attack on –F [28]. Furthermore, CP7 represented a highly hydroxylated product, while CP8 was formed by replacing the –NH$_2$ of CP5 with –OH. An alternative defluorination method directly released fluoride when the C–F bond was excited or through water addition [29]. In Pathway II, the oxidation of the piperazine ring may occur due to the attack of electrophilic agents such as holes and $^1O_2$. The radicals generated during this attack can form a dialdehyde with an m/z of 362 through a ring opening [30]. Intermediate CP1 underwent sequential elimination of the two aldehyde moieties (–CO), resulting in the formation of intermediates CP2 and CP3. In line with previous studies, CP3 was preferentially attacked by h$^+$ or •OH, leading to the formation of CP4 and CP5 through dealkylation. The opening of the piperazine ring

resulted in the formation of CP9 (m/z = 288), which could further undergo stepwise conversion to CP10 and CP11 (m/z = 245) [31]. The list of intermediate products and their details are provided in the Table.6.8. The proposed degradation pathway of CIP is shown in Fig.6.30.
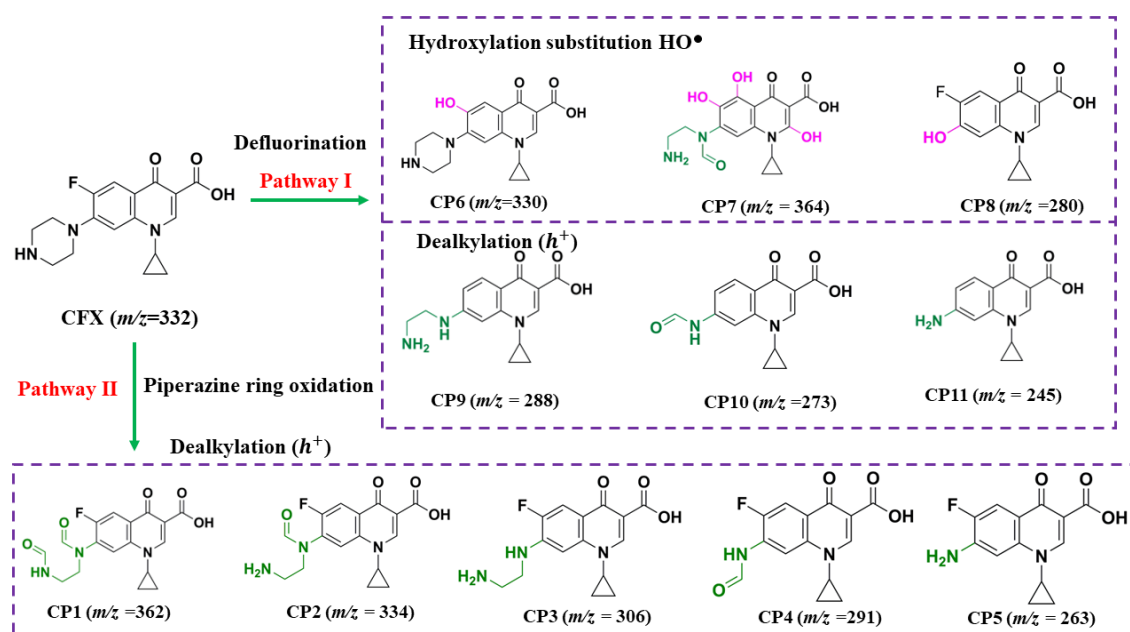
Fig.6.30. *Proposed photocatalytic degradation pathways of CIP.*

The photocatalytic decomposition of TCH can progress through three distinct pathways. In the first pathway, the N-demethylation reaction occurred quickly, accompanied by hydroxylation, resulting in the formation of intermediate TP1. Subsequently, TP1 underwent ring cleavage, dihydroxylation, and deamination, leading to the formation of intermediate TP4. In the second pathway, TCH undergoes hydroxylation and dehydrogenation to produce intermediate TP2, which then experiences ring cleavage and deoxidation, resulting in intermediate TP5. Further ring cleavage reactions occurred, transforming TP4 and TP5 into intermediate TP7. In the third pathway, intermediate TP3 was generated through hydroxylation, which underwent ring cleavage and hydroxylation to generate intermediate TP6. TP6 then underwent ring cleavage to form TP8 and TP9. Subsequently, TP7-TP9 continued to be transformed, giving rise to three other possible intermediates (TP10-TP12). Ultimately, all the intermediates mentioned would undergo further mineralization under the sustained influence of reactive oxygen species (ROS) during photocatalytic degradation [32]. The Table 6.9. lists the intermediate products and their respective details. The proposed degradation pathway of TCH is shown in Fig.6.31.
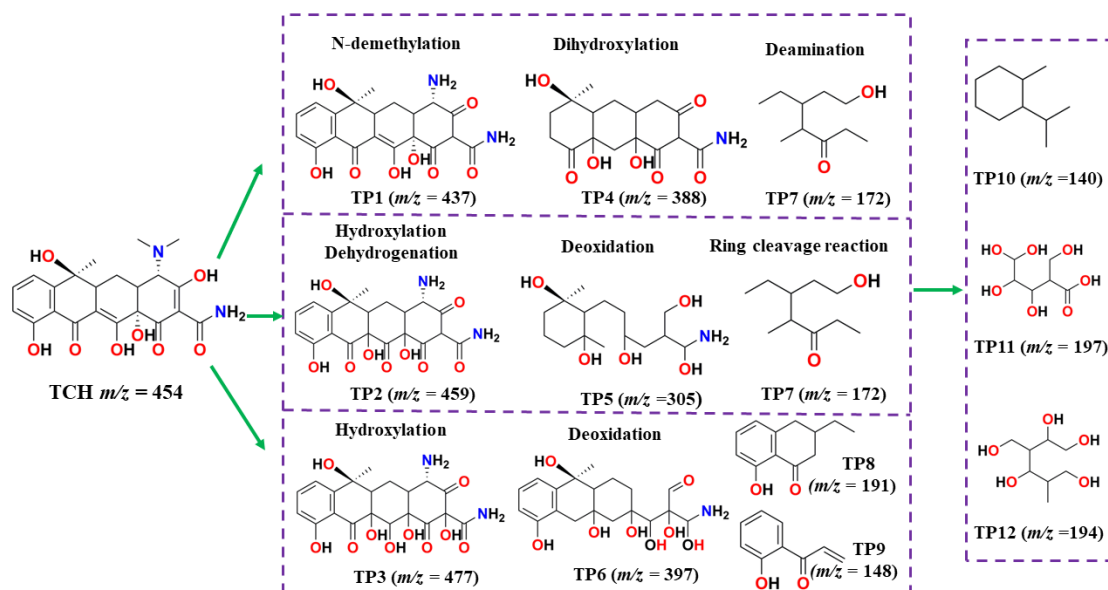
Fig.6.31. *Proposed photocatalytic degradation pathway of TCH.*

Table.6.8. *List of intermediates formed in the photocatalytic degradation of CIP*

Intermediates	t_R (min)	m/z	Chemical structure
CIP	-	332	
CP1	4.57	362	
CP2	4.24	334	
CP3	3.95	306	
CP4	3.95	291	
CP5	4.63	263	

Intermediate	t_R (min)	m/z	Chemical structure
CP6	0.06	330	
CP7	3.95	364	
CP8	3.84	280	
CP9	4.33	288	
CP10	3.95	273	
CP11	0.06	245	

Table.6.9. *List of intermediates formed in the photocatalytic degradation of TCH.*

Intermediates	t_R (min)	m/z	Chemical structure
TCH	-	445	
TP1	1.58	437	
TP2	2.11	459	
TP3	1.97	477	

TP4	2.60	338	
TP5	1.74	305	
TP6	1.67	397	
TP7	1.69	172	
TP8	1.38	191	
TP9	1.68	148	
TP10	1.79	140	
TP11	2.07	197	
TP12	2.28	194	

6.3.14. Mechanism of photocatalysis

Photocatalytic degradation of antibiotics relies on the generation of electrons (e^-), holes (h^+), and hydroxyl radicals (•OH) as active species. A $BiOBr_{(1-x)}Cl_x$ solid solution generates electron-hole pairs when illuminated with light at or above its bandgap energy. These reactive species engage in redox reactions, with holes in the valence band oxidizing water to produce hydroxyl radicals (•OH). The highly reactive •OH radicals act as potent oxidizing agents, initiating the breakdown of antibiotic molecules, as illustrated in degradation pathways (Fig.10 and Fig.11) [33]. The collaborative action of electrons, holes, and •OH radicals ensures a thorough degradation process, exemplified in the schematic representation of the degradation mechanism of CIP and TCH, illustrated in Fig.6.32.
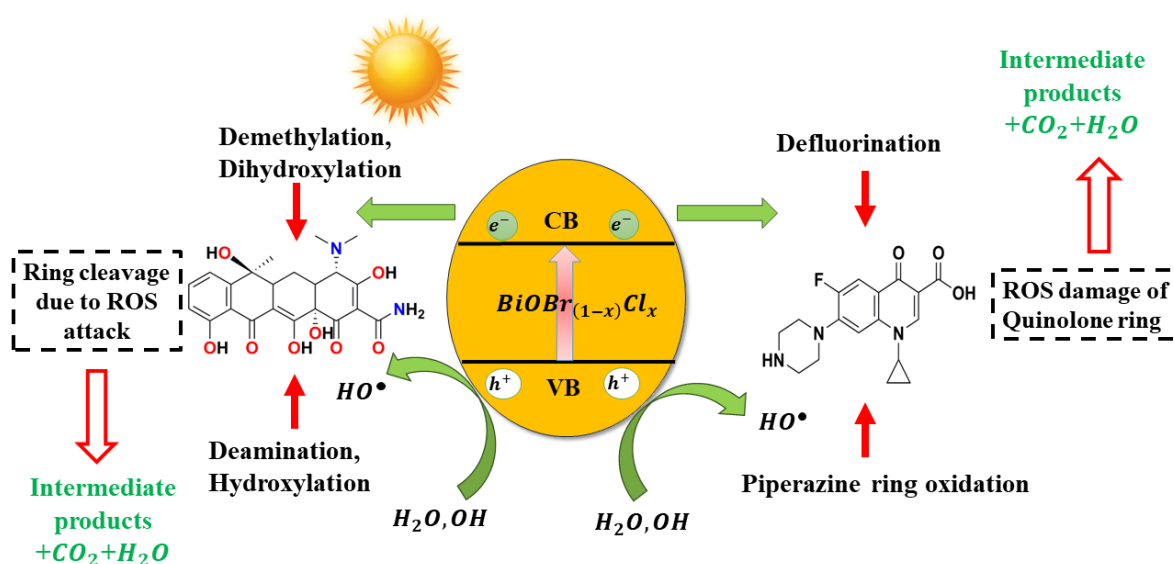
Fig.6.32. *Schematic representation of the photocatalytic degradation of CIP and TCH.*

Table 6.10. provides a comprehensive overview of diverse photocatalysts employed for the degradation of ciprofloxacin (CIP) and tetracycline hydrochloride (TCH) antibiotics under varying experimental conditions. A meticulous examination of this table reveals that the solid solution photocatalysts exhibit significantly superior and accelerated photocatalytic degradation efficiency when compared to other photocatalysts documented in previous studies.

Table 6.10. *Summary of the various photocatalysts used for the degradation of CIP and TCH.*

Photocatalysts	Antibiotics	Expt. conditions	Degradation efficiency (%)	Time for degradation (min.)	Reference
MoS_2/ZnO composite	CIP	Initial conc. 16 ppm Dosage = 0.5 g/L 250 W metal halide lamp	92	120	Y.M. Hunge *et.al.* [34]
ZnO/SOD	CIP	Initial Conc. 10 ppm Dosage = 0.16 g/L 120W Hg vapour lamp	99.8	120	Santos *et.al.* [35]
MnS/Ppy composite	CIP	Initial Conc. 5 ppm Dosage = 1.6 g/L 300 W Xe lamp	88	300	Miao Lv *et.al.* [36]
Bi_2MoO_6	CIP	Initial Conc. 20 ppm Dosage = 0.4 g/L 300 W Xe lamp	96	60	Xiao Xu *et.al.* [37]
Ag/silica	CIP	Initial Conc. = 40 ppm Dosage = 0.6 g/L	98.2	180	Morteza G olmoham madi *et. al.* [38]
Ag_3PO_4	TCH	Initial Conc. = 20 ppm Dosage = 0.1 g/L	86	60	Lizhe Ma *et al.* [39]

Porous ionic polymers	TCH	Initial Conc. = 20 ppm Dosage = 0.15 g/L 300 W xenon lamp	98	60	Shuaishuai Shang *et al.* [40]
BiOBr/MIL-101(Cr)	TCH	Initial Con. = 20 ppm Dosage = 0.5 g/L 400 W Xe lamp	86	100	Mingkun Wu *et.al.* [41]
ZIF-8@CHs catalysts	TCH	Initial Conc. = 30 ppm Dosage = 0.3 g/L 350 W Xenon lamp	80	180	Juan Wang *et al.* [42]
PDI/FePc	TCH	Initial Conc. = 20 ppm Dosage = 0.5 g/L 350 W Xe lamp	78.6	60	Kaiyang Shi *et. al.* [43]
$BiOBr_{(1-x)}Cl_x$ solid solution	CIP	Initial Conc. 20 ppm Dosage = 0.5 g/L 300 W Xe lamp	89	20	Present study
	TCH		99	20	Present study

6.4. CONCLUSION

In summary, through a rapid co-precipitation method, we successfully synthesized pristine and $BiOBr_{(1-x)}Cl_x$ solid solution semiconducting photocatalysts. This novel approach allows precise adjustment of the structural and electronic properties by tuning the Br:Cl molar ratio. Comprehensive examinations of morphological, optical, and structural characteristics revealed successful tuning of the optical bandgap from 3.39 eV to 2.75 eV in the samples for light harvesting applications - facilitated by the halide alloying process.

The $BiOBr_{(1-x)}Cl_x$ solid solutions demonstrated excellent photocatalytic activity in degrading CIP and TCH, outperforming pristine BiOBr and BiOCl photocatalysts in single and binary mixtures. This study underscores the significance of interface formation and distortions in solid solutions, promoting enhanced photocatalytic activity. The $BiOBr_{0.25}Cl_{0.75}$ sample exhibited high carrier concentration, mobility, conductivity, surface heterogeneity, visible light absorption capacity, and effective charge transfer, contributing to its exceptional photocatalytic activity.

Thermodynamic studies confirmed that all photocatalytic degradations are exothermic, enthalpy-driven, and spontaneous reactions. Free-radical trapping tests identified electrons (e-), holes (h^+), and hydroxyl radicals (•OH) as crucial active radicals during photocatalysis. HPLC techniques were employed to investigate the degradation pathways of antibiotics. HPLC-MS was used to detect intermediate products during the photocatalytic degradation of CIP and TCH, revealing their degradation pathways. CIP degraded primarily through defluorination and piperazine ring oxidation, while TCH followed three pathways, with rapid N-demethylation and hydroxylation leading to intermediates. All intermediates eventually underwent mineralization under the sustained influence of reactive oxygen species (ROS). This work introduces a facile synthesis method for controlling the growth of $BiOBr_{(1-x)}Cl_x$ solid solutions, providing a non-toxic, low-cost, inexpensive, noble metal-free, and highly efficient photocatalyst for environmental remediation.

6.5. REFERENCES

[1] Qu, J., Meng, Q., Peng, W., Shi, J., Dong, Z., Li, Z., ... & Zhang, Y. (2023). Application of functionalized biochar for adsorption of organic pollutants from environmental media: Synthesis strategies, removal mechanisms and outlook. *Journal of Cleaner Production*, 423, 2023, 138690

[2] Sarwar, T., & Khan, S. (2023). Antibiotics and antibiotics resistance genes in poultry and animals' manure and their effects on environment and human health. In *Fate of Biological Contaminants During Recycling of Organic Wastes* (pp. 229-258). Elsevier.

[3] Mahmoud, M. A., Alsehli, B. R., Alotaibi, M. T., Hosni, M., & Shahat, A. (2024). A comprehensive review on the application of semiconducting materials in the degradation of effluents and water splitting. *Environmental Science and Pollution Research*, 3466–3494 (2024)

[4] Thakur, A. K., Kumar, R., Kumar, A., Shankar, R., Khan, N. A., Gupta, K. N., ... & Arya, R. K. (2023). Pharmaceutical wastewater treatment via advanced oxidation based integrated processes: An engineering and economic perspective. *Journal of Water Process Engineering*, *54*, 103977.

[5] Jabbar, Z. H., Graimed, B. H., Ammar, S. H., Sabit, D. A., Najim, A. A., Radeef, A. Y., & Taher, A. G. (2024). The latest progress in the design and application of semiconductor photocatalysis systems for degradation of environmental pollutants in wastewater: Mechanism insight and theoretical calculations. *Materials Science in Semiconductor Processing*, *173*, 108153.

[6] Ahmad, I., Zou, Y., Yan, J., Liu, Y., Shukrullah, S., Naz, M. Y., ... & Khalid, N. R. (2023). Semiconductor photocatalysts: A critical review highlighting the various strategies to boost the photocatalytic performances for diverse applications. *Advances in Colloid and Interface Science*, *311*, 102830.

[7] Chen, L., Guan, B., Guo, J., Chen, Y., Ma, Z., Chen, J., ... & Huang, Z. (2023). Review on the preparation and performance improvement methods of bismuth photocatalyst materials. *Catalysis Science & Technology*, *13*(19), 5478-5529.

[8] Chen, L., Guan, B., Guo, J., Chen, Y., Ma, Z., Chen, J., ... & Huang, Z. (2023). Review on the preparation and performance improvement methods of bismuth photocatalyst materials. *Catalysis Science & Technology*, *13*(19), 5478-5529.

[9] Mohseni, N., Haghighi, M., & Shabani, M. (2020). Sunlight-activated 3D-mesoporous-flowerlike Cl–Br bismuth oxides nanosheet solid solution: In situ EG-thermal-sonication

synthesis with excellent photodecomposition of ciprofloxacin. *Environmental Research*, *188*, 109810.

[10] Chen, L., Guan, B., Guo, J., Chen, Y., Ma, Z., Chen, J., ... & Huang, Z. (2023). Review on the preparation and performance improvement methods of bismuth photocatalyst materials. *Catalysis Science & Technology*, *13*(19), 5478-5529.

[11] Adhikari, S., Mandal, S., & Kim, D. H. (2023). Recent Development Strategies for Bismuth-Driven Materials in Sustainable Energy Systems and Environmental Restoration. *Small*, *19*(10), 2206003.

[12] Han, Z., Lv, M., Shi, X., Li, G., Zhao, J., & Zhao, X. (2023). Regulating the Electronic Structure of Fe3+-Doped BiOCl x I1–x Solid Solution by an Amidoxime-Functionalized Fibrous Support for Efficient Photocatalysis. *Advanced Fiber Materials*, *5*(1), 266-281.

[13] Xia, P., Song, Y., Liu, Y. Z., Long, M. X., Yang, C., Zhang, X. Y., & Zhang, T. (2024). Advances in optical and electronic properties and applications of bismuth-based semiconductor materials. *Journal of Materials Chemistry C*. 2024, **12**, 1609-1624

[14] Wang, J., & Zhang, Z. (2020). Co-precipitation synthesis and photocatalytic properties of BiOCl microflowers. *Optik*, *204*, 164149.

[15] Tripathi, G. K., & Kurchania, R. (2017). Photocatalytic behavior of BiOX (X= Cl/Br, Cl/I and Br/I) composites/heterogeneous nanostructures with organic dye. *Optical and Quantum Electronics*, *49*, 1-17.

[16] Chen, H., Yu, X., Zhu, Y., Fu, X., & Zhang, Y. (2016). Controlled synthesis of {001} facets-dominated dye-sensitized BiOCl with high photocatalytic efficiency under visible-light irradiation. *Journal of Nanoparticle Research*, *18*, 1-13.

[17] Shang, J., Gao, Y., Zhao, B., Shen, S., & Wang, X. (2020). Design of a novel carbon/BiOBr nanosheet photoanode and its photoelectrochemical application. *Journal of Materials Science: Materials in Electronics*, *31*, 20858-20867.

[18] Sravandas, P., & Alexander, L. K. (2023). Fast catalytic degradation of an industrial surfactant driven by Hemi-micellization on facile synthesized CuS nanoflower. *Emergent Materials*, 1-12, **7**, 209–220.

[19] Vidyarajan, N., & Alexander, L. K. (2018). Strain induced optical properties of perovskite LaFeO3. *Materials Research Express*, *6*(1), 015610.

[20] Nanakkal, A. R., & Alexander, L. K. (2017). Photocatalytic activity of graphene/ZnO nanocomposite fabricated by two-step electrochemical route. *Journal of Chemical Sciences*, *129*, 95-102.

[21] Paul, D. R., Sharma, R., Singh, S., Singh, P., Panchal, P., Sharma, A., ... & Nehra, S. P. (2023). Mg/Li Co-doped g-C3N4: An excellent photocatalyst for wastewater remediation and hydrogen production applications towards sustainable development. *International Journal of Hydrogen Energy*. 48 (96), 37746-37761,

[22] Bramhaiah, K., & Bhattacharyya, S. (2023). Interface Engineering of Nano-Photocatalysts for Hydrogen Evolution Reaction and Degradation of Organic Pollutants. In *Photocatalysis for Environmental Remediation and Energy Production: Recent Advances and Applications* (pp. 449-479). Cham: Springer International Publishing.

[23] Mehdaoui, R., Agren, S., El Haskouri, J., Beyou, E., Lahcini, M., & Baouab, M. H. V. (2023). An optimized sono-heterogeneous Fenton degradation of olive-oil mill wastewater organic matter by new magnetic glutarlaldehyde-crosslinked developed cellulose. *Environmental Science and Pollution Research*, *30*(8), 20450-20468.

[24] Nizam, N. U. M., Hanafiah, M. M., Mahmoudi, E., & Mohammad, A. W. (2023). Synthesis of highly fluorescent carbon quantum dots from rubber seed shells for the adsorption and photocatalytic degradation of dyes. *Scientific reports*, *13*(1), 12777.

[25] Soleymani, A. R., Rahnama, A., & Azimi, S. Hybrid Photocatalytic/Photochemical Degradation of 1, 2-Dichlorobenzene: Kinetic, Thermodynamic, Operating Cost, Synergism and Mineralization Study. *Thermodynamic, Operating Cost, Synergism and Mineralization Study.* **21**, 1977–1996.

[26] Kumar, V., Das, D., & Mahto, V. K. (2023). A kinetic study and thermometric analysis on waste cooking oil. *Biomass Conversion and Biorefinery*, 1-10.

[27] Hojjati-Najafabadi, A., Aygun, A., Tiri, R. N. E., Gulbagca, F., Lounissaa, M. I., Feng, P., ... & Sen, F. (2023). Bacillus thuringiensis-based ruthenium/nickel Co-doped zinc as a green nanocatalyst: enhanced photocatalytic activity, mechanism, and efficient H2 production from sodium borohydride methanolysis. *Industrial & Engineering Chemistry Research*, *62*(11), 4655-4664.

[28] Sahoo, D. P., Das, K. K., Patnaik, S., & Parida, K. (2020). Double charge carrier mechanism through 2D/2D interface-assisted ultrafast water reduction and antibiotic degradation over architectural S, P co-doped gC 3 N 4/ZnCr LDH photocatalyst. *Inorganic Chemistry Frontiers*, *7*(19), 3695-3717.

[29] Wang, J., Gao, H., Shi, C., Chen, G., Tan, X., Chen, X., ... & Li, H. (2021). Recent advances in radical-based C–F bond activation of polyfluoroarenes and gem-difluoroalkenes. *Chemical Communications*, *57*(92), 12203-12217.

[30]   Liu, H., Zou, X., Chen, Q., Fan, W., & Gong, Z. (2022). Pumice-loaded rGO@ MnO2 nanomesh photocatalyst with visible light response for rapid degradation of ciprofloxacin. *Separation and Purification Technology*, *297*, 121502.

[31]   Kaushal, N., Sarraf, S., Basu, A. K., Mishra, S., & Saha, A. (2024). Facile microwave synthesis of Zinc Ferrite@ NCDs for photocatalytic degradation of fluoroquinolone antibiotics. *Materials Chemistry and Physics*, *314*, 128823.

[32]   Hua, X., Chen, H., Rong, C., Addison, F., Dong, D., Qu, J., ... & Liu, H. (2023). Visible-light-driven photocatalytic degradation of tetracycline hydrochloride by Z-scheme Ag3PO4/1T@ 2H-MoS2 heterojunction: Degradation mechanism, toxicity assessment, and potential applications. *Journal of Hazardous Materials*, *448*, 130951.

[33]   Wang, J., & Wang, S. (2020). Reactive species in advanced oxidation processes: Formation, identification and reaction mechanism. *Chemical Engineering Journal*, *401*, 126158.

[34]   Hunge, Y. M., Yadav, A. A., Kang, S. W., Lim, S. J., & Kim, H. (2023). Visible light activated MoS2/ZnO composites for photocatalytic degradation of ciprofloxacin antibiotic and hydrogen production. *Journal of Photochemistry and Photobiology A: Chemistry*, *434*, 114250.

[35]   Santos, W. D., Teixeira, M. M., Campos, I. R., de Lima, R. B., Mantilla, A., Osajima, J. A., ... & Alcântara, A. C. (2023). Photocatalytic degradation of ciprofloxacin using semiconductor derived from heterostructured ZIF-8-based materials. *Microporous and Mesoporous Materials*, *359*, 112657.

[36]   Lv, M., Liu, H., He, L., Zheng, B., Tan, Q., Hassan, M., ... & Gong, Z. (2023). Efficient photocatalytic degradation of ciprofloxacin by graphite felt-supported MnS/Polypyrrole composite: Dominant reactive species and reaction mechanisms. *Environmental Research*, *231*, 116218.

[37]   Xu, X., Ding, X., Yang, X., Wang, P., Li, S., Lu, Z., & Chen, H. (2019). Oxygen vacancy boosted photocatalytic decomposition of ciprofloxacin over Bi2MoO6: Oxygen vacancy engineering, biotoxicity evaluation and mechanism study. *Journal of hazardous materials*, *364*, 691-699.

[38]   Golmohammadi, M., Hanafi-Bojd, H., & Shiva, M. (2023). Photocatalytic degradation of ciprofloxacin antibiotic in water by biosynthesized silica supported silver nanoparticles. *Ceramics International*, *49*(5), 7717-7726.

[39] Ma, L., Cai, Q., Ong, S. L., Yang, Z., Zhao, W., Duan, J., & Hu, J. (2023). Photonic efficiency optimization-oriented dependence model of characteristic coupling spectrum on catalytic absorbance in photocatalytic degradation of tetracycline hydrochloride. *Chemical Engineering Journal*, *451*, 138623.

[40] Shang, S., Li, S., Peng, C., Liu, H., & Hu, J. (2023). Building internal electric fields in porous ionic polymers for fast photocatalytic degradation of tetracycline hydrochloride. *Journal of Materials Chemistry C*, *11*(22), 7397-7404.

[41] Wu, M., Huang, M., Zhang, B., Li, Y., Liu, S., Wang, H., ... & Chen, G. (2023). Construction of 3D porous BiOBr/MIL-101 (Cr) Z-scheme heterostructure for boosted photocatalytic degradation of tetracycline hydrochloride. *Separation and Purification Technology*, *307*, 122744.

[42] Wang, J., Shi, K., Liu, W., Yin, L., Xu, Y., Kong, D., ... & He, H. (2023). Novel ZIF-8@ CHs catalysts for photocatalytic degradation of tetracycline hydrochloride. *Chemical Engineering Journal*, *461*, 142130.

[43] Shi, K., Zhou, M., Wang, F., Li, X., Huang, W., Lu, K., ... & Yu, C. (2023). Perylene diimide/iron phthalocyanine Z-scheme heterojunction with strong interfacial charge transfer through π-π interaction: Efficient photocatalytic degradation of tetracycline hydrochloride. *Chemosphere*, *329*, 138617.

CHAPTER 7

Sonophotocatalytic Degradation of Rhodamine B using BiVO₄ Heterostructure.
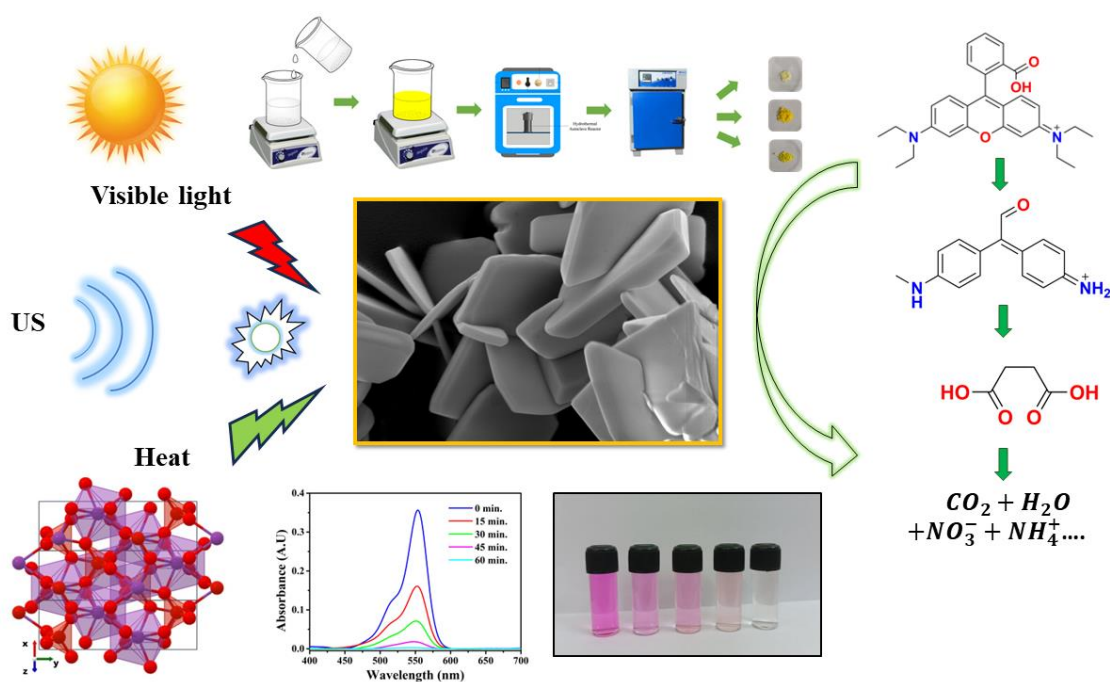
Highlights

- *Isotype BiVO₄ heterojunction is tuned via varying surfactant dosage.*
- *Demonstration of sonophotocatalysis with an isotype heterojunction.*
- *Examination of the correlation between crystal phases and sonophotocatalysis.*
- *Isotype heterojunction as a platform to study photo-sono-induced charge carriers.*

ABSTRACT

Owing to its suitable energy band and strong catalytic capacity, BiVO₄ has received extensive attention in photocatalysis. Here, we suggest a straightforward approach to address the challenges of insufficient compatibility, poor charge transport characteristics, and limited surface adsorption properties commonly found in traditional BiVO₄ photocatalysts. A heterojunction BiVO₄ structure is developed by incorporating two distinct crystal phases within a single semiconducting material. A facile hydrothermal procedure is used to synthesize distinct crystalline phases of BiVO₄ photocatalysts, viz., tetragonal, monoclinic, and monoclinic/tetragonal heterophase. The physicochemical characteristics of the pristine and isotype BiVO₄ heterojunctions were characterized using various techniques. The photocatalytic activity of BiVO₄ samples was examined by monitoring the degradation of rhodamine B (RhB). In order to boost the degradation reaction, ultrasonic sound waves are employed within the reaction medium. The present study examined the photocatalytic, sonocatalytic, and sonophotocatalytic activity of BiVO₄ microcrystals in relation to the degradation of RhB dye. The results show that the crystalline phases of BiVO₄ samples significantly influence the behaviour of photo-sono-induced charges. An interface in the monoclinic/tetragonal heterophase creates a spatial environment that facilitates charge transfer and enhances the separation of photo-sono-induced electron-hole pairs. The paper extensively examines the correlation between the behaviour of photo-sono-induced charge carriers and the level of sonophotocatalytic activity. This would provide greater insight into the intrinsic reasons for the enhancement in sonophotocatalytic activity.

Key words: *Photocatalysis, hectero junction, sonocatalysis, sonophotocatalysis.*

7.1. INTRODUCTION

Bismuth vanadate is a promising option for visible-light-driven water splitting and organic contaminant decomposition due to its suitable band gap, non-toxicity, high stability, and effective sunlight utilization [1, 2]. $BiVO_4$ can exist in three primary crystalline phases: monoclinic scheelite, tetragonal zircon, and tetragonal scheelite [3]. Tetragonal $BiVO_4$ has a band gap of 2.9 eV and mostly shows a UV absorption band. Monoclinic scheelite $BiVO_4$ has a band gap of 2.4 eV and shows visible light and UV absorption bands [4]. Both tetragonal and monoclinic $BiVO_4$ exhibit UV bands due to the band transition from O 2p to V 3d orbitals. Visible light, on the other hand, is absorbed when a valence band (VB) made up of Bi 6s or a hybrid orbital of Bi 6s and O 2p changes into a conduction band (CB) made up of V 3d lines [5]. This distinct band structure extends the absorption into the visible range. However, scientific research has confirmed that pristine $BiVO_4$ exhibits limited photocatalytic efficiency due to its suboptimal charge transport characteristics and inadequate surface adsorption properties [6]. Comprehensive analysis suggests that inherent deficiencies in charge transport act as a barrier to the effective utilization of photogenerated electron-hole pairs, thereby impeding the overall efficiency of the photocatalytic process. Additionally, the inadequate surface adsorption characteristics of unmodified $BiVO_4$ hinder its ability to effectively engage with desired molecules, thereby constraining its overall catalytic efficiency [7]. These observations emphasize the need for innovative approaches to enhance the photocatalytic efficiency of $BiVO_4$.

To enhance the photocatalytic activity of monoclinic $BiVO_4$, various approaches have been proposed, including the formation of heterojunction structures, loading co-catalysts, doping with impurities, controlling morphology, utilizing structure deformation-based catalysis, and incorporating sensitizers [8, 9, 10]. Among these methods, the coexistence of heterostructures emerges as a promising avenue. However, as the semiconductor composite photocatalyst is at the interface of different materials, each possessing distinct physiochemical properties, it results in poor compatibility for intimate contact between junctions, which hinders the charge separation process [11]. Recent literature surveys have shown that these restrictions and limitations can be resolved by creating an isotype heterojunction structure between two distinct phases of exclusive semiconductor materials [12]. The construction of isotype heterojunctions involving two dissimilar crystal phases within a single semiconductor offers an advanced

band alignment strategy. Numerous reports have showcased the efficacy of isotype heterojunctions in photocatalytic applications. For instance, Bera *et al*. demonstrated that the α/β-Bi_2O_3 isotype crystal phase junction displayed exceptional photocatalytic performance, more effectively degrading rhodamine B and methyl orange under visible light than the pristine materials [13]. The efficient separation and transfer of charge carriers at the phase junction interface is responsible for this enhanced activity. Similarly, An *et al*. observed a significant enhancement in the photocatalytic performance for the H_2 evolution reaction by forming an isotype heterojunction between the surface anatase and rutile phases [14].

Considering the discussions above and various perspectives, we recognize the pressing need and exciting opportunity to develop and explore an isotype heterojunction involving $BiVO_4$ and assess its impact on catalysis. We anticipate that the monoclinic-tetragonal heterostructured $BiVO_4$ will significantly enhance the separation of photoinduced electron-hole pairs. The presence of interfaces within the monoclinic/tetragonal heterophase provides favourable conditions for charge transfer, thereby improving the separation of these pairs and redirecting the migration direction of these carriers.

The changes in the local structure that occur during the formation of a heterojunction in $BiVO_4$ lead to modifications in its electronic structure, contributing to its high visible light photocatalytic activity [15]. We can assess symmetry distortions in the local structure of $BiVO_4$ by observing shifts in Raman peaks and X-ray diffraction patterns. These distortions likely impact the separation and delocalization of photogenerated electrons and holes. Therefore, a deeper understanding of the relationship between structural distortion and the transfer of photoinduced charge carriers will provide valuable insights into the underlying reasons for the enhanced catalytic activity.

The photocatalytic process is a commonly employed method for water and wastewater treatment. However, it has drawbacks, such as the lengthy reaction time required and its reduced effectiveness when dealing with various water pollutants, limiting its practical application [16]. In this regard, ultrasound irradiation offers a potential solution to enhance catalytic efficiency through the simultaneous irradiation of ultrasound and visible light. Ultrasound is a versatile and supplementary method that can eliminate a wide range of organic compounds in wastewater [17]. Sonolysis, a process where ultrasound passes through an aqueous solution, facilitates the breaking of chemical

bonds. This involves phenomena like nucleation, cavitation, bubble dynamics and interactions, and chemical processes that lead to the formation of free radicals [18]. The combination of visible light irradiation and ultrasound emerges as a promising approach for degrading organic pollutants in wastewater, known as sonophotocatalysis. This combined approach presents an excellent opportunity to reduce reaction time and the number of reagents needed without extreme physical conditions [19].

In this study, we synthesized and thoroughly characterized various crystalline phases of BiVO4, including tetragonal, monoclinic, and a combination of both tetragonal and monoclinic phases. Our objective was to assess the catalytic activity of these BiVO4 catalysts by examining the degradation of rhodamine B (RhB), a common model dye contaminant, under visible light and ultrasound irradiation. To the best of our knowledge, there is no prior report on using hierarchical BiVO4 structures as a sonophotocatalyst for degrading organic pollutants under visible light. This chapter provides experimental evidence and insights into the significance of isotype heterojunctions and the effect of sono-photo-induced electron-hole pairs in catalysis. Furthermore, we investigated the synergistic effects of the sonophotocatalytic process on RhB degradation and presented a comprehensive evaluation by comparing the outcomes with those of individual processes.

7.2. EXPERIMENTAL

7.2.1. Reagents and chemicals

Bismuth nitrate pentahydrate $(Bi(NO_3)_3.5H_2O > 99\% \ Alfa \ aesar)$, Ammonium vanadate $(NH_4VO_3 > 99\% \ Alfa \ aesar)$, Sodium lauryl sulfate $(NaC_{12}H_{25}SO_4 > 96\% \ Spectrochem)$, Sodium hydroxide $(NaOH > 98\% \ Qualigens)$, Nitric acid $(HNO_3, \ Qualigens)$, and Rhodamine B $(C_{28}H_{31}CIN_2O_3, > 98\% \ Alfa \ aesar)$ were analytical reagents used for this study. Deionized water was used as a solvent in all synthesis and other experiments.

7.2.2. Synthesis of the catalysts

$Bi(NO_3)_3.5H_2O$ and NH_4VO_3 were dissolved in 30.0 mL of 2M HNO_3, and NaOH in a molar ratio of 1:1. To both of the above solutions, 0.1 g of sodium lauryl sulphate was added. After stirring for 30 minutes, the two solutions were slowly mixed, resulting in a bisque solution. The pH of the solution was adjusted to 7 using a 2M NaOH solution, and the mixture was stirred for another 30 minutes. This precursor solution was poured into a Teflon-lined stainless-steel container with a capacity of 100.0 mL. The

autoclave was then sealed, heated up to 200°C, and maintained at that temperature for 1.5 hours. Finally, it was cooled to room temperature naturally. The resulting yellow precipitate was separated by filtration, washed with distilled water and absolute ethanol several times, and then dried in a vacuum oven overnight. This procedure was done without the addition of sodium lauryl sulphate and with the addition of 0.2g of sodium lauryl sulphate to the precursor solutions. Bismuth vanadium oxide made without sodium lauryl sulphate is denoted as BVO-0.0. Bismuth vanadium oxide made with 0.1 g and 0.2 g of sodium lauryl sulphate is designated as BVO-0.1 and BVO-0.2, respectively.

The schematic representation of the sample synthesis is shown in Fig.7.1.
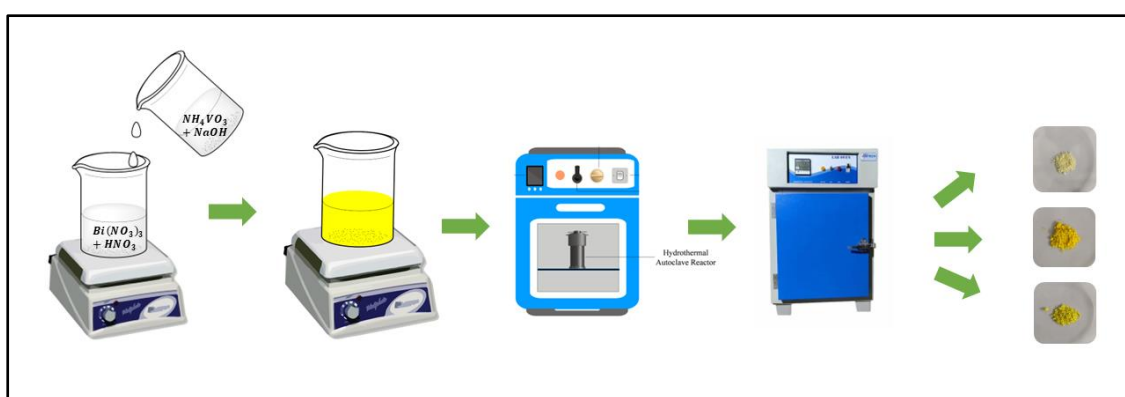
Fig.7.1. *The schematic representation of hydrothermal synthesis of BiVO₄ heterostructures.*

7.2.3. Catalytic experiments

The catalytic performance of the synthesized samples for the degradation of rhodamine B (RhB) was evaluated in the presence of visible light and ultrasonic sound. In each experiment, 35 mg of photocatalyst was added to 50 mL of an aqueous solution containing the RhB with a concentration of 5 ppm. Prior to light irradiation, the suspensions were magnetically stirred in the dark for 30 minutes to reach adsorption-desorption equilibrium. For sonocatalytic studies, the suspensions were sonicated in the dark using a GT ultrasonic cleaner (GT sonic, 50 W, 40 kHz). The photocatalytic degradation of RhB was conducted in a chamber equipped with a 150W Xe arc lamp as the light source.

Additionally, for sonophotocatalytic activity, the suspensions were exposed to visible light while continuously subjected to ultrasonic sound irradiation. We have irradiated the reaction medium with ultrasonic sound and visible light for up to 90 minutes. At regular intervals (10 min.), 3.0 mL of the solution was sampled, centrifuged,

and measured to determine the degradation of pollutants using a UV-visible spectrophotometer (Jasco 750). The efficiency of the process was evaluated by plotting the changes in C_t/C_0 of pollutants against irradiation time, where C_0 and C_t represent the total concentration of RhB at time $(t = 0)$ and time t, respectively. The efficiency of RhB degradation can be calculated using the equation:

$$\text{Degradation efficiency } \% = \frac{C_0 - C_t}{C_o} \times 100 \dots \dots (7.1)$$

To elucidate the degradation mechanism of degradation, different scavengers were added during the catalytic process. KI, isopropanol, $AgNO_3$ and benzoquinone were added separately as $h^+, OH^{\cdot}, e^-$ and O_2^- scavengers in solution.

7.3. RESULT AND DISCUSSION

7.3.1. Structural characterization

Fig.7.2. displays the XRD pattern of the synthesized samples. The diffraction peaks of BVO-0.0 exhibit the tetragonal zircon phase (z-t) of $BiVO_4$, which agrees well with JCPDS card no. 14-0133 [20]. The diffraction peaks of the BVO-0.1 sample can be readily identified as the scheelite-monoclinic (s-m) phase of $BiVO_4$, corresponding to JCPDS card no. 14-0688 [21]. However, the diffraction peaks of the BVO-0.2 sample indicate a mixed phase of tetragonal and monoclinic $BiVO_4$. Therefore, samples BVO-0.0 and BVO-0.1 can be regarded as the pure tetragonal and monoclinic phases of $BiVO_4$, respectively. In contrast, the BVO-0.2 sample can be characterized as a composite phase comprising both tetragonal and monoclinic $BiVO_4$.

The percentage composition of monoclinic and tetragonal phases of $BiVO_4$ in the composite has been calculated based on the normalized ratio of relative intensities of the (121) peak (28.92^0) of the monoclinic phase against that for (200) peak (24.39^0) of the tetragonal phase [22]. If η_{mono} and η_{tetra} are the percentage of the monoclinic phase and tetragonal phase, respectively, then

$$\eta_{mono}(\%) = \frac{I_{mono} \times 100}{I_{mono} + I_{tetra}} \dots \dots (7.2.a)$$

$$\eta_{tetra}(\%) = 100 - \eta_{mono} \dots \dots (7.2.b)$$

Table.7.1 displays the estimated percentage composition of the monoclinic and tetragonal phases of $BiVO_4$. The results indicate that 97.9% of the BVO-0.0 sample consists of the tetragonal phase, while 97.6% of the BVO-0.1 sample comprises the

monoclinic phase. However, in the case of BVO-0.2, the percentage of the monoclinic phase is 46.5%, and the tetragonal phase is 53.5%. Thus, the sample is approximately an equal combination of monoclinic and tetragonal phases.
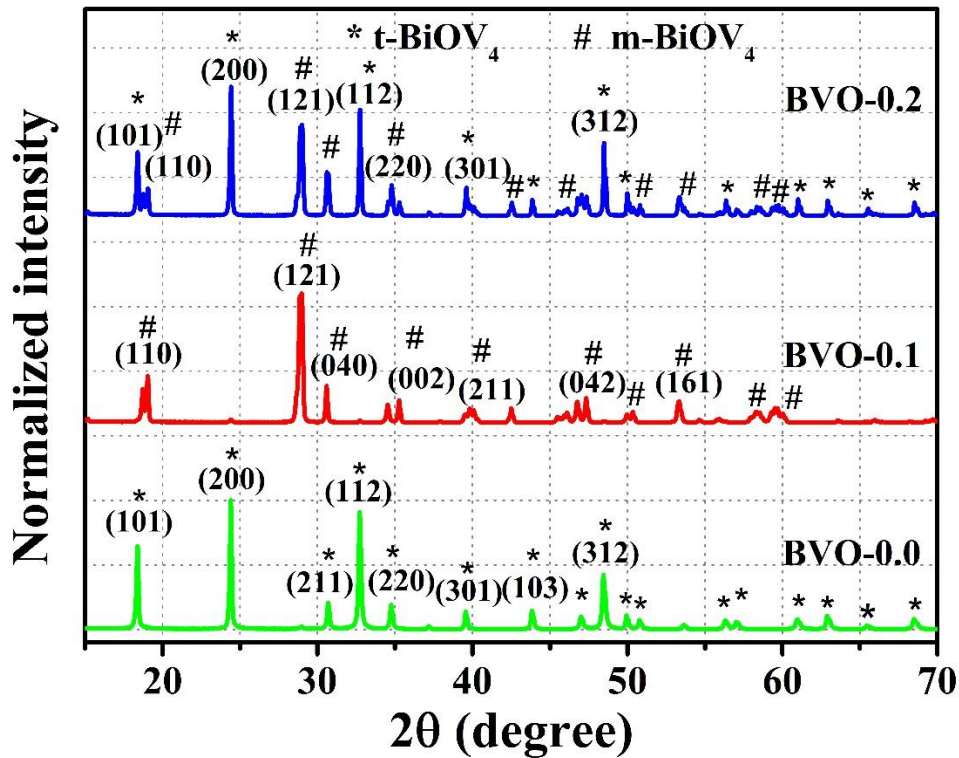
Fig.7.2. *XRD pattern of synthesized samples. The characteristic peaks of the tetragonal phase of $BiVO_4$ are indexed by *, and that of the monoclinic phase are indexed by #. The sample BOV-0.2 contains the peaks of the tetragonal and monoclinic phases.*

The crystallite size of the synthesized samples can be calculated using Debye–Scherrer formula $D = \dfrac{K\lambda}{\beta \cos\theta}$, where D is the crystallite size, K is the dimensionless shape factor (here taken to be 0.94), λ is the wavelength of the X-ray used, and β is the full width at half maximum corresponding to Bragg's angle θ. The estimated value of the crystallite size of the synthesized samples is shown in Table 7.1. It is evident that the crystallite size of the samples slightly increases when they form the composite phase.

Table 7.1. *The estimated values of percentage composition of monoclinic and tetragonal phase of $BiVO_4$ and its crystallite size.*

Sample	$\eta_{mono}(\%)$	$\eta_{tetra}(\%)$	Crystallite size (nm)
$BVO - 0.0$	2.1	97.9	54.7 ± 1.7
$BVO - 0.1$	97.6	2.4	28.8 ± 1.0
$BVO - 0.2$	46.5	53.5	56.7 ± 1.1 (Tetragonal) 31.8 ± 1.0 (Monoclinic)

7.3.2. Raman analysis

The Raman spectrum of the synthesized samples is shown in Fig.7.3. The Raman bands at 325, 366, 717, and 830 cm^{-1} represent the characteristic Raman peaks of monoclinic-BiVO$_4$. The band appearing at 830 cm^{-1} is assigned to the symmetric V–O stretching mode (A$_g$ symmetry), and the weak shoulder at about 717 cm^{-1} is set to antisymmetric V–O stretching (B$_g$ symmetry) corresponding to the V–O bond, providing valuable structural information. The symmetric V-O stretching mode in the tetragonal phase of BiVO$_4$ is fully accountable for the prominent band observed at 856 cm^{-1} of BVO-0.0. The bands at 366 cm^{-1} and 325 cm^{-1} are due to the bending modes of the V–O bonds, assigned to the symmetric (A$_g$) and asymmetric (B$_g$) deformation modes of the $(VO)_4{}^{3-}$ tetrahedron, respectively [23]. The remaining two Raman peaks, located at 210 cm^{-1} and 127 cm^{-1}, respectively, are related to the external mode of BiVO$_4$ and provide minimal structural information. For BVO-0.2, the Raman bands around 721 and 830 cm^{-1} coexist with tetragonal bands around 763 and 856 cm-^{1} confirming the existence of mixed phases.
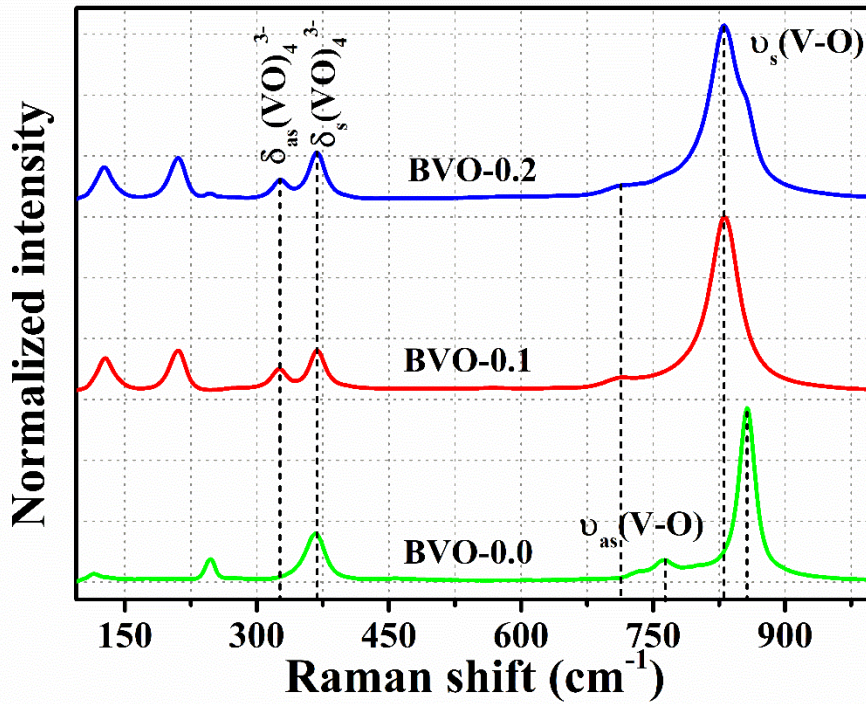
Fig.7.3. The Raman spectrum of the synthesized samples. The most intense Raman band at about 830 cm^{-1} is assigned to the symmetric. $\upsilon_s(V-O)$ stretching mode (A_g), the weak shoulder at about 717 cm^{-1} is assigned to antisymmetric $\upsilon_{as}(V-O)$ stretch (B_g), the symmetric $\delta_s(VO)_4{}^{3-}$ (A_g) and antisymmetric $\delta_{as}(VO)_4{}^{3-}$ (B_g) bending modes are at 366 and about 325 cm^{-1}, respectively.

The variations in the length of the V-O bond can be correlated with the Raman shift. A lower stretching frequency corresponds to a longer metal-oxygen bond length, as indicated by the inverse relationship between Raman stretching frequencies and the respective metal-oxygen bond lengths. The following expression is used to calculate the bond length of V-O [24]:

$$\upsilon(cm^{-1}) = 21349\, exp\left[-1.9176R(\text{Å})\right] \dots\dots (7.3)$$

wherein υ corresponds to the Raman frequency of the symmetric stretching mode (A_g) of the V–O bond, and R is the length of the vanadium–oxygen bond.

Brown and Wu have connected the interatomic distance R and the cation-oxygen bond valences. The empirical formula for relating the length of a V-O bond to its bond valence is [25]-

$$s(V-O) = \left\{0.2912\ln\left(\frac{21349}{\upsilon}\right)\right\}^{-5.1} \dots\dots (7.4)$$

Where s is the Pauling V–O bond strength in valence units. Table.7.2 summarises the V-O bond length and bond strength calculated by eqn. (7.3) & (7.4).
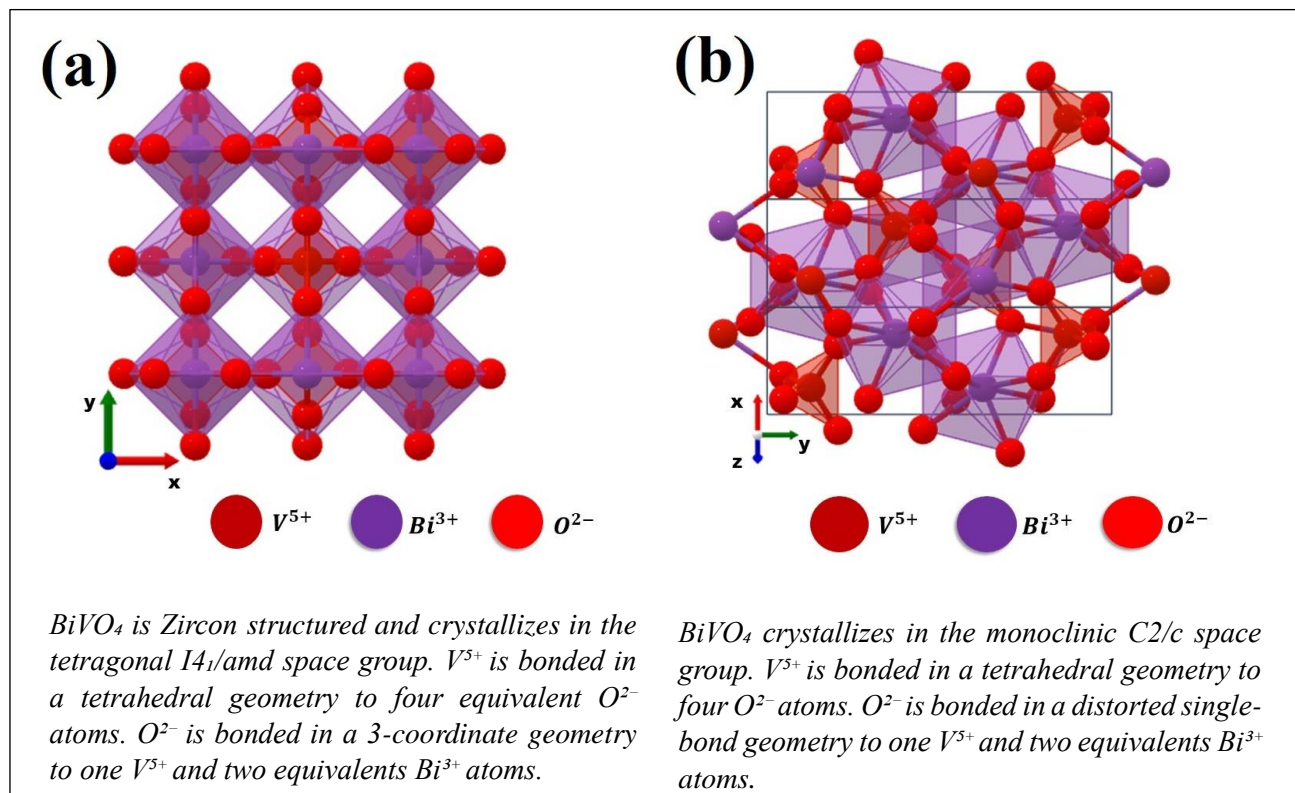
Table.7.2. Estimated value of V-O bond length using Raman characterization. The positions of the most intense bands near 830 cm^{-1} and 856 cm^{-1} were determined by fitting the Lorentzian peak function.

Sample	Raman frequency $v\ (cm^{-1})$	V-O bond length (Å)	V-O bond strength (valence unit)
BVO-0.0	856.60 ± 0.04	1.6769 ± 0.0001	1.3978 ± 0.0003
	761.53 ± 0.09	1.7383 ± 0.0002	1.1637 ± 0.0007
BVO-0.1	830.84 ± 0.04	1.6929 ± 0.0001	1.3320 ± 0.0003
	717.91 ± 0.09	1.7691 ± 0.0002	1.0641 ± 0.0006
BVO-0.2	856.63 ± 0.09	1.6769 ± 0.0001	1.3979 ± 0.0007
	763.77 ± 0.08	1.7367 ± 0.0002	1.1690 ± 0.0006
	830.52 ± 0.05	1.6931 ± 0.0001	1.3316 ± 0.0004
	721.85 ± 0.08	1.7662 ± 0.0002	1.0739 ± 0.0006

Different combinations of V-O bond strengths, which correspond to the experimentally determined +5 valence of the vanadium cation, can identify the structure of vanadate species. In the case of BVO-0.1, the combination of three V-O bonds with a calculated bond strength of 1.3320 units and one V-O bond with a calculated bond strength of 1.0641 units results in a total of 5.0601 valence units. This value closely matches the expected +5 valence state of the vanadium cation, indicating a certain degree of distortion in the $(VO)_4{}^{3-}$ tetrahedron of bismuth vanadate [25]. The calculated valence state of V^{+5} in the BVO-0.2 sample is 5.0687 valence units - slightly higher than that of the BVO-0.1 sample. This suggests a more significant distortion of the $(VO)_4{}^{3-}$ tetrahedron in bismuth vanadate in the BVO-0.2 sample. Based on these calculations, it is proposed that BiVO$_4$ nanostructures are formed with distorted $(VO)_4{}^{3-}$ units containing two uneven sets of V-

O bonds. We expect the tetrahedron to undergo permanent distortion due to the irreversible phase transition. Previous reports have highlighted that the distortion of the $(VO)_4{}^{3-}$ tetrahedron is a critical factor that enhances the catalytic activity of bismuth vanadate [26]. The extent of distortion of the tetrahedron is greater in BVO-0.2, which leads to enhanced catalytic degradation compared to BVO-0.0 and BVO-0.1. Fig.7.4 shows the crystal structure representations of the tetragonal and monoclinic phases of BiVO₄ [27, 28].


BiVO₄ is Zircon structured and crystallizes in the tetragonal I4₁/amd space group. V⁵⁺ is bonded in a tetrahedral geometry to four equivalent O²⁻ atoms. O²⁻ is bonded in a 3-coordinate geometry to one V⁵⁺ and two equivalents Bi³⁺ atoms.

BiVO₄ crystallizes in the monoclinic C2/c space group. V⁵⁺ is bonded in a tetrahedral geometry to four O²⁻ atoms. O²⁻ is bonded in a distorted single-bond geometry to one V⁵⁺ and two equivalents Bi³⁺ atoms.

Fig.7.4. *Crystal structure representation of tetragonal zircon (fig.3.a) and scheelite monoclinic phase (fig.3.b) of BiVO₄ with an indication of BiO₈ dodecahedra (in purple) and $(VO)_4{}^{3-}$ tetrahedron (in red shade).*

7.3.3. Morphological analysis

Fig.7.5. – 7.7. display the FE-SEM images of the synthesized samples. Fig.7.5. shows the FE-SEM image of BVO-0.0, revealing a nanofinger-like morphology. Fig.7.6. illustrates the morphology of BVO-0.1, exhibiting nano-tiles with precise crystal facets. The thickness of the nano-tiles ranges from 50 to 200 nm. In contrast, BVO-0.2 (Fig.7.7.) displays an agglomerated nanostructure with irregular morphology. Notably, in this study, we observed that the surfactant dosage impacts the morphology and crystal structure of the samples. SLS, being an anionic surfactant, can form micelles in an aqueous solution under specific conditions. During the synthesis process, the SLS ions

can adhere to the surface of the bismuth vanadate nanoparticles and influence their growth. Therefore, adsorbed SLS on the precursor particles are suggested to promote the development of distinct crystal structures and morphologies. This mechanism of crystal formation, facilitated by organic agents, is commonly referred to as oriented aggregation-based crystal growth and has been frequently reported in recent studies.
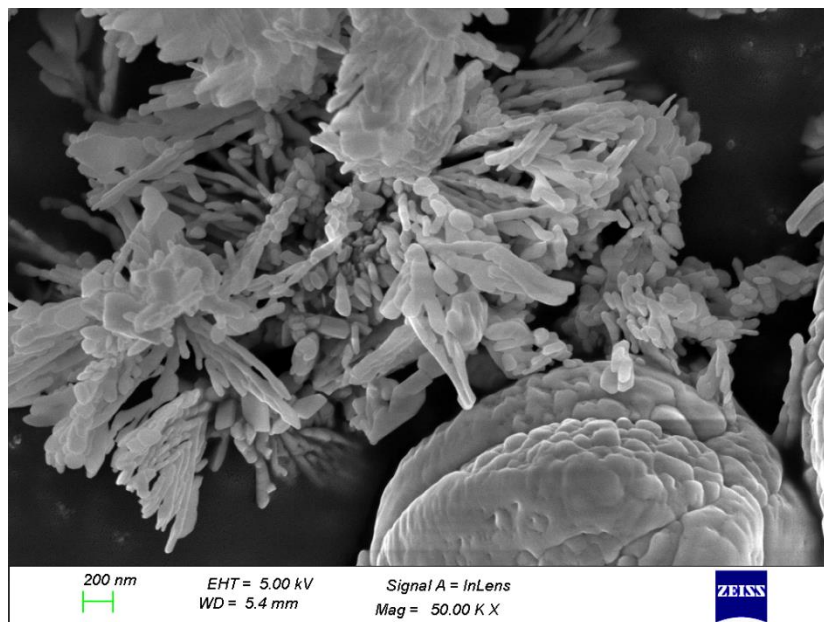
Fig.7.5*. The FESEM images of BVO-0.0 exhibits a nanofinger-like morphology.*
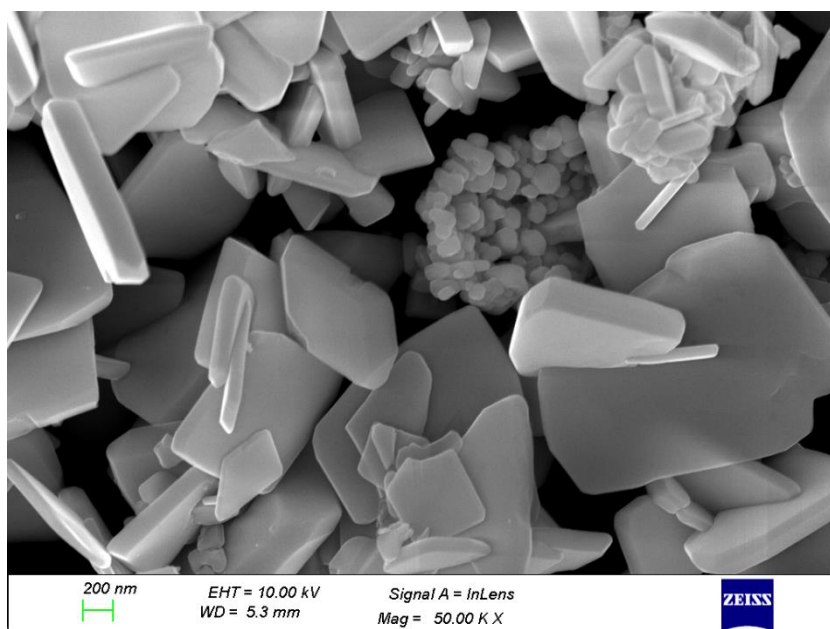
Fig.7.6*. The FESEM images of BVO-0.1 which displays Nano-tiles with distinct crystal faces.*
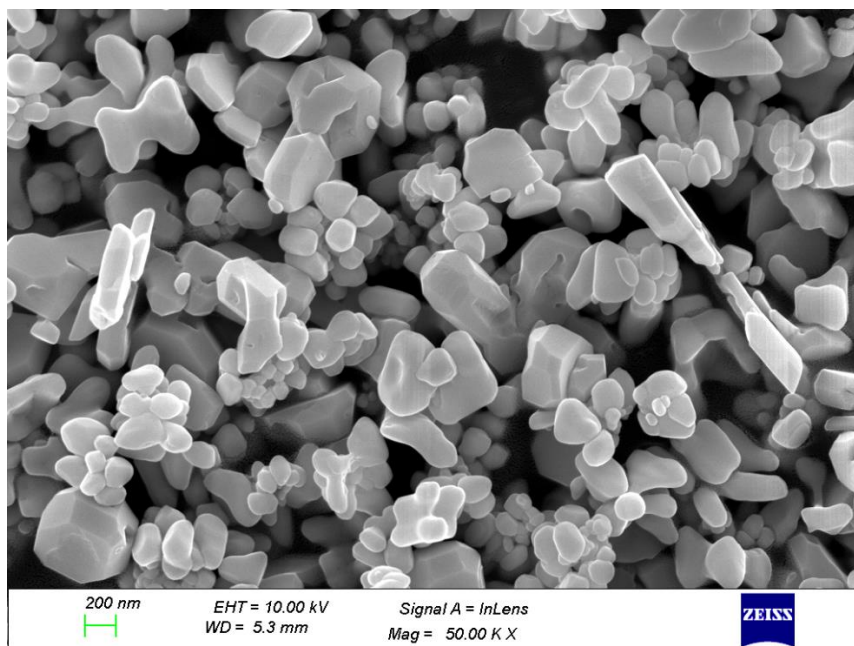
Fig.7.7. *The FESEM images of BVO-0.2, showing an arbitrary morphology.*

7.3.4. Surface area and porosity analysis

To assess the specific surface area and pore distribution of the samples, we conducted N_2 adsorption-desorption isotherm tests, and the results are illustrated in Fig.7.8. The isotherms for the samples exhibit a classical type II pattern with a hysteresis loop observed in the relative pressure (P/P$_0$) range of 0.8-1.0, indicating the presence of surface mesopores and interparticle pores of significant size due to the composite nature of the material [32]. The specific surface area of the samples was estimated to be $0.49 \pm 0.02\ m^2/g$, $1.68 \pm 0.04\ m^2/g$, $3.43 \pm 0.11 m^2/g$ for BVO-0.0, BVO-0.1 and BVO-0.2 respectively. The BET isotherm fitted data is shown in Fig.7.10. As shown in shown in Fig.7.9. Barrett-Joyner-Halenda (BJH) pore distribution analysis reveals that the samples exhibit micro-mesoporous distributions, with a more pronounced mesoporous distribution in BVO-0.2 and an average pore radius of approximately 20 nm.
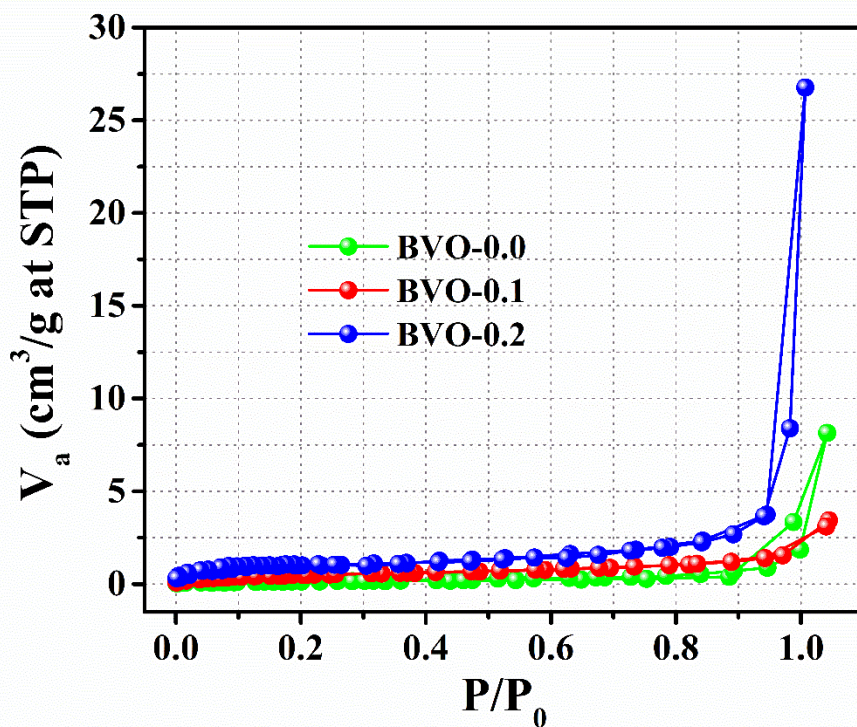
Fig.7.8. *The N₂ adsorption-desorption isotherm shows that the isotherms for the samples exhibit a classical type II pattern with a hysteresis loop and micro-mesoporous distributions.*
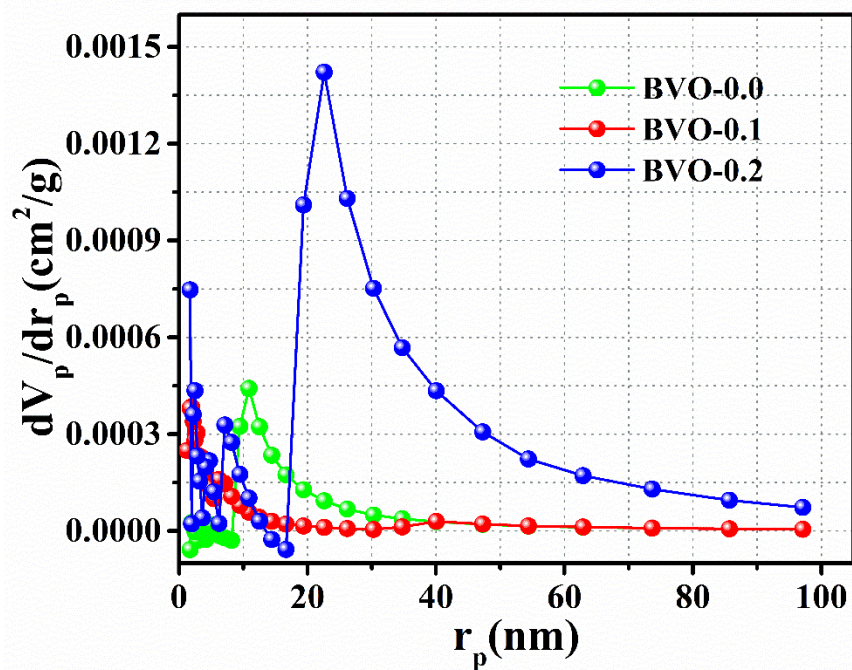
Fig.7.9. *The Barrett-Joyner-Halenda (BJH) pore distribution curve of the samples.*

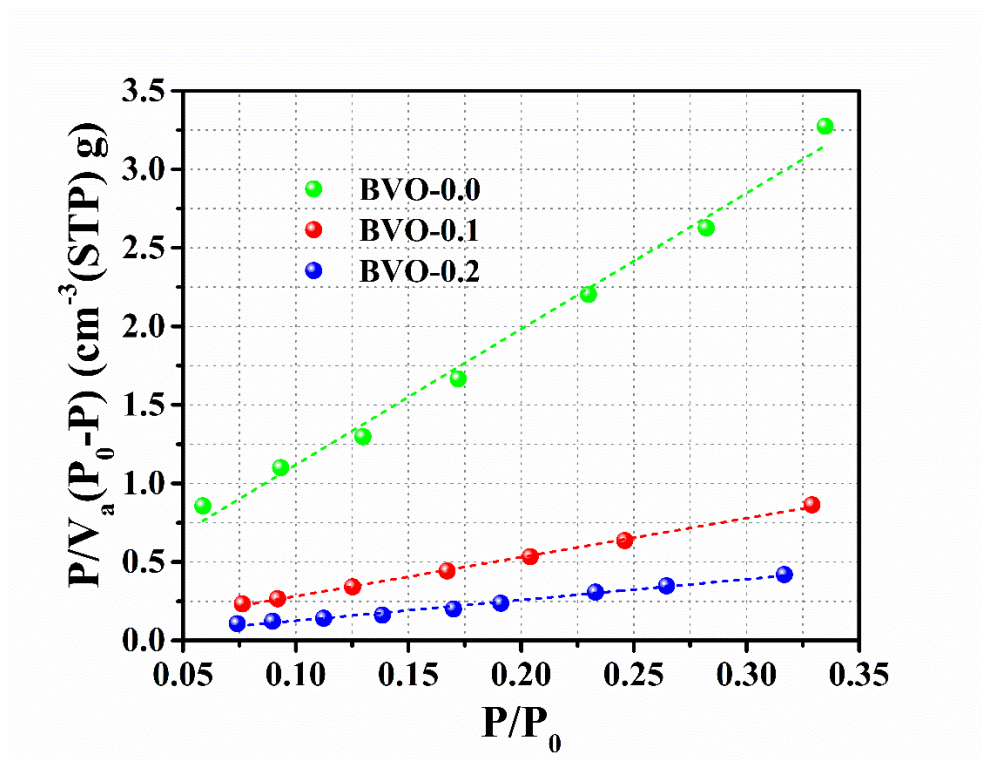**Fig.7.10.** *The linear fit of P/Va(P0-P) versus P/P0 data points for the estimation of BET surface area.*

7.3.5. Optical absorption analysis

UV-visible diffused reflectance spectra (UV-DRS) were utilized to study the optical absorption behaviour of the synthesized samples. All samples exhibit strong absorption in the UV-visible region, displaying a distinct and sharp absorption edge, which is evident in Fig.7.11. The band gaps were calculated by extrapolating the horizontal and sharply ascending portions of the Tauc plot as shown in Fig.7.12.

These findings indicate that the absorption of visible light is primarily attributed to intrinsic bandgap transitions. The Raman analysis suggests an observable distortion in $(VO)_4{}^{3-}$ in the sample BVO-0.2. The estimated valence state of V^{5+} is greater than the expected +5 valence state of vanadium cation, implying that an increased positive charge on vanadium may be the root cause of distortion of the 6s lone pair of Bi^{3+}. This distortion may be the probable reason for its band gap values increasing. Since the $BiVO_4$ conduction band is made up of V 3d states, an increase in its valence state may lead to its displacement, causing an increase in the band gap values [33]. According to reports, $BiVO_4$ has optical properties that are more influenced by electronic structure than particle size. For instance, Zhao *et al.* has reported that a slight structure distortion enhances the

lone pair impact of the Bi 6s states, resulting in unique optical properties and excellent photocatalytic activities [34].
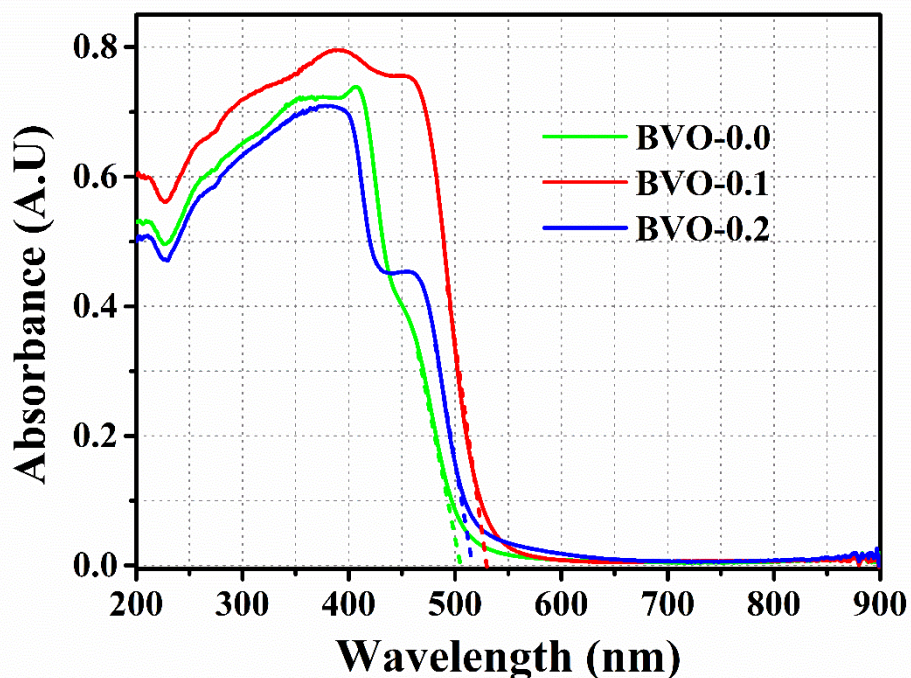
Fig.7.11. *The UV-visible absorption spectrum of the samples. The absorption band edge positions are nearly 505 nm,530 nm and 516 nm for BVO-0.0, BVO-0.1 and BVO-0.2 respectively.*
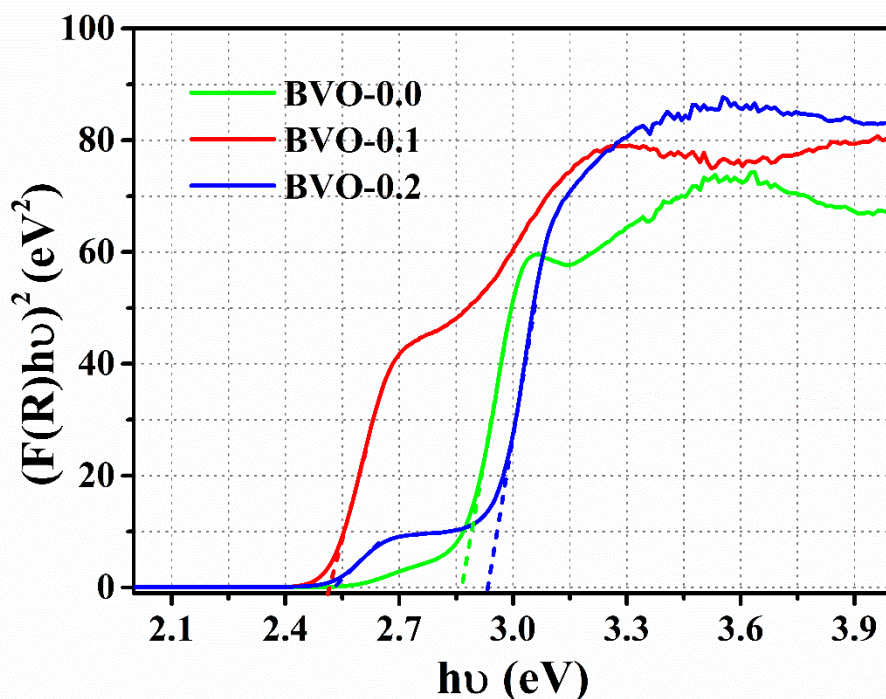
Fig.7.12. *Estimating the optical band gap of the samples using the Kubelka-Munk function.*

Table .7.3. The estimated values of band-edge positions and band gap of the samples.

Sample	Band edge (nm)	Bandgap (eV)
$BVO-0.0$	505 ± 1	2.85 ± 0.05
$BVO-0.1$	530 ± 1	2.51 ± 0.05
$BVO-0.2$	516 ± 1	2.93 ± 0.05

7.3.6. Catalytic performance of BiVO₄

The catalytic performance of BVO samples was investigated by the degradation of RhB dye in the presence of ultrasonic sound and visible light. The degradation of RhB that occurs when exposed to visible light is referred to as photolysis, while sonolysis is the term used when only ultrasonic sound is used. When ultrasonic sound and visible light are used in conjunction, the process is called sonophotolysis. If $BiVO_4$ is used as the catalyst with visible light, the process is referred to as photocatalysis, and when $BiVO_4$ is used as the catalyst with ultrasonic sound, it is called sonocatalysis. Finally, when all three - ultrasonic sound, visible light, and $BiVO_4$ catalysts - are used, the process is known as sonophotocatalysis.

The Fig.7.13. displays the temporal evolution of sonophotocatalytic degradation of RhB. In the sonophotolytic degradation, approximately 16% of the RhB was decomposed. However, the addition of $BiVO_4$ catalysts considerably impacted the degradation efficiency of this process. Within 90 minutes of ultrasonic sound and visible light irradiation, the BVO-0.0, BVO-0.1, and BVO-0.2 catalysts can achieve degradation efficiencies of approximately 96%, 88%, and 100%, respectively. The temporal evolution of photocatalytic and sonocatalytic degradation of RhB is displayed in Fig.7.14. and Fig.7.15.
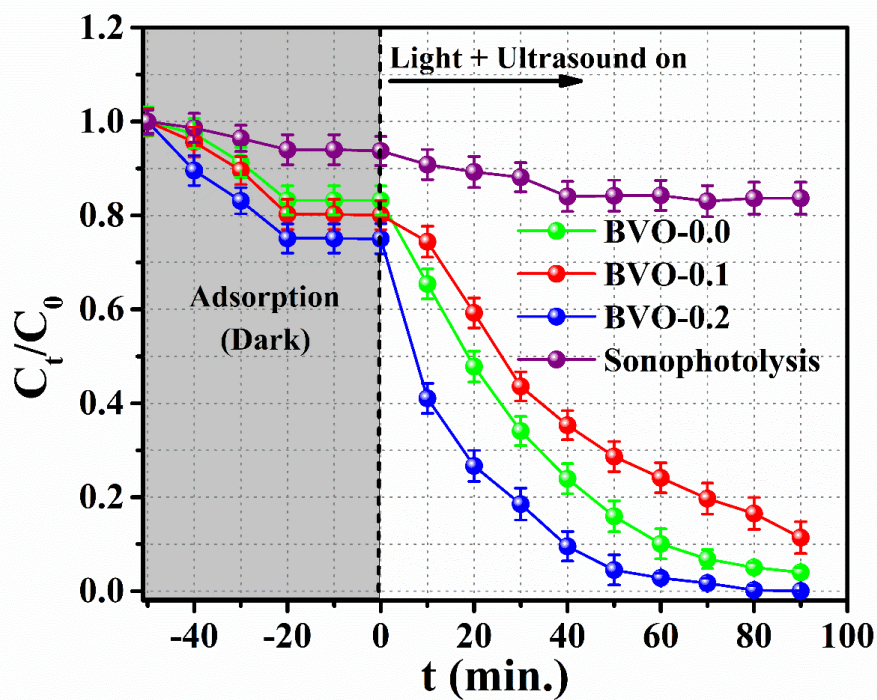
Fig.7.13. *The temporal evolution of sonophotocatalytic degradation of RhB.*
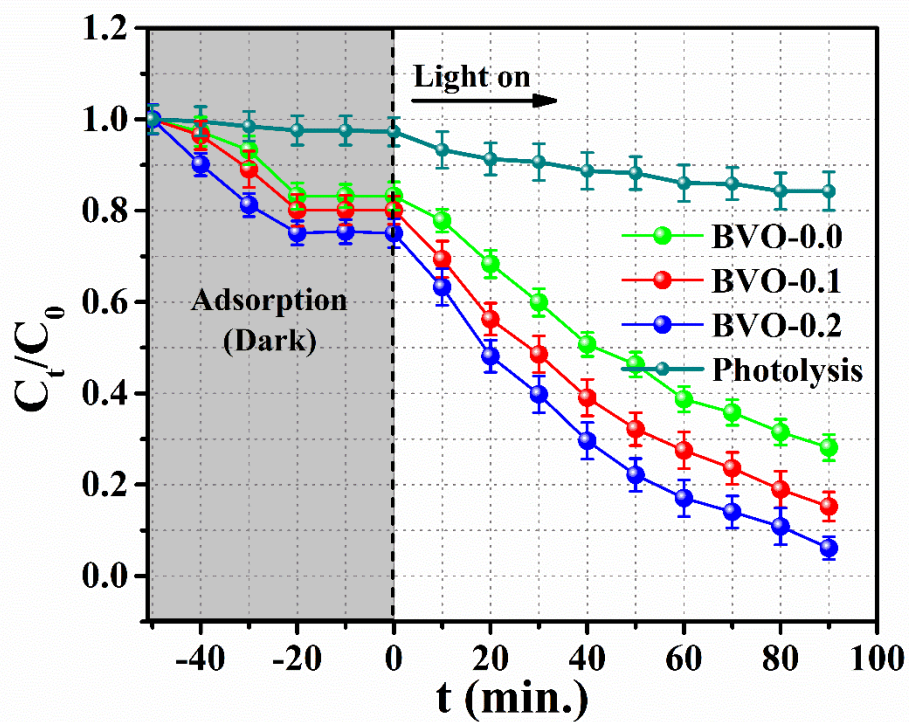
Fig.7.14. *The temporal evolution of photocatalytic degradation of RhB.*

Table.7.4. estimates and demonstrates the degradation efficiency of the catalysts for various catalysis. It is evident that, combining ultrasound irradiation with visible light enhanced the catalytic degradation reaction. The efficiency of sonophotocatalysis is significantly higher than that of bare photocatalysis or sonocatalysis alone. Experimental studies demonstrated a synergistic effect in the catalytic degradation of RhB when both visible light and ultrasound were present. Our experimental studies show that bismuth vanadate's tetragonal phase exhibits higher sonocatalytic and sonophotocatalytic activity than its monoclinic phase. The mixed phase of bismuth vanadate is more actively engaged in all catalytic processes than its single crystalline phases.
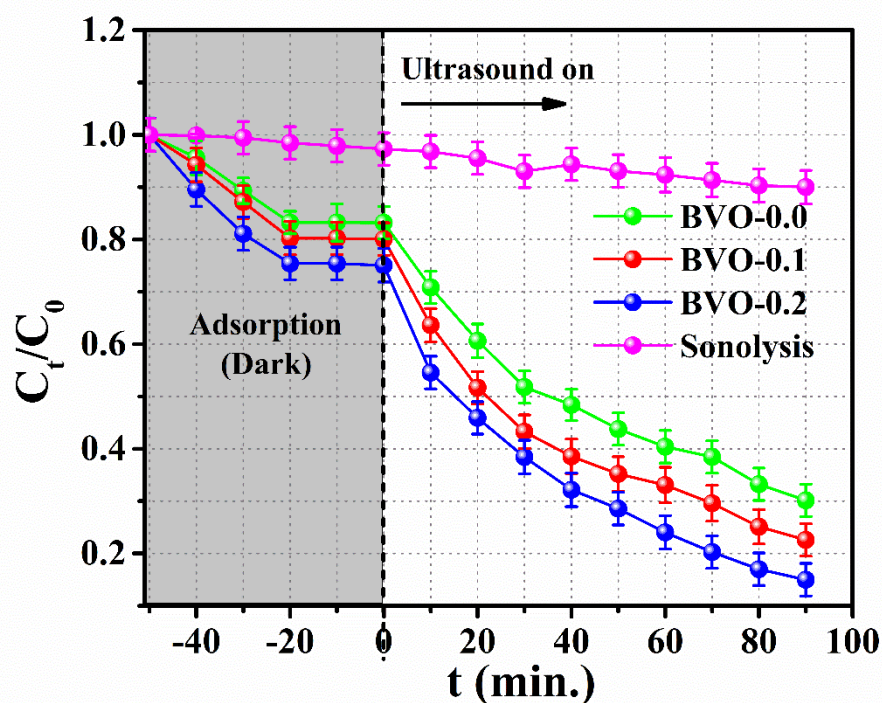
Fig.7.15. The temporal evolution of soocatalytic degradation of RhB.

To comprehend the quantitative approach to the catalytic reaction, we have examined the kinetics of the catalytic degradation of RhB by BiVO$_4$, employing the pseudo-first-order reaction kinetics as $C_t = C_0 e^{-k_{app} t}$. Thus, the apparent rate constant of the reaction k_{app} can be obtained by estimating the slope of the linear fit of $\ln\left(\frac{C_0}{C_t}\right)$ versus time (t).

The Fig.7.16. depicts the linear fit of a pseudo-first-order kinetic model of sonophotocatalysis. The linear fit of photocatalytic and sonocatalytic reactions is shown

in Fig.7.17. and Fig.7.18. All catalytic reactions confirmed the linear fitting of pseudo-first-order kinetics and Table 7.5. lists the calculated apparent rate constants.
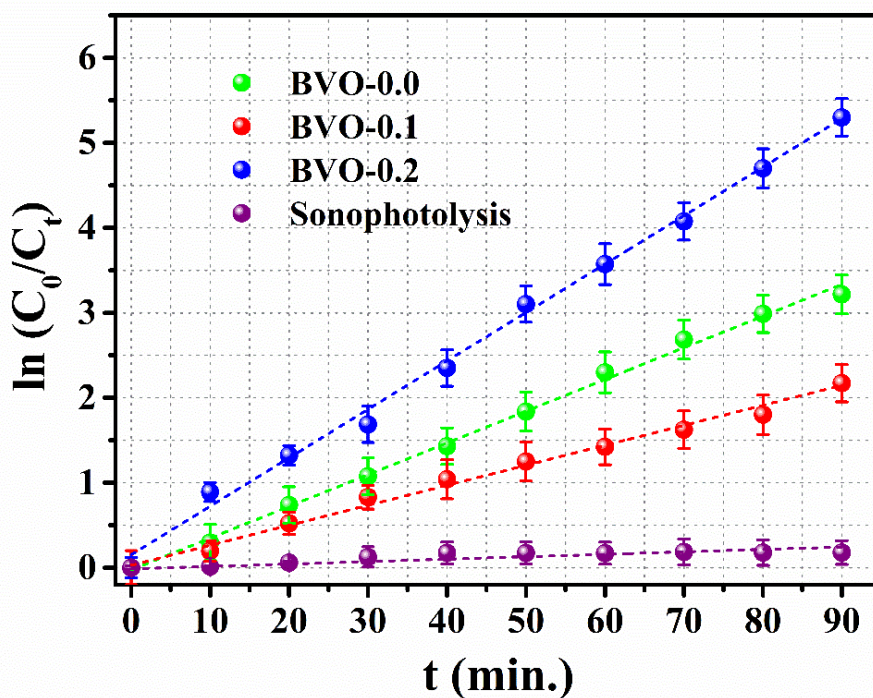
Fig.7.16. *The linear fit of the Pseudo-first order (PFO) kinetic model of sonophotocatalytic degradation of RhB.*
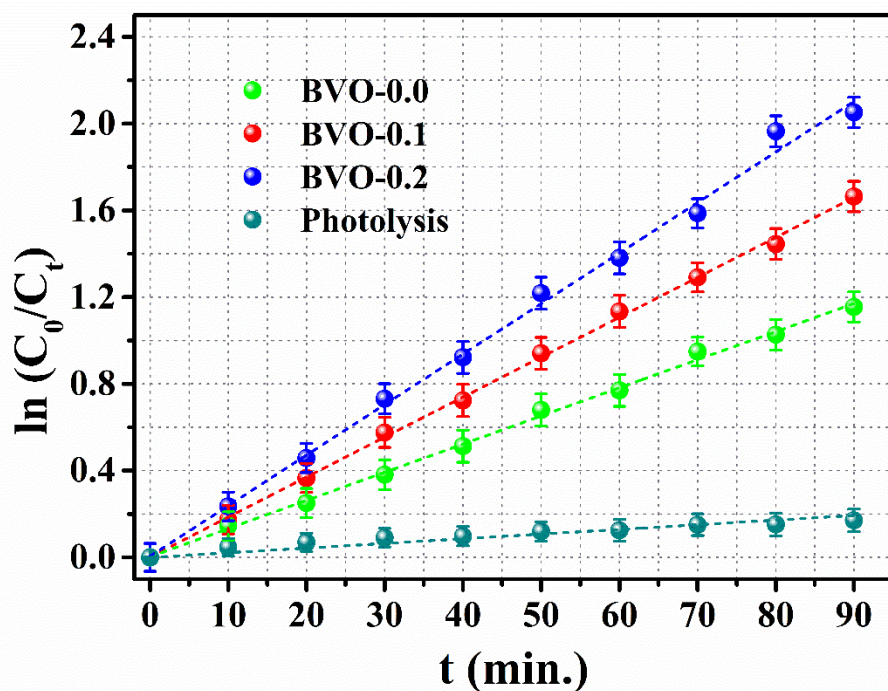
Fig.7.17. *The linear fit of the Pseudo-first order (PFO) kinetic model of photocatalytic degradation of RhB.*
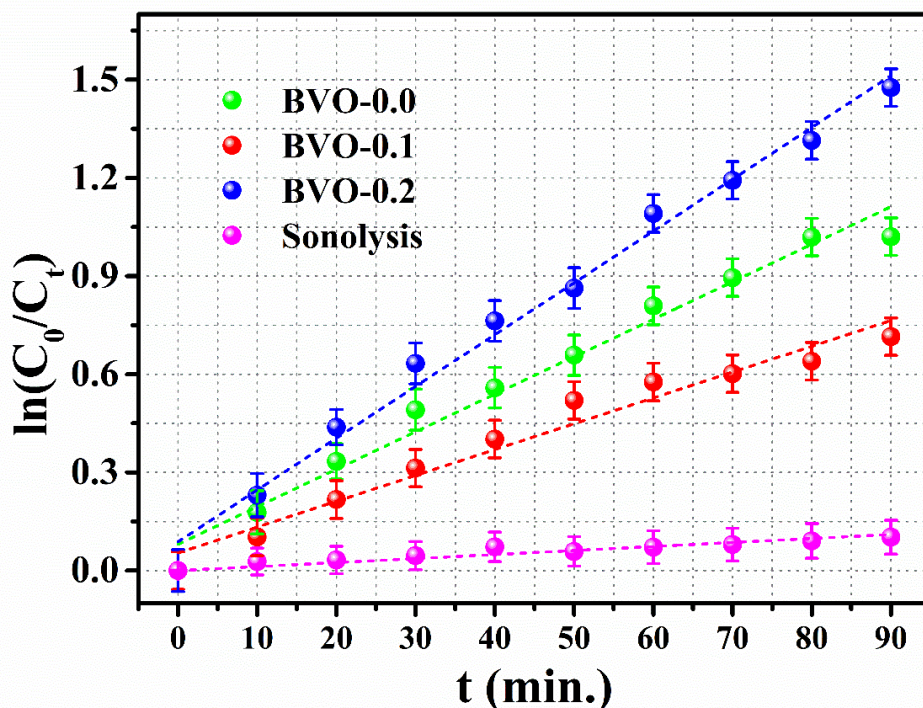
Fig.7.18. *The linear fit of the Pseudo-first order (PFO) kinetic model of sonocatalytic degradation of RhB.*

This quantitative kinetic analysis of catalysis establishes that BVO-0.2 outperforms the monoclinic and tetragonal phases of BiVO₄ in all catalytic processes. In particular, BVO-0.2 has an apparent rate constant that is 1.5 times greater than BVO-0.0 and 2.5 times greater than BVO-0.1 for sonophotocatalysis.

Table.7.4. *Estimated values of the removal efficiency of RhB of the reactions (within 90 min.)*

Sample	% of removal (Sonocatalysis)	% of removal (Photocatalysis)	% of removal (Sonophotocatalysis)
Without the catalyst	9	15	16
BVO-0.0	64	68	96
BVO-0.1	51	81	88
BVO-0.2	78	90	100

Table.7.5. Estimated values of the apparent rate constant of the reactions.

Sample	Sonocatalysis $k_{app}(\times 10^{-2} min^{-1})$	Photocatalysis $k_{app}(\times 10^{-2} min^{-1})$	Sonophotocatalysis $k_{app}(\times 10^{-2} min^{-1})$
Without the catalyst	0.12 ± 0.01	0.20 ± 0.01	0.28 ± 0.01
BVO-0.0	1.14 ± 0.02	1.29 ± 0.02	3.73 ± 0.03
BVO-0.1	0.78 ± 0.03	1.84 ± 0.02	2.35 ± 0.03
BVO-0.2	1.58 ± 0.04	2.32 ± 0.04	5.70 ± 0.04

The reason behind the enhanced catalytic degradation in BVO-0.2 can be attributed to the more significant distortion of the $(VO)_4^{3-}$ tetrahedron, which is caused by differences in valence states and is also evident in their bond lengths as computed by equation (7.2). Additionally, the agglomerates in BVO-0.2 may have a larger surface area because of the loosely packed nanoparticles, which increases the number of active sites available for catalysis. The catalytic performance of BVO-0.0 and BVO-0.1 demonstrates how the crystal phase of BiVO$_4$ influences its catalytic activity, indicating that the transition from tetragonal to monoclinic crystal structures leads to a reduction in catalytic activity due to the smoothing of the surface, which in turn decreases the surface heterogeneity. Therefore, tetragonal scheelite crystal structures exhibit better photo, sono, and sonophoto catalytic activity in all catalytic processes compared to their monoclinic scheelite counterparts. This study highlights the dependency of catalytic performance on the crystal phase of BiVO$_4$.

7.3.7. Hall measurements of the catalysts

Kweon and Hwang used hybrid DFT to predict the structural, bonding, and electronic properties of BiVO$_4$, paying particular attention to the difference between its tetragonal and monoclinic phases [36]. The authors provided theoretical proof for how the localization and transport of holes in bismuth vanadate depend on its crystal phase. In the tetragonal phase, an additional hole tends to be centred around a BiO$_8$ polyhedron, which causes significant lattice distortion. On the other hand, in the monoclinic phase,

the hole spreads out across several lattice sites [36]. This promotes the migration of the produced holes, allowing them to spread over multiple lattice sites. Therefore, the mobility of holes dependent on the phase could explain the more significant catalytic activity exhibited by BiVO₄.

For this, the DC field Hall effect measurements were used to obtain values for carrier mobility (μ) and carrier concentration (n) for the synthesized samples. The conductivity of the samples is estimated using the equation $\sigma = ne\mu$, where e is the electron's charge. Table 4 shows the Hall measurement results and estimated conductivity value of the samples. Since all the samples show a positive carrier concentration, they are p-type semiconductors. BVO-0.2 exhibits a significantly greater carrier concentration, mobility, and conductivity, favouring enhanced catalytic performance than the other two samples.

Table .7.6. *The carrier concentration, mobility and conductivity of the catalysts obtained from DC Hall measurements.*

Sample	Carrier concentration n $(\times 10^{17} cm^{-3})$	Mobility μ $(\times 10^2 cm^2 V^{-1} s^{-1})$	Conductivity σ $(\Omega^{-1} cm^{-1})$
BVO-0.0	1.65 ± 0.43	2.24 ± 0.14	5.90 ± 0.55
BVO-0.1	1.27 ± 0.23	2.03 ± 0.35	4.00 ± 0.35
BVO-0.2	3.54 ± 0.31	7.38 ± 1.34	42.51 ± 1.12

7.3.8. Photoluminescence studies of the catalysts

In Fig.7.19., we present a comparative PL study of tetragonal, monoclinic, and isotype heterojunctions of BiVO₄, utilizing an excitation wavelength of 380 nm. The PL spectrum of the samples reveals emission peaks within the 400–650 nm range. Notably, the isotype BiVO₄ heterojunction sample exhibits a relatively low PL emission intensity compared to the other samples, indicating a controlled rate of charge recombination and, consequently, a higher photocatalytic performance. This observation is attributed to the efficient transfer of photoinduced electrons from the tetragonal to the monoclinic phase, resulting in increased spatial separation and extended lifetimes of the photoinduced charge carriers. The enhanced separation of electron-hole pairs is made possible by effectively advancing the charge anti-recombination process within the material [37]. It's

worth noting that the distortion of bonds in monoclinic BiVO4, evident in Raman analysis, contributes to the increased efficiency in separating photoinduced electrons and holes.
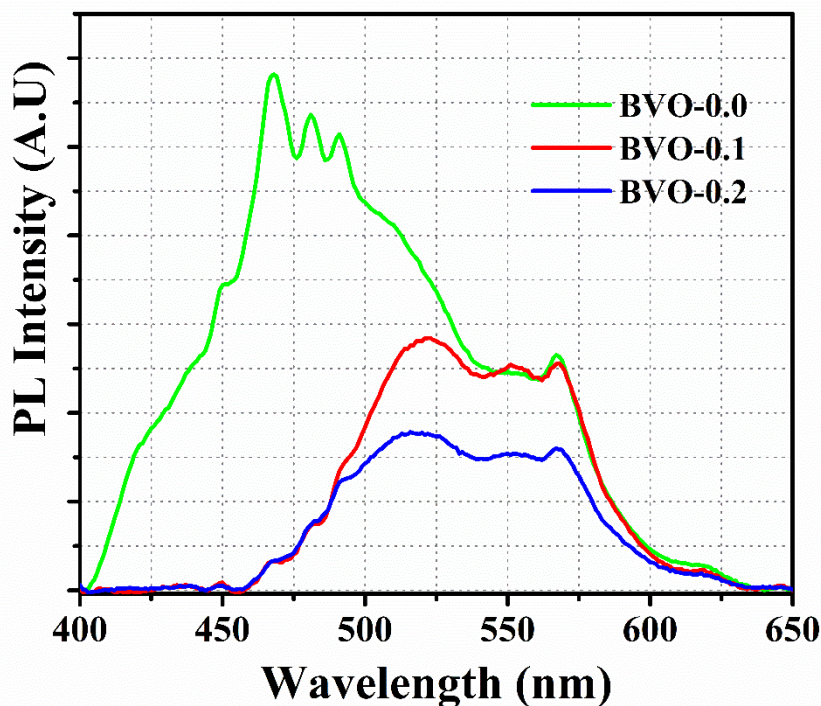
***Fig.7.19.** The PL spectra of the prepared samples. The isotype BiVO₄ sample displays noticeably lower PL emission intensity when contrasted with the other samples. Data suggests a well-regulated charge recombination rate, leading to superior sonophotocatalytic performance.*

7.3.9. Thermodynamics of the catalysis

The transition state theory (TST) [38] developed by Henry Eyring was used to analyze the thermodynamics of the catalytic degradation of RhB by BiVO4. According to the TST, the pre-equilibrium rate of the reaction related to various thermodynamic parameters of the reaction is

$$\ln\left(\frac{k}{T}\right) = -\frac{\Delta H}{R}\left(\frac{1}{T}\right) + \frac{\Delta S}{R} + \ln\left(\frac{k_B}{h}\right) \dots\dots (7.5)$$

where ΔH and ΔS are the enthalpy and entropy change of the reaction, respectively. And k_B, h, are, respectively, the constants of Boltzmann $(1.38 \times 10^{-23} J/K)$, Planck $(6.62 \times 10^{-34} Js)$.

By considering rate constant $k = k_{app}$, Eq.7.5 can be rewritten as follows:

$$\ln\left(\frac{k_{app}}{T}\right) = -\frac{\Delta H}{R}\left(\frac{1}{T}\right) + \frac{\Delta S}{R} + \ln\left(\frac{k_B}{h}\right) \dots\dots (7.6)$$

The values of ΔH and ΔS for the catalytic degradation of RhB by BiVO$_4$ were calculated from the slope and intercept of the $\ln\left(\frac{k_{app}}{T}\right) - \frac{1}{T}$ plot. This is depicted in Fig.7.20. The description of thermodynamics oof catalysis is thoroughly explained in Section 2.7 of Chapter 2.

Table 7.7. The estimated values of thermodynamic parameters of the various catalytic reactions.

Catalysis	ΔH ($kJ\,mol^{-1}$)	ΔS (JK^{-1})	E_a (kJ/mol)
Sonocatalysis	$+18.9 \pm 1.0$	-251.8 ± 4.7	21.5 ± 0.9
Photocatalysis	$+9.6 \pm 1.3$	-281.6 ± 4.3	12.3 ± 1.3
Sonophotocatalysis	$+5.9 \pm 1.6$	-291.1 ± 5.7	9.8 ± 1.5
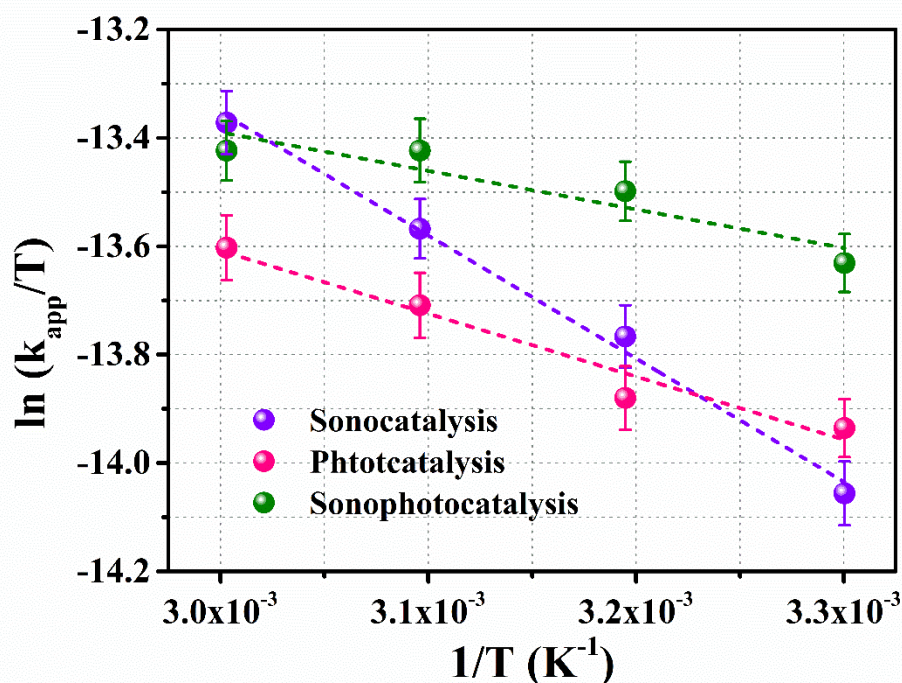
Fig.7.20. The $\ln\left(\frac{k_{app}}{T}\right) - \frac{1}{T}$ plot for estimating the various thermodynamic parameters of the catalytic reactions.

Table.7.7 displays the estimated enthalpy change (ΔH) and entropy change (ΔS) for different catalytic reactions. In all cases, the enthalpy change of the reactions is positive, and the entropy change is negative. The physical significance of a positive enthalpy change in a catalytic reaction is that the catalytic process is endothermic, absorbing heat from the surroundings [39]. A negative ΔS indicates a decrease in the overall disorder or randomness of the system during the catalytic reaction. The positive ΔH and negative ΔS combinations indicate a non-spontaneous reaction under standard conditions. Additional factors, such as the presence of a catalyst or external energy input, may be required to drive the reaction forward. These external factors are the reaction medium's visible light and ultrasonic sound waves [39]. The physical significance of having a lower ΔH and significant ΔS for sonophotocatalysis lies in its enhanced reaction spontaneity, improved reaction efficiency, enhanced catalyst effectiveness, and potential energy savings. The variation of Gibb's free energy of the reaction with temperatures is shown in Fig.7.21.
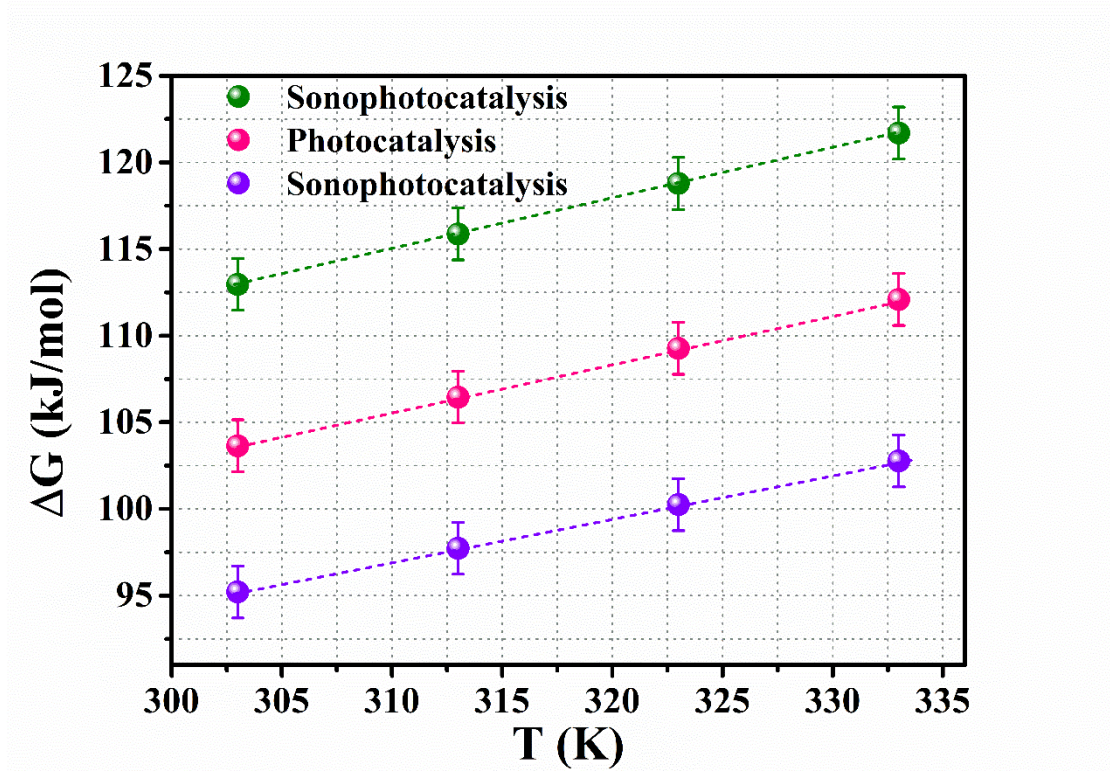
Fig.7.21. *The variation of Gibb's free energy of the reaction with temperatures.*

The kinetic experiments were conducted in the temperature range of 298–318 K to assess the impact of temperature on the reaction rate. The Arrhenius equation was employed to calculate the activation energy of the reaction (E_a) and the frequency factor (A):

$$k_{app} = A\exp\left(-\frac{E_a}{RT}\right) \Rightarrow \ln k_{app} = -\frac{E_a}{R}\left(\frac{1}{T}\right) + \ln A \ \dots\dots (7.7)$$

where R and T are the universal gas constant $(8.314\,J\,K^{-1}mol^{-1})$ and absolute temperature (K), respectively. The slope of the $\ln k_{app} - \frac{1}{T}$ plot provided E_a. This is shown in Fig.7.22.
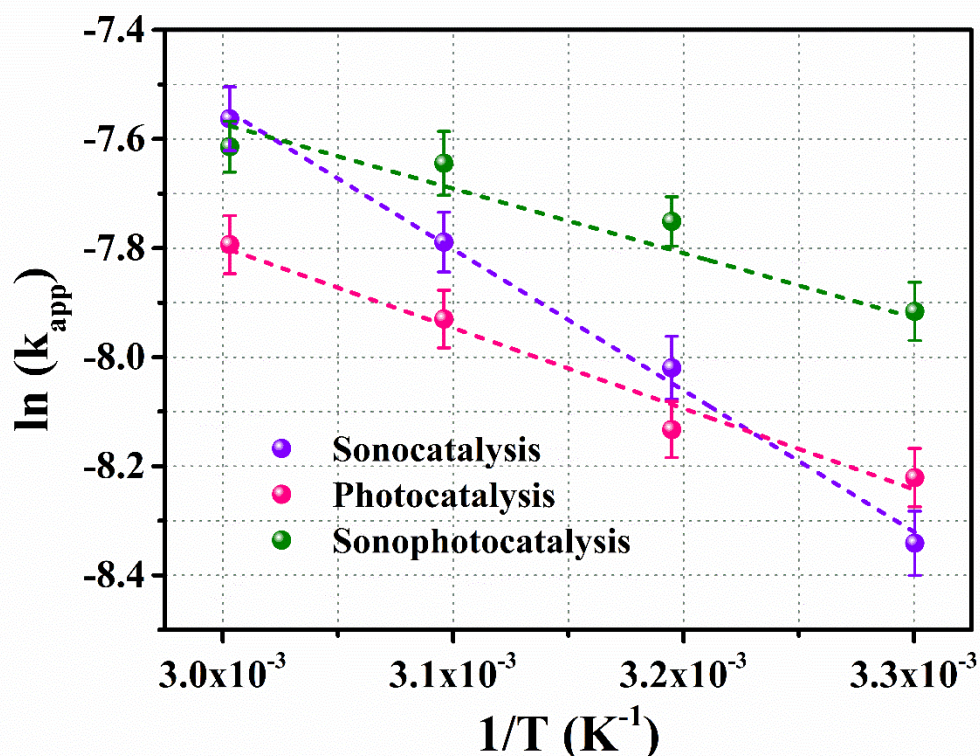
Fig.7.22. *The linear fit of $\ln k_{app} - \frac{1}{T}$ graph for the estimation of activation energy of the catalytic process.*

The activation energy represents the minimum energy required for a chemical reaction. Thus, a lower activation energy signifies the catalytic activity and effectiveness in accelerating the reaction rate. Table 5 shows that activation energy is the least for the sonophotocatalytic process. This shows the sonophotocatalytic reaction can favour specific pathways by providing lower energy barriers for desired reactions while hindering undesired ones. It also indicates less pronounced temperature dependence of the reaction rate [40].

7.3.10. Effect of the catalyst dosage

The catalyst dosage significantly affects dye degradation, as shown by varying the dose from 0.25 g/L to 1.25 g/L. The Fig.7.23. demonstrates that higher catalyst doses generate more active sites and active species, leading to increased degradation efficiency in all catalytic degradations. This higher dosage reduces diffusion limitations, providing a shorter path for pollutant molecules to reach the active sites on the catalyst surface. Consequently, more active sites are available for adsorption and degradation, increasing the probability of pollutant molecules contacting the catalyst and enhancing degradation efficiency [42].
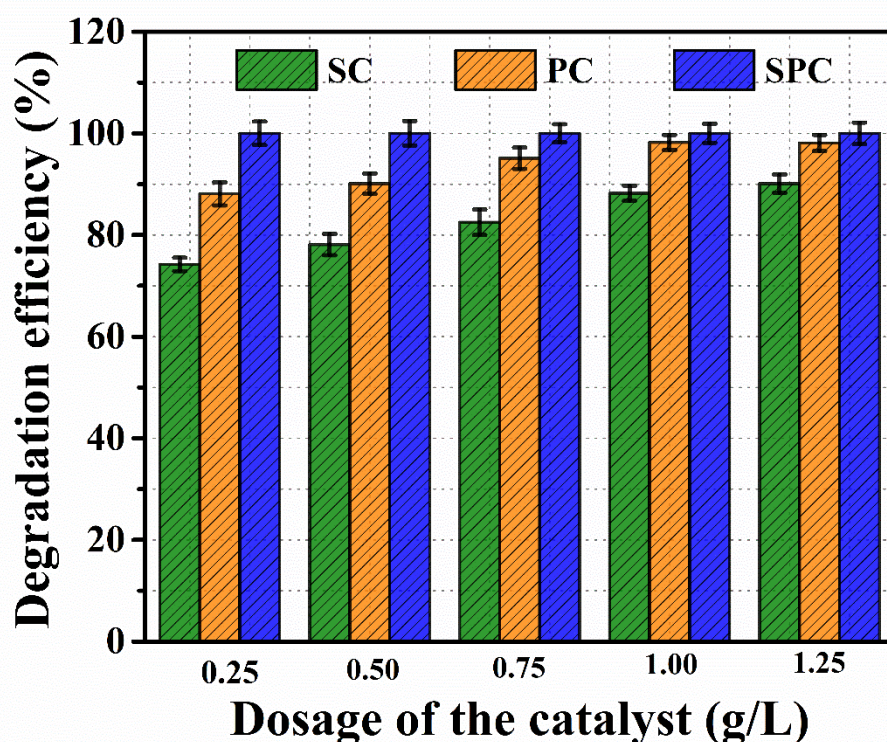
Fig.7.23. *Effect of dosage of the catalyst on catalytic degradation of RhB.*

7.3.11. Reusability of the catalyst

The reusability tests of the BVO-0.2 catalyst were further investigated in the sonophotocatalytic reaction (Fig.7.24.). In the sonophotocatalytic reaction, the catalysts showed excellent recyclability. Even after five cycles, it retained around 90% of its initial degradation efficiency. The slight decrease in efficiency is attributed to the deposition of catalyst particles on the reactor wall, leading to the loss of active sites.
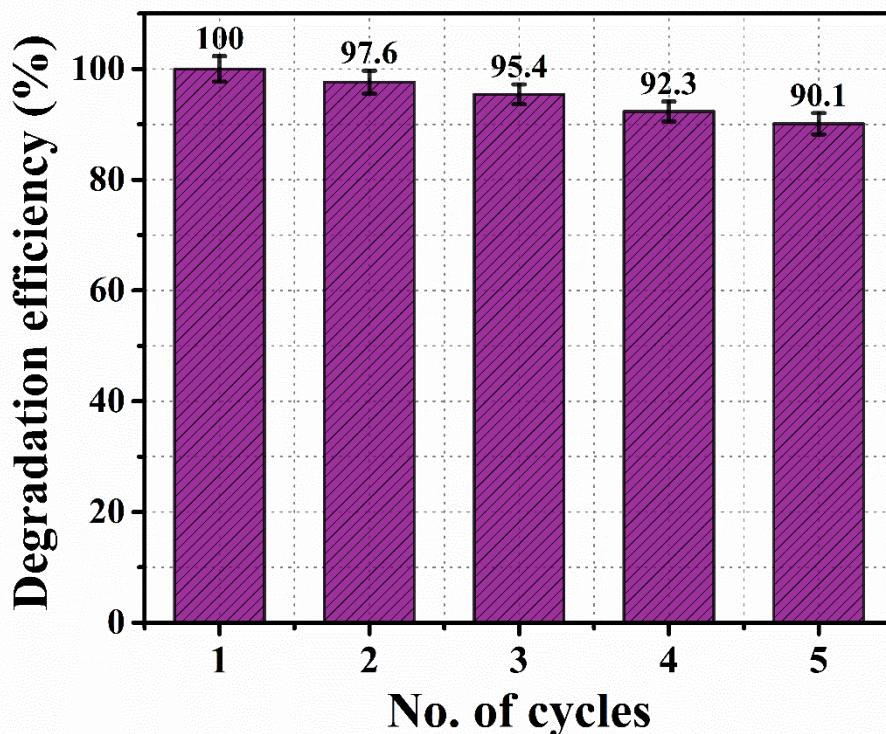
Fig.7.24. *Recyclability test of the catalyst- under sonophotocatalysis.*

7.3.12. Active species reaction test

Active reaction species are intermediate species or reactive entities that play a crucial role in catalyst-surface chemical reactions within advanced oxidation process-based catalysis. To elucidate the sonophotocatalytic mechanism during the degradation reaction in the presence of the BVO-0.2 sample, a trapping test was conducted to detect the active species. This is shown in Fig.7.25. The experimental findings revealed the presence of dominant oxidative species, namely $\bullet O_2$, h^+, $\bullet OH$ and electron as identified by the use of Benzoquinone (BQ), potassium iodide (KI) and isopropanol (IPA), and silver nitrate (AgNO$_3$) respectively. Active species scavenging experiments demonstrated the significant involvement of reactive species, including electrons (e^+), holes (h^+), and hydroxyl radicals ($\bullet OH$), in the sonophotocatalytic process, out of which h^+ and $\bullet OH$ radicals showed active involvement in the degradation process. The holes in the valence band can actively participate in the degradation reaction by producing highly oxidative reactive species such as $\bullet OH$ radicals.
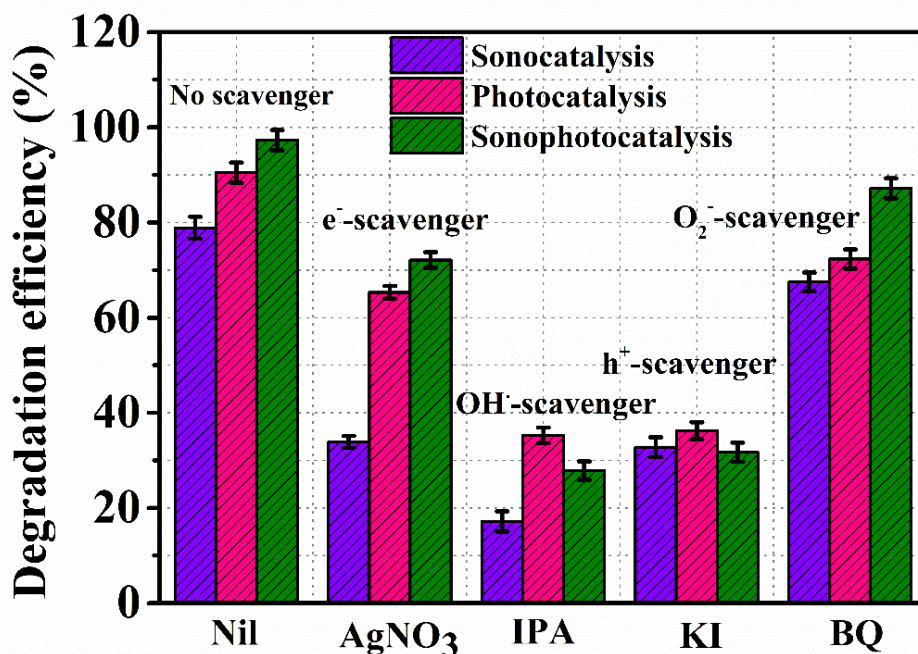
Fig.7.25. *The effect of the sacrificial agents on the various catalytic processes.*

7.3.13. Proposed mechanism for the degradation of Rhodamine B

To gain insight into the degradation mechanism of RhB, we used HPLC to identify the intermediates generated in the process. The intermediates and their identification results are summarized in Table.7.8. and Fig.7.26. The sonophotocatalytic degradation pathway of RhB involves four main processes: N-de-ethylation, chromophore cleavage, ring-opening, and mineralization.

Initially, N-deethylation occurred on the nitrogen atoms of RhB molecules due to the attack of h^+, resulting in various intermediates including P1 ($m/z = 359$), P2 ($m/z = 415$), and P3 ($m/z = 387$) [44]. Subsequently, the chromophore structures of these deethylated products were destroyed through cleavage of the conjugated xanthene structure, leading to intermediates with lower molecular weights, such as products P4 ($m/z = 300$), P5 ($m/z = 239$), P6 ($m/z = 226$), P7 ($m/z = 195$), and P8 ($m/z = 217$) [44]. The benzene ring structures of these intermediates were continuously attacked and oxidized to products P9 ($m/z = 114$) and P10 ($m/z = 118$). Ultimately, the formed products could be mineralized to CO_2 and H_2O [44].
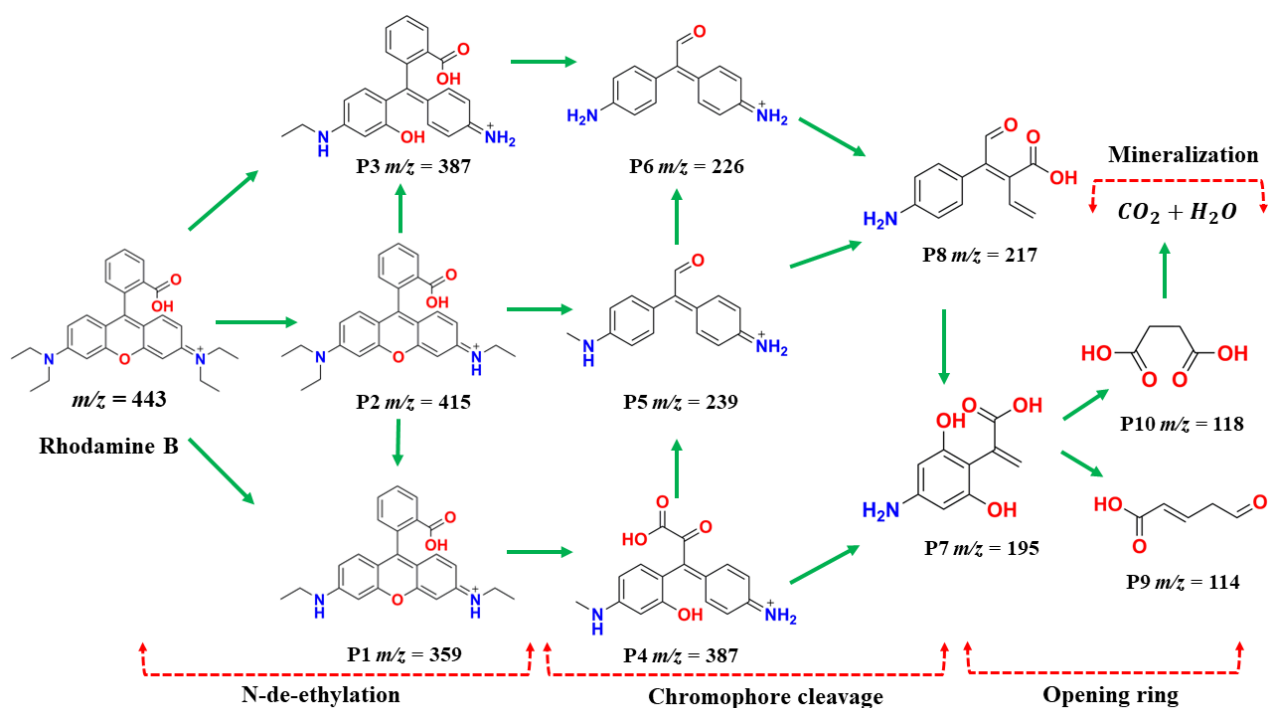
Fig.7.26. *The possible sonophotodegradation pathways of RhB.*

Table 7.8. *Degradation products of RhB identified by HPLC*

Intermediates	t_R (min)	m/z	Chemical structure
	-	443	
P1	2.48	359	
P2	2.01	415	
P3	3.69	387	

			Structure
P4	1.75	300	
P5	2.08	239	
P6	1.14	226	
P7	1.66	195	
P8	1.41	217	
P9	1.75	114	
P10	2.12	118	

7.3.14. Mechanism of sonophotocatalysis

The sonophotocatalytic processes typically operate based on the hot-spot theory, the sonoluminescence phenomenon, and visible light-driven photocatalysis. By combining visible light and ultrasonic waves, the degradation of RhB occurs through the following sequence of events [45]: First, cavitation bubbles undergo a nucleation process, which is facilitated by the presence of nano solid particles in the solution. Nucleation is relatively easier on the surface of these solid particles. Next, these cavitation bubbles grow continuously under the action of ultrasonic waves. Eventually, they reach a certain size and collapse, leading to the formation of 'sonic luminescence' (SL) and the generation of high temperatures. This process causes hydrothermal decomposition, generating hydroxyl radicals [46]. The light and heat generated by ultrasonic cavitation excite

nanoparticles, resulting in the continuous formation of electron-hole pairs, known as sono-photo induced electron hole pairs. These pairs play a key role in enhancing the degradation reaction through an advanced oxidation process.

The degradation is facilitated by free radicals generated through water pyrolysis and photo-thermal catalysis pathways [46]. Results from active species test experiments indicate the significant involvement of electrons (e⁻), holes (h⁺), and hydroxyl radicals (•OH) in supporting the sonophotocatalytic degradation of RhB. Sonoluminescence, caused by ultrasound irradiation, can excite $BiVO_4$ to form sono-photo-generated hole-electron pairs. These generated holes (h⁺) can transfer to the surface of $BiVO_4$ and oxidize the adsorbed H_2O molecules, or –OH to produce •OH, which directly degrades RhB adsorbed on the surface of $BiVO_4$. The reaction equations are as follows [47]:

$$BiVO_4 + h\nu \rightarrow h^+ + e^-$$

$$h^+ + H_2O \rightarrow \bullet OH + \bullet H$$

$$h^+ + OH^- \rightarrow \bullet OH$$

$$h^+ + RhB \rightarrow H_2O + CO_2 + NO_3^- + NH_4^-$$

$$\bullet OH + RhB \rightarrow H_2O + CO_2 + NO_3^- + NH_4^-$$
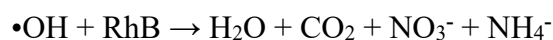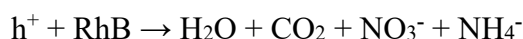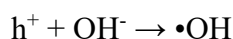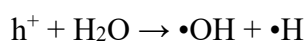
The sonophotocatalytic degradation combines sonochemical and photocatalytic processes, with the degradation rate of RhB higher than the sum of their individual rates.
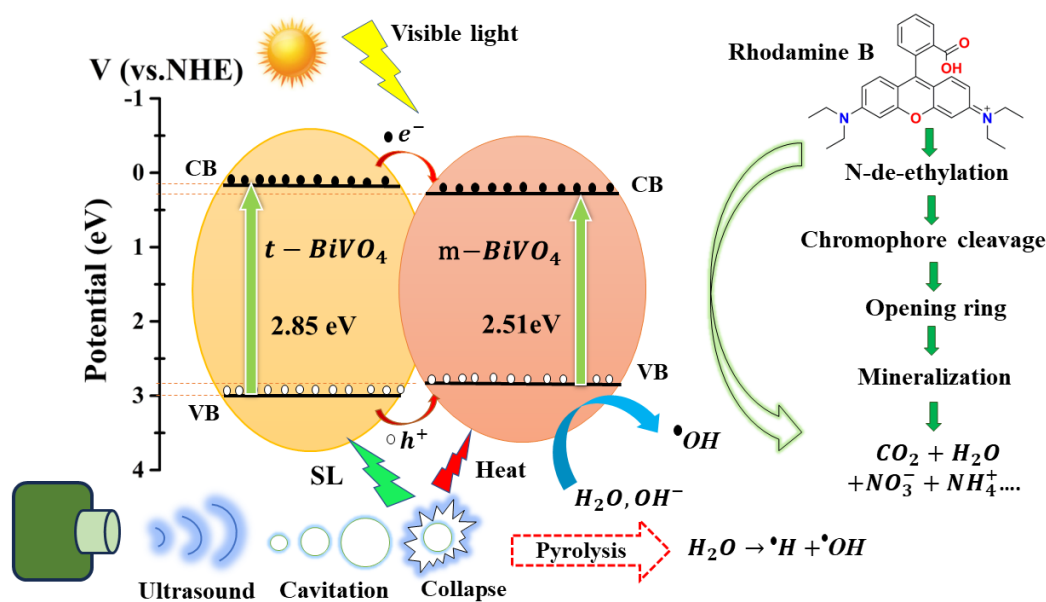
Fig.7.27. The mechanism of degradation of RhB under the irradiation of ultrasonic sound and visible light in the m-t-BiVO₄ heterostructure.

This enhancement may be attributed to the physical effects of cavitation bubbles facilitating the transfer of RhB from the bulk solution to the BiVO₄ surface and the cleaning of degradation products from the surface. This cleaning enhances the rate of RhB degradation by increasing the number of active reaction sites on BiVO₄.

 The schematic diagram of the mechanism of degradation of RhB under the irradiation of visible light and ultrasonic sound is shown in Fig.7.27.

Numerous investigations have established a strong correlation between the photocatalytic performance of BiVO₄ materials and their crystal structure and morphology [47]. In our current study, we have observed that the BVO-0.2 sample, which possesses a mixed-phase structure of BiVO₄, exhibits superior photocatalytic, sonocatalytic, and sonophotocatalytic efficiency when subjected to visible light and ultrasonic sound. The enhanced efficiency of the BVO-0.2 sample can be attributed to its high carrier concentration, mobility, and conductivity. The distortion in the $(VO)_4{}^{3-}$ tetrahedron enhances the impact of Bi 6s states, leading to unique optical properties and excellent photocatalytic activity. The sample's suitable bandgap prevents the recombination of photogenerated electron-hole pairs, while its surface roughness improves adsorptive behaviour.

In addition, the presence of two distinct crystal structures within BVO-0.2 enables a type of semiconductor coupling, thereby facilitating activation across a broader range of visible. An interfacial heterojunction structure between the tetragonal type and monoclinic phases of BiVO₄ facilitates efficient electron tunnelling from the CB of the tetragonal phase to the CB of the monoclinic phase. Additionally, holes originating from the valence band of the tetragonal zircon BiVO₄ phase effectively inject into the valence band of the monoclinic BiVO₄ phase, preventing electron-hole recombination and thus enhancing the photocatalytic activity. The transport properties of photoinduced charge carriers in the semiconductor material significantly contribute to improved sonophotocatalytic performance.

We compared the degradation efficiency of BVO-0.2 with other catalysts used in the sonophotocatalytic removal of RhB. The comparison is summarized in Table.7.9. in the supplementary section. It illustrates that the isotype BiVO₄ heterojunction serves as an excellent catalyst for removing RhB from water.

Table.7.9. *Comparison with other catalysts for the removal of RhB using sonophotocatalysis.*

Catalyst	Experimental condition	Dosage of the catalyst (g/L)	Degradation efficiency (%)	Time (min.)	Reference
NiTiO$_3$/ZnO	5 ppm Xe lamp 35W Ultrasound sonicator 60 KHz,37W	0.5	95	120	María E. Zarazúa-Morín *et al*. [48]
MgWO$_4$ modified Ag NPs	~5 ppm UV-C lamp 20W OSRAM Ultrasound sonicator 40 KHz, 100W	1.0	92.3	240	Vitoria E.M. Vieira *et al*. [49]
Bi$_2$WO$_6$	10 ppm Xe lamp (400 W, XT-400-E40) ultrasonic horn (BRANSON, digital Sonifier 450, and 20 kHz)	1.0	100	120	Mahboobeh Zargazi *et al*. [50]
N-Ti^{3+} co-doped TiO$_2$-Bi$_2$WO$_6$	20 ppm 500 W Xenon lamp ultrasonic cleaner 35 kHz, 180 W,	0.5	97	100	Mingxuan Sun *et al*. [51]
CeO$_2$/Ag$_2$CrO$_4$	6 ppm LED lamp	1.25	89.78	40	M M Sabzehmeidani *et al*. [52]
BiVO$_4$	**10 ppm Xe arc lamp 300W Ultrasonic cleaner 40kHz, 50 W**	**0.5**	**100**	**90**	**Present work**

7.4.CONCLUSION

As a result of a quick and facile hydrothermal method, pure and mixed phases of BiVO$_4$ visible-light and ultrasonic sound-driven semiconducting catalysts have been successfully synthesized. Significantly, this novel approach offers a productive way to adjust the structural, morphological, and electronic properties of BiVO$_4$ by carefully adjusting the dosage of the surfactants. The morphological and structural characteristics of synthesized BiVO$_4$ were thoroughly examined. Additionally, it was shown how the phase transformation affected the local structural variations in bond length and bond strength of the $(VO)_4{}^{3-}$ tetrahedral unit of BiVO$_4$. The deviations in electronic properties in mixed-phase BiVO$_4$ were attributed to the abrupt change in band gap energy in accordance with structural transformation. Significantly, under both visible light and ultrasonic sound waves, mixed phase BiVO$_4$ displays the highest sonophotocatalytic degradation efficiency of Rhodamine B (RhB) dye at 100% with an average kinetics rate $k_{app} = (5.70 \pm 0.04) \times 10^{-2} min^{-1}$. The current study proved the significance of interface formation and distortions in mixed-phase BiVO$_4$, which promotes the sonophotocatalytic activity, and demonstrated the comparative sonophotocatalytic activity of the monoclinic, tetragonal, and mixed-phase BiVO$_4$ materials. The high carrier concentration, mobility, conductivity, and distortions in the $(VO)_4{}^{3-}$ tetrahedron, which resulted in unique optical properties and excellent catalytic activity, are attributed to the high degradation rate of RhB by the BVO-0.2 sample. The electrons (e$^-$), holes (h$^+$), and hydroxyl radicals (•OH) are important active radicals during sonophotocatalysis, according to the results of the free-radical trapping (scavenger) tests. Various factors affecting the degradation reaction, such as temperature, catalyst dosage, and initial dye concentration, were examined to optimize reaction conditions for industrial applications. Additionally, the catalyst retained 90% degradation efficiency even after five cycles of use. Degradation products were identified using HPLC analysis, proposing a degradation pathway for RhB. The study on isotype BiVO$_4$ will pave the way for developing mixed-phase sonophotocatalysts for environmental remediation.

7.5. REFERENCES

[1] Subhiksha, V., Kokilavani, S., & Khan, S. S. (2022). Recent advances in degradation of organic pollutant in aqueous solutions using bismuth based photocatalysts: A review. *Chemosphere*, *290*, 133228.

[2] Zhong, X., Li, Y., Wu, H., & Xie, R. (2023). Recent progress in BiVO4-based heterojunction nanomaterials for photocatalytic applications. *Materials Science and Engineering: B*, *289*, 116278.

[3] Rashmi, Gyanprakash, M. D., Gadhewal, M., Pala, R. G. S., & Sivakumar, S. (2022). Deconvoluting Photoelectrochemical Activity in Monoclinic–Scheelite BiVO4 Facet Selected Thin Films. *The Journal of Physical Chemistry C*, *126*(38), 16477-16491.

[4] Tian, K., Wu, L., Han, T., Gao, L., Wang, P., Chai, H., & Jin, J. (2022). Dual modification of BiVO4 photoanode by rare earth element neodymium doping and further NiFe2O4 co-catalyst deposition for efficient photoelectrochemical water oxidation. *Journal of Alloys and Compounds*, *923*, 166352.

[5] Usai, S., Obregón, S., Becerro, A. I., & Colón, G. (2013). Monoclinic–tetragonal heterostructured BiVO4 by yttrium doping with improved photocatalytic activity. *The Journal of Physical Chemistry C*, *117*(46), 24479-24484.

[6] Hong, S. J., Lee, S., Jang, J. S., & Lee, J. S. (2011). Heterojunction BiVO 4/WO 3 electrodes for enhanced photoactivity of water oxidation. *Energy & Environmental Science*, *4*(5), 1781-1787.

[7] Yao, W., Iwai, H., & Ye, J. (2008). Effects of molybdenum substitution on the photocatalytic behavior of BiVO 4. *Dalton Transactions*, (11), 1426-1430.

[8] Quang, N. D., Van, P. C., Majumder, S., Jeong, J. R., Kim, D., & Kim, C. (2022). Optimization of photogenerated charge transport using type-II heterojunction structure of CoP/BiVO4: WO3 for high efficient solar-driver water splitting. *Journal of Alloys and Compounds*, *899*, 163292.

[9] Wang, S., Cui, D., Hao, W., & Du, Y. (2022). Roles of Co-catalysts on BiVO4 Photoanodes for Photoelectrochemical Water Oxidation: A Minireview. *Energy & Fuels*, *36*(19), 11394-11403.

[10] Wang, F., Xie, L., Sun, N., Zhi, T., Zhang, M., Liu, Y., ... & Wang, L. (2024). Deformable Catalytic Material Derived from Mechanical Flexibility for Hydrogen Evolution Reaction. *Nano-Micro Letters*, *16*(1), 1-25.

[11] Wu, X., Tan, H. L., Zhang, C., Teng, Z., Liu, Z., Ng, Y. H., ... & Su, C. (2023). Recent advances in two-dimensional ultrathin Bi-based photocatalysts. *Progress in Materials Science*, *133*, 101047.

[12] Sajid, M. M., Alomayri, T., Zhai, H., & Kareem, A. A. (2023). Construction of novel an in-situ m-BiVO4/t-BiVO4 isotype heterojunction photocatalyst for improved visible light-dependent degradation of dye. *Inorganic Chemistry Communications*, *157*, 111335.

[13] Bera, K. K., Chakraborty, M., Mondal, M., Banik, S., & Bhattacharya, S. K. (2020). Synthesis of α-β Bi2O3 heterojunction photocatalyst and evaluation of reaction

mechanism for degradation of RhB dye under natural sunlight. *Ceramics International*, *46*(6), 7667-7680.

[14]   An, X., Hu, C., Liu, H., & Qu, J. (2018). Hierarchical nanotubular anatase/rutile/TiO2 (B) heterophase junction with oxygen vacancies for enhanced photocatalytic H2 production. *Langmuir*, *34*(5), 1883-1889.

[15]   Fung, C. M., Ng, B. J., Er, C. C., Chong, W. K., Low, J., Guo, X., ... & Chai, S. P. (2023). Engineering Nanoscale Homo–Heterojunction for Robust Z-Scheme CO2 Conversion through Synchronous Amalgamation of Oxygen-Defective Ultrathin BiVO4 and Red/Black Phosphorus. *Small Structures*, 2300083.

[16]   Huang, L., Huang, X., Yan, J., Liu, Y., Jiang, H., Zhang, H., ... & Liu, Q. (2023). Research progresses on the application of perovskite in adsorption and photocatalytic removal of water pollutants. *Journal of Hazardous Materials*, *442*, 130024.

[17]   Bao, J., Guo, S., Fan, D., Cheng, J., Zhang, Y., & Pang, X. (2023). Sonoactivated Nanomaterials: A potent armament for wastewater treatment. *Ultrasonics Sonochemistry*, *99*, 106569.

[18]   Zheng, H., Zheng, Y., & Zhu, J. (2022). Recent developments in hydrodynamic cavitation reactors: Cavitation mechanism, reactor design, and applications. *Engineering*.

[19]   Fan, G., Cai, C., Yang, S., Du, B., Luo, J., Chen, Y., ... & Wang, Y. (2022). Sonophotocatalytic degradation of ciprofloxacin by Bi2MoO6/FeVO4 heterojunction: Insights into performance, mechanism and pathway. *Separation and Purification Technology*, *303*, 122251.

[20]   Guo, Y., Wei, X., Zhang, K., Zhang, J., Mi, L., Wu, Z., ... & Qi, X. (2023). Study on the growth mechanism of dispersed monoclinic BiVO4 in hydrothermal process and its photocatalytic activity. *Journal of Dispersion Science and Technology*, *44*(9), 1549-1561.

[21]   Correa, A. S., Rabelo, L. G., Rosa, W. S., Khan, N., Krishnamurthy, S., Khan, S., & Gonçalves, R. V. (2023). Interfacial band alignment and photoelectrochemical properties of all-sputtered BiVO 4/FeNiO x and BiVO 4/FeMnO xp–n heterojunctions. *Energy Advances*, *2*(1), 123-136.

[22]   Nanakkal, A. R., & Alexander, L. K. (2017). Graphene/BiVO 4/TiO 2 nanocomposite: tuning band gap energies for superior photocatalytic activity under visible light. *Journal of Materials Science*, *52*, 7997-8006.

[23]   Dheivasigamani, T., Ammasai, K., Shanmugam, P., Selvam, G. S., & Arulmozhi, D. (2023). Size and surface-engineered BiVO 4 catalytic smooth spheres for efficient electrochemical detection of bifenox herbicide. *New Journal of Chemistry*, *47*(33), 15609-15621.

[24]   Hardcastle, F. D., & Wachs, I. E. (1991). Determination of vanadium-oxygen bond distances and bond orders by Raman spectroscopy. *The Journal of Physical Chemistry*, *95*(13), 5031-5041.

[25]   Nikam, S., & Joshi, S. (2016). Irreversible phase transition in BiVO 4 nanostructures synthesized by a polyol method and enhancement in photo degradation of methylene blue. *RSC advances*, *6*(109), 107463-107474.

[26]   Ilyas, A., Rafiq, K., Abid, M. Z., Rauf, A., & Hussain, E. (2023). Growth of villi-microstructured bismuth vanadate (Vm-BiVO 4) for photocatalytic degradation of crystal violet dye. *RSC advances*, *13*(4), 2379-2391.

[27]   Dreyer, G., & Tillmanns, E. (1981). Dreyerit: ein natürliches, tetragonales Wismutvanadat von Hirschhorn/Pfalz.

[28]   Sleight, A. W., Chen, H. Y., Ferretti, A., & Cox, D. E. (1979). Crystal growth and structure of BiVO4. *Materials Research Bulletin*, *14*(12), 1571-1581.

[29]   Chen, Y., Liu, Y., Xie, X., Li, C., Si, Y., Zhang, M., & Yan, Q. (2019). Synthesis flower-like BiVO 4/BiOI core/shell heterostructure photocatalyst for tetracycline degradation under visible-light irradiation. *Journal of Materials Science: Materials in Electronics*, *30*, 9311-9321.

[30]   Ge, J., Ding, X., Jiang, D., Zhang, L., & Du, P. (2021). Efficient improved charge separation of FeP decorated worm-like nanoporous BiVO 4 photoanodes for solar-driven water splitting. *Catalysis Letters*, *151*, 1231-1238.

[31]   Kamble, G. S., & Ling, Y. C. (2020). Solvothermal synthesis of facet-dependent BiVO4 photocatalyst with enhanced visible-light-driven photocatalytic degradation of organic pollutant: assessment of toxicity by zebrafish embryo. *Scientific Reports*, *10*(1), 12993.

[32]   Zhang, X., Wang, G., Liu, X., Xu, Y., & Kong, L. (2022). Microstructural analysis of pore characteristics of natural structured clay. *Bulletin of Engineering Geology and the Environment*, *81*(11), 473.

[33]   Merupo, V. I., Velumani, S., Ordon, K., Errien, N., Szade, J., & Kassiba, A. H. (2015). Structural and optical characterization of ball-milled copper-doped bismuth vanadium oxide (BiVO 4). *CrystEngComm*, *17*(17), 3366-3375.

[34]   Zhao, Z., Li, Z., & Zou, Z. (2011). Electronic structure and optical properties of monoclinic clinobisvanite BiVO 4. *Physical Chemistry Chemical Physics*, *13*(10), 4746-4753.

[35]   Cho, Y. S., Nguyen, H. H., & Nguyen, T. T. H. (2023). Modeling of slurry-type photocatalytic reactors containing core-shell particles for predicting transient behaviours based on Langmuir-Hinshelwood kinetics. *Catalysis Today*, *411*, 113909.

[36]   Kweon, K. E., & Hwang, G. S. (2013). Structural phase-dependent hole localization and transport in bismuth vanadate. *Physical Review B*, *87*(20), 205202.

[37] Rani, M., & Shanker, U. (2023). Highly efficient sunlight driven photo-adsorptive degradation of organic pollutants by green synthesized Z-Scheme heterojunction CeO2@ ZnO nanocomposite. *Environmental Science: Nano*.

[38] Laidler, K. J., & King, M. C. (1983). The development of transition-state theory. *J. phys. Chem*, *87*(15), 2657-2664.

[39] Rub, M. A., Hasan, T., Akter, R., Kumar, D., Asiri, A. M., & Hoque, M. A. (2023). Physico-chemical investigation of the assembly and clouding development nature of the mixture of metformin hydrochloride and ionic/nonionic surfactants: Influences of hydrotropes. *Journal of Molecular Liquids*, *371*, 121070.

[40] Kumar, V., Das, D., & Mahto, V. K. (2023). A kinetic study and thermometric analysis on waste cooking oil. *Biomass Conversion and Biorefinery*, 1-10.

[41] Groeneveld, I., Kanelli, M., Ariese, F., & van Bommel, M. R. (2023). Parameters that affect the photodegradation of dyes and pigments in solution and on substrate–An overview. *Dyes and Pigments*, *210*, 110999.

[42] Wu, S., Li, X., Tian, Y., Lin, Y., & Hu, Y. H. (2021). Excellent photocatalytic degradation of tetracycline over black anatase-TiO2 under visible light. *Chemical Engineering Journal*, *406*, 126747.

[43] Zhang, J., Li, X., Chen, H., Qi, M., Zhang, G., Hu, H., & Ma, X. (2017). Hydrogen production by catalytic methane decomposition: Carbon materials as catalysts or catalyst supports. *International Journal of Hydrogen Energy*, *42*(31), 19755-19775.

[44] Xie, R., Fang, K., Liu, Y., Chen, W., Fan, J., Wang, X., ... & Song, Y. (2020). Z-scheme In 2 O 3/WO 3 heterogeneous photocatalysts with enhanced visible-light-driven photocatalytic activity toward degradation of organic dyes. *Journal of Materials Science*, *55*, 11919-11937.

[45] Mehrizad, A., Behnajady, M. A., Gharbani, P., & Sabbagh, S. (2019). Sonocatalytic degradation of Acid Red 1 by sonochemically synthesized zinc sulfide-titanium dioxide nanotubes: Optimization, kinetics and thermodynamics studies. *Journal of cleaner production*, *215*, 1341-1350.

[46] Xu, L., An, H. L., Wu, X. Q., Ju, W. T., Wang, Y., Wang, X. F., & Wang, X. (2023). Sonocatalytic degradation of tetracycline by Cu2O/MgFe2O4 nanocomposites: Operational parameters, sonocatalytic mechanism, degradation pathways, and environmental toxicity. *Surfaces and Interfaces*, *41*, 103202.

[47]   Wang, T., Cai, J., Zheng, J., Fang, K., Hussain, I., & Husein, D. Z. (2022). Facile synthesis of activated biochar/BiVO4 heterojunction photocatalyst to enhance visible light efficient degradation for dye and antibiotics: applications and mechanisms. *Journal of Materials Research and Technology*, *19*, 5017-5036.

[48]   Zarazúa-Morín, M. E., Galindo-Luna, A. S., Gallegos-Sánchez, V. J., Zermeño-Resendiz, B. B., & Torres-Martínez, L. M. (2022). Novel hydrothermal-assisted microwave synthesis of NiTiO3/ZnO and sonophotocatalytic effect for degradation of rhodamine B. *Topics in Catalysis*, *65*(13), 1182-1190.

[49]   Vieira, V. E., Lopes, F. H., Noleto, L. F., Costa, M. J., Silva, R. M., Gusmão, G. O., ... & Luz Jr, G. E. (2023). Sonophotocatalytic degradation of Rhodamine b dye on MgWO4 crystals modified with AgNPs. *Journal of Photochemistry and Photobiology A: Chemistry*, *444*, 114943.

[50]   Zargazi, M., & Entezari, M. H. (2019). Sonochemical versus hydrothermal synthesis of bismuth tungstate nanostructures: Photocatalytic, sonocatalytic and sonophotocatalytic activities. *Ultrasonics sonochemistry*, *51*, 1-11.

[51]   Sun, M., Yao, Y., Ding, W., & Anandan, S. (2020). N/Ti3+ co-doping biphasic TiO2/Bi2WO6 heterojunctions: hydrothermal fabrication and sonophotocatalytic degradation of organic pollutants. *Journal of Alloys and Compounds*, *820*, 153172.

[52]   Sabzehmeidani, M. M., Karimi, H., & Ghaedi, M. (2019). Sonophotocatalytic treatment of rhodamine B using visible-light-driven CeO 2/Ag 2 CrO 4 composite in a batch mode based on ribbon-like CeO 2 nanofibers via electrospinning. *Environmental Science and Pollution Research*, *26*, 8050-8068.

CHAPTER 8

Summary and Conclusion
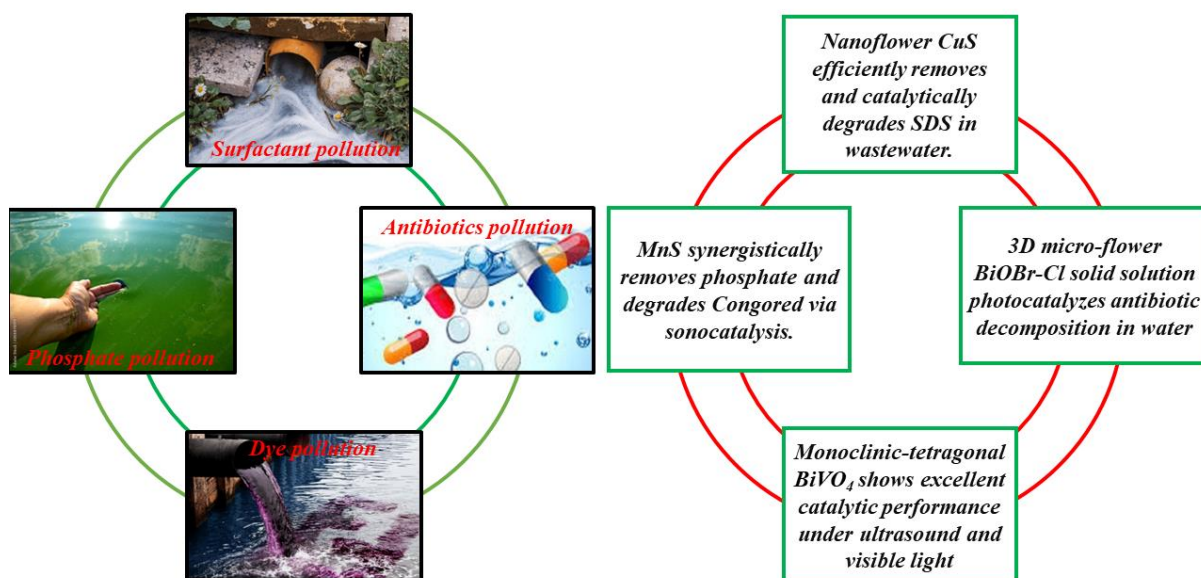
This chapter presents a comprehensive summary of the thesis, aligned with the primary objectives, and concludes the research work.

The thesis, ***Insights on Adsorptive and Catalytic Water Remediation Using Metal Chalcogenides and Bismuth-Based Nanomaterials,*** explores water remediation using adsorption and advanced oxidation processes. It targets pollutants like surfactants, phosphate ions, antibiotics, and industrial dyes, achieving nearly 100% removal efficiency through the development of four nanomaterials. The study investigates mechanisms, kinetics, thermodynamics, and pollutant degradation pathways.

To enhance adsorption, morphology and crystalline phases were optimized by varying synthesis conditions. CuS nanoflowers were developed for removing sodium dodecyl sulfate, while MnS nanomaterials with varying crystalline phases were studied for phosphate adsorption.

Catalytic activity was improved using two strategies: solid solution formation and isotype heterojunctions. BiOBr-Cl solid solutions tuned the optical bandgap from 3.39 eV to 2.75 eV through halide alloying, enhancing photocatalytic performance. $BiOBr_{0.25}Cl_{0.75}$ proved effective for antibiotic degradation. Additionally, mixed-phase $BiVO_4$ heterostructures demonstrated superior sonocatalytic and photocatalytic activity. The monoclinic-tetragonal heterojunctions enhanced charge separation and transfer, significantly improving photocatalytic efficiency.

Concisely, our investigation in the thesis was mainly focused on the five objectives outlined in Chapter 1, Section 1.8. Based on these objectives, we have endeavoured to explore the various properties of metal chalcogenides and Bi-based nanomaterials for water purification.

The brief description of the thesis is the following:

In this thesis, we efficiently decomposed sodium dodecyl sulfate (SDS) from industrial effluents using CuS nanoflowers as an efficient adsorbent and catalyst. The efficient adsorption and fast catalytic decomposition of SDS into CO_2 and water was driven by hemi-micelle enhanced adsorption and the synergistic action of H_2O_2. The mechanism of surfactant adsorption on CuS nanoflowers was analyzed using various adsorption isotherm models, with adsorption kinetics governed by pseudo-first-order kinetics and intraparticle diffusion. The process was endothermic and enthalpy-driven, and the catalytic activity resembled a Fenton-like process, which is rare in chalcogenides. This study highlights the potential of copper chalcogenides for industrially scalable, energy-efficient surfactant remediation.

We also introduced a dual-functional MnS nanomaterial for removing phosphate ions and Congo Red dye. MnS nanomaterials, synthesized via a hydrothermal route, showed a phosphate adsorption capacity of 160.73 mg P/g and demonstrated a spontaneous, exothermic adsorption process. FTIR analysis confirmed that the adsorption mechanism involved electrostatic attraction, surface complexation, and ion exchange. MnS maintained its adsorption capacity despite competing ions and exhibited high sonocatalytic efficiency, degrading Congo Red dye within 10 minutes of ultrasonic irradiation. These findings underscore MnS as a promising alternative to lanthanum or zirconium-based materials for the removal of phosphate and textile dyes from wastewater. The results suggest that MnS nanomaterials are promising for practical applications in phosphate removal and textile dye degradation from wastewater.

For the removal of residual antibiotics in water, we explored the potential of photocatalytic processes as an eco-friendly solution. We synthesized $BiOBr_{(1-x)}Cl_x$ nanoplates solid solutions with varied Br:Cl molar ratios through a simple co-precipitation method. These solid solutions exhibited superior visible-light-driven photocatalytic activity compared to pristine BiOCl and BiOBr. The $BiOBr_{0.25}Cl_{0.75}$ sample achieved 89% and 99% degradation efficiency for ciprofloxacin (CIP) and tetracycline hydrochloride (TCH), respectively, within 20 minutes under optimum conditions. The performance was attributed to a large specific surface area, suitable morphology and band gap, effective separation of photo-generated electron-hole pairs, and meso-size pores. The solid solution demonstrated facile recyclability, robust stability, and adaptability to aquatic environments.

Additionally, we developed a heterojunction $BiVO_4$ structure by incorporating two distinct crystal phases within a single semiconducting material. We synthesized tetragonal, monoclinic, and monoclinic/tetragonal heterophase $BiVO_4$ photocatalysts using a hydrothermal procedure. The photocatalytic activity of $BiVO_4$ samples was examined by monitoring the degradation of Rhodamine B (RhB). Ultrasonic sound waves were employed to enhance the degradation reaction. The study examined the photocatalytic, sonocatalytic, and sonophotocatalytic activity of $BiVO_4$ microcrystals in relation to the degradation of RhB dye. The results showed that the crystalline phases of $BiVO_4$ samples significantly influenced the behaviour of photo-sono-induced charges. An interface in the monoclinic/tetragonal heterophase facilitated charge transfer and

enhanced the separation of photo-sono-induced electron-hole pairs. This study provides insight into the reasons for the enhancement in sonophotocatalytic activity.

Through this work, we have successfully achieved all our research objectives. To address the first objective, we synthesized CuS nanoflowers and demonstrated their ability to completely remove and decompose SDS molecules. For the second objective, we synthesized MnS nanostructures, which effectively removed phosphate ions from water. To fulfill the third objective, we utilized MnS nanostructures and BiVO$_4$ for the sonocatalytic degradation of Congo Red and Rhodamine B dyes in water. We also investigated the synergistic effect of sonocatalysis and photocatalysis in the degradation of Rhodamine B using BiVO$_4$ heterostructures. To achieve the fourth objective, bismuth oxyhalide solid solutions were employed for the degradation of antibiotics in wastewater. For the fifth objective, isotype BiVO$_4$ heterostructures were synthesized and used for sonophotocatalytic degradation of industrial dye in wastewater.

In conclusion, this thesis presents significant advancements in water remediation using metal chalcogenides and Bi-based nanomaterials. Through systematic research, we developed four nanomaterials - CuS nanoflowers, MnS nanomaterials, $BiOBr_{(1-x)}Cl_x$ solid solutions, and heterojunction BiVO$_4$ structures—each demonstrating exceptional performance in removing various industrial pollutants, viz. sodium dodecyl sulfate, phosphate ions, antibiotics, congo red dye and rhodamine B dye. These findings underscore the potential of these nanomaterials for scalable water purification and provide deeper insights into the mechanisms governing adsorption and catalytic processes. This research highlights the promise of metal chalcogenides and bismuth-based nanomaterials as innovative solutions for addressing water pollution challenges.

CHAPTER 9

Recommendations

This chapter outlines recommendations for future research directions based on the findings of this study.

RECOMMENDATIONS FOR THE FUTURE WORKS

The present research introduces four novel nanomaterials specifically designed to target four different types of pollutants commonly found in industrial effluents. These nanomaterials have been effectively demonstrated for removing contaminants in an aqueous medium at the laboratory level, showcasing their potential for practical application. The successful integration of the described physico-chemical methods into existing wastewater treatment systems can significantly advance the potential of this work, as discussed in this thesis, to facilitate the implementation of practical water treatment solutions.

The catalysts synthesised in this study are currently demonstrated at a laboratory scale. Throughout the thesis, keeping in mind the industrial scalability, we have attempted to explore the utility of naturally abundant nanomaterials synthesised using facile routes. These catalysts need to be synthesised on a larger scale with high purity for practical applications in water treatment systems.

The adsorbents synthesised in this research can be integrated with commercial adsorbents such as activated carbon, carbon nanotubes (CNT), and graphitic carbon nitride (g-C_3N_4). This combination is expected to enhance the adsorptive properties of the materials, improving their efficiency for practical applications. By leveraging the synergistic effects of these hybrid materials, the overall adsorption capacity and selectivity can be improved, facilitating their commercialisation for large-scale environmental remediation efforts.

For future work, it is recommended to systematically study the impact of multiple impurities on the efficiency of water purification system to ensure the real-world applicability of the developed nanomaterials. Evaluating how various co-existing contaminants influence the removal performance of the synthesised nanomaterials under different operational conditions will be crucial. These studies will optimise the design and application of the materials in complex wastewater matrices, enhancing their practical utility in industrial effluent treatment systems.

It is also recommended to incorporate advanced characterisation techniques such as X-ray photoelectron spectroscopy (XPS), electrochemical impedance spectroscopy (EIS), Mott-Schottky analysis, and electron paramagnetic resonance (EPR) under an applied magnetic field. These techniques will provide valuable insights into the electronic

structure, surface chemistry, charge carrier dynamics and magnetic properties of the developed nanomaterials. Such comprehensive analyses will enhance understanding of the mechanisms driving the observed catalytic and adsorption behaviours, informing the optimisation and development of more efficient materials for environmental remediation applications.

Developing a comprehensive wastewater treatment system that integrates the adsorption techniques and various catalytic processes discussed in this thesis is recommended. This system should be designed to optimise the removal of diverse contaminants from industrial effluents by leveraging the synergistic effects of advanced adsorbents and catalysts. Implementing such a system will enhance the overall efficiency and effectiveness of wastewater treatment, facilitating the practical application of the research findings in real-world scenarios.

"Our biggest challenge in this new century is to take an idea that seems abstract – sustainable development – and turn it into a reality for all the world's people."

— Kofi Annan

****